POLITECNICO
MILANO 1863

Department of Civil & Environmental Engineering

Doctoral Program in Structural,
Seismic and Geotechnical Engineering

XXXIV Cycle

---

# THE PHASE-FIELD MODELING OF FRACTURE EVOLUTION IN DUCTILE MATERIALS WITH APPLICATION TO PAPERBOARD MECHANICS

---

Doctoral Dissertation of:
Alessandro Marengo

Supervisor:
Prof. Umberto Perego

Tutor:
Prof. Luca Martinelli

The Chair of the Doctoral Program:
Prof. Stefano Mariani

---

Milan - February 2023

# THE PHASE-FIELD MODELING OF FRACTURE EVOLUTION IN DUCTILE MATERIALS WITH APPLICATION TO PAPERBOARD MECHANICS

A Thesis
Presented to
The Academic Faculty

by

**Alessandro Marengo**

In Partial Fulfilment
of the Requirements for the Degree of
Doctor of Philosophy

in
Structural, Seismic and Geotechnical Engineering

February 2023

THE PHASE-FIELD MODELING OF FRACTURE EVOLUTION IN DUCTILE MATERIALS WITH APPLICATION TO PAPERBOARD MECHANICS

PhD thesis by Alessandro Marengo
Advisor: Prof. Umberto Perego



Doctoral Program in Structural, Seismic and Geotechnical Engineering
Department of Civil & Environmental Engineering
Politecnico di Milano

XXXIV Cycle - 2018-2021

# Acknowledgments

This is the final stage of a long path started many years ago, where the PhD was only the last step. The first acknowledgment goes to my supervisor professor Umberto Perego. He helped me along the way with never-ending meetings discussing formulations and mathematical models. Yet, always with a smile and a natural inclination to make jokes. He shared a wide part of his knowledge and his contacts with me, and I will always be grateful for this. The second acknowledgment goes to the funders of my research activity. The interest in paperboard mechanics comes from Innovhub - Stazioni sperimentali per l'industria and Politecnico di Milano. An unexpected surprise came with the acquaintance of professor Matti Ristinmaa during my stage at Lund University (Sweden). This was a tough time, since it coincided with the pandemic outbreak. Still, I had a fantastic experience with a great expert in mechanics of materials that taught me everything I know about programming in Fortran language. A further acknowledgment goes to Tetra Pak. Specifically, I would like to thank Eric Borgqvist and Johan Tryding for the fruitful advices on paperboard modeling and for the support in terms of experimental results present in this thesis. A special thank is for the colleagues in Pavia University. Professors Alessandro Reali and Matteo Negri together with the doctor Alessia Patton helped me to enter in the world of research in the most beautiful manner. I will always recall our long meetings discussing phase-field formulations followed by the amazing pizza lunch in Pavia. Alessia and I spent a lot of time both working hard on sorting out problems in our research, but we also shared beautiful moments outside university. A warm thank goes to my colleagues. I mention Andrea and Giorgio, especially. We shared a lot of time during the pandemic, being among the few people trying to go at the office every day. I will never forget the long discussions on finite elements, on programming practice, and last, but not least, our awful jokes. I also thank Luca, Marco, Michele, Paolo, Matteo, Cheng, Daniel, Ayrton for being such good companions in this journey. A grateful acknowledgment goes to professor José Reinoso and his coworker Aamir Dean for the help on the Abaqus implementation of phase-field. A great experience was also the stage in ETH Zurich where I had the possibility to interact with professors Laura De Lorenzis and Corrado Maurini, together with Pietro Carrara. A special thanks goes also to Francesco and Camilla. I would like to thank all my friends and my family for the support during these years.

# Abstract

Paperboard is one of the many layers composing the layered packaging material employed in the food industry for preservation of liquid products. Its purpose is to provide the mechanical properties to the final package in terms of strength and stiffness. The yearly production of this kind of packages amounts at several hundred billions units. This number motivates the intense research activity aimed at characterizing and improving the packaging material to reduce waste. Despite experimental tests may provide useful information, practical applications require a mathematical modeling based on a profound understanding of the material response. The mathematical description of paperboard response has been extensively explored in the literature in the elastoplastic regime preceding the onset of damage and fracture. The main objective of the current work is to extend the state-of-the-art elastoplastic modeling of paperboard material to include the development of damage and subsequent crack propagation.

In Computational Mechanics, the modeling of fracture evolution introduces the fundamental challenge of dealing with discontinuous displacements. In the last two decades, the phase-field approach has overcome this problem changing the description of the crack topology. Indeed, the sharp geometry is substituted with a smooth regularization governed by the order parameter called *phase-field*.

In the present work, a computationally efficient and explicit algorithm for the rigorous enforcement of the irreversibility constraint in the phase-field modeling of brittle fracture is presented. The proposed approach relies on the alternate minimization of the total energy functional. The phase-field evolution turns out to be governed by a complementarity boundary-value problem, where the complementarity stems from the irreversibility, while the boundary-value problem stems from the presence of the gradient term in the phase-field functional. A solution strategy based on the Projected Successive Over-Relaxation (PSOR) method for constrained optimization, where an iterative explicit scheme is used for the solution of symmetric linear complementarity problems, is presented.

A variational formulation of ductile fracture, based on a phase-field modeling of crack propagation, is then proposed for isotropic materials both in small and large deformations. The formulation is based on an effective stress approach, combined with an AT1 phase-field model. Starting from established variational statements of finite-step elastoplasticity for generalized standard

materials, a mixed variational statement is consistently derived, incorporating in a rigorous way a variational finite-step update for both the elastoplastic and the phase-field dissipations. The complex interaction between ductile and brittle dissipation mechanisms is modeled by assuming a plasticity driven crack propagation model. A non-variational function of the equivalent plastic strain is then introduced to modulate the phase-field dissipation based on the developed plastic strains. In the context of small strains, a gradient-extended plasticity framework has been proposed to prevent the pathological mesh-dependence due to the combination of the softening response and the continuing plastic deformation induced by the effective stress approach. Particular care has been devoted to the formulation of a consistent Newton-Raphson scheme for the gradient-extended model in the case of Mises plasticity, with a global return mapping and relative tangent matrix, supplemented by a line-search scheme, for fixed phase field. The resulting algorithm has proved to be very robust and computationally effective.

To approach the phase-field modeling of fracture in paperboard the proposed ductile fracture formulation has been extended to orthotropic materials, being ductility and orthotropy the fundamental features of the paperboard mechanical response. The resulting orthotropic, small strain phase field model for ductile fracture, based on a state-of-the-art elastoplastic in-plane model, has been applied to the simulation of failure experimental tests on paperboard strips, with excellent results in terms of accuracy and scale independence. As a first step towards the inclusion in the model of the large strain out-of-plane paperboard behavior, a large strain isotropic elastoplastic model for ductile phase-field fracture has been proposed, based on a variational update of the large strain finite-step elastoplastic phase-field problem. The gradient extension of the model and its application to orthotropic paperboard are then left for a future development.

# Contents

# 1 Introduction

## 1.1 Motivation

The reliable simulation of the initiation and evolution of fracture processes in solid media is a problem of paramount importance in Computational Mechanics, involving significant difficulties and challenges, but opening the door to fundamental real-life applications. In the wide range of possible applications, the interest of the current work is restricted to the description of the mechanical response of ductile material and, more specifically, of paperboard materials. Paperboard is in particular one of the many layers composing the layered packaging material employed in the food industry for preservation of liquid products. The main purpose of the paperboard material is to provide the mechanical properties to the final package in terms of strength and stiffness. The yearly production of this kind of packages amounts at several hundred billions units. This number motivates the intense research activity aimed at characterizing and improving the packaging material to reduce waste. Despite experimental test may provide useful information, practical applications require a mathematical modeling based on a profound understanding of the material response. Thus, the development of formulations and numerical tools able to predict the mechanical response is of immediate practical impact. The mathematical description of paperboard response has been extensively explored in the literature in the elastoplastic regime preceding the onset of damage and fracture. The main objective of the current work is the introduction of these last features into the state-of-the-art modeling of paperboard material.

## 1.2 State of the art

### 1.2.1 Brittle fracture

In this part of the introduction, we focus in particular on crack propagation in brittle elastic media. Within this context, we start from the pioneering work of Griffith (1920) who, motivated by experimental evidence, assumed that the formation of a crack dissipates a specific amount of elastic strain energy proportional to the crack surface through the fracture toughness $G_c$,

also known as the critical energy release rate. The crack does not propagate if such an energy is larger than the elastic energy spent during a virtual crack propagation. The first successful attempt to formalize this energetic theory into a variational setting can be found in Francfort and Marigo (1998), where a variational model of quasi-static brittle fracture is proposed. The novelty of this approach stems from the absence of constraints in terms of having a pre-existing crack and a well-defined crack path. Specifically, the crack pattern in the elastic medium is sought as the minimization of a suitable total energy functional, which is the sum of the internal elastic energy and of the dissipation energy associated to the crack surface propagation.

The main problem of this formulation is the necessity to deal with a sharp discontinuity on the displacement field of the body due to the formation of a crack. To overcome this issue, a regularization of the total energy functional was introduced in Bourdin et al. (2000). The idea is to use the approximation introduced in Mumford and Shah (1989) by means of elliptic functionals for image segmentation as proposed in Ambrosio and Tortorelli (1990). In the latter work, the concept of $\Gamma$-convergence (see, e.g., Dal Maso (1993)) was adopted regularizing (or diffusing) a sharp discontinuity inside a domain by means of a scalar variable, referred to as order parameter, approximating the discontinuity with a smooth transition from the continuum to the discontinuum part. A crucial feature of the approximation is the introduction of an internal length measuring the portion of the domain where the discontinuity is diffused. When the internal length parameter tends to zero, the approximation $\Gamma$-converges to the sharp discontinuity. In Bourdin et al. (2000), a two-fields functional was introduced, with the first field representing the displacement of the body, while the second one is a scalar field (typically referred to as *phase field*), ranging from 0 to 1, and playing the role of interpolating the unbroken and fully broken state of the material over a small region of the domain, proportional to the internal length-scale. Therefore, the variational principle involves the minimization of a two-fields functional and the solution of a coupled problem. It is worth noticing that the approximation of the crack surface functional contains a gradient term of the phase-field variable. Due to the non-convexity of the approximated functional, an alternate minimization iterative solution strategy (*staggered scheme*) is in general preferred to a Newton-Raphson iterative strategy involving the two fields at the same time (*monolithic scheme*). The idea is to search a stationary point of the total energy functional alternatively freezing one of the two fields and iterating until a certain convergence criterion is met. The interest in this algorithmic strategy lies on the observation that the functional to be minimized is convex in each single field. The enforcement of the stationarity with respect to the phase-field variable requires the solution of a boundary-value problem due to the presence in the functional of the gradient of the order parameter. Furthermore, in combination with the definition of the internal length, this avoids mesh-dependence of the spatial discretization when material softening occurs. Such a formulation can therefore be classified within

the framework of gradient-type models for damage mechanics.

In the early phase-field formulations of brittle fracture, the irreversibility of the evolution of the order parameter represented a main limitation, with the thermodynamic nature of this constraint directly stemming from the irreversibility of the crack propagation process. This problem was overcome in two important works Bourdin (2007); Francfort et al. (2008) where the search of local minimizers for the total energy functional is performed in time-discrete steps and the crack is prevented to heal via irreversibility of the phase-field evolution. A study on the $\Gamma$-convergence of the evolution problem can be found in Giacomini (2005).

Despite the highlighted interesting features of the models in Bourdin (2007) and Francfort et al. (2008), both of them are characterized by a symmetric behavior in tension and compression and allow for negative displacement jumps, leading to material interpenetration in cracks associated to compressive states. This issue is addressed in Amor et al. (2009), where a constraint based on the so-called unilateral contact model is introduced. The idea is to split the internal elastic energy into spherical and deviatoric parts and to account for the sign of the local volumetric change, such that the material recovers the original stiffness when experiencing a volumetric compression. A proof of $\Gamma$-convergence for this model is contained in Chambolle et al. (2018). We highlight that a similar approach based on a volumetric-deviatoric energy split was investigated for concrete damage mechanics in Comi and Perego (2001) where two different activation criteria were introduced for the damage onset in tension and compression.

The first thermodynamically consistent framework for phase-field modeling of brittle fracture was introduced in Miehe et al. (2010b). Here, the thermodynamic nature of the irreversibility constraint is explicitly stated, the unilateral contact model is reproduced with a spectral decomposition of the strain tensor, and the coupled problem is solved with a monolithic scheme. The monotonicity of the order parameter is enforced with two different approaches: (i) a rate-independent model using an approximated indicator function; (ii) a rate-dependent model involving a viscous regularization of the original functional. In a subsequent work, Miehe et al. (2010a) introduced a novel enforcement of irreversibility, yet violating the variational nature of the formulation. The idea is to shift the constraint from the phase-field variable to its driving force, via a history variable accounting for the maximum crack driving force experienced during the loading history. The coupled problem is then solved with a non-iterative staggered scheme and the introduction of a viscous regularization of the functional. The latter is used to prevent unstable crack evolutions.

A comprehensive review on different phase-field models and numerical approaches for brittle fracture can be found in Ambati et al. (2015a), where an interesting discussion on the convergence of staggered schemes is also reported. Despite many clearly positive features, it must be noted that one of the major limitations of the phase-field technique, especially for engineering-scale appli-

cations, resides in its high computational cost due to the necessity of very fine meshes along crack paths to resolve the internal length parameter. Therefore, the development of efficient solution algorithms is fundamental to tackle industrial problems.

An extensive comparison between monolithic and staggered solutions is proposed in Gerasimov and De Lorenzis (2016), while a variationally consistent approach accounting for the irreversibility of the phase-field model of brittle fracture can be found in Gerasimov and De Lorenzis (2019), where a penalization term was introduced in the variational formulation. The authors also discuss in detail the important issue of a suitable choice of the penalization coefficient, in order to avoid ill-conditioning of the finite element discretization problem.

A variationally consistent enforcement of the irreversibility constraint is proposed in Marengo et al. (2021) following the procedure outlined in Mangasarian (1977) for the solution of Symmetric Linear Complementarity Problems (SLCP), and already used in Comi and Perego (1996a) in the context of gradient plasticity with constitutive softening behavior.

### 1.2.2 Ductile fracture

Fracture propagation in elastoplastic solids presents a ductile dissipation mechanism, due to the development of plastic strains, competing and interacting with a brittle dissipation mechanism, due to the generation of new fracture surfaces. The existence of a large plastic zone with the consequent energy dissipation makes Griffith approach to brittle fracture inapplicable, as much as its elegant and well-established phase-field variational formulation introduced in Bourdin et al. (2000); Francfort and Marigo (1998). Several authors have proposed extensions of the phase-field formulation of brittle fracture incorporating plastic dissipation mechanisms. In the small deformation framework, local plasticity has been addressed, e.g., in Alessi et al. (2014); Ambati et al. (2015b,b); Choo and Sun (2018); Duda et al. (2015); Fang et al. (2019); Huang and Gao (2019); Yin and Kaliske (2020), while gradient plasticity mechanisms have been considered in Rodriguez et al. (2018); Shishvan et al. (2021); Ulloa et al. (2016); Wambacq et al. (2021). In the large deformation framework, the models Ambati et al. (2016); Borden et al. (2016); Han et al. (2022); Hu et al. (2021); Talamini et al. (2021) deal with local plasticity, while gradient plasticity has been included in the formulation in e.g., Dittmann et al. (2018); Miehe et al. (2016, 2017). A comparative review of some small-strain ductile fracture models can be found in Alessi et al. (2018a).

In Chapter 3, a variational formulation of small strain ductile fracture, based on a phase-field modeling of crack propagation, is proposed first. Starting from established variational statements of finite-step elastoplasticity for generalized standard materials Comi et al. (1991, 1992); Comi and Perego (1995); Corigliano (1994); Ortiz and Martin (1989); Reddy et al. (1987); Simo and

Honein (1990), a rather general mixed variational statement, applicable to a wide class of elastoplastic materials, is consistently derived, incorporating in a rigorous way a variational finite-step update for both the elastoplastic and the phase-field dissipations.

The formulation is based on an effective stress description of gradient plasticity, see e.g., Choo and Sun (2018); Huang and Gao (2019); Miehe et al. (2017); Ulloa et al. (2016); Wambacq et al. (2021), combined with an AT1 phase-field model as in Alessi et al. (2018b); Hu et al. (2021); Samaniego et al. (2021); Talamini et al. (2021); Wambacq et al. (2021). The term *effective stress* refers here to the true stress acting on the undamaged portion of the bulk material. The value of the effective stress is then not affected by developing damage. The main consequence of this choice is that plasticity continues to develop until the very final state of material failure, where damage approaches unity. This is in contrast to what happens when plasticity is described in terms of nominal stresses, i.e., stresses reduced by the current value of damage. In this latter case, as soon as damage starts to develop, the nominal stress decreases and the yield condition is no more satisfied, so that the final part of material deformation is purely brittle (for a discussion on effective vs nominal stresses see, e.g., Choo and Sun (2018)).

The fact that effective stresses are used and that plasticity continues to develop also in the damage localization phase, implies that, after damage has started to develop and the global structural response has become softening, incremental plastic strains tend to localize in a one-element-thick band, giving rise to a pathological mesh dependence in the final stage of rupture, see, e.g., Miehe et al. (2016). To avoid the problem, the simple and effective gradient plasticity regularization proposed in Comi and Perego (1996b) is here adopted. The presence of the gradient plasticity term introduces computational difficulties for the finite-step time integration of the nonlocal constitutive law. A computationally effective and robust Newton-Raphson scheme for the solution of the gradient elastoplastic problem for fixed damage is therefore proposed for the case of Mises plasticity, together with its global return mapping algorithm and expression of the global consistent tangent matrix. This global return mapping scheme allows to formulate the finite-step elastoplastic problem as a global linear complementarity problem. The same has been done for the phase-field problem, so that irreversibility of both plastic and brittle dissipation turns out to be enforced in a rigorous way. Both linear complementarity problems have been solved using the Projected Successive Over-Relaxation (PSOR) algorithm of Mangasarian (1977), following the approach proposed in Comi and Perego (1996b); Marengo et al. (2021).

In ductile fracture, either already existing voids, or voids nucleated under the effect of developing plastic strains at inclusions or second-phase particles, grow until they coalesce giving rise to a continuous fracture path. Voids nucleation and growth is associated to locally high levels of plastic deformation, suggesting that in most cases ductile fracture requires high levels of energy

absorption (see, e.g., Garrison and Moody (1987)). Based on these physical observations, in the proposed phase-field plasticity model, crack nucleation and propagation is assumed to be driven by plasticity. Damage development is then possible when the plastic process zone in a stress concentration region reaches a critical level, measured by the equivalent plastic strain. In practical terms, this is achieved in the model by introducing a function of the equivalent plastic strain, modulating the effective value of the material fracture energy. This is somehow in line with what has been done by several other authors (Hu et al. (2021); Huang and Gao (2019); Yin and Kaliske (2020) ), though making use of a substantially different definition of the fracture energy modulation function. Another important aspect, clearly emerging from the considered numerical applications, is the capability of the proposed plasticity driven approach to predict crack nucleation in the absence of a pre-existing crack (for a discussion on phase-field prediction of crack nucleation see, e.g., Kumar et al. (2020); Tanné et al. (2018)).

The AT1 model used here has some key conceptual and practical advantages over the AT2 model: it has a non-zero elastic limit, preventing diffuse damage at small loading and the damage localization band is of finite width Tanné et al. (2018). Both features are of importance in the considered plasticity driven framework: i) the material response remains linear elastic until the yield limit is achieved, without any damage development; ii) having a finite width, it is possible to define the phase-field characteristic length so that the phase-field localization band remains entirely contained within the plasticity process zone.

### 1.2.3 Ductile fracture of orthotropic materials

The crack evolution in elastic or elastoplastic media is a non-trivial issue in the case of material orthotropy. The directional behavior of the material can lie at different levels of the response: in the elastic, the elastoplastic, or in the fracture evolution.

The phase-field brittle fracture in large strain of an orthotropic elastic material has been considered in Raina and Miehe (2016), where the fracture dissipation remains isotropic, while the driving force is modified in a non-variational fashion. A principal stress activation criterion is postulated where only positive principal stresses are assumed to contribute to the crack propagation. Here, a structural tensor accounts for the material orientation in the activation criterion.

A structural tensor is introduced in the gradient term to turn the fracture dissipation from isotropic to orthotropic in Dean et al. (2020); Li and Maurini (2019); Quintanas-Corominas et al. (2019); Teichtmeister et al. (2017), inducing an orientation-dependent toughness. In Dean et al. (2020); Quintanas-Corominas et al. (2019); Teichtmeister et al. (2017) an orthotropic elastic energy is employed too.

The issue of the energy split to account for the promotion of crack onset

and propagation in tensile-dominated portions of the domain is addressed in Teichtmeister et al. (2017) both with an energetic approach, using the complementary energy, and with a stress criterion (see also Raina and Miehe (2016)). Both approaches rely on the spectral decomposition of the effective stress tensor. A completely different approach consists in postulating the existence of multiple failure mechanisms associated with multiple damage variables Bleyer and Alessi (2018).

The extension of orthotropic phase-field fracture to elastoplastic materials can be found in Dean et al. (2020), where the orthotropic behavior is introduced in the elastic energy, in the volumetric-dependent yield criterion, and in the fracture energy via a structural tensor approach.

### 1.2.4 Paperboard

One of the main interests in studying paperboard material lies in its wide application in the food packaging industry. Among the different layers that constitute the packaging material, paperboard provides the mechanical properties to the final product. During package forming, the paperboard sheet undergoes converting and filling procedures that mechanically stress the material. Thus, a proper mathematical modeling of the paper mechanical behavior would minimize the occurrence of manufacturing defects.

The paperboard is composed of wood-fibers that are mainly arranged into planes stacked one on to the other. The presence of multiple plies of fibers introduces a high degree of anisotropy between the in-plane and the out-of-plane (called ZD) directions of the paper sheet. The manufacturing process of the blank paperboard sheet induces an in-plane preferential orientation of the fibers too. Accordingly, two in-plane material directions can be recognized, i.e., the machine direction (MD) and the cross direction (CD). Thus, the main mechanical feature of paperboard is its orthotropic behavior in MD, CD and ZD directions, see, e.g., Borgqvist et al. (2014, 2015); Mäkelä and Östlund (2003).

A recent review on the state-of-the-art approaches for paper modeling can be found in Simon (2021). In most models as in Borgqvist et al. (2015, 2016), the hypothesis of decoupled in-plane and out-of-plane behavior is introduced. This is justified by the experimental evidence that the out-of-plane Poisson ratio is nearly zero, see, e.g., Stenberg and Fellers (2002). An in-plane orthotropic elastoplastic model of paperboard with multi-surfaces yield criterion was proposed by Xia et al. (2002). It is able to distinguish between yielding in tension and compression along the different material directions, while the out-of-plane is treated as elastic. An application to non-isotropic hardening plasticity is proposed in Borgqvist et al. (2014), where the different in-plane yield mechanisms present a coupled hardening behavior. The Xia's formulation has been subsequently extended including an elastoplastic out-of-plane behavior to capture the material response during the converting procedures. First, a cohesive elastoplastic model was used to simulate delamination in Nygårds et al. (2005);

Nygårds et al. (2009). Then, the yield criterion has been enhanced to include the additional yield mechanisms of the out-of-plane response in Borgqvist et al. (2015, 2016). A non-trivial problem concerns the modeling of damage and fracture in paperboard. The need of a nonlocal model for damage in random fiber networks has been addressed in Isaksson and Hägglund (2009). The damage localization width is related to the fiber average length as outlined in Niskanen et al. (2001). The problem of damage onset and propagation has been addressed in Isaksson et al. (2006) for isotropic paper sheets. Here a nonlocal isotropic scalar damage variable is used. The experimental justification lies in the observation that the main damage mechanism is fiber bonds failure. A more realistic nonlocal damage model for orthotropic paperboard is proposed in Isaksson et al. (2004), where three scalar internal variables are introduced to capture material failure in the directions of orthotropy MD, CD, and ZD. Here, damage irreversibility is accounted for, a unique internal length scale parameter governs the nonlocal model, and only the elastic free energy is subjected to degradation. The idea of a damage variable associated with each set of fibers can be also found in Chen and Silberstein (2019).

### 1.2.5 Reduced integration

The 4-nodes and 8-nodes linear elements are widely used in many engineering applications. The reduced integration (or one-point integration for linear shape functions) has two main objectives: the reduction of the computational cost for the element integration and the relaxation of locking phenomena. The main drawback of the reduced integration is that some fundamental deformation modes remain stressless at the element level and, then, without energy. These are spurious or zero-energy modes, and they are often named hourglass modes because of the corresponding deformed shape shown by the element in solid mechanics applications. From a mathematical point of view, the fully integrated discrete gradient, i.e., the space discretization of the shape functions physical derivatives, has the kernel dimension equal to the number of rigid body motions. Conversely, when a single-point integration is performed, the dimension of the kernel increases, since more fundamental modes produce no displacement gradients. As a matter of fact, this issue impacts also the element stiffness matrix that will show additional zero-eigenvalues corresponding to the stressless eigenmodes. This produces instability in the solution of the finite element problem, since very small perturbations exciting these modes produce a sudden onset and propagation of spurious modes. The remedy to this problem is the introduction of an artificial stabilization of the stiffness matrix at the element level. An extensive review of hourglass control in the reduced integration setting is out of the scope of the current thesis. Thus, only the relevant contributions to the proposed implementation are presented.

The pioneering work of Flanagan and Belytschko (1981) tackled the problem by defining a suitable measure of the hourglass deformation. This deformation

is responsible for the hourglass forces needed to stabilize the element against the spurious modes. The idea lies in the energy-orthogonality between the hourglass deformation and the deformation corresponding to a linear displacement field. This procedure ensures that the element passes the patch test. In this work, the kinematics, the constitutive model and the hourglass forces are linear. Here, the hourglass parameters are defined through an eigenvalue analysis of the element stiffness matrix.

In Bonet and Bhargava (1995) a novel formulation for the hourglass control is proposed for hyperelastic materials. The idea closely resembles the early work of Flanagan and Belytschko (1981). In fact, a suitable measure of the hourglass mode is computed extracting the linear displacement part from the deformation gradient and the correspondent forces are defined. Then, the 8-node element is formulated with a constant deformation gradient through a Hu-Washizu variational approach.

## 1.3 Thesis structure

The thesis is structured as follows. In Chapter 2, the phase-field variational formulation to brittle fracture is presented. While the theoretical framework is rather standard, the focus concerns the rigorous enforcement of the irreversibility constraint on the damage-like variable. In Chapter 3, a novel AT1 effective stress approach to phase-field ductile fracture with gradient-extended plasticity is introduced in small deformations. A scalar modulation function is adopted in the fracture activation criterion to model the interaction between the plastic and brittle dissipation mechanisms. Specific attention is paid to algorithmic aspects. First, a robust and efficient solution procedure for the balance of linear momentum of an elastoplastic material with non-local yield criterion is proposed. Then, to overcome the pathological locking phenomenon arising from the effective stress approach, a reduced integration with an original hourglass stabilization accounting for the material non-linearity is employed. In Chapter 4, the ductile fracture model proposed in the previous chapter is extended from isotropic to orthotropic materials. The modulation function encapsulates the orthotropic behavior. Since crack onset and propagation are assumed to be plasticity driven, the function modulating the resistance to the crack propagation is postulated to depend on a weighted scalar measure of the plastic strains, the weights being defined by the specific activated yield mode. Different yield modes are associated to the material orthotropy directions. The formulation is validated for the in-plane response of paperboard sheets, and the model predictivity is assessed through the comparison of numerical simulations with experimental tests. Finally, in Chapter 5, the ductile fracture model of Chapter 3 is extended to the large strain framework, as a preliminary step for a possible future extension of the model to include paperboard out-of-plane failure.

# 2 Brittle Fracture

## 2.1 Introduction

A brittle fracture model describes the evolution of cracks within an elastic medium. A standard phase-field regularization is introduced with a staggered solution procedure of the coupled mechanical problem. This procedure relies on the alternate minimization of the total energy functional, searching for stationary points for one of state variables (the displacement and the phase-field) while the other is frozen. The optimization with respect to the displacement field leads to the usual balance of linear momentum with elastic constants degraded by the presence of the order parameter. On the other hand, the minimization with respect to the phase-field variable leads to a variational inequality due to the irreversibility constraint. The main consequence is that the crack evolution is governed by a *complementarity boundary-value problem*, where the complementarity stems from the irreversibility, while the boundary-value problem stems from the presence of the gradient term in the surface functional approximation. The spatial discretization of the complementarity problem by means of a Galerkin formulation turns the crack evolution into a symmetric complementarity problem (SCP), where the symmetry derives from the constitutive functional. The solution algorithm for the SCP is inspired to the one in Comi and Perego (1996a), where a gradient-plasticity model is introduced in the minimization principle to prevent ill-posedness of the boundary-value problem in the presence of material softening behaviour. This solution strategy is based on the work of Mangasarian (1977), where an iterative explicit scheme is proposed for the solution of Symmetric Linear Complementarity Problems (SLCP) and proofs of convergence are provided for the solution sequences. The linearity stems from the linear dependence in the complementarity problem of the activation condition upon the phase-field increment. The adopted algorithm resembles what is called a Projected Successive Over-Relaxation (PSOR) scheme for constrained optimization. It is important to notice that the application is limited to linear activation functions. Finally, the outlined method is compared with the variationally consistent penalization procedure proposed in Gerasimov and De Lorenzis (2019).

## 2.2 REGULARIZATION OF CRACK TOPOLOGY

The phase-field approach to fracture mechanics aims to change the crack description from sharp to regularized topology. The idea is to diffuse the discontinuity interface (i.e., the crack surface) inside the domain with the introduction of an additional dimension measured by the internal length scale parameter $l_{0d}$. The latter measures the portion of the domain where the crack is diffused. In

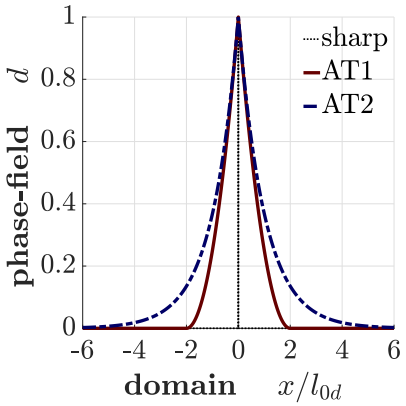


**Figure 2.1:** One-dimensional phase-field regularization of sharp crack topology.

Figure 2.1 a one-dimensional exemplification shows two different type of regularizations, referred as Ambrosio-Tortorelli (AT). The sharp crack topology is formulated as

$$d^{(s)}(x) = \begin{cases} 1 & \text{if} \quad x = 0 \\ 0 & \text{if} \quad \textit{otherwise} \end{cases} , \tag{2.1}$$

while the diffused counterparts AT1 and AT2 are respectively

$$d^{(1)}(x) = \begin{cases} \left(1 - \dfrac{|x|}{2l_{0d}}\right)^2 & \text{if} \quad |x| \leq 2l_{0d} \\ 0 & \text{if} \quad \textit{otherwise} \end{cases} , \quad d^{(2)}(x) = \exp\left(-\frac{|x|}{l_{0d}}\right) . \tag{2.2}$$

The two formulations differ for the support of the regularization profile. The AT1 profile has a compact support with measure $4l_{0d}$, while the AT2 diffusion presents an infinite support. Thus, the same symbol $l_{0d}$ refers to different quantities in the two approaches.

The phase-field profiles $d^{(1)}$ and $d^{(2)}$ are derived from the variational formulation:

$$d(x) = \arg\min \Big\{ \Gamma(d, \boldsymbol{\nabla} d) \Big\} , \tag{2.3}$$

being the surface functional and the surface functional density per unit volume

$$\Gamma(d, \boldsymbol{\nabla} d) = \int_\Omega \gamma(d, \boldsymbol{\nabla} d) \, \mathrm{d}\Omega , \quad \gamma(d, \boldsymbol{\nabla} d) := \frac{1}{c_w \, l_{0d}} \Big( \mathtt{w}(d) + l_{0d}^2 \, \boldsymbol{\nabla} d \cdot \boldsymbol{\nabla} d \Big) , \tag{2.4}$$

where $\Omega$ is body domain; while $c_w$ is a constant, $\mathtt{w}(d)$ is the local part of the functional, and they both depend upon the specific formulation (see Table 2.1). The optimal profile of the AT2 formulation $d^{(2)}$ is included into the interval

| | AT1 | AT2 |
|---|---|---|
| $c_w$ | $^8/_3$ | 2 |
| $\mathtt{w}(d)$ | $d$ | $d^2$ |

**Table 2.1:** Phase-field regularization parameter and local functional.

$[0,1]$, while the optimal profile of the AT1 approach $d^{(1)}$ ranges in $(-\infty,1]$. Thus, the latter approach requires the addition of the constraint $d \geq 0$ to (2.3) to admit the minimizer $(2.2)_1$.

The condition $d \in [0,1]$ is required for the application of the phase-field formulation to fracture mechanics, since the order parameter can be interpreted as a damage-like variable interpolating the unbroken and fully-broken state of the material. Moreover, the internal length $l_{0d}$ works as a material parameter measuring the damage process zone width.

A final remark lies in the mathematical robustness of the phase-field approach. The surface functional $\Gamma$ is a measure of the crack surface, despite being defined as a volume integral. The property of $\gamma$-*convergence* ensures that, for $l_{0d} \to 0$, the surface functional tends to the exact measure of the sharp crack topology.

## 2.3 PHASE-FIELD VARIATIONAL FORMULATION

### 2.3.1 STATE VARIABLES AND ELASTIC EVOLUTION

Let $\Omega \subset \mathbb{R}^{n_{dim}}$ be the reference domain, where $n_{dim}$ is the problem dimension. It is subject to Dirichelet boundary conditions on $\partial\Omega_D$ and Neumann boundary conditions on $\partial\Omega_N$ with $\partial\Omega_D \cup \partial\Omega_N = \partial\Omega$ and $\partial\Omega_D \cap \partial\Omega_N = \emptyset$. The displacement field $\mathbf{u}$ is subject to $\mathbf{u} = \mathbf{u}_D$ on $\partial\Omega_D$.

The state variables are the total strain tensor $\boldsymbol{\varepsilon} := \boldsymbol{\nabla}^s\mathbf{u}$ (being $\boldsymbol{\nabla}^s(\cdot)$ the symmetric gradient tensor operator), and the phase-field damage-like variable $d$. The material degradation function $\omega(d)$, also often referred to as *continuity function*, accounts for the presence of damage in the material bulk and it is such that $\omega(0) = 1$, $\omega(1) = 0$ and $\omega'(d) < 0$. The elastic free energy $\psi$ density is assumed to be multiplicatively split:

$$\psi(\boldsymbol{\varepsilon}, d) := \omega(d)\,\widetilde{\psi}^A(\boldsymbol{\varepsilon}) + \widetilde{\psi}^I(\boldsymbol{\varepsilon})\,, \quad \widetilde{\psi} = \widetilde{\psi}^A + \widetilde{\psi}^I\,, \tag{2.5}$$

where $\widetilde{\psi}$ is the elastic free energy corresponding to the response of the undamaged material to the compatible displacement field, $\widetilde{\psi}^A$ and $\widetilde{\psi}^I$ are the *active* and *inactive* part of the elastic energy promoting the crack evolution.

The Clausius-Duhem inequality states that the specific dissipation rate $\dot{\phi}$ must increase in every transformation, i.e., $\dot{\phi} := \boldsymbol{\sigma} : \dot{\boldsymbol{\varepsilon}} - \dot{\psi} \geq 0$, where $\boldsymbol{\sigma}$ is the

Cauchy stress tensor, $\dot{\boldsymbol{\varepsilon}}$ is the total strain rate, and $\dot{\psi}$ is the free energy rate. The introduction of (2.5) into the dissipation inequality reads:

$$\dot{\phi} := \boldsymbol{\sigma} : \dot{\boldsymbol{\varepsilon}} - \dot{\psi} = \underbrace{\left(\boldsymbol{\sigma} - \omega\, \partial_{\boldsymbol{\varepsilon}} \widetilde{\psi}^A - \partial_{\boldsymbol{\varepsilon}} \widetilde{\psi}^I\right) : \dot{\boldsymbol{\varepsilon}}}_{elastic} - \underbrace{\omega'\, \widetilde{\psi}^A\, \dot{d}}_{fracture} \geq 0\,. \tag{2.6}$$

During an elastic or reversible transformation, no evolution of damage $\dot{d} = 0$ occurs and, hence, no dissipation increase is produced (i.e., $\dot{\phi} = 0$). Therefore, the only term left is $(\boldsymbol{\sigma} - \omega\, \partial_{\boldsymbol{\varepsilon}} \widetilde{\psi}^A - \partial_{\boldsymbol{\varepsilon}} \widetilde{\psi}^I) : \dot{\boldsymbol{\varepsilon}} = 0$. Since it must hold for all reversible transformations $\dot{\boldsymbol{\varepsilon}}$, the elastic evolution law read:

$$\boldsymbol{\sigma} = \omega\, \widetilde{\boldsymbol{\sigma}}^A + \widetilde{\boldsymbol{\sigma}}^I\,, \quad \widetilde{\boldsymbol{\sigma}} := \widetilde{\boldsymbol{\sigma}}^A + \widetilde{\boldsymbol{\sigma}}^I = \partial_{\boldsymbol{\varepsilon}} \widetilde{\psi}^A + \partial_{\boldsymbol{\varepsilon}} \widetilde{\psi}^I\,, \tag{2.7}$$

being $\widetilde{\boldsymbol{\sigma}}^A$ and $\widetilde{\boldsymbol{\sigma}}^I$ the active and inactive parts of the Cauchy stress tensor corresponding to the response of the unbroken material to the compatible displacement field $\mathbf{u}$. Finally, the brittle-fracture specific dissipation rate $\dot{\phi}^f$ reads:

$$\dot{\phi}^f = -\omega'\, \widetilde{\psi}^A \dot{d} \geq 0\,. \tag{2.8}$$

The equality between the fracture dissipation rate and the elastic energy release rate $\dot{\phi}^f = -\omega'\, \widetilde{\psi}^A \dot{d}$ represents the local power balance principle and it can be expressed as follows:

$$Y_c \dot{d} := \dot{\phi}^f\,, \quad Y\dot{d} := -\omega'\, \widetilde{\psi}^A \dot{d} \quad \rightarrow \quad (Y_c - Y)\, \dot{d} = 0\,, \tag{2.9}$$

where $Y$ and $Y_c$ are the energy release rate and the critical energy release rate respectively. The fulfillment of the fracture dissipation inequality (2.8) demands to the phase-field variable being a non-decreasing function during the fracture evolution. In fact, the critical energy energy release rate represents the energy dissipated per unit damage growth and it must be strictly positive $Y_c \geq 0$. Thus, the damage-like variable rate is sign-constrained, i.e., it is subject to the *irreversibility* condition:

$$\dot{d} \geq 0\,. \tag{2.10}$$

### 2.3.2 VARIATIONAL FORMULATION

The solution of the variational formulation is defined by the set degrees of freedom displacement vector $\mathbf{u}$ and phase-field $d$. The total energy functional is introduced

$$\Pi(\mathbf{u}, d) := \mathcal{E}(\mathbf{u}, d) + \mathcal{D}_f(d, \boldsymbol{\nabla} d) - \mathcal{W}(\mathbf{u})\,, \tag{2.11}$$

where the internal energy, the fracture dissipated energy, and the work of external forces are

$$\begin{aligned} \mathcal{E}(\mathbf{u}, d) &:= \int_\Omega \left[\omega(d)\, \widetilde{\psi}^A(\boldsymbol{\varepsilon}) + \widetilde{\psi}^I(\boldsymbol{\varepsilon})\right] \mathrm{d}\Omega\,, \\ \mathcal{D}_f(d, \boldsymbol{\nabla} d) &:= \int_\Omega \phi^f(d, \boldsymbol{\nabla} d)\, \mathrm{d}\Omega\,, \\ \mathcal{W}(\mathbf{u}) &:= \int_\Omega \mathbf{b} \cdot \mathbf{u}\, \mathrm{d}\Omega + \int_{\partial\Omega_N} \mathbf{t} \cdot \mathbf{u}\, \mathrm{d}\Gamma\,, \end{aligned} \tag{2.12}$$

subject to

$$\boldsymbol{\varepsilon} = \boldsymbol{\nabla}^s \mathbf{u}\,, \quad \boldsymbol{\sigma} = \omega\, \partial_{\boldsymbol{\varepsilon}} \widetilde{\psi}^A + \partial_{\boldsymbol{\varepsilon}} \widetilde{\psi}^I\,, \quad \dot{d} \geq 0\,, \quad \mathbf{u} = \mathbf{u}_D \text{ on } \partial\Omega_D\,. \tag{2.13}$$

The vectors $\mathbf{b}$ and $\mathbf{t}$ are the body forces and the tractions, respectively, applied on the Neumann portion $\partial\Omega_N$ of the boundary. In the standard phase-field formulation, the brittle fracture dissipation density read

$$\phi^f(d, \boldsymbol{\nabla} d) = w(d) + 1/2\, c_d\, \boldsymbol{\nabla} d \cdot \boldsymbol{\nabla} d\,, \tag{2.14}$$

where $w(d)$ is the local phase-field specific dissipation. The constant parameter $c_d$ measures the damage diffusion bandwidth and it is related to the fracture internal lengths $l_{0d}$. The solution of the considered brittle fracture boundary value problem makes the functional $\Pi$ stationary with respect to variations of the fields $(\mathbf{u}, d)$. The inequality constraint $\dot{d}$ make the variational problem a variational inequality.

#### 2.3.2.1 Stationarity conditions

The stationarity conditions for the total energy functional $\Pi$ read:

$$\partial_{\mathbf{u}} \Pi(\mathbf{u}, d)[\delta\mathbf{u}] = 0 \quad \rightarrow \quad \int_\Omega \boldsymbol{\sigma} : \delta\boldsymbol{\varepsilon}\, \mathrm{d}\Omega - \int_\Omega \mathbf{b} \cdot \delta\mathbf{u}\, \mathrm{d}\Omega - \int_{\partial\Omega_N} \mathbf{t} \cdot \delta\mathbf{u}\, \mathrm{d}\Gamma = 0\,, \tag{2.15a}$$

$$\partial_d \Pi(\mathbf{u}, d)[\delta d] \geq 0 \quad \rightarrow \quad \int_\Omega \Big[ \left(\omega'\, \widetilde{\psi}^A + w'\right) \delta d + c_d\, \boldsymbol{\nabla} d \cdot \boldsymbol{\nabla} \delta d \Big]\, \mathrm{d}\Omega \geq 0\,, \tag{2.15b}$$

where $\delta d = d' - d$ is not sign-constrained, while $\dot{d}' \geq 0$ and $\dot{d} \geq 0$ are arbitrary, non-negative scalar functions. The conditions above correspond to: (2.15a) equilibrium equations, and (2.15b) non-local fracture evolution criterion.

#### 2.3.2.2 Governing equations

The energy release rate $\mathcal{Y}$ and critical energy release rate $\mathcal{Y}_c$ functionals are defined as:

$$\mathcal{Y}(\boldsymbol{\varepsilon}, d)[\delta d] := -\int_\Omega \omega'(d)\, \widetilde{\psi}^A(\boldsymbol{\varepsilon})\, \delta d\, \mathrm{d}\Omega\,, \tag{2.16a}$$

$$\mathcal{Y}_c(d)[\delta d] := \int_\Omega \Big[ w'(d)\, \delta d + c_d\, \boldsymbol{\nabla} d \cdot \boldsymbol{\nabla} \delta d \Big]\, \mathrm{d}\Omega\,. \tag{2.16b}$$

They represent the variational counterpart of the local energy release rate $Y$ and critical energy release rate $Y_c$ in (2.9). The non-local fracture activation functional $\mathcal{F}_d$ is then defined as:

$$\mathcal{F}_d(\boldsymbol{\varepsilon}, d)[\delta d] := \Big(\mathcal{Y}(\boldsymbol{\varepsilon}, d) - \mathcal{Y}_c(d)\Big)[\delta d]\,. \tag{2.17}$$

The condition (2.15b) works as a variational counterpart of the Griffith activation criterion for brittle fracture and it can be cast into a set of Kuhn-Tucker conditions following standard arguments in constrained optimization, see e.g., Alessi et al. (2018b). Thus, the *irreversibility* condition, the *activation criterion*, and the *energy balance* read:

$$\dot{d} \geq 0\,, \quad \mathcal{F}_d(\boldsymbol{\varepsilon}, d) \leq 0\,, \quad \mathcal{F}_d(\boldsymbol{\varepsilon}, d)[\dot{d}] = 0\,, \tag{2.18}$$

providing the non-local fracture activation criterion for brittle fracture.

The governing equations are conveniently cast into the general format

$$\begin{cases} \partial_{\mathbf{u}}\Pi(\mathbf{u}, d)[\delta\mathbf{u}] = 0\,, \quad \mathbf{u} = \mathbf{u}_D \text{ on } \partial\Omega_D\,, \\ \partial_d\Pi(\mathbf{u}, d)[\dot{d}] = 0\,, \quad -\partial_d\Pi(\mathbf{u}, d) \leq 0\,, \quad \dot{d} \geq 0\,. \end{cases} \tag{2.19}$$

### 2.3.3 CONSTITUTIVE ASSUMPTIONS

For the implementation considered in this work, the general framework described so far is restricted to isotropic linear elastic materials, i.e.

$$\widetilde{\psi}(\boldsymbol{\varepsilon}) = {}^1\!/_2\, K_0\, \epsilon_v^2 + {}^1\!/_2\, 2G_0\, \mathbf{e} : \mathbf{e}\,, \tag{2.20}$$

where $K_0$ is the bulk modulus, $G_0$ is the shear modulus, $\epsilon_v := \boldsymbol{\varepsilon} : \mathbf{I}$ is the total volumetric strain, $\mathbf{I}$ being the identity tensor, $\mathbf{e} = \boldsymbol{\varepsilon} - {}^1\!/_3\epsilon_v\mathbf{I}$ is the deviatoric total strain. The definition of the active and inactive part of the free energy follows the volumetric-deviatoric split proposed by Amor et al. (2009). The positive and negative parts of the volumetric strain are defined as $\epsilon_v^{\pm} := \langle\epsilon_v\rangle_{\pm}$, being $\langle\cdot\rangle_{\pm}$ the Macaulay bracket operator, then

$$\widetilde{\psi}^A(\boldsymbol{\varepsilon}) = {}^1\!/_2\, K_0\, (\epsilon_v^+)^2 + {}^1\!/_2\, 2G_0\, \mathbf{e} : \mathbf{e}\,, \quad \widetilde{\psi}^I(\boldsymbol{\varepsilon}) = {}^1\!/_2\, K_0\, (\epsilon_v^-)^2\,. \tag{2.21}$$

The phase-field degradation function $\omega(d)$ and the brittle dissipation energy density $\phi^f(d, \boldsymbol{\nabla} d)$ are defined as

$$\omega(d) = (1-d)^2\,, \quad \phi^f(d, \boldsymbol{\nabla} d) = G_c\, \gamma(d, \boldsymbol{\nabla} d)\,, \tag{2.22}$$

where $\gamma$ is the phase-field regularization surface density functional (2.4), and $G_c$ is the material toughness, i.e., the fracture energy release per unit surface growth. Thus, the local part of the brittle dissipation $w(d)$ and the diffusion coefficient $c_d$ in (2.14) read:

$$w(d) = \frac{G_c}{c_w\, l_{0d}}\, \mathtt{w}(d) \quad c_d = 2\,\frac{G_c}{c_w}\, l_{0d}\,. \tag{2.23}$$

## 2.4 Time discretization and staggered evolution

Given a time increment $\Delta t > 0$ we consider the finite time sequence $t_n = n\Delta t$ for $n = 0, ..., N$. The evolution is defined by the following incremental problem. Known $\mathbf{u}_n$ and $d_n$ at time $t_n$, we introduce the auxiliary sequences $\mathbf{u}^i$ and $d^i$ defined recursively by the following staggered scheme Bourdin et al. (2000): $\mathbf{u}^0 = \mathbf{u}_n$ , $d^0 = d_n$ and

$$\begin{cases} \mathbf{u}^{i+1} \in \operatorname{argmin}\{\Pi_{n+1}(\mathbf{u}, d^i) : \mathbf{u} = \mathbf{u}_D \text{ on } \partial\Omega_D\} \\ d^{i+1} \in \operatorname{argmin}\{\Pi_{n+1}(\mathbf{u}^{i+1}, d) : d \geq d_n = d^0\}, \end{cases} \tag{2.24}$$

where $\Pi_{n+1}$ denotes the energy functional with boundary and loading conditions prescribed at time $t_{n+1}$. Ideally, the above scheme introduces infinite sequences $\mathbf{u}^i$ and $d^i$ for $i \in \mathbb{N}$ and thus we may define $\mathbf{u}_{n+1} = \lim_{i\to+\infty} \mathbf{u}^i$ and $d_{n+1} = \lim_{i\to+\infty} d^i$ . In practice, the scheme ends when a certain stopping criterion is met, say, at the staggered iteration $i = I$ (see Algorithm 1). In this case, we would set $\mathbf{u}_{n+1} = \mathbf{u}^I$ and $d_{n+1} = d^I$. For ease of presentation, let us stick with the former case, so that the limit configuration $(\mathbf{u}_{n+1}, d_{n+1})$ solves the following system (formally passing to the limit in (2.24) as $i \to +\infty$)

$$\begin{cases} \mathbf{u}_{n+1} \in \operatorname{argmin}\{\Pi_{n+1}(\mathbf{u}, d_{n+1}) : \mathbf{u} = \mathbf{u}_D \text{ on } \partial\Omega_D\} \\ d_{n+1} \in \operatorname{argmin}\{\Pi_{n+1}(\mathbf{u}_{n+1}, d) : d \geq d_n\}. \end{cases} \tag{2.25}$$

In other terms the couple $(\mathbf{u}_{n+1}, d_{n+1})$ is a separate minimizer of the energy. We remark that, being $\Pi$ non-convex, $(\mathbf{u}_{n+1}, d_{n+1})$ is not necessarily a global minimizer of $\Pi_{n+1}$, i.e., it may happen that

$$(\mathbf{u}_{n+1}, d_{n+1}) \notin \operatorname{argmin}\{\Pi_{n+1}(\mathbf{u}, d) : \mathbf{u} = \mathbf{u}_D \text{ on } \partial\Omega_D,\ d \geq d_n\}.$$

However, computing a global minimizer of the non-convex energy $\Pi_{n+1}$ is not convenient from the computational point of view, and not necessary in view of solving (2.19). Indeed, the system (2.25) is equivalent to the following variational system

$$\begin{cases} \partial_{\mathbf{u}}\Pi_{n+1}(\mathbf{u}_{n+1}, d_{n+1})[\delta\mathbf{u}] = 0\,, \quad \delta\mathbf{u} = \mathbf{0} \text{ on } \partial\Omega_D, \\ \partial_d\Pi_{n+1}(\mathbf{u}_{n+1}, d_{n+1})[\delta d] \geq 0\,, \quad \delta d = d' - d_{n+1} \text{ with } d' \geq d_n\,, d \geq d_n\,. \end{cases} \tag{2.26}$$

Adopting a backward Euler time integration of the phase-field rate, i.e., $\dot{d}_{n+1} := (d_{n+1} - d_n)/\Delta t = \Delta d_{n+1}/\Delta t$, and noting that, according to the definition in (2.26), $\delta d = \Delta d' - \Delta d_{n+1}$, with $\Delta d' := d' - d_n$, is not sign constrained, the

above variational system can be written in complementarity form as[1]

$$\begin{cases} \partial_{\mathbf{u}}\Pi_{n+1}(\mathbf{u}_{n+1}, d_{n+1}) = \mathbf{0}, \\ \partial_d\Pi_{n+1}(\mathbf{u}_{n+1}, d_{n+1})[\Delta d_{n+1}] = 0, \quad \partial_d\Pi_{n+1}(\mathbf{u}_{n+1}, d_{n+1}) \geq 0, \quad \Delta d_{n+1} \geq 0, \end{cases} \tag{2.27}$$

which provides the time discretization of (2.19). In conclusion, the staggered scheme provides a sequence $(\mathbf{u}^i, d^i)$ converging to the configuration $(\mathbf{u}_{n+1}, d_{n+1})$ which solves (2.27).

The choice of the convergence criterion to stop the staggered iteration scheme is not unique. The most common possibilities used in the literature check the variation between two subsequent iterations of either the total energy functional $\Pi_{n+1}$ or the phase-field variable. The latter option is equivalent to controlling the dissipated energy $\mathcal{D}_{f,n+1}$, since it provides a global measure of the damage inside the domain. A third choice would be to employ the first variation of the total energy, either with respect to the displacement variable or with respect to the phase-field one. The distinction is then made according to how the staggered scheme is structured, i.e., whether the algorithm solves first the balance of linear momentum equation or the complementarity problem.

In our case, the staggered algorithm is arrested when the out-of-balance work $\texttt{Res}_{\text{STAG}}$ (see Algorithm 1) is smaller than the assigned tolerance $\texttt{TOL}_{\text{STAG}}$

$$\texttt{Res}_{\text{STAG}} = \left|\partial_{\mathbf{u}}\Pi_{n+1}(\mathbf{u}^i, d^i)[\Delta\mathbf{u}^i]\right| \leq \texttt{TOL}_{\text{STAG}}\,. \tag{2.28}$$

We remark that both equations reported in Algorithm 1, i.e., the first variation of the total energy with respect to the displacement variable and to the phase-field one, are nonlinear. The nonlinearity of $\partial_{\mathbf{u}}\Pi$ is due to the decomposition of the free energy (2.5), whereas for $\partial_d\Pi$ it is caused by the constrained nature of the minimization problem. Therefore, to solve $\partial_{\mathbf{u}}\Pi = \mathbf{0}$ we use a Newton-Raphson procedure to iteratively compute $\mathbf{u}^i$ for a fixed damage variable $d^{i-1}$, while the strategy to solve the phase-field problem will be thoroughly discussed in Section 2.6.

[1] First, note that any $\delta d \geq 0$ is admissible in (2.26), therefore we have $\partial_d\Pi_{n+1}(\mathbf{u}_{n+1}, d_{n+1}) \geq 0$. Choosing $\Delta d' = 0$ and $\Delta d' = 2\Delta d_{n+1}$ we get respectively $\delta d = -\Delta d_{n+1}$ and $\delta d = \Delta d_{n+1}$. Hence, by (2.26) we have both

$$\partial_d\Pi_{n+1}(\mathbf{u}_{n+1}, d_{n+1})[\Delta d_{n+1}] \leq 0 \;\text{ and }\; \partial_d\Pi_{n+1}(\mathbf{u}_{n+1}, d_{n+1})[\Delta d_{n+1}] \geq 0\,,$$

which imply the complementarity condition $\partial_d\Pi_{n+1}(\mathbf{u}_{n+1}, d_{n+1})[\Delta d_{n+1}] = 0$.

**Algorithm 1:** Staggered iteration algorithm.

**input :** $(\mathbf{u},\, d)_n$, $\mathbf{u}_{D,n+1}$, $\mathbf{b}_{n+1}$, $\mathbf{t}_{n+1}$

`initialize` $i = 0\,, \quad (\mathbf{u}, d)^0 = (\mathbf{u}, d)_n$

**while** ( $\mathit{Res}_{STAG} > \mathit{TOL}_{STAG}$ ) **do**

`update` $i = i + 1$

`solve` $\partial_{\mathbf{u}} \Pi_{n+1}(\mathbf{u}, d^{i-1}) = \mathbf{0} \rightarrow \mathbf{u}^i$

`solve` $\partial_d \Pi_{n+1}(\mathbf{u}^i, d)[\Delta d] = 0\,,\ \partial_d \Pi_{n+1}(\mathbf{u}^i, d) \geq 0\,,\ \Delta d \geq 0 \rightarrow d^i$

`compute` $\mathtt{Res}_{\mathrm{STAG}} = \left|\partial_{\mathbf{u}} \Pi_{n+1}(\mathbf{u}^i, d^i)[\Delta \mathbf{u}^i]\right|$

**end**

$(\mathbf{u},\ d)_{n+1} = (\mathbf{u},\ d)^i$

**output:** $(\mathbf{u},\ d)_{n+1}$

## 2.5 Space discretization

The problem physical dimension is $n_{dim}$, the element number of nodes is $n_{en}$, the element number of displacement degrees of freedom is $n_{ldof} = n_{dim}\, n_{en}$. The global number of nodes is $n_{np}$ and the global number of displacement degrees of freedom is $n_{dof} = n_{dim}\, n_{np}$. The number of independent strain tensor components is $n_\varepsilon$. The local, elemental and global solutions of the brittle fracture problem can be cast into the column vectors:

$$\boldsymbol{\mathcal{S}}_l = (\mathbf{u}, d)\,, \quad \boldsymbol{\mathcal{S}}_e = (\widehat{\mathbf{u}}_e, \widehat{\mathbf{d}}_e)\,, \quad \boldsymbol{\mathcal{S}}_g = (\widehat{\mathbf{u}}, \widehat{\mathbf{d}})\,, \tag{2.29}$$

where $\mathbf{u}$ is the displacement vector, of dimensions $(n_{dim}, 1)$, and $d$ is the scalar phase field. The element nodal displacement vector $\widehat{\mathbf{u}}_e$ has dimensions $(n_{ldof}, 1)$, and the element phase-field vector $\widehat{\mathbf{d}}_e$ has dimensions $(n_{en}, 1)$. $\widehat{\mathbf{u}}$ $(n_{dof}, 1)$ is the global nodal displacement vector, and $\widehat{\mathbf{d}}$ $(n_{np}, 1)$ is the global nodal phase-field vector. The element local solution together with the spatial gradients, i.e. the total deformation $\boldsymbol{\varepsilon}$ $(n_\varepsilon, 1)$, and the phase-field gradient $\boldsymbol{\nabla} d$ $(n_{dim}, 1)$ are modeled at the element level as:

$$\mathbf{u} = \mathbf{N}_{\mathrm{u}}\, \widehat{\mathbf{u}}_e\,, \qquad d = \mathbf{N}_{\mathrm{d}}\, \widehat{\mathbf{d}}_e\,, \tag{2.30a}$$

$$\boldsymbol{\varepsilon} = \mathbf{B}_{\mathrm{u}}\, \widehat{\mathbf{u}}_e\,, \qquad \boldsymbol{\nabla} d = \mathbf{B}_{\mathrm{d}}\, \widehat{\mathbf{d}}_e\,, \tag{2.30b}$$

where $\mathbf{N}_{\mathrm{u}}$ is the displacement shape function matrix $(n_{dim}, n_{ldof})$, $\mathbf{B}_{\mathrm{u}}$ is displacement compatibility matrix $(n_\varepsilon, n_{ldof})$, $\mathbf{N}_{\mathrm{d}}$ is the phase-field shape function vector $(1, n_{en})$, and $\mathbf{B}_{\mathrm{d}}$ is the phase-field gradient matrix $(n_{dim}, n_{en})$. The

global assembly is formally performed with the boolean connectivity matrices $\mathbf{C}_{e,\mathrm{u}}\ (n_{ldof}, n_{dof})$, and $\mathbf{C}_{e,\mathrm{d}}\ (n_{en}, n_{np})$ such that:

$$\widehat{\mathbf{u}}_e = \mathbf{C}_{e,\mathrm{u}}\,\widehat{\mathbf{u}}\,, \qquad \widehat{\mathbf{d}}_e = \mathbf{C}_{e,\mathrm{d}}\,\widehat{\mathbf{d}}\,. \tag{2.31}$$

### 2.5.1 Governing equations

The weak form of the equilibrium equation (2.15a), and fracture complementarity equation $(2.18)_c$ are spatially discretized:

$$\delta\widehat{\mathbf{u}}^{\mathrm{T}}\left[\sum_{e=1}^{n_{el}} \mathbf{C}_{e,\mathrm{u}}^{\mathrm{T}}\left(\mathbf{F}_{\mathrm{I},e} - \mathbf{F}_{\mathrm{E},e}\right)\right] = 0\,, \quad \Delta\widehat{\mathbf{d}}^{\mathrm{T}}\left[\sum_{e=1}^{n_{el}} \mathbf{C}_{e,\mathrm{d}}^{\mathrm{T}}\,\mathbf{f}_{\mathrm{D},e}\right] = 0\,, \tag{2.32}$$

where $e$ denotes the element label and $n_{el}$ is the total number of elements in the mesh. The element internal force vector $\mathbf{F}_{\mathrm{I},e}\ (n_{ldof}, 1)$, the external force vector $\mathbf{F}_{\mathrm{E},e}\ (n_{ldof}, 1)$, and the fracture activation vector $\mathbf{f}_{\mathrm{D},e}\ (n_{en}, 1)$ are

$$\mathbf{F}_{\mathrm{I},e} := \int_{\Omega_e} \mathbf{B}_{\mathrm{u}}^{\mathrm{T}}\left(\omega\,\widetilde{\boldsymbol{\sigma}}^{A} + \widetilde{\boldsymbol{\sigma}}^{I}\right)\mathrm{d}\Omega_e\,, \tag{2.33a}$$

$$\mathbf{F}_{\mathrm{E},e} := \int_{\Omega_e} \mathbf{N}_{\mathrm{u}}^{\mathrm{T}}\,\mathbf{b}\,\mathrm{d}\Omega_e + \int_{\partial\Omega_e} \mathbf{N}_{\mathrm{u}}^{\mathrm{T}}\,\mathbf{t}\,\mathrm{d}\Gamma_e\,, \tag{2.33b}$$

$$\mathbf{f}_{\mathrm{D},e} := -\int_{\Omega_e} \left\{\mathbf{N}_{\mathrm{d}}^{\mathrm{T}}\left[\omega'\,\widetilde{\psi}^{A} + w'\right] + c_d\,\mathbf{B}_{\mathrm{d}}^{\mathrm{T}}\,\boldsymbol{\nabla} d\right\}\mathrm{d}\Omega_e\,, \tag{2.33c}$$

where $\widetilde{\boldsymbol{\sigma}}^{A}$, $\widetilde{\boldsymbol{\sigma}}^{I}$ are the active and inactive stresses defined in (2.7). The stress tensor in Voigt notation $\boldsymbol{\sigma}$ is a vector with dimension $(n_\sigma, 1)$, being $n_\sigma = n_\varepsilon$ the number of independent stress components. The same symbol is used for tensor and Voigt notation. The spatially discretized governing equations are:

$$\mathbf{F}_{\mathrm{I}} - \mathbf{F}_{\mathrm{E}} = \mathbf{0}\,, \tag{2.34a}$$

$$\Delta\widehat{\mathbf{d}} \geq \mathbf{0}\,, \quad \mathbf{f}_{\mathrm{D}} \leq \mathbf{0}\,, \quad \Delta\widehat{\mathbf{d}}^{\mathrm{T}}\,\mathbf{f}_{\mathrm{D}} = 0\,. \tag{2.34b}$$

## 2.6 Solution strategy of the fracture evolution

### 2.6.1 Symmetric linear complementarity problem

The constitutive functionals in Section 2.3.3 lead to a fracture activation criterion (2.18) with an activation functional (2.17) that is linear in the phase-field variable $d$. This property stems from the quadratic nature of the degradation function $\omega(d) = (1-d)^2$ and the local brittle dissipation $w(d)$ that for the AT1 and AT2 is linear and quadratic respectively (see Section 2.2). In the current chapter of brittle fracture, the attention is restricted to the quadratic formulation of the AT2 approach. Thus, the phase-field dissipation density reads:

$$\phi^f(d, \boldsymbol{\nabla} d) = \frac{G_c}{2\,l_{0d}}\left(d^2 + l_{0d}^2\,\boldsymbol{\nabla} d \cdot \boldsymbol{\nabla} d\right). \tag{2.35}$$

The resulting element fracture activation vector (2.33c) assumes the linear form

$$\mathbf{f}_{\mathrm{D},e} = \underbrace{\left\{ \int_{\Omega_e} \left[ \mathbf{N}_{\mathrm{d}}^{\mathrm{T}} \left( 2\widetilde{\psi}^A - \left( 2\widetilde{\psi}^A + \frac{G_c}{l_{0d}} \right) d_n \right) - G_c \, l_{0d} \, \mathbf{B}_{\mathrm{d}}^{\mathrm{T}} \boldsymbol{\nabla} d_n \right] \mathrm{d}\Omega_e \right\}}_{\mathbf{f}_{\mathrm{D},e}^{tr}} - \underbrace{\left\{ \int_{\Omega_e} \left[ \left( 2\widetilde{\psi}^A + \frac{G_c}{l_{0d}} \right) \mathbf{N}_{\mathrm{d}}^{\mathrm{T}} \mathbf{N}_{\mathrm{d}} + G_c \, l_{0d} \mathbf{B}_{\mathrm{d}}^{\mathrm{T}} \mathbf{B}_{\mathrm{d}} \right] \mathrm{d}\Omega_e \right\}}_{\mathbf{K}_{dd,e}} \Delta \widehat{\mathbf{d}}_e \,,$$

where the trial activation vector $\mathbf{f}_{\mathrm{D},e}^{tr}$ and the phase-field stiffness matrix $\mathbf{K}_{dd,e}$ are introduced

$$\mathbf{f}_{\mathrm{D},e}^{tr} := \int_{\Omega_e} \left[ \mathbf{N}_{\mathrm{d}}^{\mathrm{T}} \left( 2\widetilde{\psi}^A - \left( 2\widetilde{\psi}^A + \frac{G_c}{l_{0d}} \right) d_n \right) - G_c \, l_{0d} \, \mathbf{B}_{\mathrm{d}}^{\mathrm{T}} \boldsymbol{\nabla} d_n \right] \mathrm{d}\Omega_e, \quad (2.36a)$$

$$\mathbf{K}_{dd,e} := \int_{\Omega_e} \left[ \left( 2\widetilde{\psi}^A + \frac{G_c}{l_{0d}} \right) \mathbf{N}_{\mathrm{d}}^{\mathrm{T}} \mathbf{N}_{\mathrm{d}} + G_c \, l_{0d} \mathbf{B}_{\mathrm{d}}^{\mathrm{T}} \mathbf{B}_{\mathrm{d}} \right] \mathrm{d}\Omega_e \,. \quad (2.36b)$$

Thus, the fracture activation criterion (2.34b) turns into the *Symmetric Linear Complementarity Problem* (SLCP)

$$\Delta \widehat{\mathbf{d}} \geq \mathbf{0} \,, \quad \left( \mathbf{f}_{\mathrm{D}}^{tr} - \mathbf{K}_{dd} \Delta \widehat{\mathbf{d}} \right) \leq \mathbf{0} \,, \quad \Delta \widehat{\mathbf{d}}^{\mathrm{T}} \left( \mathbf{f}_{\mathrm{D}}^{tr} - \mathbf{K}_{dd} \Delta \widehat{\mathbf{d}} \right) = 0 \,, \quad (2.37)$$

where the constitutive vectors and matrices are obtained by assembling the relevant element quantities. The symmetry of the complementarity problem stems from the symmetry of the constitutive functionals, while the linearity derives from the quadratic nature of the total energy with respect to the phase-field variable. The Kuhn-Tucker conditions (2.37) correspond to the non-smooth quadratic programming problem:

$$\Delta \widehat{\mathbf{d}} = \arg\min \left\{ \frac{1}{2} \Delta \widehat{\mathbf{d}}^{\mathrm{T}} \mathbf{K}_{dd} \, \Delta \widehat{\mathbf{d}} - \Delta \widehat{\mathbf{d}}^{\mathrm{T}} \, \mathbf{f}_{\mathrm{D}}^{tr} \; ; \;\; \Delta \widehat{\mathbf{d}} \geq \mathbf{0} \right\} . \quad (2.38)$$

### 2.6.2 Penalization of the irreversibility constraint

In the penalty approach proposed in Gerasimov and De Lorenzis (2019) to solve the unilateral incremental problem for the phase field $d$, the idea is to replace the constrained minimization (2.38) with the following *unconstrained* problem

$$\Delta \widehat{\mathbf{d}} = \arg\min \left\{ \frac{1}{2} \Delta \widehat{\mathbf{d}}^{\mathrm{T}} \mathbf{K}_{dd} \, \Delta \widehat{\mathbf{d}} - \Delta \widehat{\mathbf{d}}^{\mathrm{T}} \, \mathbf{f}_{\mathrm{D}}^{tr} + p(\Delta d) \right\} , \quad (2.39)$$

where the nonlinear penalty term $p(\Delta d)$ results from the discretization of the functional

$$p(\Delta d) := \frac{1}{2} \gamma_p \int_{\Omega} \langle d - d_n \rangle_-^2 \, \mathrm{d}\Omega \,. \quad (2.40)$$

The main purpose of the penalization is to introduce an extra energy term in the total energy penalizing the violation of the irreversibility condition $d - d_n > 0$. When $\gamma_p \to +\infty$ the unilateral constraint $d \geq d_n$ and its discretization $\Delta d \geq 0$ is recovered. It is worthwhile to notice that the penalization coefficient $\gamma_p$ is a dimensional quantity and a wrong choice may lead to ill-conditioning of the solving system associated to (2.39). A detailed analysis of the computational performance of this approach and a criterion for the choice of the coefficient $\gamma_p$ are available in Gerasimov and De Lorenzis (2019).

The minimization with respect to $\Delta d$ of the penalized total energy functional leads to the following nonlinear equation in the phase-field finite increment:

$$\mathbf{K}_{dd}\,\Delta\widehat{\mathbf{d}} - \mathbf{f}_{\mathrm{D}}^{tr} + \mathbf{p}(\Delta\widehat{\mathbf{d}}) = \mathbf{0}. \tag{2.41}$$

The element penalization residual vector $\mathbf{p}_e$ can be computed as follows:

$$\mathbf{p}_e(\Delta\widehat{\mathbf{d}}_e) = \int_{\Omega_e} \gamma_p \,\langle \mathbf{N}_{\mathrm{d}} \Delta\widehat{\mathbf{d}}_e \rangle_- \,\mathbf{N}_{\mathrm{d}}^{\mathrm{T}}\,\mathrm{d}\Omega_e\,, \tag{2.42}$$

where the discretized element phase-field increment $\Delta d$, see (2.30), must be evaluated at the Gauss points for numerical integration. The solution of (2.41) requires a Newton-Raphson iterative scheme in view of the nonlinearity entailed by the presence of the Macaulay brackets. The penalty contribution to the element consistent tangent matrix reads:

$$\frac{\partial \mathbf{p}_e}{\partial \Delta\widehat{\mathbf{d}}_e}(\Delta\widehat{\mathbf{d}}_e) = \int_{\Omega_e} \gamma_p \,\mathrm{H}^-\left(\mathbf{N}_{\mathrm{d}} \Delta\widehat{\mathbf{d}}_e\right)\, \mathbf{N}_{\mathrm{d}}^{\mathrm{T}}\,\mathbf{N}_{\mathrm{d}}\,\mathrm{d}\Omega_e\,, \tag{2.43}$$

where $\mathrm{H}^-(\cdot)$ is the negative Heaviside function. Here, the importance of the penalty coefficient for the numerical stability of the solver seems clear. At each Newton-Raphson iteration, different entries of the tangent matrix have an additional contribution of the order of magnitude of $\gamma_p$.

The convergence criterion used in the iterative scheme controls the variation of the solution at the mesh nodes between two subsequent iterations associated to the nonlinear equation (2.41), namely:

$$\mathtt{Res}_{\mathrm{d}}^{(k)} := \left\| \,\Delta\widehat{\mathbf{d}}^{k} - \Delta\widehat{\mathbf{d}}^{k-1}\, \right\|_{L^\infty} \leq \mathtt{TOL}_{\mathrm{d}}, \tag{2.44}$$

where $k$ is the iteration number and $\mathtt{TOL}_{\mathrm{d}}$ is the prescribed tolerance.

### 2.6.3 Projected Successive Over-Relaxation Algorithm

The SLCP defined in (2.37) is solved at each staggered iteration using an explicit algorithm, the *Projected Successive Over-Relaxation* (PSOR) algorithm, proposed by Mangasarian (1977). In his paper, the author discusses various algorithms specifically conceived for the solution of SLCPs. As already shown in Comi and Perego (1996a) in the context of gradient plasticity, the algorithm

is computationally efficient and robust, though its application is limited to symmetric and linear complementarity problems.

For the sake of clarity in the presentation of the algorithm, the phase-field SLCP in (2.37) is written in the standard form:

$$\Delta\widehat{\mathbf{d}} \geq \mathbf{0}\,, \quad \left(\mathbf{q} + \mathbf{Q}\,\Delta\widehat{\mathbf{d}}\right) \geq \mathbf{0}\,, \quad \Delta\widehat{\mathbf{d}}^{\mathrm{T}}\left(\mathbf{q} + \mathbf{Q}\,\Delta\widehat{\mathbf{d}}\right) = 0\,. \tag{2.45}$$

According to the PSOR algorithm, the matrix $\mathbf{Q}$ is additively decomposed as $\mathbf{Q} = \mathbf{L} + \mathbf{D} + \mathbf{L}^T$, where $\mathbf{L}$ is its strictly lower triangular part, $\mathbf{D}$, its diagonal, and $\mathbf{L}^T$ its strictly upper triangular part (because of the symmetry of the constitutive matrix). To simplify the notation, the index $i$ of the staggered iteration is dropped from the constitutive matrix. For the same reason, the $r$-th component of the solution vector is denoted with $\Delta d_r := [\Delta\widehat{\mathbf{d}}]_r$. Finally, the $rc$-th component of the constitutive matrix is denoted as $Q_{rc} := [\mathbf{Q}]_{rc}$, where $r$ represents the row-index and $c$ the column-index. The algorithm is iterative and the solution at the $k$-th PSOR iteration reads:

$$\Delta d_r^k = \left\langle \Delta d_r^{k-1} - D_{rr}^{-1}\,\left[Q_{rc}\,\Delta d_c^{k-1} + q_r + L_{rc}\,(\Delta d_c^k - \Delta d_c^{k-1})\right]\right\rangle_+\,, \tag{2.46}$$

where $L_{rc} := Q_{r>c}$, $D_{rc} := Q_{r=c}$, and $\langle\cdot\rangle_+$ denotes the positive part of the argument. It is worthwhile noticing that irreversibility is enforced component-wise in a strong form by the Macaulay bracket operator, while the explicit nature of the algorithm is guaranteed by the strictly lower triangular format of the matrix $\mathbf{L}$. This aspect can be better appreciated by looking at the first two components of the solution vector at the $k$-th PSOR iteration:

$$\begin{aligned}
\Delta d_1^k &= \left\langle \Delta d_1^{k-1} - Q_{11}^{-1}\,\left[Q_{1c}\,\Delta d_c^{k-1} + q_1\right]\right\rangle_+ \\
\Delta d_2^k &= \left\langle \Delta d_2^{k-1} - Q_{22}^{-1}\,\left[Q_{2c}\,\Delta d_c^{k-1} + q_1 + Q_{21}\,(\Delta d_1^k - \Delta d_1^{k-1})\right]\right\rangle_+ \\
&\ldots
\end{aligned}$$

By Corollary 2.2 in Mangasarian (1977), the sequence $\Delta d^k$ defined above is proved to converge to the unique minimizer of problem (2.45). The symmetric matrix $\mathbf{Q} = \mathbf{K}_{dd}$ (2.36b) of the SLCP possesses another fundamental feature: it is a sparse matrix because of the finite support of the shape functions of the spatial discretization. This feature, together with the explicit nature of the algorithm, allows for a particularly compact and effective implementation of the PSOR algorithm, which is illustrated in detail in Appendix A.

The solution of the SLCP involves the fulfillment of the three complementarity conditions in (2.45). Different checks are introduced to ensure the convergence of the PSOR algorithm. The irreversibility constraint on the phase-field variable $(2.45)_1$ is automatically satisfied by the presence of the Macaulay bracket in (2.46). Therefore, in the first criterion the norm $\mathtt{Res}_{\mathrm{d}}^{(k)}$ of the variation of the phase-field increment between two subsequent iterations is

checked against the prescribed tolerance as in (2.44). Since the phase field is non-dimensional and ranges from 0 to 1, this measure is already normalized with respect to the reference maximum value $d = 1$. The maximum increment that would be experienced in a single load step cannot be more then the unit and $\texttt{TOL}_\text{d} = 10^{-4}$ has been set as a reasonable tolerance. On the other hand, the activation condition $(2.45)_2$ can be violated in two ways. At the $k$-th iteration, the generic solution component is denoted with $r$. Let $\mathcal{C}_+^{(k)} := \{\, r \in [1, n_{np}] : \Delta d_r^k > 0 \,\}$ define the set of components where the phase-field increment is positive, and $\mathcal{C}_0^{(k)} := \{\, r \in [1, n_{np}] : \Delta d_r^k = 0 \,\}$ the set where it is zero. For every $r \in \mathcal{C}_+^{(k)}$ the activation condition must be $Q_{rc}\Delta d_c^k + q_r = 0$, while for every $r \in \mathcal{C}_0^{(k)}$ is should be $Q_{rc}\Delta d_c^k + q_r > 0$. In the first case, a criterion checks whether the absolute value of the activation function is different from zero. In the second case, another criterion checks whether the positiveness of the activation function is violated:

$$\texttt{Res}_{\text{d}+}^{(k)} := \max_{r \,\in\, \mathcal{C}_+^{(k)}} \left| Q_{rc}\Delta d_c^k + q_r \right| , \tag{2.48a}$$

$$\texttt{Res}_{\text{d}0}^{(k)} := - \min_{r \,\in\, \mathcal{C}_0^{(k)}} \langle Q_{rc}\Delta d_c^k + q_r \rangle_- . \tag{2.48b}$$

The residuals above are problem-dependent since they are dimensional. Therefore, a severe tolerance is introduced and $\texttt{TOL}_{\text{d}+} = \texttt{TOL}_{\text{d}0} = 10^{-9}$ is employed. In our tests, it has been observed that the fulfillment of $\texttt{Res}_\text{d}^{(k)} \leq \texttt{TOL}_\text{d}$ requires from few to some dozens of iterations, depending on the prescribed tolerance. $\texttt{Res}_{\text{d}0}^{(k)} \leq \texttt{TOL}_{\text{d}0}$ is usually satisfied at all iterations. $\texttt{Res}_{\text{d}+}^{(k)} \leq \texttt{TOL}_{\text{d}+}$ turns out to define the most strict criterion, taking from few dozens to some hundreds of iterations, depending on the prescribed tolerance. Finally, the complementarity condition $(2.45)_3$ converges faster to zero since it comes from the product of $(2.45)_2$ and $(2.45)_1$.

## 2.7 Numerical simulations

In this section, two numerical tests proposed in Gerasimov and De Lorenzis (2019) are considered and the performance of the two solution strategies described in the previous section, namely, the penalty approach and the PSOR algorithm, is comparatively assessed. In both cases, a plane strain specimen is subjected to a quasi-static loading-unloading, displacement-controlled regime, under the hypothesis of small displacements. In the first case, a single edge notched (SEN) specimen under shear is considered, while the second test concerns an L-shaped specimen. The material parameters used for both tests are reported in Table 2.2, while geometry, mesh, and time history are described in the relevant sections. Finally, the finite element discretization consists of structured meshes of 4-nodes quadrilateral elements with full integration.

| Material | $E_0$ | $\nu$ | $G_c$ | $l_{0d}$ |
|---|---|---|---|---|
| I | 210.00 | 0.33 | 2.700 | 0.01 |
| II | 25.85 | 0.18 | 0.095 | 5.00 |
| | GPa | - | N/mm | mm |

**Table 2.2:** Material properties

Since the alternate minimization algorithm solves the balance of linear momentum equation first, in the numerical tests the chosen convergence criterion controls the discretized counterpart of the out-of-balance work (2.28), defined as

$$\texttt{Res}_{\text{STAG}} = \left| \Delta\widehat{\mathbf{u}}^{\text{T}} \left( \mathbf{F}_{\text{I}}(\Delta\widehat{\mathbf{u}}, \Delta\widehat{\mathbf{d}}) - \mathbf{F}_{\text{E}} \right) \right| . \tag{2.49}$$

Following Gerasimov and De Lorenzis (2019), a tolerance $\texttt{TOL}_{\text{STAG}} = 10^{-7}$ kJ is set for the residual $\texttt{Res}_{\text{STAG}}$ (see Algorithm 1). Additionally, we set the tolerances for the PSOR algorithm and for the penalty method to $\texttt{TOL}_{\text{d}} = 10^{-4}$ (see Section 2.6). We further test both algorithms also with the tolerance $\texttt{TOL}_{\text{d}} = 10^{-6}$, to assess their performance under a more severe convergence criterion.

Moreover, the tolerance for the iterations for enforcement of the balance of linear momentum has been set to $\texttt{TOL}_{\text{NR,u}} = 10^{-9}$ kJ, being the residual $\texttt{Res}_{\text{NR,u}} = \left| (\mathbf{F}_{\text{I}} - \mathbf{F}_{\text{E}})^{\text{T}} (\mathbf{F}_{\text{I}} - \mathbf{F}_{\text{E}}) \right|$.

Finally, the computing performance of the PSOR method is compared to that of the penalty method and assessed for each considered benchmark. Specifically, the elapsed time for the phase-field subroutine call is measured using the stopwatch timer function "`tic toc`" in Matlab.

### 2.7.1 SINGLE EDGE NOTCHED SPECIMEN (SEN) UNDER SHEAR

The SEN example, originally considered in Bourdin et al. (2000), consists of a crack propagation problem in a shear-loaded square plate with a pre-existing crack modeled by a physical geometrical discontinuity (see Figure 2.2). The material parameters are those of material I of Table 2.2.

The initial crack length is $a$, while the square specimen has width $2a = 1$ mm. The geometry is spatially discretized by a uniform structured mesh of 400x400 4-nodes elements with bilinear shape functions. Therefore, the internal length $l_{0d}$ is resolved with 4 elements. The specimen is subject to Dirichlet boundary conditions on the bottom and top sides. The first one is clamped, while the latter undergoes a horizontal imposed displacement of magnitude $u$, with prevented vertical displacement. The load history is subdivided in time steps denoted with $n$. The reference displacement increment is $\Delta u_n = 3 \cdot 10^{-4}$ mm. Since the first part of the response is linear elastic, a refined time step is not needed and therefore the initial displacement is set to $u_0 = 6 \cdot 10^{-3}$ mm. Then, for $n = 2, ..., 21$ the loading branch is characterized by $u_{n+1} = u_n + \Delta u_n$,

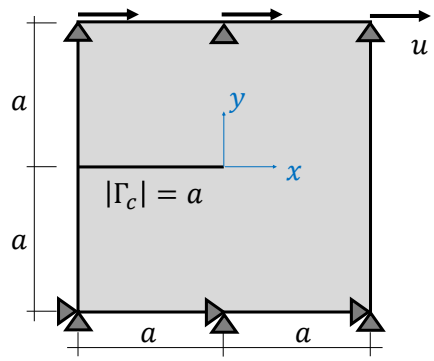


**Figure 2.2:** SEN specimen under shear loading. Geometry and boundary conditions.

while in the unloading part of the time history, for $n = 22, ..., 34$, the imposed displacement is $u_{n+1} = u_n - 3\Delta u_n$.

The global response in terms of reaction force $R$, internal energy $\mathcal{E}$, and brittle fracture dissipation $\mathcal{D}_f$ is reported as a function of the imposed displacement $u$ in Figure 2.3. The response is nearly linear elastic until the peak corresponding to the end of step 13. Note that the initial part of the elastic energy curve in Figure 2.3 should be almost quadratic, even though it does not appear to be so due to the very coarse time step used in the initial part of the analysis. At the end of step 13, the stress concentration at the notch tip drives the growth of the phase field until the crack onset, after which the specimen response enters the softening branch. As expected, the unloading path is linear elastic with no further phase field growth. Here, the reaction force is linear, with reduced (degraded) stiffness, the internal energy is quadratic, and the dissipation is constant. It is interesting to note that the fracture dissipation $\mathcal{D}_f$ grows monotonically along the staggered iteration sequence, while the total energy decreases, as a consequence of the minimization process. During shear loading, the phase field deviates from the symmetry axis as it can be noticed in Figure 2.4. This is a direct consequence of the non-symmetric degradation of the elastic free energy due to the splitting into positive and negative volumetric components.

The convergence of the staggered algorithm is shown in Figure 2.5 for the critical load increment 14 corresponding to the crack onset. The criterion used for stopping the iterations involves the first variation of the total energy with respect to the displacement (2.28) in its space discrete counterpart (2.49). In the same figure, other two quantities are plotted: the total energy (2.11) and the fracture dissipation $(2.12)_2$. Both of them could also be used to define alternative convergence criteria. The choice of a suitable stopping criterion is a delicate point of the staggered scheme. This can be appreciated in Figure 2.6, where contour plots of the phase-field variable are shown at different staggered iterations. All of them qualitatively seem reasonable solutions for the crack propagation problem, but they actually correspond to out-of-balance states

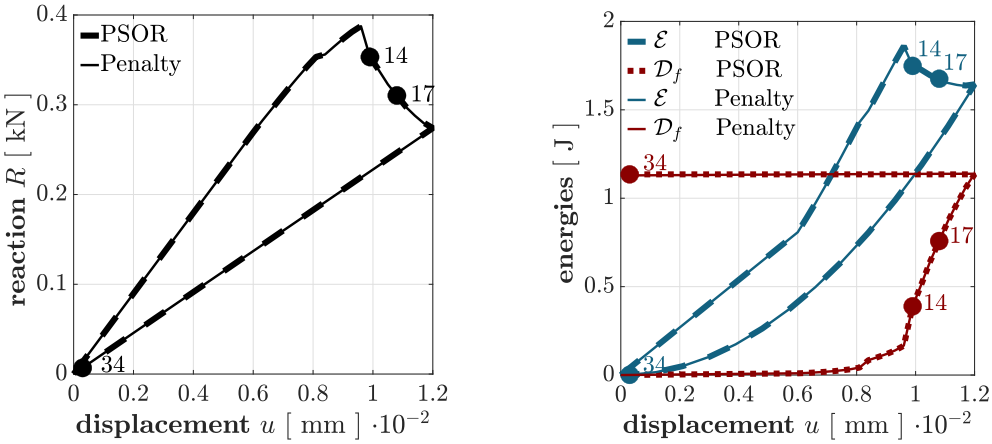


**Figure 2.3:** SEN specimen under shear loading. Global response in terms of reaction force and energies versus imposed displacement. Curves are obtained with both PSOR and penalty methods. Solid marks denote the end of three relevant steps of the time history: step 14, first step in the softening branch, step 17, intermediate between peak and unloading branch, step 34 corresponding to the end of the time history.

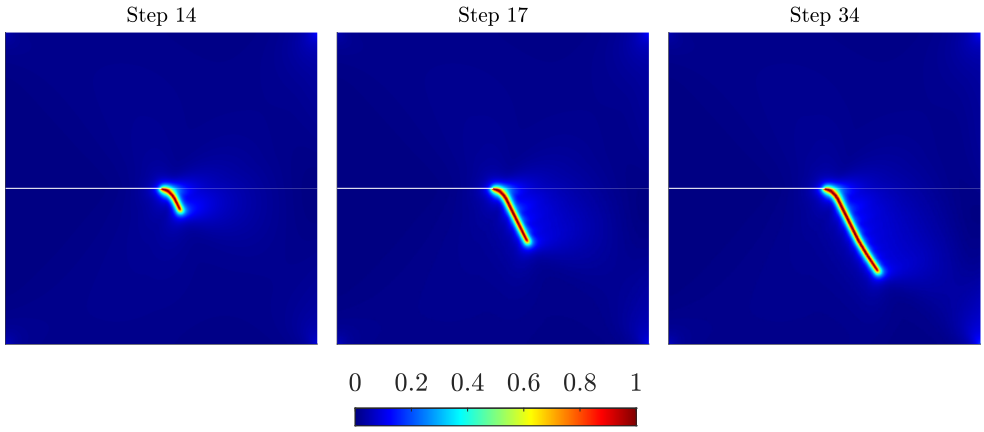


**Figure 2.4:** SEN specimen under shear loading. Phase-field evolution at the end of three different steps: loading branch, steps 14 and 17, and unloading branch 21-34 (step 21 is the last loading step; the phase field does not evolve during unloading).

between internal and external forces.

Finally, the overall computing time of the analysis at each load step is depicted in Figure 2.7. It corresponds to the sum of the execution time for the subroutine calls for all staggered iterations within a load step. The non-negligible reduction in the analysis time due to the explicit nature of the PSOR algorithm can be clearly appreciated. Furthermore, it is worthwhile noticing the unloading steps $n = 22, ..., 34$, where the PSOR method does not iterate, while

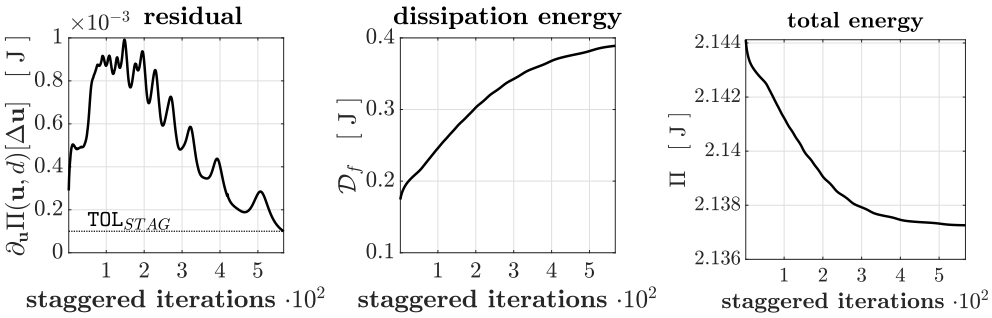


**Figure 2.5:** SEN specimen under shear loading. Evolutions at step 14 of (a) staggered residual, (b) dissipation energy, and (c) total energy are shown during the staggered iterations.

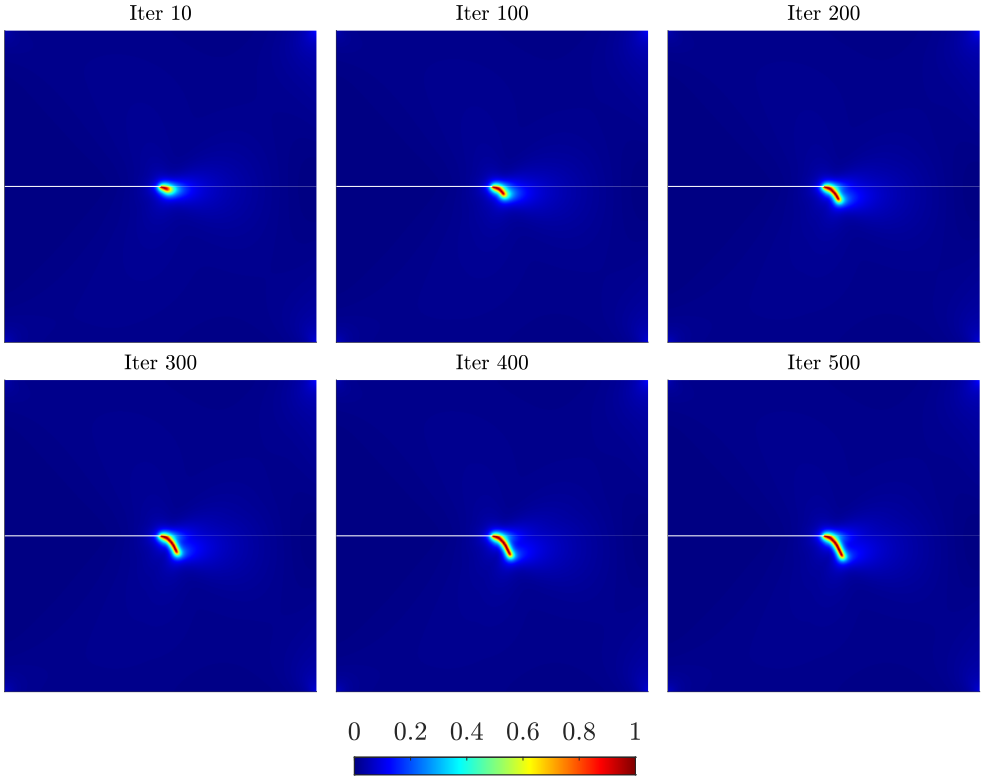


**Figure 2.6:** SEN specimen under shear loading. Phase field evolution during the staggered iterations of step 14.

the penalty method requires at least a couple of Newton-Raphson iterations. For the sake of completeness, the time required for the execution of the phase-field subroutine in the staggered iterations of step 14 is reported in Figure 2.8. The stability of the PSOR method in terms of number of iterations and,

consequently, of computing time necessary to reach convergence can be clearly appreciated. The same stable trend is achieved by the penalty method as long as the staggered iterations proceed. It should be mentioned, however, that these results are strictly related to the choice of the tolerance in the two methods. More specifically, if more severe tolerances $\texttt{TOL}_{\text{PSOR}} = \texttt{TOL}_{\text{NR,d}} = 10^{-6}$ are used, the two approaches exhibit a different behavior close to the solution. The PSOR method needs a significantly larger number of iterations to meet the more severe stopping criterion. In contrast, the Newton-Raphson method achieves the usual quadratic convergence rate, even for reduced tolerances.

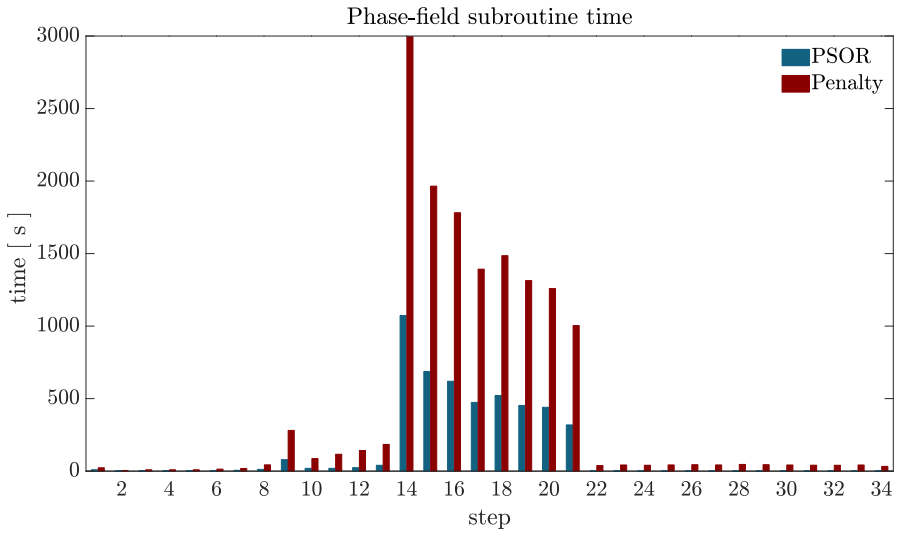


**Figure 2.7:** SEN specimen under shear loading. Elapsed time for the execution of the phase-field subroutine at each load step. Comparison between PSOR and penalty methods.

### 2.7.2 L-SHAPED SPECIMEN TEST

The L-shaped specimen test, as described in Winkler (2001), does not consider a pre-existing crack and involves fracture nucleation as well as propagation, resulting in a more elaborate test. The problem setup, comprising the geometry and the boundary conditions, is shown in Figure 2.9, where $a = 250$ mm, while the specimen thickness is $t = 100$ mm. The material parameters are assumed to be those of material type II in Table 2.2. The zoomed detail in Figure 2.9 shows the trapezoidal reinforcement, glued on the lower wing of the L-shaped panel to avoid localized stress singularities inside the specimen. An upward vertical displacement $u$ is applied to the shorter base of this ancillary item, while its horizontal degrees of freedom are restrained. The L-shaped structure is also completely clamped at $y = -a$.

A loading-unloading displacement history is applied under plane strain conditions: starting from $u_1 = 0.01$ mm and considering a load increment

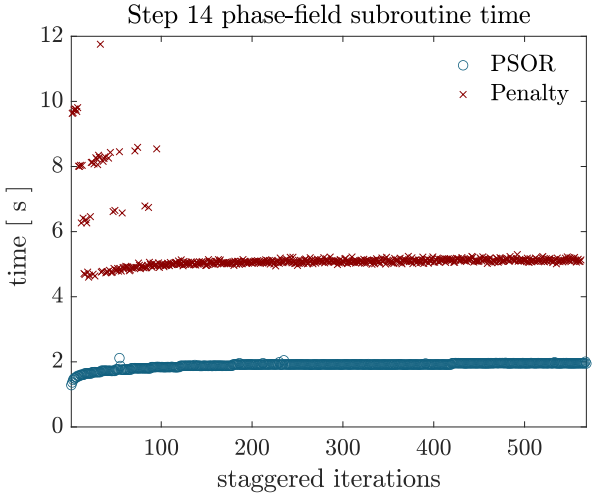


**Figure 2.8:** SEN specimen under shear loading. Elapsed time for the execution of the phase-field subroutine at load step 14. Comparison between PSOR and penalty methods.

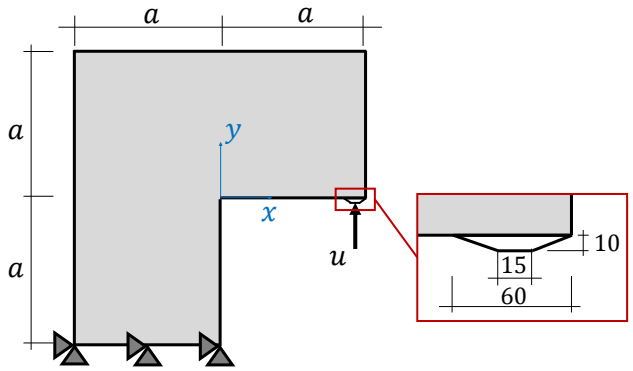


**Figure 2.9:** L-shaped specimen test. Geometry and boundary conditions. The enlarged frame shows the detail of the reinforcement where the upward displacement is imposed with dimensions in [mm].

$\Delta u_n = 0.01$ mm, 35 loading steps are applied (from 2 to 36), followed by 11 unloading steps (from 37 to 47) using $3\Delta u_n$. The uniform and structured 4-nodes quadrilateral mesh has typical element size $h_e = 1/4\, l_{0d}$.

In Figure 2.10, we show the global response for the L-shaped specimen in terms of reaction force $R$, internal energy $\mathcal{E}$, and fracture dissipation $\mathcal{D}_f$, at each imposed vertical displacement $u$. Three different behaviors of the considered sample can be identified. Until step 23, corresponding to the peak, no propagation occurs and the response is nearly elastic. From step 24 to 36, crack nucleation (see Figure 2.11, step 24) and propagation (see, e.g., Figure 2.11, step 31) take place, defining the softening part of the reaction force curve and leading to a significant increase of specific dissipation and to a corresponding

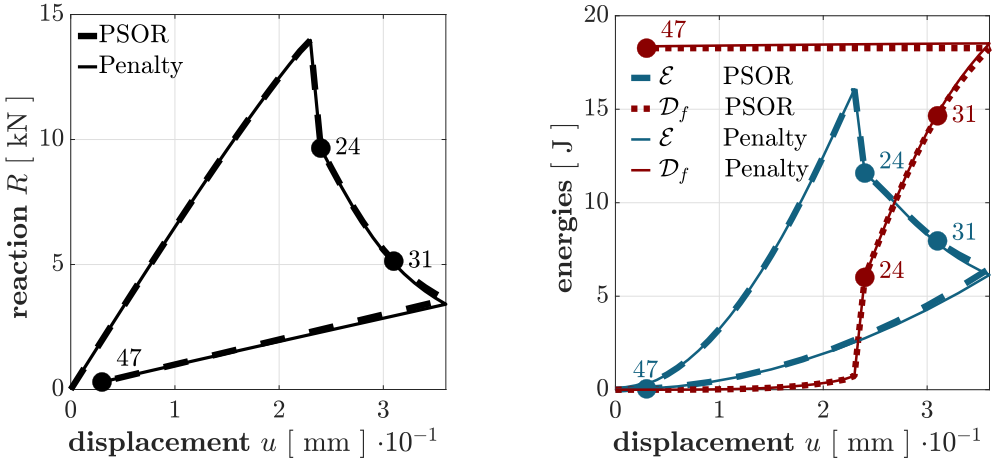


**Figure 2.10:** L-shaped specimen test. Global response with PSOR and penalty methods in terms of reaction force $R$, internal energy $\mathcal{E}$, and specific dissipation $\mathcal{D}_f$ *versus* imposed displacement $u$. Solid marks denote the end of three relevant steps of the time history: step 24 corresponds to the first step after the beginning of the softening branch, step 31 is an intermediate step between the peak (step 23) and the beginning of the unloading branch, and step 47 is the end of the time history.

reduction of elastic energy, noticeable in Figure 2.10. Finally, we highlight that during the elastic unloading stage starting after step 36, the level of dissipation remains constant and the crack no longer propagates (see Figure 2.11, step 47), satisfying the irreversibility constraint. Furthermore, in the L-shaped panel test, the penalty method seems to be less accurate, producing a slightly non-constant dissipation in the unloading stage, as one can notice from the slight downward slope for decreasing $u$ in the final part of the $\mathcal{D}_f - u$ curve.

In Figure 2.12, we present the convergence of the staggered algorithm at the loading step 24, at the beginning of crack propagation. In particular, we consider the first variation of the total energy with respect to the displacement, the total energy, and the specific dissipation (see Figure 2.12). We highlight that, for the L-shaped benchmark, the convergence criterion (2.49) based on the first variation $\partial_{\mathbf{u}}\Pi$ of the total energy with respect to the displacement variable seems to represent a conservative choice, due to the fact that the total energy at iteration 250 (see Figure 2.12) appears to be already minimized, while $\texttt{Res}_{\text{STAG}}$ suggests the need for further iterations. Moreover, Figure 2.13 confirms that there is no remarkable difference in terms of the phase-field solution obtained between iteration 300 and 500 of loading step 24.

The results presented in Figures 2.11, 2.12, and 2.13 are obtained using the PSOR method and lead to virtually indistinguishable solutions with respect to the penalty method.

A comparison between the total times required for the execution of the phase-field subroutine *via* the PSOR and penalty methods is shown in Figure

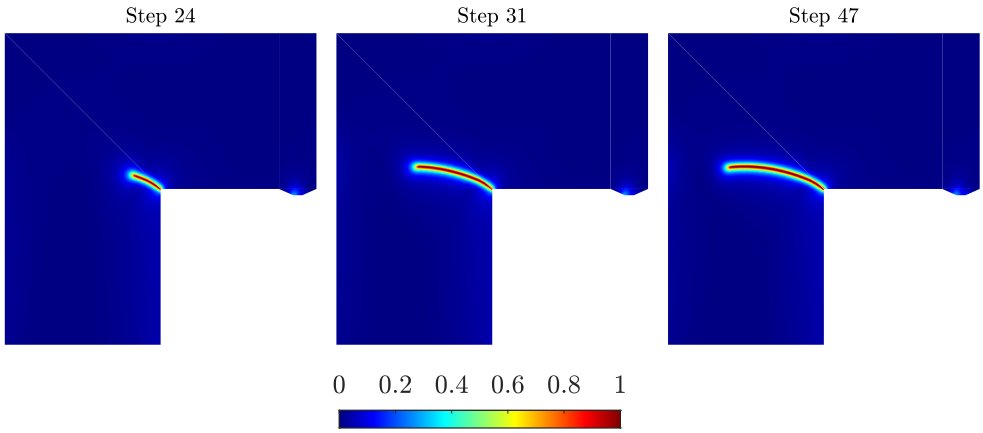


**Figure 2.11:** L-shaped specimen test. The phase-field problem is solved *via* the PSOR algorithm and we consider the phase-field evolution at three different steps: steps 24 and 31 correspond to the loading branch, while step 47 is at the end of the unloading branch. During the unloading phase, from step 35 to step 47, the phase field does not evolve.

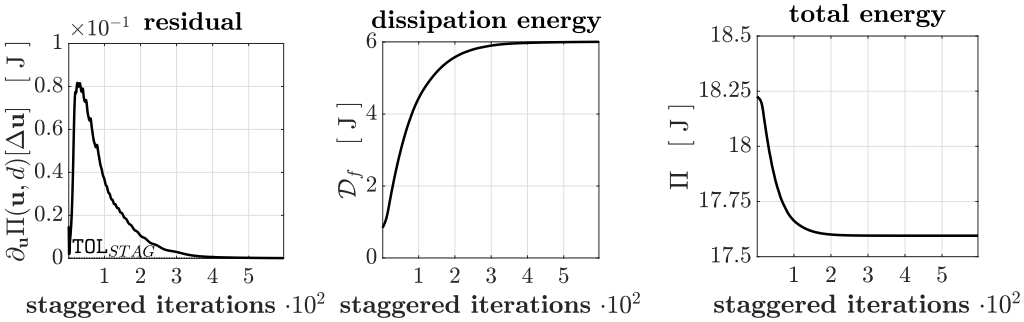


**Figure 2.12:** L-shaped specimen test. Convergence of the staggered algorithm at the loading step 24 in terms of the first variation of the total energy with respect to the displacement variable $\partial_{\mathbf{u}}\Pi$ ($\texttt{Res}_{\text{STAG}}$), of the dissipated energy $\mathcal{D}_f$, and of the total energy functional $\Pi$ *versus* the number of staggered iterations.

2.14, while, in Figure 2.15, we assess the performance of the PSOR and penalty algorithms in terms of computing time at each staggered iteration of step 24. The explicit nature of the PSOR algorithm leads to a time-saving performance, especially at the computationally more demanding step 24, during which the crack field nucleates. Figures 2.14 and 2.15 show a similar behavior of the PSOR and penalty method as we reported for the SEN specimen in Section 2.7.1.

Finally, to assess the PSOR algorithm we tested two tolerances (i.e., $\texttt{TOL}_{\text{PSOR}} = 10^{-4}$ and $\texttt{TOL}_{\text{PSOR}} = 10^{-6}$) also for the L-shaped specimen test. While for the SEN specimen example, a dramatic reduction of $\texttt{TOL}_{\text{PSOR}}$ value leads to the

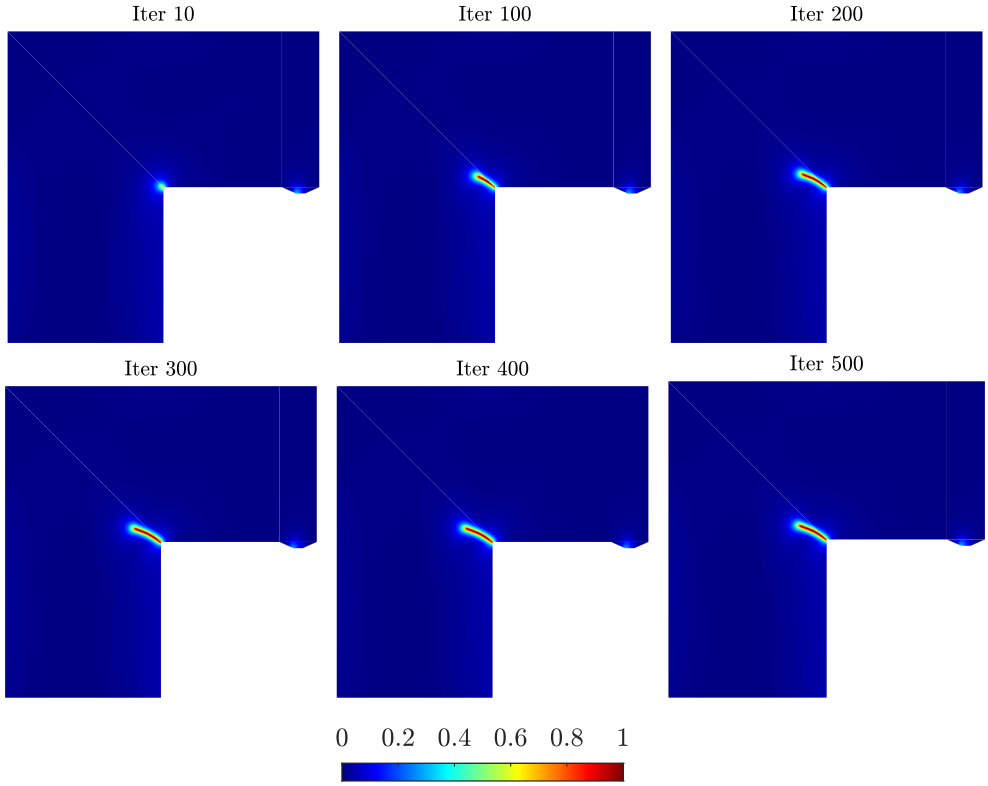


**Figure 2.13:** L-shaped specimen test. Phase-field evolution during the staggered iterations (iterations 10, 100, 200, 300, 400, and 500) at the loading step 24 for the PSOR method.

same results in terms of time performance with respect to the penalty method, this is not the case for the L-shaped panel test, which proved to be more computationally demanding for the PSOR method when a tolerance equal to $10^{-6}$ is considered. Conversely, the performance of the penalty method in terms of required elapsed total subroutine time is less sensitive to the chosen tolerance. This issue is related to the tuning of the penalty parameter $\gamma_p$ that strongly depends on the toughness-internal length ratio. In fact, the value of $\gamma_p$ for the L-shaped panel test is much smaller than its counterpart for the SEN specimen benchmark, thereby representing a more relaxed constraint.

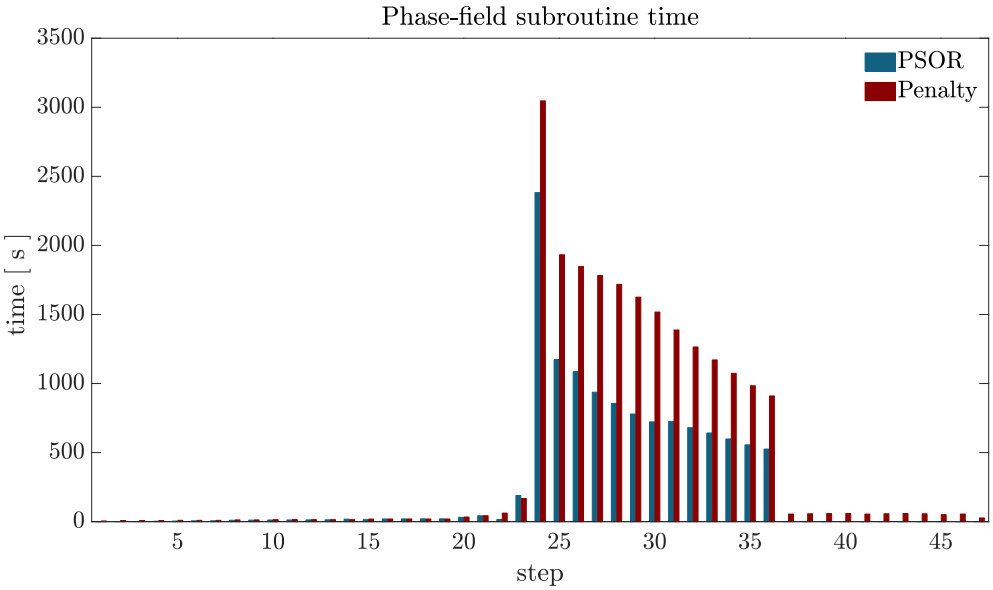


**Figure 2.14:** L-shaped specimen test. Total elapsed time to execute the phase-field subroutine at each load step. Comparison between PSOR and penalty methods.

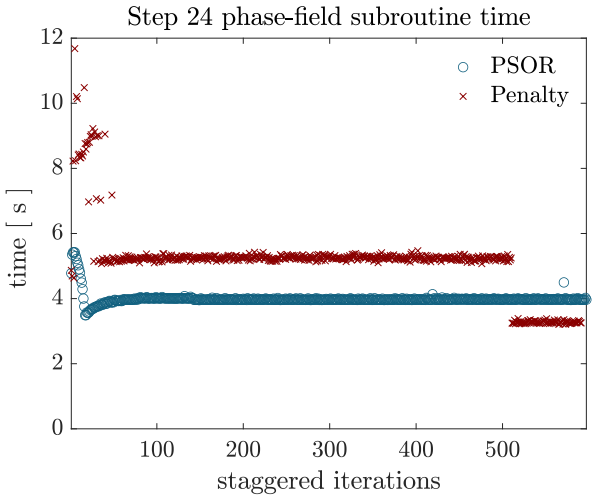


**Figure 2.15:** L-shaped specimen test. Total elapsed time to execute the phase-field subroutine at the loading step 24. Comparison between PSOR and penalty methods.

# 3 Ductile Fracture in Small Deformations

## 3.1 Introduction

In ductile materials two dissipation mechanisms are present: the development of plastic strains, and the propagation of brittle cracks. Experimental observations show that either already existing voids, or voids nucleated under the effect of developing plastic strains at inclusions or second-phase particles, grow until they coalesce giving rise to a continuous fracture path. Based on these physical evidences, in the proposed phase-field plasticity model, crack nucleation and propagation are assumed to be driven by plasticity. Damage development is then possible when the plastic process zone in a strain concentration region reaches a critical level, measured by the equivalent plastic strain. The formulation is based on an effective stress description of gradient plasticity, combined with an AT1 phase-field model. The term effective stress refers here to the true stress acting on the undamaged portion of the bulk material. The main consequence of this choice is that plasticity continues to develop until the final state of material failure, where damage approaches unity. After damage has started to develop and the global structural response has become softening, incremental plastic strains tend to localize in a one-element-thick band, giving rise to a pathological mesh dependence in the final stage of rupture. To avoid the problem, a gradient plasticity regularization is adopted. Starting from established variational statements of finite-step elastoplasticity for generalized standard materials, a mixed variational statement is derived, incorporating in a rigorous way a variational finite-step update for both the elastoplastic and the phase-field dissipations. To obtain a plasticity driven damage development, a function of the equivalent plastic strain, modulating the current value of the material fracture energy, is introduced in the functional. A staggered scheme is adopted for its stationarity enforcement. A computationally effective and robust Newton-Raphson scheme for the solution of the gradient elastoplastic problem for fixed damage is proposed for the case of Mises plasticity, together with its global return mapping algorithm and expression of the global consistent

tangent matrix. A further consequence of the effective stress approach is the occurrence of locking phenomena due to the development of large plastic strains after damage onset. This is cured with a standard reduced integration technique together with hourglass stabilization. A novel formulation is proposed to account for material non-linearity in the hourglass internal forces.

## 3.2 Phase-field variational formulation

### 3.2.1 Nominal & effective responses

In the damaged state, $\mathrm{d}\Omega$ defines the infinitesimal nominal volume, equal to the original undamaged volume, while $\mathrm{d}\widetilde{\Omega} = \omega\ \mathrm{d}\Omega$ is the current effective volume, i.e., the nominal volume minus the volume of the defects, being $\omega$ the degradation function introduced in Section 2.3.1. A sketch of the different volumes is shown in Figure 3.1, where $\Omega_V$ is the micro-voids volume. Note that, while $\Omega$ denotes the nominal volume and $\Omega$ the effective one, in what follows the effective quantities, i.e., quantities referred to the damaged volume, are always denoted with a tilde symbol $\widetilde{(\cdot)}$, while the nominal quantities, i.e., those referred to the undamaged volume, do not have a symbol. The point-wise transformation from effective to nominal quantity reads:

$$\underbrace{\widetilde{(\cdot)}}_{\textit{effective}}\ \overbrace{\mathrm{d}\widetilde{\Omega}}^{\textit{effective}} = \underbrace{\widetilde{(\cdot)}}_{\textit{effective}}\ \omega\ \overbrace{\mathrm{d}\Omega}^{\textit{nominal}} = \underbrace{(\cdot)}_{\textit{nominal}}\ \overbrace{\mathrm{d}\Omega}^{\textit{nominal}} \tag{3.1}$$

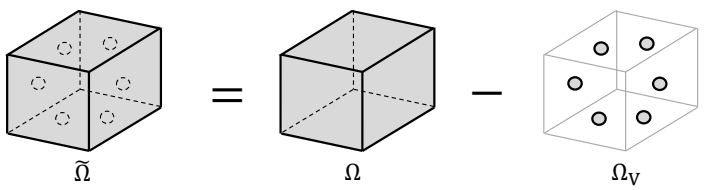


**Figure 3.1:** Nominal $\Omega$, voids $\Omega_V$, and effective $\widetilde{\Omega}$ volumes

### 3.2.2 State variables & evolution laws

An elastoplastic material, belonging to the class of *generalized standard materials* (see e.g., Halphen and Son (1975)), is considered. The material state is assumed to be completely defined by the total strain tensor $\boldsymbol{\varepsilon} := \boldsymbol{\nabla}^s\mathbf{u}$ ($\boldsymbol{\nabla}^s(\cdot)$ being the symmetric gradient operator), the plastic strain tensor $\boldsymbol{\varepsilon}^p$, the hardening internal variable $\alpha$, and the damage-like phase field $d$. In the current ductile formulation, the free energy decomposition into active and inactive part for the promotion of crack evolution will be addressed in the following. The free energy density $\psi$ is assumed to be additively decomposed into its elastic (reversible) part $\omega\,\widetilde{\psi}^e(\boldsymbol{\varepsilon}^e)$, $\boldsymbol{\varepsilon}^e = \boldsymbol{\varepsilon} - \boldsymbol{\varepsilon}^p$ denoting the elastic strain tensor, and hardening

(unrecoverable) part $\omega\,\widetilde{\psi}^p(\alpha)$, the latter being the internal elastic energy stored in the material because of irreversible deformations of the micro-structure. The energies $\widetilde{\psi}^e(\boldsymbol{\varepsilon}^e)$ and $\widetilde{\psi}^p(\alpha)$, assumed to be convex functions of their arguments, are the undamaged or *effective* elastic and hardening free energies. The *nominal* and *effective* free energy densities are defined as:

$$\psi := \omega\,\widetilde{\psi} \quad , \quad \widetilde{\psi} := \widetilde{\psi}^e + \widetilde{\psi}^p \tag{3.2}$$

The Clausius-Duhem inequality states that the specific dissipation rate $\dot{\phi}$ must increase in every transformation, i.e. $\dot{\phi} := \boldsymbol{\sigma} : \dot{\boldsymbol{\varepsilon}} - \dot{\psi} \geq 0$, where $\boldsymbol{\sigma}$ is the Cauchy stress tensor, $\dot{\boldsymbol{\varepsilon}}$ is the total strain rate, and $\dot{\psi}$ is the free energy rate. The introduction of (3.2) into the dissipation inequality reads:

$$\dot{\phi} := \boldsymbol{\sigma} : \dot{\boldsymbol{\varepsilon}} - \dot{\psi} = \underbrace{\left(\boldsymbol{\sigma} - \omega\,\partial_{\boldsymbol{\varepsilon}^e}\widetilde{\psi}^e\right) : \dot{\boldsymbol{\varepsilon}}^e}_{elastic} + \underbrace{\boldsymbol{\sigma} : \dot{\boldsymbol{\varepsilon}}^p - \omega\,\partial_\alpha\widetilde{\psi}^p\,\dot{\alpha}}_{plastic} - \underbrace{\omega'\,\widetilde{\psi}\,\dot{d}}_{fracture} \geq 0 \tag{3.3}$$

During an elastic or reversible transformation, no evolution of the plastic deformations $\dot{\boldsymbol{\varepsilon}}^p = \mathbf{0}$, of the hardening variable $\dot{\alpha} = 0$ or of damage $\dot{d} = 0$ occurs and, hence, no dissipation increase is produced (i.e., $\dot{\phi} = 0$). Therefore, the only term left is $(\boldsymbol{\sigma} - \omega\,\partial_{\boldsymbol{\varepsilon}^e}\widetilde{\psi}^e) : \dot{\boldsymbol{\varepsilon}}^e = 0$. Since it must hold for all reversible transformations $\dot{\boldsymbol{\varepsilon}}$, the nominal and effective elastic evolution laws read:

$$\boldsymbol{\sigma} = \omega\,\widetilde{\boldsymbol{\sigma}} \quad , \quad \widetilde{\boldsymbol{\sigma}} := \partial_{\boldsymbol{\varepsilon}^e}\widetilde{\psi}^e \tag{3.4}$$

Consideration of the dissipation inequality in the conditions of no damage, $\dot{d} = 0$, allows to define:

$$\dot{\phi}^p = \omega\,\dot{\widetilde{\phi}}^p \quad , \quad \dot{\widetilde{\phi}}^p := \widetilde{\boldsymbol{\sigma}} : \dot{\boldsymbol{\varepsilon}}^p - \widetilde{\chi}\,\dot{\alpha} \geq 0 \tag{3.5}$$

where $\dot{\widetilde{\phi}}^p$ denotes the dissipation rate due to plasticity only and $\widetilde{\chi}$ is the effective *static* hardening variable, i.e. the thermodynamic force work-conjugated to the internal variable $\alpha$. From (3.3), it turns out to be defined as:

$$\widetilde{\chi} := \partial_\alpha\widetilde{\psi}^p \tag{3.6}$$

The elastoplastic dissipation inequality $(3.5)_2$ can be also expressed in terms of its effective counterpart, i.e., $\dot{\phi}^p d\Omega = \dot{\widetilde{\phi}}^p d\widetilde{\Omega} \geq 0$. The effective yield stress associated to the internal variable $\alpha$ is $\widetilde{\sigma}_y(\alpha) = \bar{\sigma}_{y0} + \widetilde{\chi}(\alpha)$, where $\bar{\sigma}_{y0}$ is the initial yield stress. The elastoplastic evolution has to satisfy the additional constraint that the admissible set of effective stress and hardening parameter $(\widetilde{\boldsymbol{\sigma}}^*, \widetilde{\chi}^*)$ has to fulfill the yield criterion $f_y(\widetilde{\boldsymbol{\sigma}}^*, \widetilde{\chi}^*) \leq 0$, where $f_y$ is the local yield function, convex in the space of stress and static internal variable. The yield criterion is postulated in terms of effective quantities, since only the continuous, non-damaged part of the volume is undergoing plastic deformations. The stationarity conditions associated to the (effective) principle of maximum dissipation provide the *effective elastoplastic evolution laws*:

$$\dot{\boldsymbol{\varepsilon}}^p = \dot{\lambda}\,\partial_{\widetilde{\boldsymbol{\sigma}}} f_y \quad , \quad \dot{\alpha} = -\dot{\lambda}\,\partial_{\widetilde{\chi}} f_y \quad , \quad \dot{\lambda} \geq 0 \quad , \quad f_y \leq 0 \quad , \quad \dot{\lambda}\,f_y = 0 \tag{3.7}$$

where $\dot{\lambda}$ is the non-negative rate of a scalar plastic multiplier. Finally, the ductile-fracture specific dissipation rate $\dot{\phi}^{pf}$ reads:

$$\dot{\phi}^{pf} := \omega \dot{\widetilde{\phi}}^{p} + \dot{\phi}^{f} \quad , \quad \dot{\phi}^{f} := Y \dot{d} \quad , \quad Y := -\omega' \widetilde{\psi} \tag{3.8}$$

where the $\dot{\phi}^{f}$ is the brittle fracture specific dissipation rate and $Y$ is the fracture driving force. $\dot{\phi}^{pf}$ is the dissipation rate per unit nominal volume and, therefore, the elementary dissipation rate is $\dot{\phi}^{pf}\, d\Omega$.

### 3.2.3 VARIATIONAL FORMULATION OF THE FINITE-STEP PROBLEM

#### 3.2.3.1 ELASTOPLASTIC VARIATIONAL UPDATE

Let us first consider an elastoplastic material without damage. In this case, effective and nominal quantities coincide, since there are no developing defects inside the volume. The tilde symbol $\widetilde{(\cdot)}$ will be therefore used only for homogeneity with the subsequent sections. Let $\Delta\widetilde{w}^{int}$ be the specific elastoplastic internal work carried out along a deformation process between time $t^n$ and $t^{n+1}$

$$\begin{aligned} \Delta\widetilde{w}^{int} = \int_{t^n}^{t^{n+1}} \widetilde{\boldsymbol{\sigma}} : \dot{\boldsymbol{\varepsilon}} dt = \int_{t^n}^{t^{n+1}} [\widetilde{\boldsymbol{\sigma}} : \dot{\boldsymbol{\varepsilon}}^{e} + \widetilde{\chi}\, \dot{\alpha} + (\widetilde{\boldsymbol{\sigma}} : \dot{\boldsymbol{\varepsilon}}^{p} - \widetilde{\chi}\, \dot{\alpha})]\, dt = \\ = \Delta\widetilde{\psi}^{e} + \Delta\widetilde{\psi}^{p} + \Delta\widetilde{\phi}^{p} \end{aligned} \tag{3.9}$$

where the symbol $\Delta(\cdot)$ denotes the increment of the quantity $(\cdot)$ over the time step $\Delta t = t^{n+1} - t^n$. We define an extremal path as a path in strain space from $\boldsymbol{\varepsilon}^n = \boldsymbol{\varepsilon}(t^n)$ to $\boldsymbol{\varepsilon}^{n+1} = \boldsymbol{\varepsilon}(t^{n+1})$, $\boldsymbol{\varepsilon}^n$ and $\boldsymbol{\varepsilon}^{n+1}$ being prescribed strains, minimizing the internal work $\Delta\widetilde{w}^{int}$. Let $\Delta\widetilde{w}^{int}_{min}$ be the minimum value of $\Delta\widetilde{w}^{int}$, so that $\Delta\widetilde{w}^{int} \geq \Delta\widetilde{w}^{int}_{min}$ along any strain path from $\boldsymbol{\varepsilon}^n$ to $\boldsymbol{\varepsilon}^{n+1}$.

Since $\Delta\widetilde{\psi}^{e}$ and $\Delta\widetilde{\psi}^{p}$ are path independent quantities, they take the same value along any path between $\boldsymbol{\varepsilon}^n$ and $\boldsymbol{\varepsilon}^{n+1}$ and the extremal path minimizes $\Delta\widetilde{\phi}^{p}$. Let $\Delta\widetilde{\phi}^{p}_{min}$ be this minimum value. Obviously, if a feasible purely elastic path exists from $\boldsymbol{\varepsilon}^n$ to $\boldsymbol{\varepsilon}^{n+1}$, this is an extremal path. While the sum $\Delta\boldsymbol{\varepsilon} = \boldsymbol{\varepsilon}^{n+1} - \boldsymbol{\varepsilon}^n = \Delta\boldsymbol{\varepsilon}^{e} + \Delta\boldsymbol{\varepsilon}^{p}$ is prescribed, different paths lead to different increments of elastic and plastic strains. The extremal path is therefore the solution of the following minimization problem:

$$\Delta\widetilde{w}^{int}_{min} = \min_{\Delta\boldsymbol{\varepsilon}^{e}, \Delta\boldsymbol{\varepsilon}^{p}, \Delta\alpha} \{\Delta\widetilde{\psi}^{e} + \Delta\widetilde{\psi}^{p} + \Delta\widetilde{\phi}^{p} \mid \Delta\boldsymbol{\varepsilon}^{e} + \Delta\boldsymbol{\varepsilon}^{p} = \Delta\boldsymbol{\varepsilon}\} \tag{3.10}$$

where the total strain increment $\Delta\boldsymbol{\varepsilon}$ is prescribed.

Based on the principle of maximum dissipation, it has been shown in Reddy et al. (1987) and Ortiz and Martin (1989) that, for prescribed increments of $\Delta\boldsymbol{\varepsilon}^{p}$ and $\Delta\alpha$ over the time step, extremal paths in the plastic variables space (i.e., leading to the minimum increment of dissipation $\Delta\widetilde{\phi}^{p}_{min}$) are obtained by letting $\boldsymbol{\varepsilon}^{p}$ and $\alpha$ evolve only at constant stress, as it is the case when a backward-difference time integration of the elastoplastic constitutive law (often referred to as *return mapping algorithm*) is adopted. In this case, the step

can be seen to have been elastic until the end of the step and plastic evolution is allowed only when the final values $\widetilde{\boldsymbol{\sigma}}^{n+1}$ and $\widetilde{\chi}^{n+1}$ have been achieved (see Corigliano (1994) for a review of extremum properties of the generalized midpoint time integration rule). The backward-difference integrated conditions defining the extremal path, i.e. its optimality conditions, are given by (with $f_y^{n+1} = f_y(\widetilde{\boldsymbol{\sigma}}^{n+1}, \widetilde{\chi}^{n+1})$):

$$\begin{aligned} \Delta\boldsymbol{\varepsilon}^p = \Delta\lambda\, \partial_{\widetilde{\boldsymbol{\sigma}}} f_y^{n+1} \quad , \quad \Delta\alpha = -\Delta\lambda\, \partial_{\widetilde{\chi}} f_y^{n+1} \quad , \\ \Delta\lambda \geq 0 \quad , \quad f_y^{n+1} \leq 0 \quad , \quad \Delta\lambda\, f_y^{n+1} = 0 \end{aligned} \tag{3.11}$$

while the backward-difference finite-step version of the principle of maximum dissipation reads

$$\Delta\widetilde{\phi}^p_{min} = \max_{\widetilde{\boldsymbol{\sigma}}^{n+1},\, \widetilde{\chi}^{n+1} \in f_y \leq 0} \{\widetilde{\boldsymbol{\sigma}}^{n+1} : \Delta\boldsymbol{\varepsilon}^p - \widetilde{\chi}^{n+1}\Delta\alpha\} \tag{3.12}$$

For the considered class of generalized standard materials, the backward-difference integration algorithm has also been shown to preserve the symmetry of the consistent tangent, implying the existence of an incremental potential $\widetilde{w}^{int\,n}_{min}$ such that $\widetilde{\boldsymbol{\sigma}}^{n+1} = \partial\widetilde{w}^{int\,n}_{min}/\partial\boldsymbol{\varepsilon}^{n+1}$ Ortiz and Martin (1989). In view of the special extremal property of the backward-difference integrated elastoplastic constitutive law, this time-integration scheme will be adopted throughout this work and the symbol $\Delta\widetilde{\phi}^p$ (without the *min* subscript) will be used to denote its corresponding plastic dissipation increment over the time step. Assuming that the solution of the elastoplastic problem is known at time $t^n$, this choice of the integration scheme allows for a variational characterization of the solution of the finite-step elastoplastic problem, which can be shown to coincide with the solution of the following constrained minimization problem Comi et al. (1991, 1992); Corigliano (1994):

$$\min_{\mathbf{u},\Delta\boldsymbol{\varepsilon}} \left\{ \Pi_p^n = \int_{\widetilde{\Omega}} \left( \widetilde{\psi}^{n+1} + \Delta\widetilde{\phi}^p \right) d\widetilde{\Omega} - \mathcal{W}^{n+1} \right\} \tag{3.13}$$

where

$$\widetilde{\psi}^{n+1} = \widetilde{\psi}^e \left(\boldsymbol{\varepsilon}^{e\,n} + \Delta\boldsymbol{\varepsilon}^e\right) + \widetilde{\psi}^p \left(\alpha^n + \Delta\alpha\right) \tag{3.14}$$

$\mathcal{W}$ denotes the external work and the functional is subjected to the compatibility conditions

$$\boldsymbol{\varepsilon}^n + \Delta\boldsymbol{\varepsilon}^e + \Delta\boldsymbol{\varepsilon}^p = \boldsymbol{\varepsilon}^{n+1} = \boldsymbol{\nabla}^s \mathbf{u}^{n+1}, \quad \mathbf{u}^{n+1} = \mathbf{u}_D^{n+1} \text{ on } \partial\Omega_D \tag{3.15}$$

$\mathbf{u}_D^{n+1}$ being prescribed displacement values at $t = t^{n+1}$ on the constrained boundary $\partial\Omega_D$. In (3.13), $\Delta\widetilde{\phi}^p$ is the extremal dissipation increment resulting from application of the return mapping algorithm.

The minimum problem in (3.13) can be expressed in a more explicit form by writing its associated Lagrangian functional Comi and Perego (1995); Simo

and Honein (1990):

$$\mathcal{L}_p^n(\mathbf{u}^{n+1},\Delta\boldsymbol{\varepsilon}^e,\Delta\boldsymbol{\varepsilon}^p,\Delta\alpha,\widetilde{\boldsymbol{\sigma}}^{n+1},\Delta\lambda) = \Pi_p^n - \int_{\widetilde{\Omega}} f_y\left(\Delta\boldsymbol{\varepsilon}^e,\,\Delta\alpha\right)\Delta\lambda\, d\widetilde{\Omega} - \\ - \int_{\widetilde{\Omega}} \widetilde{\boldsymbol{\sigma}}^{n+1} : \left[\boldsymbol{\varepsilon}^{e\,n} + \boldsymbol{\varepsilon}^{p\,n} + \Delta\boldsymbol{\varepsilon}^e + \Delta\boldsymbol{\varepsilon}^p - \boldsymbol{\nabla}^s\mathbf{u}^{n+1}\right] d\widetilde{\Omega}, \tag{3.16}$$

subject to $\Delta\lambda \geq 0$ and $\mathbf{u}^{n+1} = \mathbf{u}_D^{n+1}$ on $\partial\Omega_D$.

In (3.16), $\widetilde{\boldsymbol{\sigma}}^{n+1}$ (not sign-constrained) and $\Delta\lambda \geq 0$ play the role of Lagrange multipliers for the compatibility and plastic admissibility constraints. It is easy to verify that the solution of the finite-step elastoplastic boundary value problem is given by the solution of the following variational problem, where the last condition is a variational inequality due to the sign constraint on $\Delta\lambda$:

$$\begin{aligned}
\partial_{\mathbf{u}}\mathcal{L}_p^n[\delta\mathbf{u}] &= 0 \quad \forall\,\delta\mathbf{u},\ \text{with } \delta\mathbf{u} = 0 \text{ on } \partial\Omega_D \\
\partial_{\Delta\boldsymbol{\varepsilon}^e}\mathcal{L}_p^n[\delta\Delta\boldsymbol{\varepsilon}^e] &= 0 \quad \forall\,\delta\Delta\boldsymbol{\varepsilon}^e \\
\partial_{\Delta\boldsymbol{\varepsilon}^p}\mathcal{L}_p^n[\delta\Delta\boldsymbol{\varepsilon}^p] &= 0 \quad \forall\,\delta\Delta\boldsymbol{\varepsilon}^p \\
\partial_{\Delta\alpha}\mathcal{L}_p^n[\delta\Delta\alpha] &= 0 \quad \forall\,\delta\Delta\alpha \\
\partial_{\widetilde{\boldsymbol{\sigma}}}\mathcal{L}_p^n[\delta\widetilde{\boldsymbol{\sigma}}^{n+1}] &= 0 \quad \forall\,\delta\widetilde{\boldsymbol{\sigma}}^{n+1} \\
\partial_{\Delta\lambda}\mathcal{L}_p^n[\delta\lambda] &\geq 0 \quad \forall\,\delta\lambda = \Delta\lambda' - \Delta\lambda,\ \text{with } \Delta\lambda' \geq 0 \text{ and } \Delta\lambda \geq 0
\end{aligned} \tag{3.17}$$

#### 3.2.3.2 PHASE-FIELD FINITE-STEP VARIATIONAL FORMULATION OF DUCTILE FRACTURE

To account for the propagation of fracture driven by the development of localized plasticity, the functional $\mathcal{L}_p^n$ in (3.16) is enriched by the addition of the energy dissipated by the damage-like phase field $d$, responsible for the material stiffness and strength degradation. Since in the presence of softening structural response plastic strains tend to localize in a zero-thickness band, a further regularization of the model becomes necessary (see, e.g., Dittmann et al. (2018); Miehe et al. (2017); Shishvan et al. (2021); Ulloa et al. (2016); Wambacq et al. (2021)). A common and effective provision, motivated by micro-scale considerations (see, e.g., Aifantis (1992); Forest (2009)) consists in introducing into the model a diffusive term of an inelastic, irreversible quantity (see, e.g., De Borst and Mühlhaus (1992); Miehe et al. (2013)). The simple and effective gradient formulation of finite-step elastoplasticity presented in Comi and Perego (1996b) is considered here. Defining the set

$$\mathcal{S} := (\mathbf{u}, \boldsymbol{\varepsilon}, \Delta\boldsymbol{\varepsilon}^p, \widetilde{\boldsymbol{\sigma}}, \widetilde{\boldsymbol{\sigma}}^p, \widetilde{\chi}, \Delta\alpha, \Delta\lambda, \Delta d) \tag{3.18}$$

of independent fields, the new, gradient-enriched functional $\mathcal{L}_{pd}^{\nabla\,n}(\mathcal{S})$ is defined below. The stress field $\widetilde{\boldsymbol{\sigma}}^p$ in $\mathcal{S}$ is a dummy field considered to facilitate the derivation of the governing equations resulting from the stationarity of the

functional. For all quantities evaluated at time $t^{n+1}$, the $n+1$ at exponent has been omitted for notation convenience:

$$
\begin{aligned}
\mathcal{L}_{pd}^{\nabla\, n}(\mathcal{S}) := & \underbrace{\int_\Omega \omega(d)\, \left[\widetilde{\psi}^e(\boldsymbol{\varepsilon} - \boldsymbol{\varepsilon}^{p\,n} - \Delta\boldsymbol{\varepsilon}^p) + \widetilde{\psi}^p(\alpha^n + \Delta\alpha)\right] \mathrm{d}\Omega}_{\textit{stored internal energy } \mathcal{E}} - \\
& - \underbrace{\int_\Omega \mathbf{b}\cdot\mathbf{u}\,\mathrm{d}\Omega - \int_{\partial\Omega_N} \mathbf{t}\cdot\mathbf{u}\,\mathrm{d}\Gamma}_{\textit{external work } \mathcal{W}} + \\
& + \underbrace{\int_\Omega \omega(d)\, \left(\widetilde{\boldsymbol{\sigma}}^p : \Delta\boldsymbol{\varepsilon}^p - \widetilde{\chi}\,\Delta\alpha\right) \mathrm{d}\Omega}_{\textit{plastic dissipation increment } \Delta\mathcal{D}^p} + \\
& + \underbrace{\int_\Omega \phi^f(d, \boldsymbol{\nabla} d)\ \mathrm{d}\Omega}_{\textit{fracture energy } \mathcal{D}_f} + \underbrace{\int_\Omega \frac{\eta_f}{2\,\Delta t}\left(\Delta d\right)^2 \mathrm{d}\Omega}_{\textit{viscous energy } \mathcal{D}_v} + \\
& + \underbrace{\int_\Omega \omega(d)\, \widetilde{\boldsymbol{\sigma}} : (\boldsymbol{\nabla}^s\mathbf{u} - \boldsymbol{\varepsilon})\, \mathrm{d}\Omega}_{\textit{compatibility constraint}} - \\
& - \underbrace{\int_\Omega \omega(d)\ \Delta\lambda\ f_y(\widetilde{\boldsymbol{\sigma}}^p, \widetilde{\chi})\, \mathrm{d}\Omega + \int_\Omega \omega(d)\ \frac{1}{2}\, c_p\, \boldsymbol{\nabla}\lambda\cdot\boldsymbol{\nabla}\lambda\, \mathrm{d}\Omega}_{\textit{plastic admissibility}}
\end{aligned}
\tag{3.19}
$$

subject to

$$
\Delta\lambda \geq 0, \quad \Delta d \geq 0, \quad \mathbf{u} = \mathbf{u}_D \text{ on } \partial\Omega_D\,. \tag{3.20}
$$

The notion of effective volume enters in the definition of the volume integrals. With the exception of the fracture energy $\mathcal{D}_f$ and of the external work $\mathcal{W}$, the energies and the constraints are defined on the continuous portion of the material volume $\Omega$ only, hence $\int_{\widetilde{\Omega}} \widetilde{(\cdot)}\, \mathrm{d}\widetilde{\Omega} = \int_\Omega \omega\, \widetilde{(\cdot)}\, \mathrm{d}\Omega$, $\Omega$ being the reference nominal volume. The vectors $\mathbf{b}$ and $\mathbf{t}$ are the body forces and the tractions, respectively, applied on the Neumann portion $\partial\Omega_N$ of the boundary. In the standard phase-field formulation,

$$
\phi^f(d, \boldsymbol{\nabla} d) = w(d) + {}^1\!/_2\, c_d\, \boldsymbol{\nabla} d\cdot\boldsymbol{\nabla} d \tag{3.21}
$$

where $w(d)$ is the local phase-field specific dissipation. The constant parameters $c_p$ and $c_d$ measure the plastic and damage diffusion bandwidths and they are related to the plastic and fracture internal lengths $l_{0p}$ and $l_{0d}$. The viscous coefficient $\eta_f$ introduces a pseudo-time measure of the crack propagation rate, while $\Delta t = t^{n+1} - t^n$ is the current time-step size. This dissipative term is introduced for algorithmic reasons, as it will be discussed later. The solution of the considered ductile fracture boundary value problem makes the functional $\mathcal{L}_{pd}^{\nabla\, n}(\mathcal{S})$ stationary with respect to variations of the fields in $\mathcal{S}$. The inequality constraints on $\Delta\lambda$ and $\Delta d$ make the variational problem a variational inequality.

#### 3.2.3.3 STATIONARITY CONDITIONS

The stationarity conditions for $\mathcal{L}^{\nabla\, n}_{pd}(\mathcal{S})$ read:

$$\partial_{\mathbf{u}}\mathcal{L}^{\nabla\, n}_{pd}(\mathcal{S})[\delta\mathbf{u}] = 0 \quad \rightarrow \quad \begin{aligned} &\int_\Omega \omega\, \widetilde{\boldsymbol{\sigma}} : \boldsymbol{\nabla}^s \delta\mathbf{u}\, \mathrm{d}\Omega - \\ &- \int_\Omega \mathbf{b}\cdot\delta\mathbf{u}\, \mathrm{d}\Omega - \int_{\partial\Omega_N} \mathbf{t}\cdot\delta\mathbf{u}\, \mathrm{d}\Gamma = 0 \end{aligned} \tag{3.22a}$$

$$\partial_{\boldsymbol{\varepsilon}}\mathcal{L}^{\nabla\, n}_{pd}(\mathcal{S})[\delta\boldsymbol{\varepsilon}] = 0 \quad \rightarrow \quad \int_\Omega \omega \left(\partial_{\boldsymbol{\varepsilon}}\widetilde{\psi}^e - \widetilde{\boldsymbol{\sigma}}\right) : \delta\boldsymbol{\varepsilon}\, \mathrm{d}\Omega = 0 \tag{3.22b}$$

$$\partial_{\widetilde{\boldsymbol{\sigma}}}\mathcal{L}^{\nabla\, n}_{pd}(\mathcal{S})[\delta\widetilde{\boldsymbol{\sigma}}] = 0 \quad \rightarrow \quad \int_\Omega \omega \left(\boldsymbol{\nabla}^s\mathbf{u} - \boldsymbol{\varepsilon}\right) : \delta\widetilde{\boldsymbol{\sigma}}\, \mathrm{d}\Omega = 0 \tag{3.22c}$$

$$\partial_{\alpha}\mathcal{L}^{\nabla\, n}_{pd}(\mathcal{S})[\delta\alpha] = 0 \quad \rightarrow \quad \int_\Omega \omega \left(\partial_{\alpha}\widetilde{\psi}^p - \widetilde{\chi}\right) \delta\alpha\, \mathrm{d}\Omega = 0 \tag{3.22d}$$

$$\partial_{\boldsymbol{\varepsilon}^p}\mathcal{L}^{\nabla\, n}_{pd}(\mathcal{S})[\delta\boldsymbol{\varepsilon}^p] = 0 \quad \rightarrow \quad \int_\Omega \omega \left(-\partial_{\boldsymbol{\varepsilon}}\widetilde{\psi}^e + \widetilde{\boldsymbol{\sigma}}^p\right) : \delta\boldsymbol{\varepsilon}^p\, \mathrm{d}\Omega = 0 \tag{3.22e}$$

$$\partial_{\widetilde{\boldsymbol{\sigma}}^p}\mathcal{L}^{\nabla\, n}_{pd}(\mathcal{S})[\delta\widetilde{\boldsymbol{\sigma}}^p] = 0 \quad \rightarrow \quad \int_\Omega \omega \left(\Delta\boldsymbol{\varepsilon}^p - \Delta\lambda\, \partial_{\widetilde{\boldsymbol{\sigma}}^p} f_y\right) : \delta\widetilde{\boldsymbol{\sigma}}^p\, \mathrm{d}\Omega = 0 \tag{3.22f}$$

$$\partial_{\widetilde{\chi}}\mathcal{L}^{\nabla\, n}_{pd}(\mathcal{S})[\delta\widetilde{\chi}] = 0 \quad \rightarrow \quad \int_\Omega -\omega \left(\Delta\alpha + \Delta\lambda\, \partial_{\widetilde{\chi}} f_y\right) \delta\widetilde{\chi}\, \mathrm{d}\Omega = 0 \tag{3.22g}$$

$$\partial_{\lambda}\mathcal{L}^{\nabla\, n}_{pd}(\mathcal{S})[\delta\lambda] \geq 0 \quad \rightarrow \quad \int_\Omega \omega \left[-\delta\lambda\, f_y + c_p\, \boldsymbol{\nabla}\lambda\cdot\boldsymbol{\nabla}\delta\lambda\right] \mathrm{d}\Omega \geq 0 \tag{3.22h}$$

$$\partial_{d}\mathcal{L}^{\nabla\, n}_{pd}(\mathcal{S})[\delta d] \geq 0 \quad \rightarrow \quad \begin{aligned} \int_\Omega \Big\{ &\left[\omega'\, \widetilde{\psi}_{ep} + w' + \frac{\eta_f}{\Delta t}\, \Delta d\, \delta d\right] + \\ &+ c_d\, \boldsymbol{\nabla} d\cdot\boldsymbol{\nabla}\delta d \Big\}\, \mathrm{d}\Omega \geq 0, \end{aligned} \tag{3.22i}$$

where $\delta\lambda = \Delta\lambda' - \Delta\lambda$, $\delta d = \Delta d' - \Delta d$ are not sign-constrained, while $\Delta\lambda' \geq 0$, $\Delta d' \geq 0$ are arbitrary, non-negative scalar functions belonging to the same spaces of $\Delta\lambda$ and $\Delta d$, respectively, and

$$\Delta\lambda \geq 0, \quad \Delta d \geq 0, \quad \mathbf{u} = \mathbf{u}_D \text{ on } \partial\Omega_D\,.$$

The driving energy $\widetilde{\psi}_{ep}$ in (3.22i) is defined as

$$\begin{aligned} \widetilde{\psi}_{ep}(\boldsymbol{\varepsilon}, \boldsymbol{\varepsilon}^p, \widetilde{\boldsymbol{\sigma}}^p, \widetilde{\chi}, \alpha, \lambda) := \widetilde{\psi}(\boldsymbol{\varepsilon}, \boldsymbol{\varepsilon}^p, \alpha) + \Delta\widetilde{\phi}^p(\boldsymbol{\varepsilon}^p, \widetilde{\boldsymbol{\sigma}}^p, \widetilde{\chi}, \alpha) - \\ - f_y(\widetilde{\boldsymbol{\sigma}}^p, \widetilde{\chi})\, \Delta\lambda + {}^1\!/_2\, c_p\, \boldsymbol{\nabla}\lambda\cdot\boldsymbol{\nabla}\lambda \end{aligned} \tag{3.23}$$

It contains the term $f_y\, \Delta\lambda$ that is non-vanishing due to the gradient plasticity term. The conditions above correspond to: (3.22a) equilibrium equations, (3.22b) elastic state equations, (3.22c) compatibility conditions, (3.22d) static hardening variable state equation, (3.22e) (together with (3.22b)) identity between the dummy stress $\widetilde{\boldsymbol{\sigma}}^p$ and the effective stress $\widetilde{\boldsymbol{\sigma}}$, (3.22f) plastic strains evolution, (3.22g) hardening variable evolution, (3.22h) non-local plastic consistency, (3.22i) non-local fracture evolution criterion. To simplify the notation

in what follows, the symbols $\alpha, \lambda, d$ are used to express the functional dependencies, rather than the corresponding increments $\Delta\alpha, \Delta\lambda, \Delta d$ as already done in (3.23).

#### 3.2.3.4 GOVERNING EQUATIONS OF THE NON-LOCAL PROBLEM

In the implemented formulation, the compatibility condition (3.22c) is enforced in strong form, i.e., $\boldsymbol{\varepsilon} = \boldsymbol{\nabla}^s \mathbf{u}$ as in standard compatible finite elements, and the dummy stress field $\widetilde{\boldsymbol{\sigma}}^p$ is eliminated assuming $\widetilde{\boldsymbol{\sigma}}^p \equiv \widetilde{\boldsymbol{\sigma}}$. Equation (3.22a), combined with the compatibility condition (3.22c), leads to the weak form of the momentum balance equation, expressed in terms of nominal quantities:

$$\int_\Omega \omega\, \widetilde{\boldsymbol{\sigma}} : \delta\boldsymbol{\varepsilon}\, \mathrm{d}\Omega = \int_\Omega \mathbf{b} \cdot \delta\mathbf{u}\, \mathrm{d}\Omega + \int_{\partial\Omega_N} \mathbf{t} \cdot \delta\mathbf{u}\, \mathrm{d}\Gamma\,. \tag{3.24}$$

The stationarity conditions (3.22b), (3.22d)-(3.22g), lead to the effective local state equations and elastoplastic evolution laws:

$$\widetilde{\boldsymbol{\sigma}} = \partial_{\boldsymbol{\varepsilon}} \widetilde{\psi}^e\,, \quad \widetilde{\chi} = \partial_\alpha \widetilde{\psi}^p\,, \quad \Delta\boldsymbol{\varepsilon}^p = \Delta\lambda\, \partial_{\widetilde{\boldsymbol{\sigma}}} f_y\,, \quad \Delta\alpha = -\Delta\lambda\, \partial_{\widetilde{\chi}} f_y\,, \tag{3.25}$$

while the corresponding nominal stress and static internal variable are obtained as $\boldsymbol{\sigma} = \omega\widetilde{\boldsymbol{\sigma}}$ , $\chi = \omega\widetilde{\chi}$.

While the variations (3.22a)-(3.22g) are standard equalities, (3.22h) and (3.22i) are variational inequalities. Using standard arguments for variational inequalities, condition (3.22h) can be written in the following equivalent form defining the elastoplastic non-local loading-unloading conditions:

$$\Delta\lambda \geq 0\,, \quad \mathcal{F}_y(\widetilde{\boldsymbol{\sigma}}, \widetilde{\chi}, \lambda, d) \leq 0\,, \quad \mathcal{F}_y(\widetilde{\boldsymbol{\sigma}}, \widetilde{\chi}, \lambda, d)[\Delta\lambda] = 0\,, \tag{3.26}$$

where the non-local yield functional $\mathcal{F}_y$ has been defined as:

$$\mathcal{F}_y(\widetilde{\boldsymbol{\sigma}}, \widetilde{\chi}, \lambda, d)[\delta\lambda] := \int_\Omega \omega(d) \left[ f_y(\widetilde{\boldsymbol{\sigma}}, \widetilde{\chi})\, \delta\lambda - c_p\, \boldsymbol{\nabla}\lambda \cdot \boldsymbol{\nabla}\delta\lambda \right] \mathrm{d}\Omega\,. \tag{3.27}$$

Similarly, the energy release rate $\mathcal{Y}$ and critical energy release rate $\mathcal{Y}_c$ functionals are defined as:

$$\mathcal{Y}(\boldsymbol{\varepsilon}, \boldsymbol{\varepsilon}^p, \alpha, \lambda, d)[\delta d] := -\int_\Omega \omega'(d)\; \widetilde{\psi}_{ep}(\boldsymbol{\varepsilon}, \boldsymbol{\varepsilon}^p, \alpha, \lambda)\; \delta d\, \mathrm{d}\Omega\,, \tag{3.28a}$$

$$\mathcal{Y}_c(d)[\delta d] := \int_\Omega \left\{ \left[ w'(d) + \frac{\eta_f}{\Delta t}\, \Delta d \right] \delta d + c_d\, \boldsymbol{\nabla} d \cdot \boldsymbol{\nabla}\delta d \right\} \mathrm{d}\Omega\,, \tag{3.28b}$$

where the evolution laws (3.25) have been used to reduce the number of independent fields in the driving energy $\widetilde{\psi}_{ep}$. The non-local fracture activation functional $\mathcal{F}_d$ is then defined as:

$$\mathcal{F}_d(\boldsymbol{\varepsilon}, \boldsymbol{\varepsilon}^p, \alpha, \lambda, d)[\delta d] := \Big( \mathcal{Y}(\boldsymbol{\varepsilon}, \boldsymbol{\varepsilon}^p, \alpha, \lambda, d) - \mathcal{Y}_c(d) \Big)[\delta d]\,, \tag{3.29}$$

and condition (3.22i) is rewritten in the equivalent form

$$\Delta d \geq 0\,, \quad \mathcal{F}_d(\boldsymbol{\varepsilon}, \boldsymbol{\varepsilon}^p, \alpha, \lambda, d) \leq 0\,, \quad \mathcal{F}_d(\boldsymbol{\varepsilon}, \boldsymbol{\varepsilon}^p, \alpha, \lambda, d)[\Delta d] = 0\,, \tag{3.30}$$

providing the non-local fracture activation criterion for elastoplastic brittle fracture. It should be noted that in this elastoplastic-brittle-fracture model the only coupling between plastic and fracture dissipation mechanisms is present in the fracture driving force $\mathcal{Y}$, while the fracture dissipation $\mathcal{Y}_c$ is the same as the one of the purely brittle case.

### 3.2.4 Constitutive assumptions

For the implementation considered in this work, the general framework described so far is restricted to isotropic linear elastic materials, obeying von-Mises plasticity criterion with linear isotropic hardening, i.e.

$$\begin{aligned} \widetilde{\psi}^e(\boldsymbol{\varepsilon} - \boldsymbol{\varepsilon}^p) &= 1/2\, K_0\, \epsilon_v^2 + 1/2\, 2G_0\, (\mathbf{e} - \boldsymbol{\varepsilon}^p) : (\mathbf{e} - \boldsymbol{\varepsilon}^p)\,, \\ \widetilde{\psi}^p(\alpha) &= 1/2\, H_0\, \alpha^2\,, \\ f_y(\widetilde{\mathbf{s}}, \widetilde{\chi}) &= \sqrt{3/2\, \widetilde{\mathbf{s}} : \widetilde{\mathbf{s}}} - \bar{\sigma}_{y0} - \widetilde{\chi}\,, \end{aligned} \tag{3.31}$$

where $K_0$ is the bulk modulus, $G_0$ is the shear modulus, $\bar{\sigma}_{y0}$ is the initial yield stress, $\epsilon_v := \boldsymbol{\varepsilon} : \mathbf{I}$ is the total volumetric strain, $\mathbf{I}$ being the identity tensor, $\mathbf{e} = \boldsymbol{\varepsilon} - 1/3 \epsilon_v \mathbf{I}$ is the deviatoric total strain, $\widetilde{\mathbf{s}} = \widetilde{\boldsymbol{\sigma}} - \widetilde{p}\mathbf{I}$, is the deviatoric effective stress, $\widetilde{p}$ being the hydrostatic pressure (taken positive if tensile) and $\widetilde{\chi} = H_0 \alpha$ is the static internal variable, $H_0$ being the hardening modulus. The restriction to von-Mises plasticity allows to identify the internal hardening variable $\alpha$ with the equivalent plastic strain and its increment is given by $\Delta\alpha = \sqrt{2/3\, \Delta\boldsymbol{\varepsilon}^p : \Delta\boldsymbol{\varepsilon}^p}$.

The phase-field functions $\omega(d)$ and $w(d)$ are defined as

$$\omega(d) = (1 - d)^2\,, \quad w(d) = \frac{3G_c}{8 l_{0d}}\, d\,, \tag{3.32}$$

where $G_c$ is the material toughness and $l_{0d}$ the phase-field internal length. This definition of $w(d)$ corresponds to an AT1 approach (see Section 2.2), implying that damage cannot develop until a critical value of the damage driving force has been achieved. Finally, the fracture diffusion coefficient $c_d$ of the AT1 model is defined as $c_d = 3/4\, G_c\, l_{0d}$, the plastic diffusion coefficient $c_p$ as $c_p = \bar{\sigma}_{y0}\, l_{0p}^2$, and the viscous coefficient as $\eta_f = \bar{\eta}\left(G_c / l_{0d}\right)$, being $\bar{\eta}$ a viscous parameter with dimension of a time.

To avoid the promotion of crack propagation by predominantly compressive states, the deviatoric-volumetric elastic energy split is adopted (see, e.g.Amor et al. (2009); Comi and Perego (1996a)). According to this technique, the elastic energy is split into an *Inactive* part $\widetilde{\psi}^{eI}$, due to negative volumetric strains, and an *Active* remainder $\widetilde{\psi}^{eA}$, which are defined as:

$$\begin{aligned} \widetilde{\psi}^{eA}(\boldsymbol{\varepsilon}, \boldsymbol{\varepsilon}^p) &= 1/2\, K_0\, \langle \epsilon_v \rangle_+^2 + 1/2\, 2G_0\, (\mathbf{e} - \boldsymbol{\varepsilon}^p) : (\mathbf{e} - \boldsymbol{\varepsilon}^p)\,, \\ \widetilde{\psi}^{eI}(\boldsymbol{\varepsilon}, \boldsymbol{\varepsilon}^p) &= 1/2\, K_0\, \langle \epsilon_v \rangle_-^2\,, \end{aligned} \tag{3.33}$$

where $\langle\cdot\rangle_{\pm}$ are the Macaulay brackets. In view of the purely deviatoric nature of plastic strains in von-Mises plasticity, no distinction is made between the tensile/compressive parts of the plastic component $\psi^p$ of the free energy density. Note that a split also of this energy component may be recommended in the presence of dilatant elastoplastic materials (see, e.g., Choo and Sun (2018) for the case of geological materials). The assumed energy split has implications on the definition of the nominal stress and of the plastic dissipation rate. Taking into account the elastic energy split, the nominal free energy is defined as

$$\psi = \omega(\widetilde{\psi}^{eA} + \widetilde{\psi}^{p}) + \widetilde{\psi}^{eI}\,, \tag{3.34}$$

and, from the dissipation inequality (3.3), one has that the nominal stress is given by:

$$\boldsymbol{\sigma} = \partial_{\boldsymbol{\varepsilon}^e}\psi^e = \omega\,\partial_{\boldsymbol{\varepsilon}^e}\widetilde{\psi}^{eA} + \partial_{\boldsymbol{\varepsilon}^e}\widetilde{\psi}^{eI} = \omega\,\widetilde{\boldsymbol{\sigma}}^{A} + \widetilde{\boldsymbol{\sigma}}^{I} \neq \omega\,\partial_{\boldsymbol{\varepsilon}^e}\widetilde{\psi}^{e} = \omega\,\widetilde{\boldsymbol{\sigma}}\,, \tag{3.35}$$

and no straightforward transformation from effective to nominal stress can be applied. The active and inactive effective stresses are defined:

$$\widetilde{\boldsymbol{\sigma}}^{A} := \partial_{\boldsymbol{\varepsilon}^e}\widetilde{\psi}^{eA}\,, \quad \widetilde{\boldsymbol{\sigma}}^{I} := \partial_{\boldsymbol{\varepsilon}^e}\widetilde{\psi}^{eI} \qquad with \qquad \widetilde{\boldsymbol{\sigma}} = \widetilde{\boldsymbol{\sigma}}^{A} + \widetilde{\boldsymbol{\sigma}}^{I}\,. \tag{3.36}$$

However, for the considered case of von-Mises plasticity and volumetric-deviatoric split, one has that $\widetilde{\boldsymbol{\sigma}}^{I} : \dot{\boldsymbol{\varepsilon}}^{p} = 0$ and the plastic dissipation rate can still be defined as

$$\dot{\phi}^{p} = \boldsymbol{\sigma} : \dot{\boldsymbol{\varepsilon}}^{p} - \chi\dot{\alpha} = \omega\,(\widetilde{\boldsymbol{\sigma}}^{A} : \dot{\boldsymbol{\varepsilon}}^{p} - \widetilde{\chi}\dot{\alpha}) = \omega\,\dot{\widetilde{\phi}}^{p}\,. \tag{3.37}$$

For the case of dilatant geological materials, see also the discussion in Choo and Sun (2018).

## 3.3 Fracture activation criterion

The proposed approach to plasticity-driven phase-field fracture propagation is based on the definition of a scalar function $f(\alpha)$ of the equivalent plastic strain, hereafter referred to as *modulation function*, modulating the evolution of the critical fracture energy $G_c$, based on the evolution of the plastic process zone. In ductile fracture, the material resistance to crack extension grows due the growth of the plastic zone at the crack tip, until it reaches a limit value (the so-called R-curve). The critical fracture energy $G_c$ represents this steady state value of the energy to be spent for a unit crack advancement, which however includes also the energy to be dissipated in the creation of the plastic process zone. In the considered model, this latter energy is explicitly taken into account by the plastic dissipation $\Delta\widetilde{\phi}^{p}$.

To account for these interaction phenomena, the proposed model is based on the assumption that damage, measured by the phase-field order parameter $d$, can grow only when the plastic process zone in a stress concentration region has fully developed, as measured by the local value of the equivalent

plastic strain $\alpha$. In practical terms, the competition between the plasticity and fracture dissipation mechanisms in the initial crack nucleation phase and their interaction in the subsequent crack propagation phase, is modulated by the addition of a new interaction term in the expression of the critical energy release rate functional $\mathcal{Y}_c$ (3.28b):

$$\begin{aligned}\mathcal{Y}_c^{\alpha}(\alpha, d)[\delta d] := & \underbrace{\int_\Omega f(\alpha)\, w'(d)\, \delta d \, \mathrm{d}\Omega}_{\textit{interaction term}} + \\ & + \underbrace{\int_\Omega \left\{ \left[ w'(d) + \frac{\eta_f}{\Delta t}\, \Delta d \right] \delta d + c_d\, \boldsymbol{\nabla} d \cdot \boldsymbol{\nabla} \delta d \right\} \mathrm{d}\Omega}_{\mathcal{Y}_c(d)[\delta d]} \, .\end{aligned} \tag{3.38}$$

The definition of the modulation function $f(\alpha)$ in (3.38) is obtained based on the study of the one-dimensional homogeneous case.

### 3.3.1 One-dimensional homogeneous case

A one-dimensional problem, with homogeneous distribution of the phase field and of plastic strains, i.e.with $\boldsymbol{\nabla} d = \mathbf{0}$, $\boldsymbol{\nabla} \Delta\lambda = \mathbf{0}$ and without viscosity, i.e. $\eta_f = 0$, is considered. Under these assumptions, the damage activation criterion (3.30) can be formulated in strong form as follows:

$$\begin{gathered}\Delta d \geq 0 \quad , \quad - \left[ \omega' \left( \widetilde{\psi} + \Delta \widetilde{\phi}^p \right) + (f+1)\, \frac{3}{8}\, \frac{G_c}{l_{0d}} \right] \leq 0 \quad , \\ \left[ \omega' \left( \widetilde{\psi} + \Delta \widetilde{\phi}^p \right) + (f+1)\, \frac{3}{8}\, \frac{G_c}{l_{0d}} \right] \Delta d = 0\end{gathered}$$

where the definition (3.32) of the local part $w(d)$ of the phase-field dissipation has been used. Note that, in this simple 1D homogeneous case and thanks to the absence of the gradient of the plastic multiplier, the complementarity condition $f_y \Delta\lambda = 0$ holds in strong form and, therefore, does not appear in the driving energy (3.23), which is simply given by $\widetilde{\psi}_{ep} = \widetilde{\psi} + \Delta \widetilde{\phi}^p$. When the phase field is evolving, i.e., when $\Delta d > 0$, and for $\omega(d) = (1-d)^2$, the activation criterion yields:

$$2(1-d) \left( \widetilde{\psi} + \Delta \widetilde{\phi}^p \right) - (f+1)\, \frac{3}{8}\, \frac{G_c}{l_{0d}} = 0$$

where the free energy $\widetilde{\psi}$ is defined in (3.2) and the increment of plastic dissipation $\Delta \widetilde{\phi}^p$ in (3.12). Defining

$$\bar{g} := \frac{3}{16}\, \frac{G_c}{l_{0d}} \tag{3.39}$$

the damage activation condition can be written as:

$$\underbrace{(1-d) \left( \widetilde{\psi} + \Delta \widetilde{\phi}^p \right)}_{\textit{driving force}} \quad - \quad \underbrace{(f+1)\, \bar{g}}_{\textit{effective fracture energy}} \quad = 0 \tag{3.40}$$

From this equation one can obtain the value of the phase-field variable $d$ for prescribed displacement and plastic deformation. The point of view is now reversed. Let us assume that a damage evolution is prescribed, such that damage is zero until a critical value $\alpha_{cr}$ of the equivalent plastic strain is achieved and that, after this, a fictitious evolution $\bar{d}(\alpha)$ is prescribed, so that (3.40) can be solved for $f(\alpha)+1$. For $\alpha \leq \alpha_{cr}$, $f(\alpha)$ should be a non-decreasing function of the equivalent plastic strain $\alpha$, since it is intended to account for the plastic dissipation. As a consequence, $\widetilde{\psi}$ in (3.40) should also be intended as a function that can only increase in time.

To account for all these different aspects, the following form of the modulation function $f(\alpha)$ has been implemented:

$$f+1 = \begin{cases} f_0 + 1 & \text{if} \quad \alpha = 0 \\ \frac{\widetilde{\mathcal{H}}}{\bar{g}} & \text{if} \quad \alpha \leq \alpha_{cr} \\ \left(1-\bar{d}\right)\frac{\widetilde{\mathcal{H}}}{\bar{g}} + \left(f_{min}+1\right)\bar{d} & \text{if} \quad \alpha_{cr} < \alpha < \alpha_{cr} + \Delta\alpha_{cr} \\ f_{min}+1 & \text{if} \quad \alpha_{cr} + \Delta\alpha_{cr} \leq \alpha \end{cases} \tag{3.41}$$

where $f_0$ is an initial value to be defined later and the history function $\widetilde{\mathcal{H}}$ is defined as:

$$\widetilde{\mathcal{H}} := \mathcal{H} + \widetilde{\psi}^p + \Delta\widetilde{\phi}^p - f_y\,\Delta\lambda + 1/2\,c_p\,\boldsymbol{\nabla}\lambda\cdot\boldsymbol{\nabla}\lambda \tag{3.42}$$

with the *history variable* $\mathcal{H}$, inspired to the one in Miehe et al. (2010a), defined as:

$$\mathcal{H} = \max\left(\widetilde{\psi}^{eA}, \mathcal{H}^n\right) \tag{3.43}$$

where $\widetilde{\psi}^{eA}$ is the active part of the elastic energy $(3.33)_1$. An important remark lies in the purely plasticity driven nature of the proposed modulation function model. The energy split (3.33) involves the positive volumetric and deviatoric free energy as driving force, nevertheless, only the deviatoric part of the stress promotes the development of plastic deformation. Thus, the combination of (3.41) with (3.43) does not allow crack evolution due to a purely dilatant volumetric deformation state, since no plastic deformations arise. This resembles the pursued objective of plasticity driven model and it is in accordance with some approaches in the literature (see e.g., Razanica et al. (2019)). For $\alpha < \alpha_{cr}$, the condition (3.43) ensures that in the case of elastic unloading, i.e., $\widetilde{\psi}^e < \widetilde{\psi}^{e\,n}$, the modulation function cannot decrease. Finally, $\Delta\alpha_{cr}$ defines the increment of $\alpha > \alpha_{cr}$ beyond which $f(\alpha)$ achieves its minimum constant value $f_{min}$, corresponding to the purely brittle portion of $G_c$, in the sense specified before. According to the definition (3.41) of $f(\alpha)$, after damage activation (i.e., for $\alpha > \alpha_{cr}$) the evolution of $f(\alpha)$ is governed by the fictitious phase-field

history $\bar{d}(\alpha)$ in (3.41), whose definition is provided analytically in the form

$$\bar{d}(\alpha) = \begin{cases} 0 & \alpha \leq \alpha_{cr} \\ \zeta^3 \left(10 - 15\,\zeta + 6\,\zeta^2\right) & \alpha_{cr} < \alpha < \alpha_{cr} + \Delta\alpha_{cr} \\ 1 & \alpha > \alpha_{cr} + \Delta\alpha_{cr} \end{cases} \qquad \zeta := \frac{\alpha - \alpha_{cr}}{\Delta\alpha_{cr}} \tag{3.44}$$

To better understand the effect of the different parameters in the modulation function $f(\alpha)$ in (3.41) and of the prescribed phase-field history $\bar{d}(\alpha)$ in (3.44), the proposed ductile-brittle phase-field approach has been applied to a single 4-node element under a uniaxial imposed displacement $u$ in plane strain conditions, with the results shown in Figure 3.2 and 3.3. The element side is $L = 1\,\text{mm}$. The element is loaded by $n_{st} = 100$ equal time steps of imposed displacement increment $\Delta u = 0.01\,\text{mm}$. The used elastoplastic material properties are those shown in Table 3.1 for Material II. The toughness is changed to the value $G_c = 100\,\text{N/mm}$ and the damage internal length is $l_{0d} = 1\,\text{mm}$. Since the element size is much smaller then the plasticity and damage characteristic lengths, the resulting fields will be uniform over the element. The viscous coefficient is set to $\bar{\eta} = 10^{-2}\,\text{s}$. Three material parameters have been introduced in (3.41): the critical equivalent plastic strain $\alpha_{cr}$, i.e., a scalar measure of the plastic deformation corresponding to the onset of damage; the minimum value $f_{min}$ of the modulation function; the plastic deformation increment $\Delta\alpha_{cr}$, beyond which the modulation function $f(\alpha)$ attains its minimum constant value $f_{min}$. Though a precise definition of $f_{min}$ appears difficult, numerical tests have shown that its influence on the overall response is minor and that it affects mainly the final part of the response curve, when the structure has almost completely failed. In the considered tests, $f_{min} = 0$ has been used obtaining accurate results. It is important to remark that the condition $\alpha_{cr} > 0$ together with the AT1 assumption ensures the existence of a purely elastoplastic stage before the start of damage. The profile of the modulation function $f(\alpha)$ and

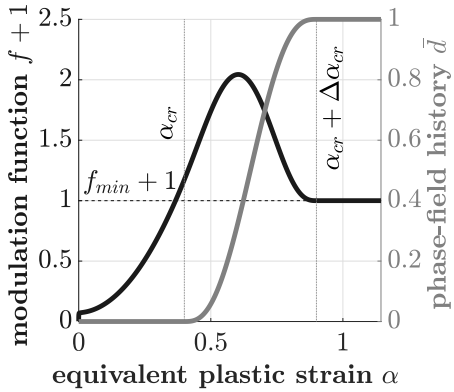


**Figure 3.2:** Modulation function $f(\alpha)+1$ and fictitious phase-field history $\bar{d}(\alpha)$. The model parameters are $\alpha_{cr} = 0.4$, $\Delta\alpha_{cr} = 0.5$, and $f_{min} = 0$.

of the fictitious phase-field history $\bar{d}(\alpha)$ are shown in Figure 3.2. The initial value $f_0 + 1$ corresponds to the first yielding at the considered material point, i.e., it is given by equation (3.41) with $\bar{d} = 0$, $\Delta\widetilde{\phi}^p = 0$, $\Delta\lambda = 0$ and $\widetilde{\psi}$ equal to its value at the yield limit, and therefore is not a model parameter. A very important feature of the proposed form of the modulation function $f(\alpha)$ is that its evolution is given by the current value of $\widetilde{\mathcal{H}}$ in (3.41), and does not require to be defined a priori. Therefore, in a multi-dimensional case, for $\alpha \leq \alpha_{cr}$ the function $f(\alpha)$ is computed from (3.41), with $\bar{d} = 0$, based on the current values of $\mathcal{H}$, $\widetilde{\psi}^p$, $\Delta\widetilde{\phi}^p$, and $\Delta\lambda$. For $\alpha \geq \alpha_{cr}$, $\bar{d}$ starts to grow, as specified in (3.44). At a certain point, the growth of $\bar{d}$ prevails on the other terms in (3.41), reducing $\mathcal{Y}_c^{\alpha}(\alpha, d)$ in (3.38), thus allowing damage to propagate. The $f(\alpha) + 1$ curve reaches a maximum value $f_{max} + 1$ and then decreases to a minimum value $f_{min} + 1$.

The effect of the material parameters $\alpha_{cr}$ and $\Delta\alpha_{cr}$ is shown in Figure 3.3 for $f_{min} = 0$. The elastoplastic hardening response curve (without damage) is in light gray, while the orange dashed line shows the elastoplastic-brittle response, obtained without the modulation function (i.e. with $f \equiv 0$). It can be clearly noticed how in this latter model there are no parameters to be tuned to better reproduce the material response. In contrast, the introduction of the modulation function allows to achieve the two objectives mentioned before: the competition between the plastic and fracture dissipation mechanisms is modulated by tuning $\alpha_{cr}$ (Figure 3.3a), while the interaction between the two mechanisms in the failure phase is modulated by tuning $\Delta\alpha_{cr}$ (Figure 3.3b). $\alpha_{cr}$ delays the beginning of the softening branch, while $\Delta\alpha_{cr}$ controls its slope. From Figure 3.3a it appears that $\alpha_{cr}$ should not be smaller than the value corresponding to the onset of damage in the $f \equiv 0$ case. The choice of $f_{min}$ has a minor influence on the response. $f_{min} = 0$ corresponds to an activation criterion without the effect of the modulation function as in the elastoplastic-brittle case, i.e., the usual value of $G_c$ is fully recovered in the final phase of the rupture process.

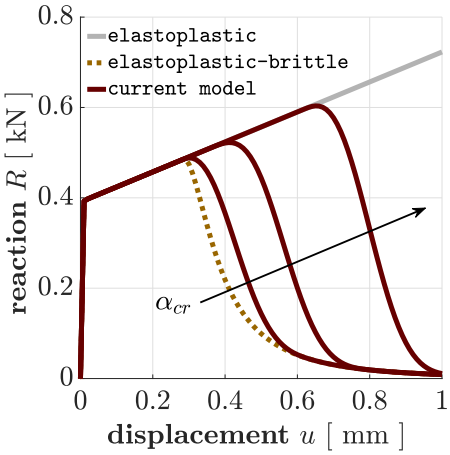


**(a)** Effects of $\alpha_{cr}$ on competition between ductile and brittle dissipation mechanisms. For fixed $\Delta\alpha_{cr} = 0.5$, the values are $\alpha_{cr} = 0.2, 0.4, 0.7$.

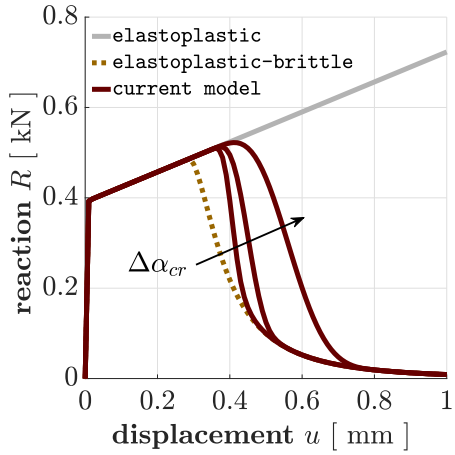


**(b)** Effects of $\Delta\alpha_{cr}$ on ductile-brittle interaction dissipation mechanism in failure phase. For fixed $\alpha_{cr} = 0.4$, the values are $\Delta\alpha_{cr} = 0.1, 0.2, 0.5$.

**Figure 3.3:** Effects of modulation function parameters.

## 3.4 SPACE DISCRETIZATION

The problem physical dimension is $n_{dim}$, the element number of nodes is $n_{en}$, the element number of displacement degrees of freedom is $n_{ldof} = n_{dim}\, n_{en}$. The global number of nodes is $n_{np}$ and the global number of displacement degrees of freedom is $n_{dof} = n_{dim}\, n_{np}$. The number of independent strain tensor components is $n_{\varepsilon}$. The local, elemental and global solutions of the ductile fracture problem can be cast into the column vectors:

$$\boldsymbol{\mathcal{S}}_l = (\mathbf{u}, \lambda, d)\,, \quad \boldsymbol{\mathcal{S}}_e = (\widehat{\mathbf{u}}_e, \widehat{\boldsymbol{\lambda}}_e, \widehat{\mathbf{d}}_e)\,, \quad \boldsymbol{\mathcal{S}}_g = (\widehat{\mathbf{u}}, \widehat{\boldsymbol{\lambda}}, \widehat{\mathbf{d}})\,, \tag{3.45}$$

where $\mathbf{u}$ is the displacement vector, of dimensions $(n_{dim}, 1)$, while $\lambda$ is the plastic multiplier and $d$ is the phase field and both are scalar fields. The element nodal displacement vector $\widehat{\mathbf{u}}_e$ has dimensions $(n_{ldof}, 1)$, the element multiplier vector $\widehat{\boldsymbol{\lambda}}_e$ has dimensions $(n_{en}, 1)$ and the element phase-field vector $\widehat{\mathbf{d}}_e$ has dimensions $(n_{en}, 1)$. $\widehat{\mathbf{u}}$ $(n_{dof}, 1)$ is the global nodal displacement vector, $\widehat{\boldsymbol{\lambda}}$ $(n_{np}, 1)$ is the global nodal multiplier vector, and $\widehat{\mathbf{d}}$ $(n_{np}, 1)$ is the global nodal phase-field vector. The element local solution together with the spatial gradients, i.e. the total deformation $\boldsymbol{\varepsilon}$ $(n_{\varepsilon}, 1)$, the plastic multiplier gradient $\boldsymbol{\nabla}\lambda$ $(n_{dim}, 1)$ and the phase-field gradient $\boldsymbol{\nabla} d$ $(n_{dim}, 1)$ are modeled at the element level as:

$$\mathbf{u} = \mathbf{N}_{\mathrm{u}}\, \widehat{\mathbf{u}}_e\,, \qquad \lambda = \mathbf{N}_{\lambda}\, \widehat{\boldsymbol{\lambda}}_e\,, \qquad d = \mathbf{N}_{\mathrm{d}}\, \widehat{\mathbf{d}}_e\,, \tag{3.46a}$$

$$\boldsymbol{\varepsilon} = \mathbf{B}_{\mathrm{u}}\, \widehat{\mathbf{u}}_e\,, \qquad \boldsymbol{\nabla}\lambda = \mathbf{B}_{\lambda}\, \widehat{\boldsymbol{\lambda}}_e\,, \qquad \boldsymbol{\nabla} d = \mathbf{B}_{\mathrm{d}}\, \widehat{\mathbf{d}}_e\,, \tag{3.46b}$$

where $\mathbf{N}_{\mathrm{u}}$ is the displacement shape function matrix $(n_{dim}, n_{ldof})$, $\mathbf{B}_{\mathrm{u}}$ is displacement compatibility matrix $(n_{\varepsilon}, n_{ldof})$, $\mathbf{N}_{\lambda}$ and $\mathbf{N}_{\mathrm{d}}$ are the plastic multiplier and phase-field shape function vectors $(1, n_{en})$, and $\mathbf{B}_{\lambda}$ and $\mathbf{B}_{\mathrm{d}}$ are plastic

multiplier and phase-field gradient matrices $(n_{dim}, n_{en})$. The global assembly is formally performed with the boolean connectivity matrices $\mathbf{C}_{e,\mathrm{u}}$ $(n_{ldof}, n_{dof})$, $\mathbf{C}_{e,\lambda}$ $(n_{en}, n_{np})$, and $\mathbf{C}_{e,\mathrm{d}}$ $(n_{en}, n_{np})$ such that:

$$\widehat{\mathbf{u}}_e = \mathbf{C}_{e,\mathrm{u}}\,\widehat{\mathbf{u}}\,, \qquad \widehat{\boldsymbol{\lambda}}_e = \mathbf{C}_{e,\lambda}\,\widehat{\boldsymbol{\lambda}}\,, \qquad \widehat{\mathbf{d}}_e = \mathbf{C}_{e,\mathrm{d}}\,\widehat{\mathbf{d}}\,. \tag{3.47}$$

### 3.4.1 GOVERNING EQUATIONS

The weak form of the equilibrium equation (3.24), the plasticity $(3.26)_c$ and fracture $(3.30)_c$ complementarity equations are spatially discretized:

$$\delta\widehat{\mathbf{u}}^{\mathrm{T}}\left[\sum_{e=1}^{n_{el}} \mathbf{C}_{e,\mathrm{u}}^{\mathrm{T}}\left(\mathbf{F}_{\mathrm{I},e} - \mathbf{F}_{\mathrm{E},e}\right)\right] = 0\,, \tag{3.48}$$

$$\Delta\widehat{\boldsymbol{\lambda}}^{\mathrm{T}}\left[\sum_{e=1}^{n_{el}} \mathbf{C}_{e,\lambda}^{\mathrm{T}}\,\mathbf{f}_{\mathrm{Y},e}\right] = 0\,, \quad \Delta\widehat{\mathbf{d}}^{\mathrm{T}}\left[\sum_{e=1}^{n_{el}} \mathbf{C}_{e,\mathrm{d}}^{\mathrm{T}}\,\mathbf{f}_{\mathrm{D},e}\right] = 0\,, \tag{3.49}$$

where $e$ denotes the element label and $n_{el}$ is the total number of elements in the mesh. The element internal force vector $\mathbf{F}_{\mathrm{I},e}$ $(n_{ldof}, 1)$, the external force vector $\mathbf{F}_{\mathrm{E},e}$ $(n_{ldof}, 1)$, the yield vector $\mathbf{f}_{\mathrm{Y},e}$ $(n_{en}, 1)$, and the fracture activation vector $\mathbf{f}_{\mathrm{D},e}$ $(n_{en}, 1)$ are:

$$\mathbf{F}_{\mathrm{I},e} := \int_{\Omega_e} \mathbf{B}_{\mathrm{u}}^{\mathrm{T}}\left(\omega\,\widetilde{\boldsymbol{\sigma}}^{A} + \widetilde{\boldsymbol{\sigma}}^{I}\right)\mathrm{d}\Omega_e\,, \tag{3.50a}$$

$$\mathbf{F}_{\mathrm{E},e} := \int_{\Omega_e} \mathbf{N}_{\mathrm{u}}^{\mathrm{T}}\,\mathbf{b}\,\mathrm{d}\Omega_e + \int_{\partial\Omega_e} \mathbf{N}_{\mathrm{u}}^{\mathrm{T}}\,\mathbf{t}\,\mathrm{d}\Gamma_e\,, \tag{3.50b}$$

$$\mathbf{f}_{\mathrm{Y},e} := \int_{\Omega_e} \omega\left(\mathbf{N}_{\lambda}^{\mathrm{T}}\,f_y - c_p\,\mathbf{B}_{\lambda}^{\mathrm{T}}\,\boldsymbol{\nabla}\lambda\right)\mathrm{d}\Omega_e\,, \tag{3.50c}$$

$$\mathbf{f}_{\mathrm{D},e} := -\int_{\Omega_e}\left\{\mathbf{N}_{\mathrm{d}}^{\mathrm{T}}\left[\omega'\,\widetilde{\psi}_{ep} + (f+1)\,w' + w'_{\epsilon} + \frac{\eta_f}{\Delta t}\,\Delta d\right] + c_d\,\mathbf{B}_{\mathrm{d}}^{\mathrm{T}}\,\boldsymbol{\nabla}d\right\}\mathrm{d}\Omega_e\,, \tag{3.50d}$$

where $\widetilde{\boldsymbol{\sigma}}^{A}$, $\widetilde{\boldsymbol{\sigma}}^{I}$ are defined in (3.36), being the effective stress tensor in Voigt notation $\widetilde{\boldsymbol{\sigma}} = \widetilde{\boldsymbol{\sigma}}^{A} + \widetilde{\boldsymbol{\sigma}}^{I}$ a vector with dimension $(n_\sigma, 1)$, with $n_\sigma = n_\varepsilon$ the number of independent stress components. The element integrals are evaluated over the element nominal volume $\Omega_e$. Then, $\boldsymbol{\nabla}\lambda$, $\Delta d$ and $\boldsymbol{\nabla}d$ are discretized as in (3.46). The additional constant term $w'_{\epsilon}$ is introduced to avoid spurious damage activations when $\alpha < \alpha_{cr}$ and is defined as:

$$w'_{\epsilon} = \epsilon\,\frac{G_c}{l_{0d}}\,\mathrm{H}^{-}\left(\alpha - \alpha_{cr}\right) \tag{3.51}$$

where $\epsilon$ is a non-dimensional, small coefficient to be set as small as possible (usually taken equal to $10^{-2}$), and $\mathrm{H}^{-}(\cdot)$ is the negative Heaviside operator.

The spatial discretization of the governing equations reads:

$$\mathbf{F}_{\mathrm{I}} - \mathbf{F}_{\mathrm{E}} = \mathbf{0}\,, \tag{3.52a}$$

$$\Delta\widehat{\boldsymbol{\lambda}} \geq \mathbf{0}\,, \quad \mathbf{f}_{\mathrm{Y}} \leq \mathbf{0}\,, \quad \Delta\widehat{\boldsymbol{\lambda}}^{\mathrm{T}}\,\mathbf{f}_{\mathrm{Y}} = 0\,, \tag{3.52b}$$

$$\Delta\widehat{\mathbf{d}} \geq \mathbf{0}\,, \quad \mathbf{f}_{\mathrm{D}} \leq \mathbf{0}\,, \quad \Delta\widehat{\mathbf{d}}^{\mathrm{T}}\,\mathbf{f}_{\mathrm{D}} = 0\,. \tag{3.52c}$$

## 3.5 Algorithmic implementation

### 3.5.1 Staggered scheme

The algorithmic solution of the set of governing equations (3.52) relies on the alternate minimization scheme illustrated in Algorithm 2. At each time step from $t^n$ to $t^{n+1}$, the input is the solution at the previous step $(\widehat{\mathbf{u}}, \widehat{\boldsymbol{\lambda}}, \widehat{\mathbf{d}})_n$, the increment of displacement Dirichelet boundary conditions $\Delta\widehat{\mathbf{u}}_{\mathrm{D}}$ and the increment of external forces $\Delta\mathbf{F}_{\mathrm{E}}$. The staggered scheme is solved with an iterative procedure, where $i$ denotes the staggered iteration counter. First, the elastoplastic problem (3.52a) and (3.52b) in $\widehat{\mathbf{u}}$ and $\Delta\widehat{\boldsymbol{\lambda}}$ is solved in a monolithic fashion with a Newton-Raphson scheme, for fixed phase-field $\Delta\widehat{\mathbf{d}}_{i-1}$. The residuum of this inner monolithic loop, with iteration counter $k$, is a suitable measure of the out-of-balance forces $\mathbf{F}_{\mathrm{I}} - \mathbf{F}_{\mathrm{E}}$ and is denoted with $\mathtt{Res}_{\mathrm{M}}$. The corresponding tolerance is $\mathtt{TOL}_{\mathrm{M}}$, where the $M$ subscript stands for monolithic. Then, the elastoplastic solution $(\widehat{\mathbf{u}}, \widehat{\boldsymbol{\lambda}})_k$ is used to solve the phase-field activation criterion for frozen displacement and plastic multiplier. Finally, the residual $\mathtt{Res}_{\mathrm{STAG}}$ of the staggered scheme is computed. It measures again the out-of-balance forces, but with the updated damage. The complementarity problems (3.52b) and (3.52c) are solved using the Projected Successive Over-Relaxation algorithm (PSOR) introduced in Mangasarian (1977) , following the approach proposed in Marengo et al. (2021), and outlined in Section 2.6.1 for the brittle counterpart of the phase-field activation criterion (3.52c). Further details are given in Appendix D.

### 3.5.2 Monolithic elastoplastic solver

The solution scheme of the elastoplastic problem (3.52a) and (3.52b) is further detailed in this section. Since in the light of the staggered scheme this problem must be solved for fixed phase-field, the explicit dependence on the damage variable is omitted for the sake of clarity. The displacement residual vector $\mathbf{R}_{\mathrm{u}}$ (the iteration counter $k$ has been omitted for notation convenience) has dimensions $(n_{dof}, 1)$ and measures the out-of-balance forces in the equilibrium equations:

$$\mathbf{R}_{\mathrm{u}}(\Delta\widehat{\mathbf{u}}, \Delta\widehat{\boldsymbol{\lambda}}) := \mathbf{F}_{\mathrm{I}}(\Delta\widehat{\mathbf{u}}, \Delta\widehat{\boldsymbol{\lambda}}) - \mathbf{F}_{\mathrm{E}} \tag{3.53}$$

The solution of the balance of linear momentum must fulfill the elastoplastic laws (3.52b). In practical terms, the loading-unloading conditions (3.52b) must be solved for fixed displacement increment, with the additional difficulty that,

**Algorithm 2:** Alternate minimization scheme

**input :** $(\widehat{\mathbf{u}}, \widehat{\boldsymbol{\lambda}}, \widehat{\mathbf{d}})_n$ , $\Delta\widehat{\mathbf{u}}_{\mathrm{D}}$, $\Delta\mathbf{F}_{\mathrm{E}}$

`initialize` $(\widehat{\mathbf{u}}, \widehat{\boldsymbol{\lambda}}, \widehat{\mathbf{d}})_i = (\widehat{\mathbf{u}}, \widehat{\boldsymbol{\lambda}}, \widehat{\mathbf{d}})_n$

**while** ( $Res_{STAG} > TOL_{STAG}$ ) **do**

  `update` $i = i + 1$

  **while** ( $Res_M > TOL_M$ ) **do**

    `update` $k = k + 1$

    `set` $\mathbf{F}_{\mathrm{I},k} = \mathbf{F}_{\mathrm{I}}(\Delta\widehat{\mathbf{u}}_k, \Delta\widehat{\boldsymbol{\lambda}}_k, \Delta\widehat{\mathbf{d}}_{i-1})$, $\mathbf{f}_{\mathrm{Y},k} = \mathbf{f}_{\mathrm{Y}}(\Delta\widehat{\mathbf{u}}_k, \Delta\widehat{\boldsymbol{\lambda}}_k, \Delta\widehat{\mathbf{d}}_{i-1})$

    `solve` $\mathbf{F}_{\mathrm{I},k} - \mathbf{F}_{\mathrm{E}} = \mathbf{0}$, $\Delta\widehat{\boldsymbol{\lambda}}_k \geq \mathbf{0}\,, \quad \mathbf{f}_{\mathrm{Y},k} \leq \mathbf{0}\,, \quad \Delta\widehat{\boldsymbol{\lambda}}_k^{\mathrm{T}}\,\mathbf{f}_{\mathrm{Y},k} = 0 \;\rightarrow\; (\Delta\widehat{\mathbf{u}}_k, \Delta\widehat{\boldsymbol{\lambda}}_k)$

    `assemble` $\mathbf{R}_{\mathrm{u},k} = \mathbf{F}_{\mathrm{I},k}(\Delta\widehat{\mathbf{u}}_k, \Delta\widehat{\boldsymbol{\lambda}}_k, \Delta\widehat{\mathbf{d}}_{i-1}) - \mathbf{F}_{\mathrm{E}}$

    `compute` $\mathtt{Res}_{\mathrm{M}} = \mathbf{R}_{\mathrm{u},k}^{\mathrm{T}}\,\mathbf{R}_{\mathrm{u},k}$

  **end**

  `set` $(\widehat{\mathbf{u}}, \widehat{\boldsymbol{\lambda}})_i = (\widehat{\mathbf{u}}, \widehat{\boldsymbol{\lambda}})_k\,, \quad \mathbf{f}_{\mathrm{D},i} = \mathbf{f}_{\mathrm{D}}(\Delta\widehat{\mathbf{u}}_i, \Delta\widehat{\boldsymbol{\lambda}}_i, \Delta\widehat{\mathbf{d}})$

  `solve` $\Delta\widehat{\mathbf{d}} \geq \mathbf{0}\,, \quad \mathbf{f}_{\mathrm{D},i} \leq \mathbf{0}\,, \quad \Delta\widehat{\mathbf{d}}^{\mathrm{T}}\,\mathbf{f}_{\mathrm{D},i} = 0 \quad \rightarrow \Delta\widehat{\mathbf{d}}_i = \Delta\widehat{\mathbf{d}}$

  `assemble` $\mathbf{R}_{\mathrm{u},i} = \mathbf{F}_{\mathrm{I}}(\Delta\widehat{\mathbf{u}}_i, \Delta\widehat{\boldsymbol{\lambda}}_i, \Delta\widehat{\mathbf{d}}_i) - \mathbf{F}_{\mathrm{E}}$

  `compute` $\mathtt{Res}_{\mathrm{STAG}} = \mathbf{R}_{\mathrm{u},i}^{T}\,\mathbf{R}_{\mathrm{u},i}$

**end**

**output:** $(\widehat{\mathbf{u}}, \widehat{\boldsymbol{\lambda}}, \widehat{\mathbf{d}})_n = (\widehat{\mathbf{u}}, \widehat{\boldsymbol{\lambda}}, \widehat{\mathbf{d}})_i$

due to the presence of the gradient term, the elastoplastic return mapping algorithm has to be formulated as a global problem and the time integration of the constitutive law cannot be carried out element by element. Once a first estimate of the nodal plastic multiplier increment $\Delta\widehat{\boldsymbol{\lambda}}$ is obtained, the set of active nodes $\mathcal{A}$ can be determined using the global PSOR algorithm:

$$\mathcal{A} := \left\{ a \in \left[1, n_{np}\right] \;\middle|\; \Delta\hat{\lambda}_a > 0 \right\} \tag{3.54}$$

where $a$ is the global node label. The vanishing of the residuum $\mathbf{R}_{\mathrm{u}}$ is enforced by means of a Newton-Raphson iterative scheme. The estimate of the displacement increment update $\delta\Delta\widehat{\mathbf{u}}$ between two successive iteration $k-1$ and $k$ can be computed from the following conditions, resulting from the linearization of $\mathbf{R}_{\mathrm{u}}$ and $\mathbf{f}_{\mathrm{Y}}$ around the current solution $\widehat{\mathbf{u}}_{k-1}$, $\Delta\widehat{\boldsymbol{\lambda}}_{k-1}$:

$$\delta\mathbf{R}_{\mathrm{u}} + \mathbf{R}_{\mathrm{u}} = \mathbf{0} \quad , \quad \delta\mathbf{f}_{\mathrm{Y}}\big|_{\mathcal{A}} = \mathbf{0} \tag{3.55}$$

where $(\cdot)|_{\mathcal{A}}$ is the restriction over the set of active nodes. The linearizations read:

$$\delta\mathbf{R}_{\mathrm{u}} = \frac{\partial\mathbf{R}_{\mathrm{u}}}{\partial\widehat{\mathbf{u}}}\,\delta\Delta\widehat{\mathbf{u}} \;+ \left.\frac{\partial\mathbf{R}_{\mathrm{u}}}{\partial\widehat{\boldsymbol{\lambda}}}\right|_{\mathcal{A}} \delta\Delta\widehat{\boldsymbol{\lambda}}\big|_{\mathcal{A}} = \mathbf{K}_{\mathrm{uu}}\,\delta\Delta\widehat{\mathbf{u}} + \mathbf{K}_{\mathrm{u}\lambda}\big|_{\mathcal{A}}\,\delta\Delta\widehat{\boldsymbol{\lambda}}\big|_{\mathcal{A}} \tag{3.56a}$$

$$\delta\mathbf{f}_{\mathrm{Y}} = \left.\frac{\partial\mathbf{f}_{\mathrm{Y}}}{\partial\widehat{\mathbf{u}}}\right|_{\mathcal{A}} \delta\Delta\widehat{\mathbf{u}} + \left.\frac{\partial\mathbf{f}_{\mathrm{Y}}}{\partial\widehat{\boldsymbol{\lambda}}}\right|_{\mathcal{A}} \delta\Delta\widehat{\boldsymbol{\lambda}}\big|_{\mathcal{A}} = \mathbf{K}_{\lambda\mathrm{u}}\,\delta\Delta\widehat{\mathbf{u}} + \mathbf{K}_{\lambda\lambda}\big|_{\mathcal{A}}\,\delta\Delta\widehat{\boldsymbol{\lambda}}\big|_{\mathcal{A}} \tag{3.56b}$$

Therefore, the solving system becomes:

$$\begin{bmatrix} \mathbf{K}_{\mathrm{uu}} & \mathbf{K}_{\mathrm{u}\lambda}\big|_{\mathcal{A}} \\ \mathbf{K}_{\lambda\mathrm{u}}\big|_{\mathcal{A}} & \mathbf{K}_{\lambda\lambda}\big|_{\mathcal{A}} \end{bmatrix}_{k-1} \begin{vmatrix} \delta\Delta\widehat{\mathbf{u}} \\ \delta\Delta\widehat{\boldsymbol{\lambda}}\big|_{\mathcal{A}} \end{vmatrix} = - \begin{vmatrix} \mathbf{R}_{\mathrm{u}} \\ \mathbf{0} \end{vmatrix}_{k-1} \tag{3.57}$$

It is important to remark that this system is needed only to recover the correct algorithmic tangent stiffness for the estimation of the displacement update $\delta\Delta\widehat{\mathbf{u}}$ through (3.56a). Once the system has been solved for $\delta\Delta\widehat{\mathbf{u}}$, the value of the update $\delta\Delta\widehat{\boldsymbol{\lambda}}\big|_{\mathcal{A}}$ is not used in the current algorithm. As shown in Algorithm 3, it is evident how the adopted procedure resembles a classical Newton-Raphson scheme for local plasticity, but with the introduction of a global return mapping. The explicit expressions of the tangent matrix and residuals are provided in Appendix B. When large time steps are used, convergence may become difficult. especially when damage is activated. To overcome convergence problems, a line search procedure has been used as outlined in Appendix C.

### 3.5.3 Reduced integration with hourglass control

The effective stress approach proposed in the current formulation has an important consequence: the plastic deformations develop in the continuous part of the material until complete failure. From a practical point of view, this involves very large plastic strains that induce a severe locking of the response. A possible solution to the problem is the use of a B-bar approach as in Simo et al. (1985). However, the use of a selective-reduced integration scheme into a staggered solution procedure (see Section 3.5.1) for a general three-dimensional problem would significantly increase the computational burden. Therefore, the solution of a reduced single-point integration has been chosen instead. Two-dimensional four-nodes and three-dimensional eight-nodes elements have been used.

#### 3.5.3.1 Linear kinematics

The implementation resembles the one in Flanagan and Belytschko (1981). For the sake of simplicity, the four-nodes element is discussed only, yet, the same conceptual passages may be extended to the eight-nodes element. The main relevant quantities are introduced in Appendix F. Let $\varphi$ be an unknown *scalar*

**Algorithm 3:** Monolithic elastoplastic solver

**input :** $(\widehat{\mathbf{u}}, \widehat{\boldsymbol{\lambda}})_n$ , $\Delta\widehat{\mathbf{u}}_{\mathrm{D}}$, $\Delta\mathbf{F}_{\mathrm{E}}$

`initialize` $(\widehat{\mathbf{u}}, \widehat{\boldsymbol{\lambda}})_k = (\widehat{\mathbf{u}}, \widehat{\boldsymbol{\lambda}}, \widehat{\mathbf{d}})_n$

**while** ( $Res_M > TOL_M$ ) **do**

`assemble` $\mathbf{K}_{\mathrm{uu}}(\Delta\widehat{\mathbf{u}}_k, \Delta\widehat{\boldsymbol{\lambda}}_k)$ , $\mathbf{K}_{\mathrm{u}\lambda}(\Delta\widehat{\mathbf{u}}_k)$ , $\mathbf{K}_{\lambda\lambda}$

`update` $k = k + 1$

`solve` $$\begin{bmatrix} \mathbf{K}_{\mathrm{uu}} & \mathbf{K}_{\mathrm{u}\lambda}\big|_{\mathcal{A}} \\ \mathbf{K}_{\lambda\mathrm{u}}\big|_{\mathcal{A}} & \mathbf{K}_{\lambda\lambda}\big|_{\mathcal{A}} \end{bmatrix}_{k-1} \begin{vmatrix} \delta\Delta\widehat{\mathbf{u}} \\ \delta\Delta\widehat{\boldsymbol{\lambda}}\big|_{\mathcal{A}} \end{vmatrix} = - \begin{vmatrix} \mathbf{R}_{\mathrm{u}} \\ \mathbf{0} \end{vmatrix}_{k-1} \quad \rightarrow \Delta\widehat{\mathbf{u}}_k$$

`set` $\mathbf{f}_{\mathrm{Y},k} = \mathbf{f}_{\mathrm{Y}}(\Delta\widehat{\mathbf{u}}_k, \Delta\widehat{\boldsymbol{\lambda}})$

`solve` $\Delta\widehat{\boldsymbol{\lambda}} \geq \mathbf{0}$ , $\mathbf{f}_{\mathrm{Y},k} \leq \mathbf{0}$ , $\Delta\widehat{\boldsymbol{\lambda}}^{\mathrm{T}}\,\mathbf{f}_{\mathrm{Y},k} = 0$ $\rightarrow \Delta\widehat{\boldsymbol{\lambda}}_k$

`define` $\mathcal{A} := \{\, a \in [1, n_{np}] \mid \Delta\hat{\lambda}_{k,a} > 0 \,\}$

`assemble` $\mathbf{R}_{\mathrm{u},k}(\Delta\widehat{\mathbf{u}}_k, \Delta\widehat{\boldsymbol{\lambda}}_k)$

`compute` $\mathtt{Res}_{\mathrm{M}} = \mathbf{R}_{\mathrm{u},k}^T\,\mathbf{R}_{\mathrm{u},k}$

**end**

**output:** $(\widehat{\mathbf{u}}, \widehat{\boldsymbol{\lambda}})_i = (\widehat{\mathbf{u}}, \widehat{\boldsymbol{\lambda}})_k$

*field*, and $\widehat{\boldsymbol{\varphi}}_e$ be the vector of its nodal values for element $e$ . It may be a displacement component, the scalar phase-field or the scalar plastic multiplier. It is additively decomposed

$$\widehat{\boldsymbol{\varphi}}_e = \widehat{\boldsymbol{\varphi}}_e^{lin} + \widehat{\boldsymbol{\varphi}}_e^{hg}\,, \tag{3.58}$$

where the linear and hourglass parts of the nodal solution vector are defined as

$$\widehat{\boldsymbol{\varphi}}_e^{lin} = a_0\mathbf{1} + a_1\hat{\mathbf{x}}_1 + a_2\hat{\mathbf{x}}_2\,, \tag{3.59}$$

$$\widehat{\boldsymbol{\varphi}}_e^{hg} = c_0\mathbf{1} + c_1\boldsymbol{b}_1 + c_2\boldsymbol{b}_2 + c_3\widehat{\mathbf{h}}\,, \tag{3.60}$$

being $a_0, a_1, a_2$ arbitrary constant coefficients, $c_0, c_1, c_2, c_3$ constant coefficients to be determined, $\hat{\mathbf{x}}_1, \hat{\mathbf{x}}_2$ the nodal coordinates vector in direction $1, 2$ respectively, and $\boldsymbol{b}_1, \boldsymbol{b}_2$ the shape functions physical derivatives vector at the element centroid (see Appendix F). It must be remarked that, while $\widehat{\boldsymbol{\varphi}}_e^{lin}$ is the exact linear part of the element solution, $\widehat{\boldsymbol{\varphi}}_e^{hg}$ is a new measure of the hourglass mode, yet, with the abuse of notation, the same symbol of Appendix F is used. The orthogonality condition is enforced

$$\widehat{\boldsymbol{\varphi}}_e^{hg\mathrm{T}}\widehat{\boldsymbol{\varphi}}_e^{lin} = 0\,, \tag{3.61}$$

allowing the definition of the coefficients $c_0, c_1, c_2, c_3$ for arbitrary $a_0, a_1, a_2$. Furthermore, the fundamental property $\boldsymbol{b}_i^{\mathrm{T}}\widehat{\boldsymbol{\varphi}}_e^{hg} \neq 0$ guarantees that the hour-

glass measure is non-vanishing for the one-point reduced integration. The solution of (3.61) with respect to the unknown coefficients provides the hourglass solution measure:

$$\widehat{\boldsymbol{\varphi}}_e^{hg} = c_3\big[\widehat{\mathbf{h}} - (\hat{\mathbf{x}}_1^{\mathrm{T}}\widehat{\mathbf{h}})\mathbf{b}_1 - (\hat{\mathbf{x}}_2^{\mathrm{T}}\widehat{\mathbf{h}})\mathbf{b}_2\big] = c_3\tilde{\boldsymbol{\gamma}}\,. \tag{3.62}$$

The $\gamma$-projection mode vector is the normalized vector $\widehat{\boldsymbol{\gamma}} := \tilde{\boldsymbol{\gamma}}/\,|\tilde{\boldsymbol{\gamma}}|$. Then, the coefficient $\bar{c}_3$ in $\widehat{\boldsymbol{\varphi}}_e^{hg} = \bar{c}_3\,\widehat{\boldsymbol{\gamma}}$ can be computed using (3.61):

$$\widehat{\boldsymbol{\gamma}}^{\mathrm{T}}\widehat{\boldsymbol{\varphi}}_e = \widehat{\boldsymbol{\gamma}}^{\mathrm{T}}(\widehat{\boldsymbol{\varphi}}_e^{lin} + \widehat{\boldsymbol{\varphi}}_e^{hg}) = \bar{c}_3\,.$$

The final shape of the hourglass solution vector reads:

$$\widehat{\boldsymbol{\varphi}}_e^{hg} = (\widehat{\boldsymbol{\gamma}}^{\mathrm{T}}\widehat{\boldsymbol{\varphi}}_e)\widehat{\boldsymbol{\gamma}} = (\widehat{\boldsymbol{\gamma}}\widehat{\boldsymbol{\gamma}}^{\mathrm{T}})\widehat{\boldsymbol{\varphi}}_e\,. \tag{3.63}$$

In the variational formulations outlined in the previous sections, the total energy or the Lagrangian functionals to be minimized are enriched with the additional term at the element level:

$$\Pi_e^{hg}(\widehat{\boldsymbol{\varphi}}_e) = {}^1\!/_2\, k_\varphi^{hg}\, \widehat{\boldsymbol{\varphi}}_e^{hg\mathrm{T}}\widehat{\boldsymbol{\varphi}}_e^{hg}\,, \tag{3.64}$$

where $k_\varphi^{hg}$ is the hourglass *stiffness* related to the scalar field $\varphi$. The corresponding stationarity with respect to the variable $\varphi$ reads:

$$\partial_{\widehat{\boldsymbol{\varphi}}_e}\Pi_e^{hg}(\widehat{\boldsymbol{\varphi}}_e)[\delta\widehat{\boldsymbol{\varphi}}_e] = \delta\widehat{\boldsymbol{\varphi}}_e^{\mathrm{T}}(k_\varphi^{hg}\,\widehat{\boldsymbol{\varphi}}_e^{hg}) = \delta\widehat{\boldsymbol{\varphi}}_e^{\mathrm{T}}\mathbf{f}_{\varphi,e}^{hg}\,.$$

Finally, the hourglass force associated to the field $\varphi$ can be written as

$$\mathbf{f}_{\varphi,e}^{hg}(\widehat{\boldsymbol{\varphi}}_e) = (k_\varphi^{hg}\,\widehat{\boldsymbol{\gamma}}\widehat{\boldsymbol{\gamma}}^{\mathrm{T}})\widehat{\boldsymbol{\varphi}}_e = \mathbf{K}_{\varphi,e}^{hg}\,\widehat{\boldsymbol{\varphi}}_e\,, \tag{3.65}$$

where $\mathbf{K}_{\varphi,e}^{hg} = k_\varphi^{hg}\,\widehat{\boldsymbol{\gamma}}\widehat{\boldsymbol{\gamma}}^{\mathrm{T}}$ is the constant hourglass stiffness and it is governed only by the parameter $k_\varphi^{hg}$. Therefore, the relation (3.65) states a linear relation between the hourglass force and the element field $\widehat{\boldsymbol{\varphi}}_e$.

#### 3.5.3.2 DISPLACEMENT HOURGLASS STIFFNESS

Let the scalar field $\varphi$ be the $i$-th displacement component $u_i$. The hourglass nodal forces correspond to a linear spring with constant stiffness according to (3.65). The definition of the hourglass coefficient $k_{u_i0}^{hg}$ (see e.g., Belytschko et al. (2014, 1984)) reads:

$$k_{u_i0}^{hg} = \bar{k}_{u_i0}\Big[\,2\,G_0\big(\mathbf{b}_i^{\mathrm{T}}\mathbf{b}_i\big)\,\Omega_e\Big]\,, \tag{3.66}$$

where the zero subscript has been introduced for reasons discussed below. The quantities inside the bracket are problem dependent, i.e., the shear modulus $G_0$, the element volume $\Omega_e$, and the one-integration point gradients of the shape

functions $\mathbf{b}_i$. Conversely, the user-defined non-dimensional coefficient $\bar{k}_{u_i 0}$ has typical values of the order 0.01.

It must be noticed that an elastic hourglass stiffness will introduce non-negligible spurious hardening responses in bending dominated problems (i.e., when the hourglass mode is more excited) in the presence of high material non-linearities. The reason lies in the observation that the internal nodal forces corresponding to the linear part of the nodal displacements (3.59) are computed according to the constitutive model (3.50a), while the hourglass nodal forces (3.69) are linearly proportional to the hourglass modes, independent of the constitutive model. To overcome this issue, the following choice has been employed: the hourglass stiffness is maintained linear, yet it is modulated by a reduction coefficient that accounts for the material nonlinearity. In the case of elastoplasticity, the reduction coefficient is inspired by the hardening law and reads:

$$c_r(\alpha) = \begin{cases} 1 & \alpha = 0 \text{ or } \Delta\alpha = 0 \\ \max\left(\frac{\sigma_{y0}(\alpha)}{\bar{\sigma}_{y0}+E_0\alpha}, c_{min}\right) & \text{otherwise} \end{cases}, \tag{3.67}$$

where $\alpha$ is the equivalent plastic strain at the element single integration point. The first condition ensures that in the elastic regime, and during elastic unloading, the elastic stiffness of the hourglass modes is recovered. The ratio $\sigma_{y0}(\alpha)/(\bar{\sigma}_{y0} + E_0\alpha)$ represents the discrepancy between the elastic $(\bar{\sigma}_{y0} + E_0\alpha)$ and elastoplastic $\sigma_{y0}(\alpha) = \bar{\sigma}_{y0} + H_0\alpha$ (see Section 3.2.4) responses in the one-dimensional case. Finally, a minimum threshold is introduced $c_{min} = 10^{-4}$ to prevent too small values of the stiffness. The implemented hourglass stiffness reads

$$k^{hg}_{u_i}(\alpha, d) = \omega_\kappa(d)\, c_r(\alpha)\, k^{hg}_{u_i 0}\,, \tag{3.68}$$

where also the damaging behaviour of the material is accounted for with the degradation function $\omega_\kappa(d) := (1-\kappa)(1-d)^2 + \kappa$, being $\kappa = 10^{-2}$ a residual stiffness coefficient to avoid ill-conditioning of the stiffness matrix.

The final hourglass forces in the $i$-th physical direction read

$$\mathbf{f}^{hg}_{u_i,e}(\widehat{\mathbf{u}}_{i,e}) = (k^{hg}_{u_i}\,\widehat{\boldsymbol{\gamma}}\widehat{\boldsymbol{\gamma}}^{\mathrm{T}})\widehat{\mathbf{u}}_{i,e} = \mathbf{K}^{hg}_{u_i,e}\,\widehat{\mathbf{u}}_{i,e}\,, \tag{3.69}$$

being $\widehat{\mathbf{u}}_{i,e}$ the nodal vector of the $i$-th displacement component. The vectors $\mathbf{f}^{hg}_{u_i,e}$, $\widehat{\mathbf{u}}_{i,e}$ have dimension $(n_{en}, 1)$, and the matrix $\mathbf{K}^{hg}_{u_i,e}$ has dimension $(n_{en}, n_{en})$, being $n_{en}$ the number of element nodes. Here, an important remark must be done on the management of the degrees of freedom of the finite element implementation. The hourglass formulation in Section 3.5.3.1 is suitable for a *scalar* field. Thus, it corresponds to a *component-wise* storage of the nodal degrees of freedom as for the vector $\widehat{\mathbf{u}}_{i,e} = (\hat{u}_i^{(1)}, \ldots, \hat{u}_i^{(n_{en})})^{\mathrm{T}}$. Conversely, the usual storage of the degrees of freedom is *node-wise* as in $\widehat{\mathbf{u}}_e = (\hat{u}_1^{(1)}, \ldots, \hat{u}_{n_{dim}}^{(1)}, \cdot, \hat{u}_1^{(n_{en})}, \ldots, \hat{u}_{n_{dim}}^{(n_{en})})^{\mathrm{T}}$ introduced in (3.45). The formal introduction of a booelan connectivity matrix $\mathbf{C}_{ui,e}\,(n_{ldof}, n_{en})$ between the

two approaches such that $\widehat{\mathbf{u}}_e = \sum_{i=1}^{n_{dim}} \mathbf{C}_{ui,e} \widehat{\mathbf{u}}_{i,e}$ allows to correctly define the hourglass force and tangent stiffness read

$$\mathbf{f}_{ue}^{hg} = \sum_{i=1}^{n_{dim}} \mathbf{C}_{ui,e}^{\mathrm{T}} \mathbf{f}_{u_i,e}^{hg}, \quad \mathbf{K}_{ue}^{hg} = \sum_{i=1}^{n_{dim}} \mathbf{C}_{ui,e}^{\mathrm{T}} \mathbf{K}_{u_i,e}^{hg} \mathbf{C}_{ui,e}. \tag{3.70}$$

Finally, while the introduction of the hourglass force $\mathbf{f}_{ue}^{hg}$ in the monolithic scheme of Section 3.5.2 is immediate, the hourglass tangent stiffness $\mathbf{K}_{ue}^{hg}$ is added to the diagonal term $\mathbf{K}_{\mathrm{uu},e}$ only, since no coupling between the displacement and the plastic multiplier is considered in the hourglass energy.

#### 3.5.3.3 PHASE-FIELD AND PLASTIC MULTIPLIER HOURGLASS STIFFNESSES

The reduced integration has been adopted also for the scalar phase-field $d$ and plastic multiplier $\lambda$. The hourglass coefficients in the two formulations read:

$$k_{\lambda 0}^{hg} = \bar{k}_{\lambda 0} \left[ \bar{\sigma}_{y0}\, l_{0p}^2 \big(\mathbf{b}_i^{\mathrm{T}} \mathbf{b}_i\big)\, \Omega_e \right], \tag{3.71}$$

$$k_{d0}^{hg} = \bar{k}_{d0} \left[ {}^{G_c}\!/_{l_{0d}} \big(\mathbf{b}_i^{\mathrm{T}} \mathbf{b}_i\big)\, \Omega_e \right]. \tag{3.72}$$

The used values are $\bar{k}_{\lambda 0} = 0.1$, $\bar{k}_{d0} = 10$. They have been calibrated to guarantee the same order of magnitude between the hourglass and the linear eigenvalues. The corresponding hourglass forces are $\mathbf{f}_{\lambda,e}^{hg}$, and $\mathbf{f}_{d,e}^{hg}$ from (3.65). They are added to $\mathbf{f}_{\mathrm{Y},e}$ (3.50c), and $\mathbf{f}_{\mathrm{D},e}$ (3.50d), respectively. A final remark concerns on the monolithic scheme for the plastic multiplier. The tangent hourglass stiffness matrix $\mathbf{K}_{\lambda,e}^{hg}$ must be summed to the diagonal term $\mathbf{K}_{\lambda\lambda,e}$, only.

## 3.6 NUMERICAL SIMULATIONS

Two-dimensional simulations are performed with 4-nodes quadrilateral elements in plane strain conditions. The staggered residual tolerance is $\texttt{TOL}_{\mathrm{STAG}} = 10^{-3}\,\mathrm{N}^2$, while the monolithic Newton-Raphson residual tolerance is $\texttt{TOL}_{\mathrm{M}} = 10^{-6}\,\mathrm{N}^2$. The mesh resolution of the phase-field localization band is reported for each test comparing the element dimension $h_e$ and the damage internal length parameter $l_{0d}$, which for the AT1 dissipation model represents a fourth of the band width (see Section 2.2).

| Material | $E_0$ | $\nu$ | $K_0$ | $G_0$ | $\bar{\sigma}_{y0}$ | $H_0$ | $l_{0p}$ | $G_c$ |
|---|---|---|---|---|---|---|---|---|
| I | 68.90 | 0.33 | - | - | 465 | 10 | 1.2 | 10 |
| II | - | - | 71.66 | 27.28 | 340 | 250 | 1.6 | 9.31 |
| | GPa | - | GPa | GPa | MPa | MPa | mm | N/mm |

**Table 3.1:** Material properties

### 3.6.1 ONE-DIMENSIONAL LOCALIZATION

The tensile loading of a one-dimensional bar is considered. The geometry and boundary conditions are depicted in Figure 3.4. The cross section is assumed to be $A = 1\,\mathrm{mm}^2$. The material properties are $E_0 = 210\,\mathrm{GPa}$, $\bar{\sigma}_{y0} = 350\,\mathrm{MPa}$, $H_0 = 650\,\mathrm{MPa}$, $l_{0p} = 0.06\,\mathrm{mm}$, and $G_c = 2\,\mathrm{N/mm}$. The fracture internal length is $l_{0d} = 0.03\,\mathrm{mm}$. The ductile fracture parameters are $\alpha_{cr} = 0.4$, $\Delta\alpha_{cr} = 0.2$ and $f_{min} = 0$. The viscous coefficient $\bar{\eta} = 5 \cdot 10^{-3}\,s$.

A uniform mesh of 500 linear one-dimensional finite elements is used with an element size $h_e = 0.002\,\mathrm{mm}$. A uniform time discretization is used to enforce the boundary conditions. The total number of steps is $n_{st} = 1000$ and the step increment is $\Delta\bar{u} = 5 \cdot 10^{-4}\,\mathrm{mm}$. The localization in the central part of the bar is obtained with a local weakening of the material properties in the central 10% of its length. In these elements, the initial yield stress $\bar{\sigma}_{y0}$ and the toughness $G_c$ are reduced by 20%. For this particular 1D example, the staggered residual tolerance is $\mathtt{TOL}_{\mathrm{STAG}} = 10^{-5}\,\mathrm{N}^2$, while the monolithic Newton-Raphson residual tolerance is $\mathtt{TOL}_{\mathrm{M}} = 10^{-10}\,\mathrm{N}^2$.

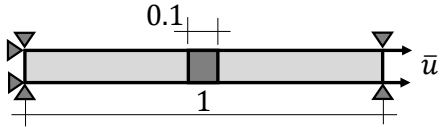


**Figure 3.4:** One-dimensional bar in tension: geometry [mm] and boundary conditions.

The global response in terms of engineering strain and stress is shown in Figure 3.5a. Here, some significant steps are highlighted with circular markers. The corresponding profiles of the modulation function $f + 1$ are then plotted in Figure 3.5b. The first time at which a point reaches $\alpha = \alpha_{cr}$ is step 680. The competition between the terms $(1 - \bar{d})$ and $\tilde{\mathcal{H}}$ starts at step 737. Until that moment, the qualitative profile of the modulation function resembles the one of the equivalent plastic deformation. After that, the points experiencing a plastic deformation $\alpha > \alpha_{cr}$ show a decrease in the value of $f + 1$, since the influence of the fictitious phase-field history $\bar{d}$ significantly intervenes into the modulation function.

The time and space evolution of the equivalent plastic deformation and of the phase field can be observed in Figure 3.6. The circular markers correspond to the mesh nodes. Before damage onset, only the plastic deformation profile is different from zero as shown in the plot of step 680, when for the first time $\alpha = \alpha_{cr}$ is reached. Here, the uniform solution of the equivalent plastic deformation is slightly perturbed by the weakening of the material parameters. In the following steps, the damage localization induces a more intense localization of plastic deformations, due to the effective stress approach adopted in the current work, with the material continuing to yield after damage development. Since the effective stress is acting on the continuous part of the material bulk and this

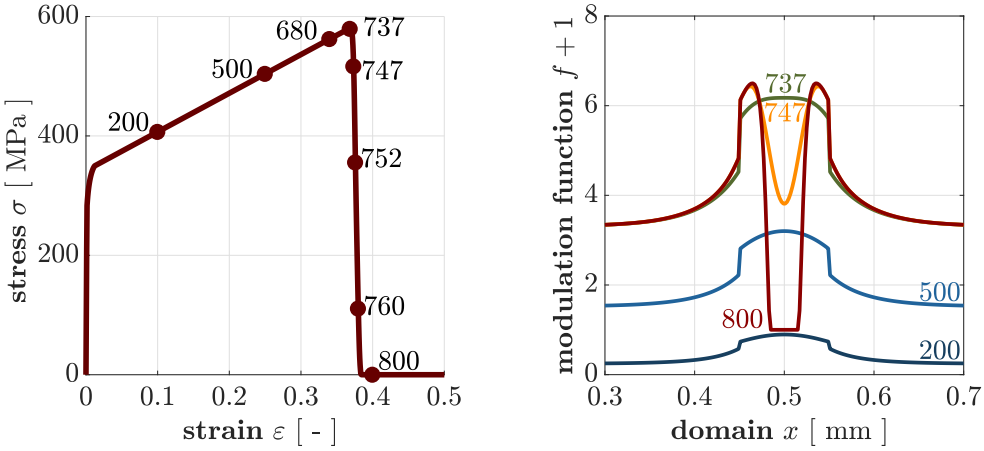


**(a)** Engineering stress vs strain curve

**(b)** Modulation function evolution

**Figure 3.5:** 1D localization. Global response (a) and modulation function time evolution (different colors correspond to different times) (b).

is progressively reducing, the plastic deformation increases considerably and, at this point, the effect of the gradient on the plastic multiplier can be appreciated because of the softening structural response. In the subsequent snapshots, it can be noticed how the damage growth is driven by the developing plastic strain. At step 752, the plastic deformation reaches $\alpha_{cr} + \Delta\alpha_{cr}$ for the first time. At step 800, the profiles of the equivalent plastic deformation and of the phase field are fully developed. The plasticity driven nature of fracture can be appreciated by noticing that the finite band-width of damage is entirely contained in the plastic localization band, since no damage occurs in the portion of the domain where $\alpha < \alpha_{cr}$.

### 3.6.2 V-NOTCHED SPECIMEN

We consider the V-notched specimen experimentally tested in Li et al. (2011). Several authors have used this benchmark for the simulation of ductile fracture (see, e.g., Miehe et al. (2017)). This is shown as a first example to demonstrate the model capabilities when crack onset and specimen failure occur without a stable propagation branch. The geometry of the specimen is depicted in Figure 3.7a. As in Li et al. (2011); Miehe et al. (2017), slightly rounded corners have been used at the notch tips to avoid sharp discontinuities in the geometry. The Dirichelet boundary conditions constrain the horizontal direction only. The material properties are shown in Table 3.1 for the case of Material I. The phase-field internal length is $l_{0d} = 0.4\,\text{mm}$ and the ductile fracture parameters are $\alpha_{cr} = 0.05$, $\Delta\alpha_{cr} = 0.03$ and $f_{min} = 0$.
The mesh is shown in Figure 3.7b. A refinement in the expected crack propagation region is used. The minimum element side is $h_e = 0.1\,\text{mm}$. The resolution of the localization zone is $l_{0p}/h_e = 12$ for the plastic deformation and $l_{0d}/h_e = 4$

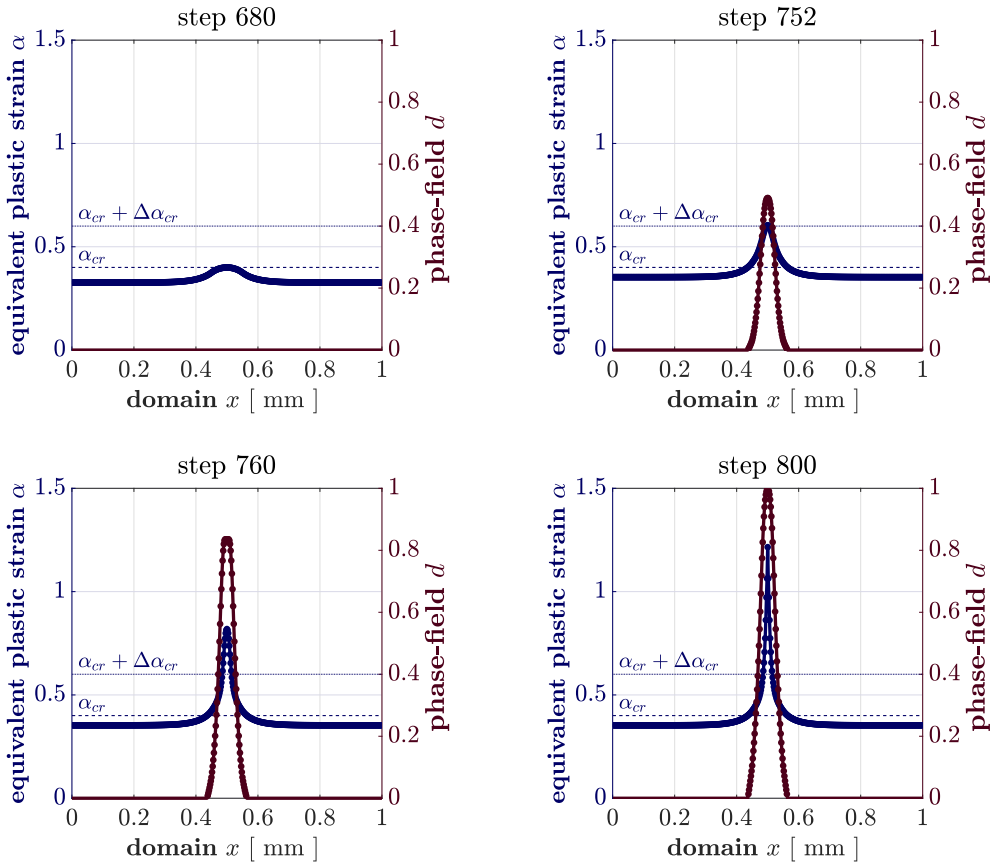


**Figure 3.6:** 1D localization. Equivalent plastic strain (blue curve) and phase-field time evolution (brown curve).

for the phase field. A total of $n_{el} = 6359$ elements and $n_{np} = 6454$ nodes have been used, with a time step $\Delta\bar{u} = 0.01\,\text{mm}$.

The global response in terms of reaction force and enforced displacement at the right edge is shown in Figure 3.8. The viscous coefficient is set to a non-negligible value $\bar{\eta} = 0.08\,\text{s}$, to prevent overly brittle crack propagation. The response is purely elastoplastic until a displacement of 0.25 mm, corresponding to step 25, is enforced. Then, damage grows at both the notch tips until crack onset occurs between step 35 and 36. The two cracks propagate with an almost linear path until step 42, when the first crack starts to branch as it can be clearly noticed in step 44. The final coalescence of the two fractures occurs at step 49. The contour plots of the plastic multiplier $\lambda$ and of the phase field $d$ at the relevant steps in the reaction curve are shown in Figure 3.9 and 3.10. It must be noticed that, due to the plasticity driven nature of the proposed ductile fracture model, the crack propagation closely follows the path of the plasticity localization band observable in the contour plots of $\lambda$.

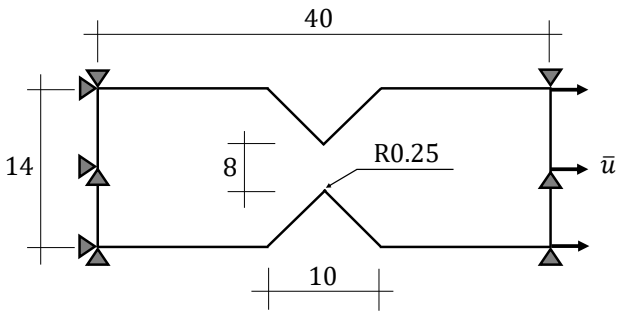


**(a)** Geometry in [mm] and boundary conditions

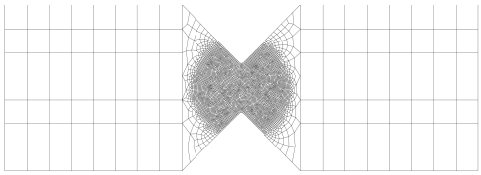

**(b)** Mesh

**Figure 3.7:** V-notched specimen. Geometry in [mm], boundary conditions and mesh.

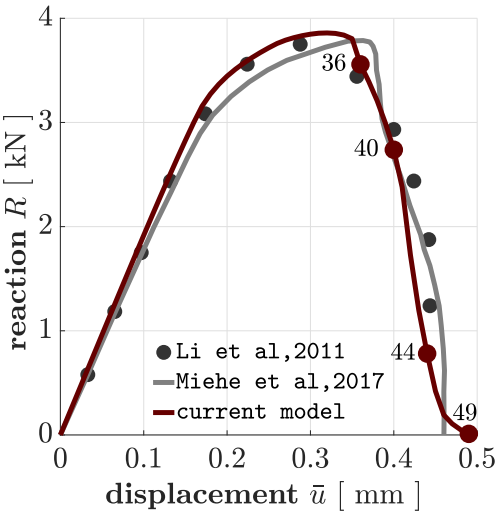


**Figure 3.8:** V-notched specimen. Reaction force vs imposed displacement. Results (solid black curve) are compared to those in Miehe et al. (2017) (light gray) and to the experimental results in Li et al. (2011) (circular markers).

### 3.6.3 SYMMETRIC NOTCHED SPECIMEN

This test has also been investigated by several authors, such as in Ambati et al. (2015b) and Yin and Kaliske (2020). In these two works, the ductile fracture

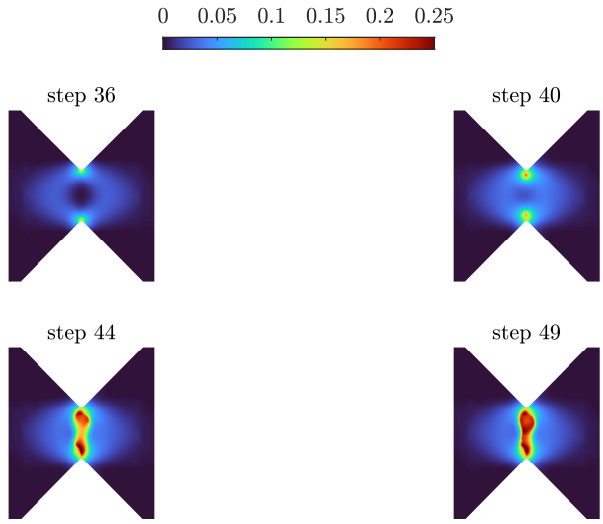


**Figure 3.9:** V-notched specimen. Plastic multiplier contourplots.

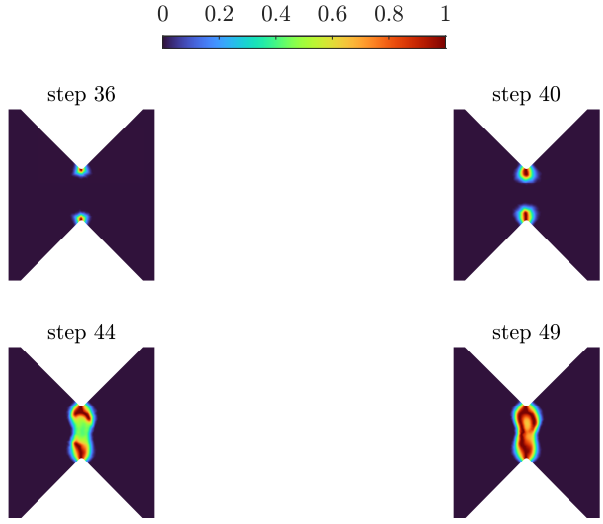


**Figure 3.10:** V-notched specimen. Phase-field contour plots.

simulation approach is significantly different from the current model. The main difference lies in the yield criterion being based on nominal stresses. When damage starts to propagate, nominal stresses decrease and the response of the damaged material becomes purely elastic, since the yield surface can be no more activated. This example is particularly interesting in view of the stable crack propagation that can be observed after damage reaches the unit value in the first notch. The geometry and boundary conditions are shown in Figure 3.11a. Both edges are clamped (i.e, no horizontal displacements are allowed) and the top boundary is subjected to an enforced vertical displacement. The uniform

increment of Dirichelet boundary conditions at each step is $\Delta\bar{u} = 0.01\,\text{mm}$.

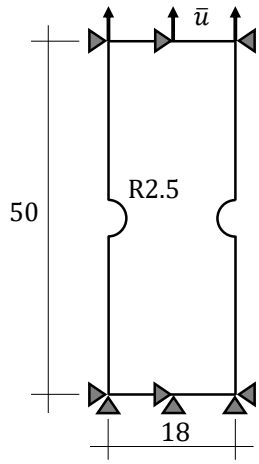


**(a)** Geometry in [mm] and boundary conditions

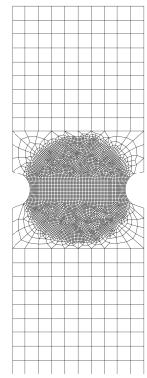

**(b)** Mesh

**Figure 3.11:** Symmetric notched specimen. Geometry in [mm], boundary conditions (a) and mesh (b).

The material properties are shown in Table 3.1 for the case of Material II. The phase-field internal length is $l_{0d} = 0.4\,\text{mm}$ and the ductile fracture parameters are $\alpha_{cr} = 0.09$, $\Delta\alpha_{cr} = 0.01$ and $f_{min} = 0$. The viscous coefficient is $\bar{\eta} = 0.01\,s$. The mesh for the simulation is shown in Figure 3.11b. A local refinement is introduced where the crack propagation is expected to occur. The minimum element side is $h_e = 0.2\,\text{mm}$. The resolution of the localization zone is $l_{0p}/h_e = 8$ for the plastic deformation and $l_{0d}/h_e = 2$ for the phase field. The number of elements is $n_{el} = 5438$ and the number of nodes is $n_{np} = 5494$.

The global response in terms of reaction force vs enforced vertical displacement at the top edge is depicted in Figure 3.12. The corresponding contour plots of plastic multiplier and phase field are shown in Figure 3.13. The response is purely elastoplastic until step 55 corresponding to $\bar{u} = 0.55\,\text{mm}$. In step 71 it is evident how shear bands form at an inclination of almost 45°. At step 80 ($\bar{u} = 0.80\,\text{mm}$), the right notch first reaches damage equal to unity. Afterwards, a long and stable horizontal crack propagation is observed from the right notch towards the opposite one. This mechanism continues until step 113 ($\bar{u} = 1.13\,\text{mm}$) with an almost linear softening slope. At this point the crack in the second notch appears. Then, in a few steps, a short stable propagation of this second crack is observed towards the opposite side. This mechanism is evident up to step 148 ($\bar{u} = 1.48\,\text{mm}$) when the cracks are so close that the merging of the two paths becomes possible. This sudden crack propagation ends with the specimen failure at step 153 ($\bar{u} = 1.53\,\text{mm}$).

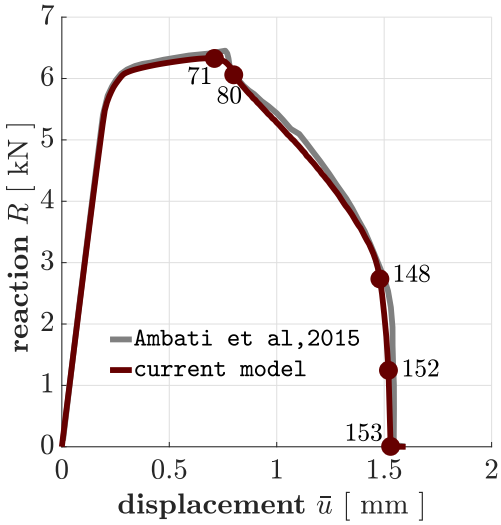


**Figure 3.12:** Symmetric notched specimen. Reaction force vs imposed displacement. Results are compared with those of the nominal stress approach proposed in Ambati et al. (2015b).

### 3.6.4 ASYMMETRIC NOTCHED SPECIMEN

The asymmetric notched specimen with the geometry and boundary conditions depicted in Fig. 3.14a is considered. The bottom edge is fully clamped, while the top edge has fully constrained horizontal displacement, with an enforced vertical displacement $\bar{u}$. The material properties correspond to Material I in Table 3.1. The phase-field internal length is $l_{0d} = 0.6\,\text{mm}$ and the ductile fracture parameters are $\alpha_{cr} = 0.086$, $\Delta\alpha_{cr} = 0.05$ and $f_{min} = 0$. The viscous coefficient is $\bar{\eta} = 0.001\,\text{s}$.

The mesh used is shown in Figure 3.14b. The spatial discretization is locally refined where the crack localization is expected to occur. The minimum element size is $h_e = 0.2\,\text{mm}$. Therefore, the resolution is $l_{0p}/h_e = 8$ and $l_{0d}/h_e = 3$. The number of elements is $n_{el} = 2637$ and the number of nodes is $n_{np} = 2686$. The time step is $\Delta\bar{u} = 0.01\,\text{mm}$.

The global response in terms of reaction force and enforced displacement is shown in Figure 3.15. The structural response is elastoplastic until step 45 where a damage starts to develop at the upper notch. At step 61, the phase-field reaches unity for the first time. At step 64, fracture starts also from the lower notch. First, the cracks propagate horizontally from the two notches, then, in few steps, the two paths start to align along the shear band, i.e., in the direction of the driving plastic deformation. Finally, an unstable crack propagation occurs between steps 79 and 81, where the cracks merge.

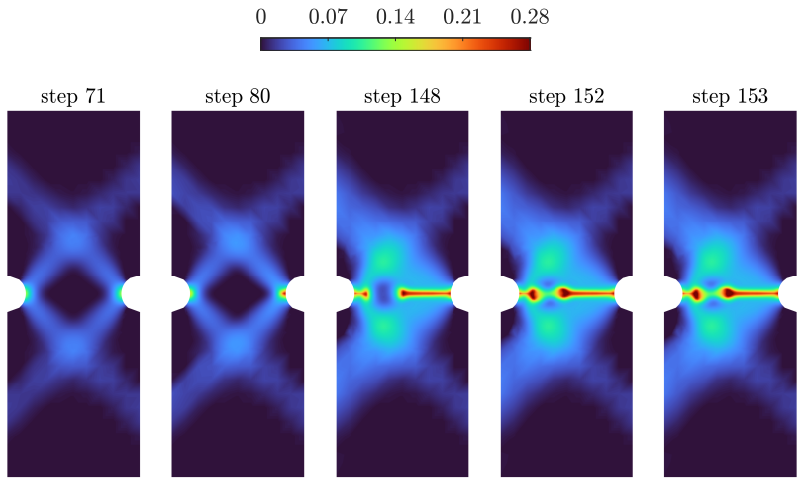


**(a)** Plastic multiplier $\lambda$

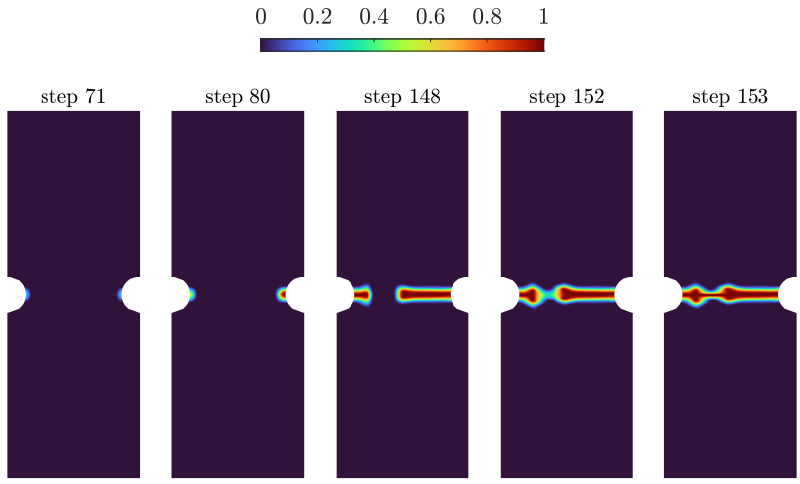


**(b)** Phase field $d$

**Figure 3.13:** Symmetric notched specimen. Plastic multiplier (a) and phase field (b) contour plots.

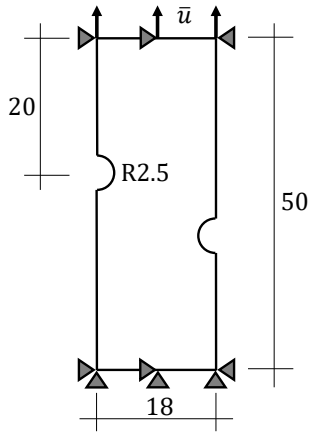


(a) Geometry in [mm] and boundary conditions

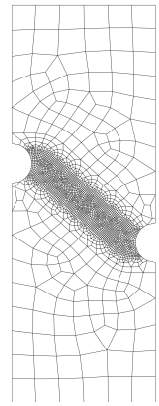

(b) Mesh

**Figure 3.14:** Asymmetric notched specimen. Geometry in [mm], boundary conditions (a) and mesh (b).

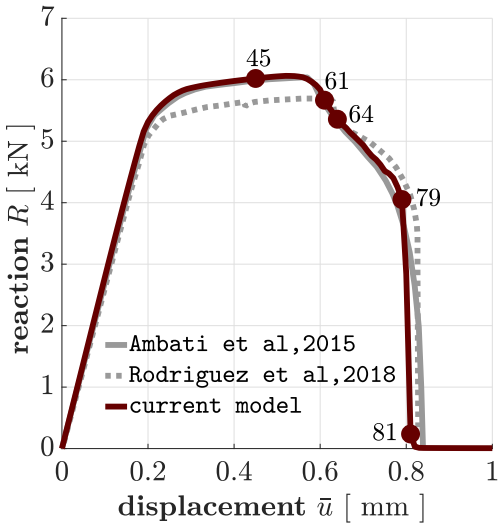


**Figure 3.15:** Asymmetric notched specimen. Reaction force vs imposed displacement. Results are compared with those obtained with the nominal stress approach proposed in Ambati et al. (2015b) and the effective stress approach proposed in Rodriguez et al. (2018).

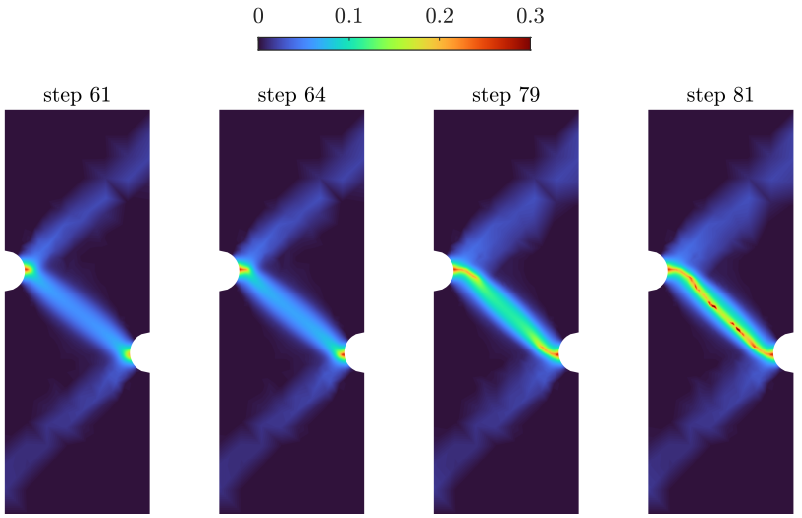


**(a)** Plastic multiplier $\lambda$

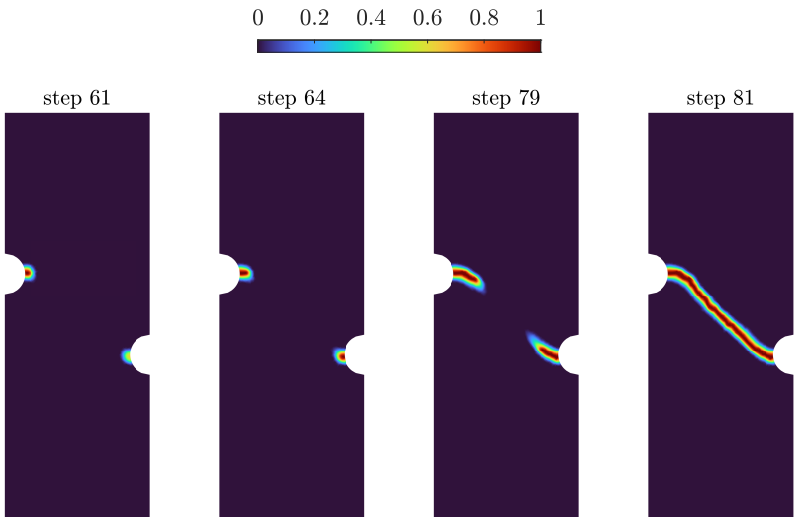


**(b)** Phase field $d$

**Figure 3.16:** Asymmetric notched specimen. Contour plots of plastic multiplier (a) and phase field (b).

# 4 In-plane Fracture of Paperboard

## 4.1 Introduction

The orthotropic nature of paperboard reflects in both the elastic response and the yield criterion. A ductile fracture model accounting for the relative orientation between the material directions and the external excitations is developed extending the modulation function approach introduced in the previous chapter for isotropic materials. The novelty of the proposed formulation is encapsulated in the definition of a scalar plastic strain measure of the orthotropic response. This follows the definition of a damage activation criterion in the material plastic strain space assessing the attainment of the critical size of the plastic localization zone. The plastic strain measure represents a sort of distance between the current state and the said critical condition. The proposed model deeply differs from other approaches available in the literature. An isotropic damage and fracture dissipation energy functional are used, while the orthotropic response lies in the plasticity-driven nature of the crack evolution, controlled by the sole modulation function. Unlike the isotropic materials outlined in Chapter 3, for orthotropic materials with multiple hardening mechanisms, it has been observed that the effective stress approach with plasticity-driven crack evolution shows no mesh-dependence when a global softening response occurs. For this reason, a local plasticity model, without gradient extension, has been used. Finally, the model predictivity is validated with experimental results.

## 4.2 Phase-field ductile fracture of orthotropic materials

The thermodynamic and variational formulation closely resemble the isotropic case in Section 3.2. The main difference lies in the presence of multiple yield mechanisms, thus, the internal variable $\alpha$ is substituted with a set of hardening internal variables $\beta_1, ..., \beta_{n_\beta}$, being $n_\beta$ the number of yield mechanisms. They are cast into a single vector $\boldsymbol{\beta} = (\beta_1, ..., \beta_{n_\beta})^{\mathrm{T}}$. Therefore, only the fundamental results are reported.

### 4.2.1 State variables & evolution laws

The state variables are the total strain tensor $\boldsymbol{\varepsilon}$ , the plastic strain tensor $\boldsymbol{\varepsilon}^p$, the set of hardening internal variables $\boldsymbol{\beta}$, and the damage-like phase field $d$. The free energy $\psi$ is assumed to be additively decomposed into its elastic (reversible) part $\omega\,\widetilde{\psi}^e(\boldsymbol{\varepsilon}^e)$, $\boldsymbol{\varepsilon}^e$ denoting the elastic strain tensor, and hardening (unrecoverable) part $\omega\,\widetilde{\psi}^p(\boldsymbol{\beta})$, the latter being the internal elastic energy stored in the material because of irreversible deformations of the micro-structure. The energies $\widetilde{\psi}^e(\boldsymbol{\varepsilon}^e)$ and $\widetilde{\psi}^p(\boldsymbol{\beta})$, are the undamaged or *effective* elastic and hardening free energies. The *nominal* and *effective* free energies are related via $\psi := \omega\,\widetilde{\psi}$, being $\widetilde{\psi} := \widetilde{\psi}^e + \widetilde{\psi}^p$.

The nominal and effective elastic stresses are $\boldsymbol{\sigma} = \omega\,\widetilde{\boldsymbol{\sigma}}$ and $\widetilde{\boldsymbol{\sigma}} := \partial_{\boldsymbol{\varepsilon}^e}\widetilde{\psi}^e$ respectively. The nominal and effective plastic dissipation rates read:

$$\dot{\phi}^p = \omega\,\dot{\widetilde{\phi}}^p\,, \quad \dot{\widetilde{\phi}}^p := \widetilde{\boldsymbol{\sigma}} : \dot{\boldsymbol{\varepsilon}}^p - \widetilde{\boldsymbol{\chi}}\cdot\dot{\boldsymbol{\beta}} \geq 0\,, \tag{4.1}$$

where $\widetilde{\boldsymbol{\chi}}$ is the effective *static* hardening variables vector, i.e., the thermodynamic forces work-conjugated to the internal variables $\boldsymbol{\beta}$. It is defined as:

$$\widetilde{\boldsymbol{\chi}} := \partial_{\boldsymbol{\beta}}\widetilde{\psi}^p\,. \tag{4.2}$$

The elastoplastic evolution has to satisfy the constraint that the admissible set of effective stress and static hardening parameters $(\widetilde{\boldsymbol{\sigma}}^*, \widetilde{\boldsymbol{\chi}}^*)$ has to comply with the yield condition $f_y(\widetilde{\boldsymbol{\sigma}}^*, \widetilde{\boldsymbol{\chi}}^*) \leq 0$, being $f_y$ the yield function, convex in the space of stress and static internal variables. The yield criterion is postulated in terms of effective quantities, as outlined in Section 3.2. The stationarity conditions associated to the (effective) principle of maximum dissipation provide the *effective elastoplastic evolution laws*:

$$\dot{\boldsymbol{\varepsilon}}^p = \dot{\lambda}\,\partial_{\widetilde{\boldsymbol{\sigma}}} f_y\,, \quad \dot{\boldsymbol{\beta}} = -\dot{\lambda}\,\partial_{\widetilde{\boldsymbol{\chi}}} f_y\,, \quad \dot{\lambda} \geq 0\,, \quad f_y \leq 0\,, \quad \dot{\lambda}\,f_y = 0\,, \tag{4.3}$$

where $\dot{\lambda}$ is the non-negative rate of a scalar plastic multiplier.

### 4.2.2 Variational formulation of the finite-step problem

#### 4.2.2.1 Phase-field finite-step variational formulation of ductile fracture

The variational principle is stated within the finite step increment. The previous and current time are $t^n$ and $t^{n+1}$ respectively. The time increment in the current step is $\Delta t = t^{n+1} - t^n$. The generic quantity increment is defined as $\Delta(\cdot) = (\cdot) - (\cdot)_n$, where for all quantities evaluated at time $t^{n+1}$, the $n+1$ at exponent has been omitted for notation convenience. The current Lagrangian functional to be minimized is $\mathcal{L}^n$, where the superscript $n$ implies that the quantities at end of the previous time step are parameters in the optimization procedure. Defining the set of independent fields

$$\mathcal{S} := (\mathbf{u}, \boldsymbol{\varepsilon}, \Delta\boldsymbol{\varepsilon}^p, \widetilde{\boldsymbol{\sigma}}, \widetilde{\boldsymbol{\sigma}}^p, \widetilde{\boldsymbol{\chi}}, \Delta\boldsymbol{\beta}, \Delta\lambda, \Delta d) \tag{4.4}$$

The stress field $\widetilde{\boldsymbol{\sigma}}^p$ in $\mathcal{S}$ is a dummy field considered to facilitate the derivation of the governing equations resulting from the stationarity of the functional.

$$\begin{aligned}\mathcal{L}^n(\mathcal{S}) := & \underbrace{\int_\Omega \omega(d)\,\left[\widetilde{\psi}^e(\boldsymbol{\varepsilon}-\boldsymbol{\varepsilon}^{p\,n}-\Delta\boldsymbol{\varepsilon}^p)+\widetilde{\psi}^p(\boldsymbol{\beta}^n+\Delta\boldsymbol{\beta})\right]\mathrm{d}\Omega}_{\textit{stored internal energy } \mathcal{E}} - \\ & - \underbrace{\int_\Omega \mathbf{b}\cdot\mathbf{u}\,\mathrm{d}\Omega - \int_{\partial\Omega_N}\mathbf{t}\cdot\mathbf{u}\,\mathrm{d}\Gamma}_{\textit{external work } \mathcal{W}} + \underbrace{\int_\Omega \omega(d)\,\left(\widetilde{\boldsymbol{\sigma}}^p:\Delta\boldsymbol{\varepsilon}^p-\widetilde{\boldsymbol{\chi}}\cdot\Delta\boldsymbol{\beta}\right)\mathrm{d}\Omega}_{\textit{plastic dissipation increment } \Delta\mathcal{D}^p} + \\ & + \underbrace{\int_\Omega \phi^f\left(d_n+\Delta d,\boldsymbol{\nabla}(d_n+\Delta d)\right)\,\mathrm{d}\Omega}_{\textit{fracture energy } \mathcal{D}_f} + \underbrace{\int_\Omega \frac{\eta_f}{2\Delta t}\left(\Delta d\right)^2\,\mathrm{d}\Omega}_{\textit{viscous energy } \mathcal{D}_v} + \\ & + \underbrace{\int_\Omega \omega(d)\,\widetilde{\boldsymbol{\sigma}}:(\boldsymbol{\nabla}^s\mathbf{u}-\boldsymbol{\varepsilon})\,\mathrm{d}\Omega}_{\textit{compatibility constraint}} - \underbrace{\int_\Omega \omega(d)\,\Delta\lambda\,f_y(\widetilde{\boldsymbol{\sigma}}^p,\widetilde{\boldsymbol{\chi}})\,\mathrm{d}\Omega}_{\textit{plastic admissibility}},\end{aligned} \tag{4.5}$$

subject to

$$\Delta\lambda\geq 0,\quad \Delta d\geq 0,\quad \mathbf{u}=\mathbf{u}_D \text{ on } \partial\Omega_D\,, \tag{4.6}$$

being $\phi^f$ the phase-field dissipation density (3.21).

#### 4.2.2.2 Governing equations of the non-local problem

The weak form of the momentum balance equation, expressed in terms of nominal quantities is (3.24). The stationarity conditions with respect to the stress tensor $\widetilde{\boldsymbol{\sigma}}$, the total strain $\boldsymbol{\varepsilon}$, the set of hardening internal variables $\boldsymbol{\beta}$ and the static internal variables $\widetilde{\boldsymbol{\chi}}$, lead to the effective local state equations and elastoplastic evolution laws:

$$\widetilde{\boldsymbol{\sigma}}=\partial_{\boldsymbol{\varepsilon}}\widetilde{\psi}^e\,,\quad \widetilde{\boldsymbol{\chi}}=\partial_{\boldsymbol{\beta}}\widetilde{\psi}^p\,,\quad \Delta\boldsymbol{\varepsilon}^p=\Delta\lambda\,\partial_{\widetilde{\boldsymbol{\sigma}}}f_y\,,\quad \Delta\boldsymbol{\beta}=-\Delta\lambda\,\partial_{\widetilde{\boldsymbol{\chi}}}f_y\,, \tag{4.7}$$

while the corresponding nominal stress and static internal variable are obtained as $\boldsymbol{\sigma}=\omega\widetilde{\boldsymbol{\sigma}}$, $\boldsymbol{\chi}=\omega\widetilde{\boldsymbol{\chi}}$. The stationarity condition with respect to $\Delta\lambda$ can be written in the following equivalent form defining the local elastoplastic loading-unloading conditions:

$$\Delta\lambda\geq 0\,,\quad f_y(\widetilde{\boldsymbol{\sigma}},\widetilde{\boldsymbol{\chi}})\leq 0\,,\quad f_y(\widetilde{\boldsymbol{\sigma}},\widetilde{\boldsymbol{\chi}})\,\Delta\lambda=0\,. \tag{4.8}$$

Finally, the energy release rate $\mathcal{Y}$ and critical energy release rate $\mathcal{Y}_c$ functionals are defined:

$$\mathcal{Y}(\boldsymbol{\varepsilon},\boldsymbol{\varepsilon}^p,\boldsymbol{\beta},d)[\delta d] := -\int_\Omega \omega'(d)\,\widetilde{\psi}_{ep}(\boldsymbol{\varepsilon},\boldsymbol{\varepsilon}^p,\boldsymbol{\beta})\,\delta d\,\mathrm{d}\Omega\,, \tag{4.9a}$$

$$\mathcal{Y}_c(d)[\delta d] := \int_\Omega \left\{\left[w'(d)+\frac{\eta_f}{\Delta t}\Delta d\right]\delta d + c_d\,\boldsymbol{\nabla}d\cdot\boldsymbol{\nabla}\delta d\right\}\mathrm{d}\Omega\,, \tag{4.9b}$$

where the driving energy $\widetilde{\psi}_{ep}$ in (4.9a) is defined as

$$\widetilde{\psi}_{ep} := \widetilde{\psi}^e + \widetilde{\psi}^p + \Delta\widetilde{\phi}^p \,, \tag{4.10}$$

and being $\delta d = \Delta d^* - \Delta d$ with $\Delta d^* \geq 0$. The non-local fracture activation functional $\mathcal{F}_d$ is then defined as:

$$\mathcal{F}_d(\boldsymbol{\varepsilon}, \boldsymbol{\varepsilon}^p, \boldsymbol{\beta}, d)[\delta d] := \Big(\mathcal{Y}(\boldsymbol{\varepsilon}, \boldsymbol{\varepsilon}^p, \boldsymbol{\beta}, d) - \mathcal{Y}_c(d)\Big)[\delta d] \,, \tag{4.11}$$

and the fracture activation criterion (i.e., stationarity with respect to $d$) is written as

$$\Delta d \geq 0 \,, \quad \mathcal{F}_d(\boldsymbol{\varepsilon}, \boldsymbol{\varepsilon}^p, \boldsymbol{\beta}, d) \leq 0 \,, \quad \mathcal{F}_d(\boldsymbol{\varepsilon}, \boldsymbol{\varepsilon}^p, \boldsymbol{\beta}, d)[\Delta d] = 0 \,. \tag{4.12}$$

### 4.2.3 CONSTITUTIVE ASSUMPTIONS

For the implementation considered in this work, the general framework described so far is restricted to the *in-plane behaviour of paperboard*. The material can be considered as ductile and orthotropic. The two in-plane material directions are the machine direction (MD) and cross-direction (CD), and they will be denoted with the subscripts 1 and 2 respectively.

#### 4.2.3.1 IN-PLANE ORTHOTROPIC ELASTOPLASTICITY FOR PAPERBOARD

The class of orthotropic elastic materials that suitably describe paperboard (see e.g., Mäkelä and Östlund (2003)) have the elastic free energy:

$$\widetilde{\psi}^e(\boldsymbol{\varepsilon} - \boldsymbol{\varepsilon}^p) := \frac{1}{2}\,(\boldsymbol{\varepsilon} - \boldsymbol{\varepsilon}^p) : \widetilde{\mathbb{D}} : (\boldsymbol{\varepsilon} - \boldsymbol{\varepsilon}^p) \,, \tag{4.13}$$

where $\widetilde{\mathbb{D}} = \partial^2_{\boldsymbol{\varepsilon}\boldsymbol{\varepsilon}}\widetilde{\psi}^e$ is the effective orthotropic elastic stiffness. The yield criterion is defined as in Xia et al. (2002):

$$f_y(\widetilde{\boldsymbol{\sigma}}, \widetilde{\boldsymbol{\chi}}) = \sum_{s=1}^{6} \left( \frac{\langle \sigma_n^{(s)}(\widetilde{\boldsymbol{\sigma}}) \rangle_+}{\sigma_y^{(s)}(\widetilde{\boldsymbol{\chi}})} \right)^{2k} - 1 \,, \tag{4.14}$$

where $s$ denotes the s-th yield mechanism. The possible yield mechanisms are MD tension ($s = 1$), CD tension ($s = 2$), positive shear ($s = 3$), MD compression ($s = 4$), CD compression ($s = 5$), and negative shear ($s = 6$). For each mechanism, the normal stress $\sigma_n^{(s)}(\widetilde{\boldsymbol{\sigma}}) := \widetilde{\boldsymbol{\sigma}} : \mathbf{n}^{(s)}$ is the projection of the stress tensor along the s-th unit normal to the yield surface $\mathbf{n}^{(s)}$. The latter is a material parameter. The s-th mechanism contributes to the summation in the yield function only if $\sigma_n^{(s)} > 0$ thanks to the positive Macaulay bracket $\langle \sigma_n^{(s)} \rangle_+$. In Figure 4.1 the in-plane Xia's yield surface is depicted for the initial yield stresses in Table 4.2. The hardening mechanisms are assumed to be uncoupled and the effective yield stress reads $\sigma_y^{(s)}(\widetilde{\boldsymbol{\chi}}) = \bar{\sigma}_y^{(s)} + \widetilde{\chi}^{(s)}$, where $\bar{\sigma}_y^{(s)}$ is the initial

effective yield stress. Finally, the coefficient $k$ governs the degree of interaction between the different mechanisms. More details can be found in Appendix E. The *static* hardening variables $\widetilde{\chi}^{(s)}$ evolve according to the logarithmic law Borgqvist et al. (2014, 2015):

$$\widetilde{\chi}^{(s)}(\beta^{(s)}) = k_1^{(s)} \log\left(k_2^{(s)}\,\beta^{(s)} + 1\right) \tag{4.15}$$

where $k_1^{(s)}$ and $k_2^{(s)}$ are material parameters to be determined experimentally. The integration of the *static* hardening variables evolution law provide the hardening energy:

$$\begin{aligned}\widetilde{\psi}^{p}(\boldsymbol{\beta}) :=& \sum_{s=1}^{6} \int_0^{\beta^{(s)}} \widetilde{\chi}^{(s)}\left(\bar{\beta}\right) \mathrm{d}\bar{\beta} = \\ =& \sum_{s=1}^{6} \left\{ \frac{k_1^{(s)}}{k_2^{(s)}} \left(k_2^{(s)}\,\beta^{(s)} + 1\right) \left[\log\left(k_2^{(s)}\,\beta^{(s)} + 1\right) - 1\right] + 1 \right\}\end{aligned} \tag{4.16}$$

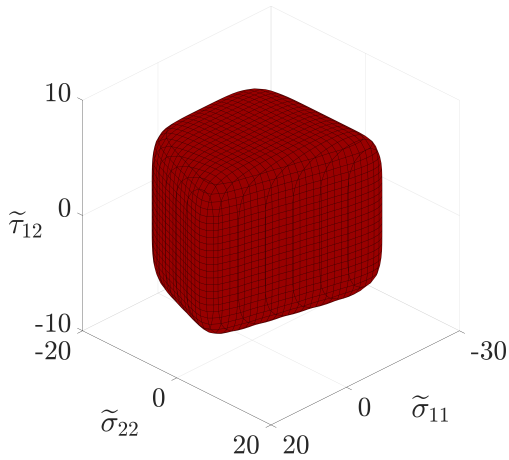


**Figure 4.1:** In-plane Xia's yield surface in the material reference frame.

#### 4.2.3.2 Brittle fracture

The phase-field functions $\omega(d)$ and $w(d)$ are define according to an AT1 approach, see Section (3.2.4). In the current model, the whole energy will be engaged in the process (i.e., no energy split is assumed), yet the activation criterion will be manipulated to avoid the promotion of crack evolution by predominantly compressive states (see Section 4.3.2).

## 4.3 Interaction between ductile-brittle dissipation mechanisms

The proposed approach to plasticity-driven phase-field fracture evolution relies on the definition of a scalar function $f(\xi)$ of a suitable scalar measure $\xi$ of

the plastic strain, hereafter referred to as *modulation function*, modulating the evolution of the critical fracture energy $G_c$, based on the evolution of the plastic process zone.

To account for these interaction phenomena, the proposed model is based on the assumption that damage, measured by the phase-field order parameter $d$, can grow only when the plastic process zone in a stress concentration region has fully developed, as measured by the plastic strain measure $\xi$. In practical terms, the competition between the plasticity and fracture dissipation mechanisms for the onset of crack and their interaction in the following crack propagation, is modulated by the introduction of a new interaction term in the expression of the critical energy release rate functional $\mathcal{Y}_c$ (4.9b):

$$\begin{aligned}\mathcal{Y}_c^p(\xi,d)[\delta d] := &\underbrace{\int_\Omega f(\xi)\, w'(d)\, \delta d \,\mathrm{d}\Omega}_{\textit{interaction term}} + \\ &+ \underbrace{\int_\Omega \left\{ \left[ w'(d) + \frac{\eta_f}{\Delta t}\,\Delta d \right] \delta d + c_d\, \boldsymbol{\nabla} d \cdot \boldsymbol{\nabla}\delta d \right\} \mathrm{d}\Omega}_{\mathcal{Y}_c(d)[\delta d]}\end{aligned} \tag{4.17}$$

The definition of the modulation function $f(\xi)$ in (4.17) is obtained based on the study of the one-dimensional homogeneous case.

### 4.3.1 Modulation function

The definition of the modulation function follows the same logical steps of Section 3.3.1. The following form of the modulation function $f(\xi)$ has been implemented:

$$f+1 = \begin{cases} f_0 + 1 & \text{if} \quad \xi = 0 \\ \dfrac{\widetilde{\mathcal{H}}}{\bar{g}} & \text{if} \quad \xi \le \xi_{cr} \\ \left(1-\bar{d}\right)\dfrac{\widetilde{\mathcal{H}}}{\bar{g}} + \left(f_{min}+1\right)\bar{d} & \text{if} \quad \xi_{cr} < \xi < \xi_{cr} + \Delta\xi_{cr} \\ f_{min}+1 & \text{if} \quad \xi \ge \xi_{cr} + \Delta\xi_{cr} \end{cases} \tag{4.18}$$

where the history function $\widetilde{\mathcal{H}}$ is defined as follows:

$$\widetilde{\mathcal{H}} := \mathcal{H} + \widetilde{\psi}^p + \Delta\widetilde{\phi}^p \tag{4.19}$$

with $f(0) = f_0$ and where $\Delta\xi_{cr}$ defines the increment of $\xi > \xi_{cr}$ beyond which $f(\xi)$ achieves its minimum constant value $f_{min}$, corresponding to the purely brittle portion of $G_c$, in the sense specified before and the *history variable* $\mathcal{H}$, inspired to the one in Miehe et al. (2010a), is defined as:

$$\mathcal{H} = \max\left(\widetilde{\psi}^e, \mathcal{H}^n\right) \tag{4.20}$$

For $\xi < \xi_{cr}$, this last condition ensures that in the case of elastic unloading, i.e., $\widetilde{\psi}^e < \widetilde{\psi}^{e\,n}$, the modulation function cannot decrease.

The fictitious phase-field history $\bar{d}(\xi)$ in (4.18) is provided analytically in the form

$$\bar{d}(\xi) = \begin{cases} 0 & \xi \le \xi_{cr} \\ \zeta^3\,(10 - 15\,\zeta + 6\,\zeta^2) & \xi_{cr} < \ \xi < \xi_{cr} + \Delta\xi_{cr} \\ 1 & \xi \ge \xi_{cr} + \Delta\xi_{cr} \end{cases} \qquad \zeta := \frac{\xi - \xi_{cr}}{\Delta\xi_{cr}} \tag{4.21}$$

### 4.3.2 Plastic strain measure

The crucial point of the formulation is to introduce a suitable measure of the plastic deformation $\xi$, accounting for the activation of the different yielding mechanisms to promote the formation of a crack. In the case of an isotropic material with single hardening mechanism and von-Mises criterion, the equivalent plastic deformation $\alpha = \int_0^t \sqrt{2/3\,\dot{\boldsymbol{\varepsilon}}^p : \dot{\boldsymbol{\varepsilon}}^p}\,\mathrm{d}\tau$ works as an internal hardening variable. Then, it is enough to define a critical equivalent plastic deformation $\alpha_{cr}$, corresponding to the onset of damage in the material $\bar{d}(\alpha > \alpha_{cr}) > 0$, and a second value $\Delta\alpha_{cr}$, accounting for the complete formation of a crack (i.e., for $\alpha \ge \alpha_{cr} + \Delta\alpha_{cr}$, $\bar{d} = 1$). The plastic strain measure in the isotropic case can be simply defined as $\xi^{iso} := \alpha/\alpha_{cr}$. Thus, the critical value is trivially $\xi^{iso}_{cr} = 1$. Therefore, the plastic strain measure $\xi^{iso}$ provides the *distance* from the critical value corresponding to the onset of damage, i.e., for $\xi^{iso} < 1$ no damage occurs, while at $\xi^{iso} = 1$ damage starts to grow. Finally, for $\xi^{iso} \ge 1 + \Delta\xi^{iso}_{cr}$ a full crack is developed $\bar{d} = 1$, where $\Delta\xi^{iso}_{cr} = \Delta\alpha_{cr}/\alpha_{cr}$. The extension to orthotropic material is performed as follows. A critical value is defined for each plastic strain component ($\varepsilon^p_1$,$\varepsilon^p_2$,$\gamma^p_{12}$) in the material reference frame defined by the orthotropy axes (i.e., for each fundamental mechanism a material parameter is introduced $\epsilon^{cr}_1$,$\epsilon^{cr}_2$,$\gamma^{cr}_{12}$). Then, inspired from the yield criterion in the stress space (4.14), a criterion for the onset of damage is introduced in the material plastic deformation space

$$\left(\frac{\langle\varepsilon^p_1\rangle_+}{\epsilon^{cr}_1}\right)^{2k_p} + \left(\frac{\langle\varepsilon^p_2\rangle_+}{\epsilon^{cr}_2}\right)^{2k_p} + \left(\frac{|\gamma^p_{12}|}{\gamma^{cr}_{12}}\right)^{2k_p} - 1 = 0\,, \tag{4.22}$$

where the material parameter $k_p$ at the exponent controls the interaction among the different modes, the Macaulay bracket $\langle\cdot\rangle_+$ is needed to avoid damage growth in compressive-dominated states, and the absolute value of the shear strain accounts for the independence of the sign. As in the isotropic case, a *scalar* plastic strain measure $\xi$, providing the *distance* of the current plastic deformation state from the critical value defined by the activation criterion (4.22), is introduced. The critical condition is still assumed to be $\xi_{cr} = 1$ and it corresponds exactly to (4.22). The activation criterion is homothetically scaled

by the factor $\xi$ as follows:

$$\left(\frac{\langle\varepsilon_1^p\rangle_+}{\xi\,\epsilon_1^{cr}}\right)^{2k_p}+\left(\frac{\langle\varepsilon_2^p\rangle_+}{\xi\,\epsilon_2^{cr}}\right)^{2k_p}+\left(\frac{|\gamma_{12}^p|}{\xi\,\gamma_{12}^{cr}}\right)^{2k_p}-1=0\,, \tag{4.23}$$

where the loci of points $\boldsymbol{\varepsilon}^p$ fulfilling this condition have constant factor $\xi$. Then, this last equation can be solved with respect to the plastic deformation measure,

$$\xi(\boldsymbol{\varepsilon}^p)=\left[\left(\frac{\langle\varepsilon_1^p\rangle_+}{\epsilon_1^{cr}}\right)^{2k_p}+\left(\frac{\langle\varepsilon_2^p\rangle_+}{\epsilon_2^{cr}}\right)^{2k_p}+\left(\frac{|\gamma_{12}^p|}{\gamma_{12}^{cr}}\right)^{2k_p}\right]^{1/2k_p}. \tag{4.24}$$

In Figure 4.2, the homothetic surfaces at constant plastic deformation measure are shown in the nominal space (i.e., where the axis are scaled with respect to the critical values). In this space, for the reference interaction parameter $k_p=1$, the activation criterion and the homothetic surfaces represent a sphere and (4.24) defines a distance. It is now clear how the condition $\xi(\boldsymbol{\varepsilon}^p)<1$

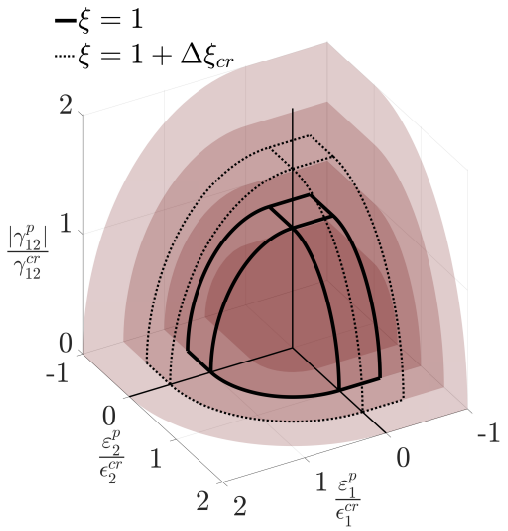


**Figure 4.2:** Loci of constant plastic strain measure $\xi$ in the space of in-plane plastic deformation components (material reference frame). The reference interaction parameter is $k_p=1$ and $\Delta\xi_{cr}=0.5$. The step between two loci is $\Delta\xi=0.5$. The solid line represents the damage onset criterion, and the dashed line the fracture onset criterion.

denotes the undamaged state, while $\xi(\boldsymbol{\varepsilon}^p)=1$ corresponds to the critical surface and consequently to the onset of damage. Finally, for $\xi(\boldsymbol{\varepsilon}^p)\geq 1+\Delta\xi_{cr}$ a complete crack is developed. A final important remark concerns the role of the Macaulay operator in the criterion (4.22). The proposed model does not include any energy split to prevent the crack propagation in compressive-dominated states. Instead, the proposed activation criterion (stated in the material reference frame) assumes that only the positive part of the normal

plastic strain components can contribute to the crack evolution, while all the shear strain contribute to trigger the damage growth, regardless the sign. In Fig. 4.2, it is evident how this is obtained with a criterion that for negative normal deformation component $\varepsilon_i^p$ (with $i = 1, 2$) assumes a constant value in the corresponding direction.

## 4.4 Numerical simulations

The model capabilities are assessed by comparison of numerical simulations and experimental results from tests carried out in the Tetra Pak laboratories (see Section 4.4.2). The simulations are performed with plane stress linear triangular elements with single integration point. The paperboard thickness is $t = 0.41\,\text{mm}$. The elastic parameters and the mechanisms interaction coefficient $k$ of the Xia's yield function (4.14) are reported in Table 4.1.

| $E_1$ | $E_2$ | $\nu_{12}$ | $G_{12}$ | $k$ |
|---|---|---|---|---|
| 5.310 | 2.203 | 0.396 | 1.370 | 3 |
| GPa | GPa | - | GPa | - |

**Table 4.1:** Elastoplastic material properties.

The in-plane yield mechanisms have been already discussed in Section 4.2.3. The mechanisms have label $s$ spanning from 1 to 6. The Xia's yield function unit normals are computed according to Appendix E. The initial yield stress $\bar{\sigma}_y$, the hardening parameters $k_1$,$k_2$ (see (4.15)), and the description of each mechanism are given in Table 4.2. Hardening is assumed to occur only in tension and shear. The same material properties are used for positive and negative shear.

| label | description | $\bar{\sigma}_y$ | $k_1$ | $k_2$ |
|---|---|---|---|---|
| 1 | tension MD | 15.00 | 12.00 | 300.00 |
| 2 | tension CD | 8.00 | 4.50 | 230.00 |
| 3 | positive shear | 5.00 | 6.00 | 150.00 |
| 4 | compression MD | 22.06 | - | - |
| 5 | compression CD | 16.70 | - | - |
| 6 | negative shear | 5.00 | 6.00 | 150.00 |
| | | GPa | - | - |

**Table 4.2:** Yielding and hardening material properties of each mechanism.

The brittle fracture material properties are the toughness $G_c = 6\,\text{N/mm}$ and the internal length scale parameter $l_{0d} = 2\,\text{mm}$ (see e.g., Niskanen et al. (2001)). The viscous coefficient is $\bar{\eta} = 10^{-2}$. The simulations are carried out in tensile conditions, where the relative orientation between the material direction CD and the load is denoted with $\theta$. The material layouts that have been tested

are tension along CD direction $\theta = 0°$; tension along MD direction $\theta = 90°$ and some intermediate directions, i.e., $\theta = 22.5°, 45°, 67.5°$. The ductile fracture material parameters are introduced for two families of materials in Table 4.3.

| Material | $\epsilon_1^{cr}$ | $\epsilon_2^{cr}$ | $\gamma_{12}^{cr}$ | $k_p$ | $\Delta\xi_{cr}$ |
|---|---|---|---|---|---|
| I | 0.200 | 0.600 | 0.600 | 1.00 | 0.5 |
| II | 0.035 | 0.087 | 0.11 | 0.75 | 0.2 |

**Table 4.3:** Ductile fracture parameters

In all simulations, the minimum value of the modulation function is $f_{min} = 0$.

### 4.4.1 SINGLE ELEMENT

A single element is used to show some of the modulation function features. In Figure 4.3 the geometry of the square shape $L = 1\,\text{mm}$, the uniaxial boundary conditions and material orientation $\theta$ are shown. A uniform step size is applied to the constrained nodes at the top, where a vertical displacement increment $\Delta\bar{u} = 0.01\,\text{mm}$ is enforced with a total number of steps $n_{step} = 100$. For this test only, the viscous coefficient is $\bar{\eta} = 0$.

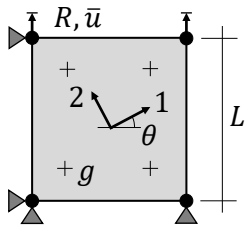


**Figure 4.3:** Single quadrilateral element geometry, boundary conditions and material orientation $\theta$.

The ductile fracture parameters are shown in Table 4.3 for Material I. The vertical engineering strain is computed as $\varepsilon = \bar{u}/L$. The reaction force $R$ is measured at the top nodes in the vertical direction. The engineering stress is then $\sigma = R/(L\,t)$. In Figure 4.4a the plot of the engineering stress versus strain is shown for the different orientations $\theta$. Here, the purely elastoplastic response, without damage, is perfectly preserved in all layouts when $\xi < 1$. Thus, the competition between the plastic and fracture dissipation mechanisms is correctly captured by the presence of the modulation function. In the subsequent figures, the modulation function $f$, the fictitious phase-field history $\bar{d}$, and the evolution of plastic deformation $\boldsymbol{\varepsilon}^p$ in the material plastic strain space are shown for all four Gauss points $g$ of the element (see Figure 4.3). In Figure 4.4b the modulation function and fictitious phase-field history are depicted versus the plastic strain measure $\xi$. The evolution of $\bar{d}$ is the same for all points

since it is defined as a function depending on the sole variable $\xi$. Conversely, the modulation function changes for different orientations and different Gauss points. Here, the importance of the definition introduced for $f$ in (4.18) can be appreciated. It is multiplicatively split into a user-defined part $(1-\bar{d})$ and a problem-dependent part $\tilde{\mathcal{H}}/\bar{g}$ that is self-adjusting according to the specific geometry, boundary conditions, and material orientation. Thus, this second contribution is responsible for the presence of different $f$ curves in Figure 4.4b, yet their peaks and minimum values occur at the same $\xi$ because of the term $(1-\bar{d})$. The fact that the MD and CD $f$ curves lie below the other orientations is justified by the presence of several plastic mechanisms that are engaged for the intermediate layouts. This increases the term $\tilde{\mathcal{H}}/\bar{g}$. A last remark can be done for the uniform condition within the element. A uniform response can be appreciated for tension along the material directions MD and CD. For the intermediate orientations the response differs at different integration points.

In Figure 4.4d, the damage activation criterion in the material plastic strain space $\left(\varepsilon_1^p, \varepsilon_2^p, \gamma_{12}^2\right)$ shown in (4.22) is depicted together with the plastic deformation evolution $\left(\langle\varepsilon_1^p\rangle_+, \langle\varepsilon_2^p\rangle_+, |\gamma_{12}^p|\right)$ for all orientations and Gauss points. Again, uniform conditions are obtained for tension in MD and CD only. The solid black line denotes the intersection of the surface $\xi = 1$, corresponding to the damage activation criterion, with the three planes $\varepsilon_1^p = 0, \varepsilon_2^p = 0, \gamma_{12}^p = 0$. The dashed line corresponds to the surface $\xi = 1 + \Delta\xi_{cr} = 1.5$ intersecting the same planes, i.e., when damage has fully developed into a crack and $\bar{d} = 1$. These two surfaces are directly related to the dashed lines present in Figure 4.4b.

### 4.4.2 EXPERIMENTAL SETUP

The experimental tests have been carried out in the Tetra Pak laboratories. A tensile testing machine with a 5 kN load cell from Instron (2530-405) has been used (see Figure 4.5). The boundary conditions enforced by the clamps constrain the displacements in all directions. The bottom constraint works as a fixed clamp, while the top one prevents all horizontal displacements and enforces a controlled vertical displacement. The specimen length $L$, to be introduced in Sections 4.4.3 and 4.4.4, measures the distance between the two constraints. The enforced deformation rate is $0.01\,s^{-1}$. The force versus displacement curves obtained from the tests on the paperboard plane strips (Section 4.4.3) are used for the calibration of the material parameters, while the results for the holed strips, obtained with the same material parameters, are employed for the assessment of the model predictive capabilities (Section 4.4.4).

In the experimental campaign, only the specimens that failed far from the clamps have been considered as reliable. This condition is rather difficult to obtain for the numerical simulations, since the material heterogeneity is not accounted for in the current model. Therefore, for the short-span plane strip specimens, where the influence of the constraints is more significant, the central elements have been weakened in terms of initial yield stresses and material

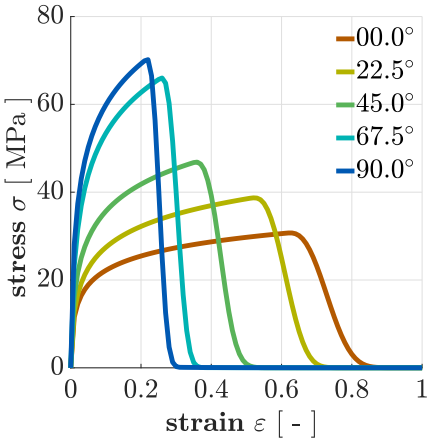


(a) Engineering stress and strain

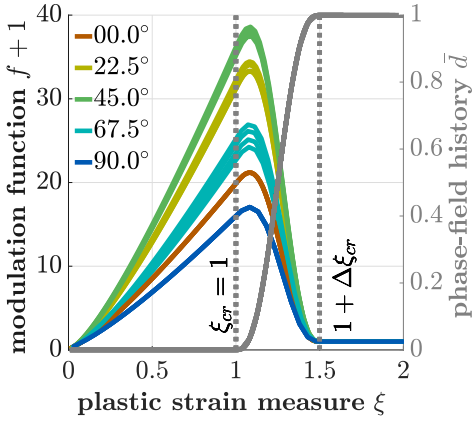


(b) Modulation function and fictitious phase-field

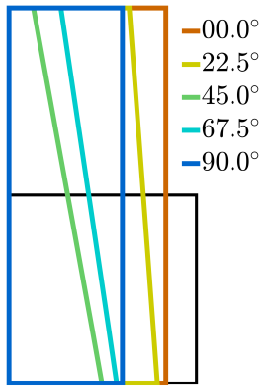


(c) Deformed shapes for the different layouts $\theta$ at the final step $u = 1\,mm$. The undeformed shape is in black.

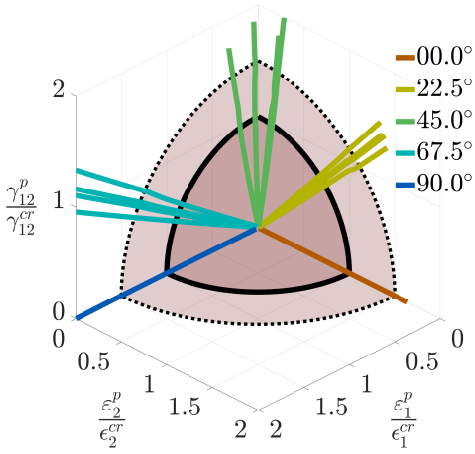


(d) Activation criterion in the plastic strain space (material frame). The solid line corresponds to $\xi = 1$, the dashed line to $\xi = 1 + \Delta\xi_{cr}$, where $\Delta\xi_{cr} = 0.5$.

**Figure 4.4:** Single quadrilateral element. The response is shown for different material orientations.

toughness. This does not affect significantly the global response in terms of reaction force, yet it drastically changes the crack pattern that otherwise would not resemble the experimental evidence.

### 4.4.3 TENSILE TEST ON PAPERBOARD STRIP

First, the model capabilities are assessed with a set of tests on plane strips. The geometry, boundary conditions, and material orientation $\theta$ are shown in Figure 4.6. The specimens have a rectangular shape, with fixed width $W = 15\,\text{mm}$

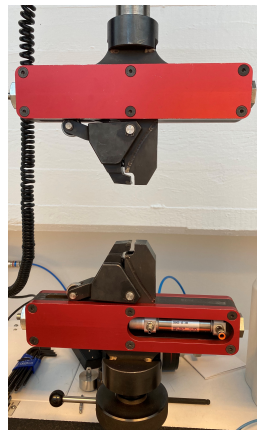

**Figure 4.5:** Tensile testing machine.

and two lengths $L = 25, 90\,\text{mm}$. The specimens with $L = 25\,\text{mm}$ are called *short-span*, while the specimens with $L = 90\,\text{mm}$ are called *long-span*. The paperboard strip is fully clamped on one of the short sides, while on the opposite side a clamp enforces a displacement $\bar{u}$ along the longitudinal direction. In the discrete time step procedure, an increment $\Delta\bar{u}$ of varying size is enforced with refinement during the damage localization.

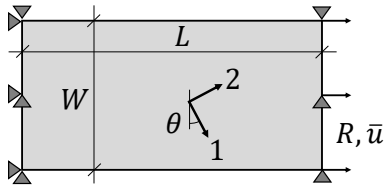


**Figure 4.6:** Tensile paperboard strip geometry, boundary conditions and material orientation $\theta$.

The material ductile properties are those in Table 4.3 for Material II. These parameters have been calibrated to match the response of the short and long-span plane strip. The minimum element size is $h_e = 0.5\,\text{mm}$ and the resolution of the phase-field internal length is $l_{0d}/h_e = 4$.

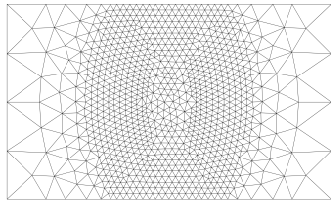

**Figure 4.7:** Tensile paperboard short-span strip mesh.

In Figure 4.7 the mesh for the short-span specimen is shown. The same mesh has been used in the localization zone of the domain also for the long-span specimen, while the element size remains longer outside this region. For both short and long tests, the initial yield stresses $\bar{\sigma}_y^{(s)}$ and the material toughness $G_c$ have been reduced in the central part of the specimens. Otherwise, a systematic failure at the clamps is observed. In Figure 4.8, the reaction force $R$ in the same direction of the enforced displacement $\bar{u}$ is shown for the different material orientations $\theta$ and for both families of specimens. The simulations (thick line) are superimposed to the experimental results (thin line). For the experimental curves only the maximum and minimum envelopes are depicted.

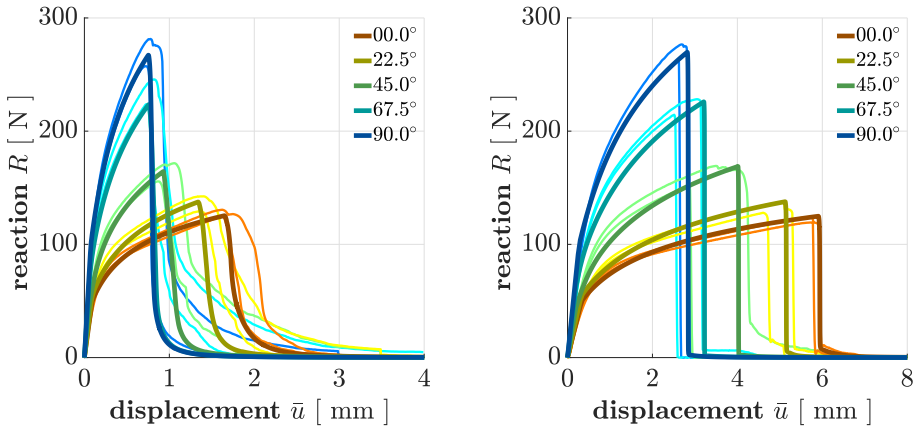


**(a)** Short-span strip **(b)** Long-span strip

**Figure 4.8:** Tensile strip. Reaction vs displacement. Experimental tests envelopes (thin line) and numerical results (thick line).

The simulations show the model capability to reproduce the orthotropic behaviour for the damage and fracture processes thanks to the anisotropic plastic strain measure $\xi$ and the activation criterion (4.22), despite the assumed isotropic damage model. Furthermore, the size-effect is well captured, reflecting in the embrittlement of the softening response. In Figure 4.9 and 4.10 the short and long-span specimens respectively are depicted at failure. Here, the phase-field contour plots, where the elements with $d \geq 0.95$ are plotted in white to render a realistic view of the crack pattern, are compared with some significant experimental tests. The results allow some comments. First, the fracture path depends on the material orientation. Yet, the exact response of the specimens is not reconstructed by the model, especially for the short-span. The reasons are of various nature: the boundary conditions and the out-of-plane constraint of the clamps can induce some structural effects that are not captured by the in-plane model; the material can be heterogeneous both in terms of mechanical properties and in terms of thickness; the heterogeneity may occur along the thickness too, and it would induce a failure mode as for the case $\theta = 67.5°$ in Figure 4.9b, where the fracture is not *extruded* through

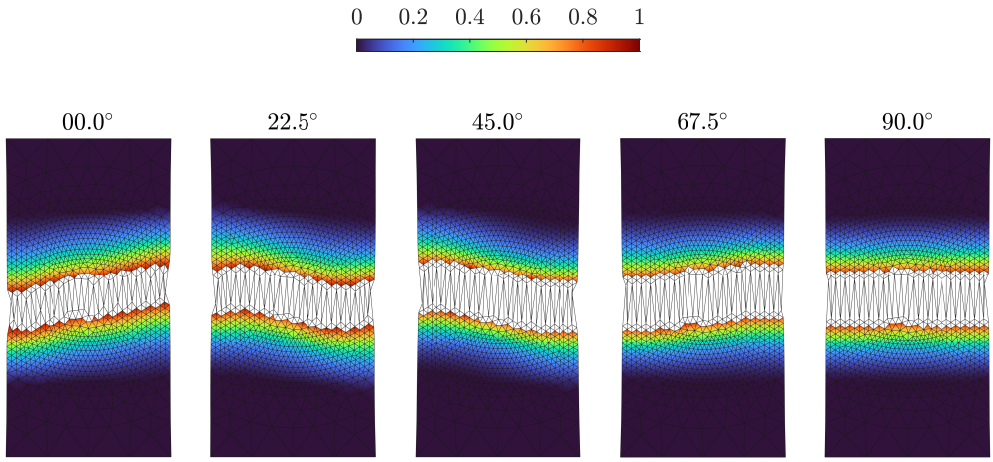


**(a)** Simulation

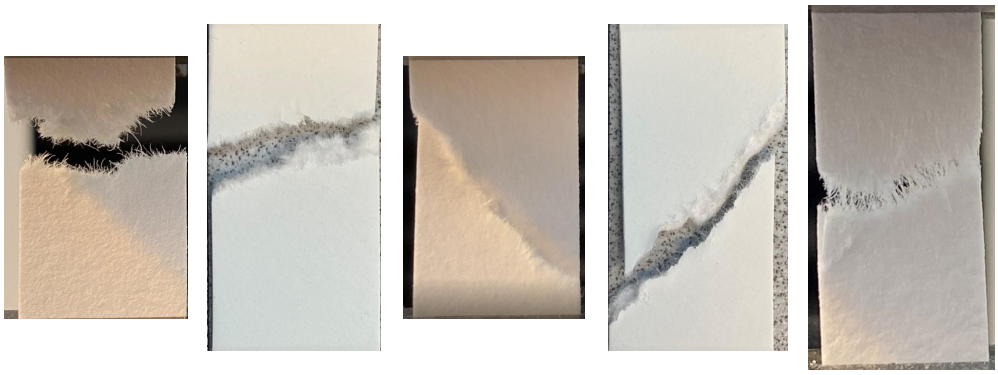

**(b)** Experimental

**Figure 4.9:** Tensile short strip. Phase-field profile and experimental specimens at failure.

the thickness, but fibers debond at different in-plane coordinates. The main conclusion is that the crack pattern can be considered as highly variable even for fixed material orientation, and this feature is not reproduced by the current approach. For the long-span specimen in Figure 4.10 the discrepancy between numerical simulations and experimental tests is less evident. In contrast, the results in terms of reaction-displacement curves are extremely accurate, for all material orientations and specimen lengths.

### 4.4.4 Tensile test on paperboard holed strip

The tensile strip tests in Section 4.4.3 have been used for the calibration of the material parameter. The subsequent step is to assess the model predictivity with a more complex boundary value problem. The holed strip geometry, boundary conditions and material orientation $\theta$ are shown in Figure 4.11. The

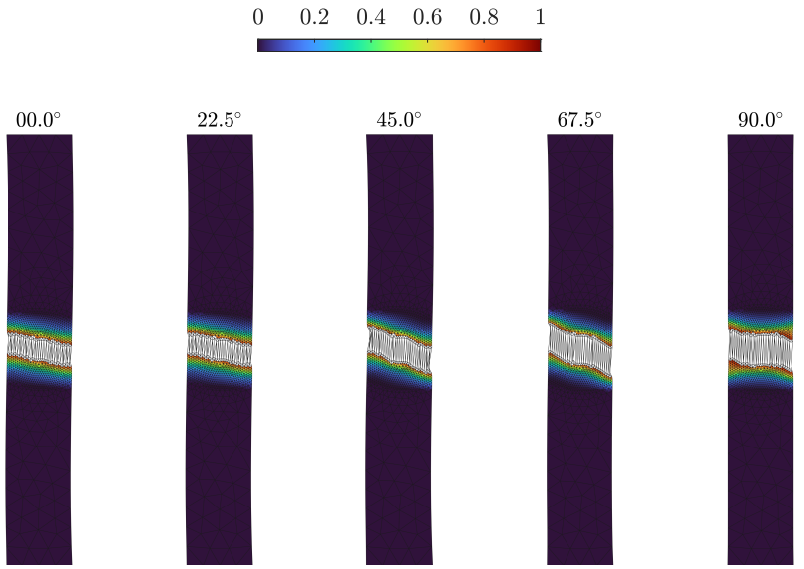


**(a)** Simulation

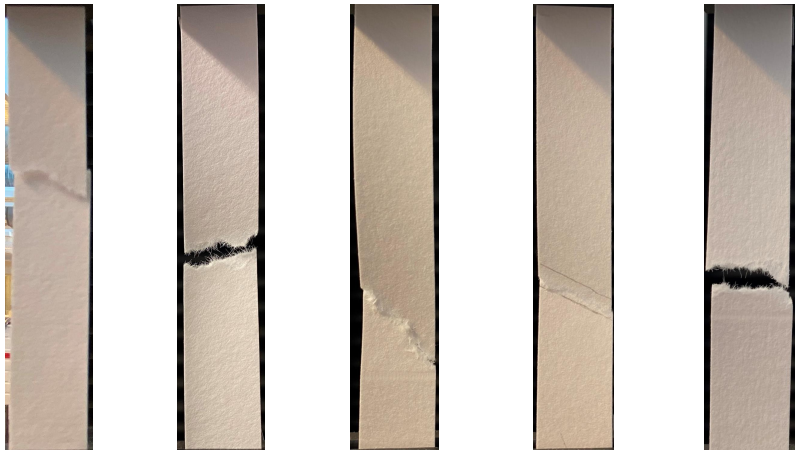

**(b)** Experimental

**Figure 4.10:** Tensile long-strip. Phase-field profile and experimental specimens at failure.

tests are restricted to the material layouts $\theta = 0°, 45°, 90°$. The specimen has a rectangular shape with fixed width $W = 15\,\text{mm}$ and two lengths $L = 25, 90\,\text{mm}$ with a central hole of diameter $\Phi = 5\,\text{mm}$ . The boundary conditions are the same of the plane strip. The material ductile properties are shown in Table 4.3 for Material II. The minimum element size is $h_e = 0.5\,\text{mm}$ and the resolution of the phase-field internal length is $l_{0d}/h_e = 4$. In Figure 4.12 the mesh for the short-span specimen is shown. The same mesh has been used in the localization zone of the domain also for the long-span specimen, while the element size

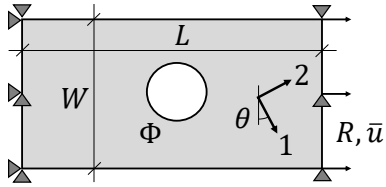


**Figure 4.11:** Tensile paperboard holed strip geometry, boundary conditions and material orientation $\theta$.

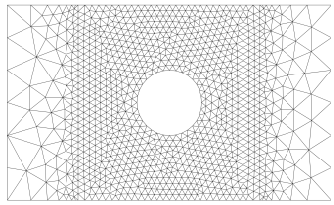

**Figure 4.12:** Tensile paperboard short-span holed strip mesh.

remains longer outside this region. In Figure 4.13 the reaction force $R$ in the same direction of the enforced displacement $\bar{u}$ is shown for the different material orientations $\theta$ and for both families of specimens. The simulations (thick line) are superimposed to the experimental results (thin line). For the experimental curves only the maximum and minimum envelopes are depicted. For the tensile

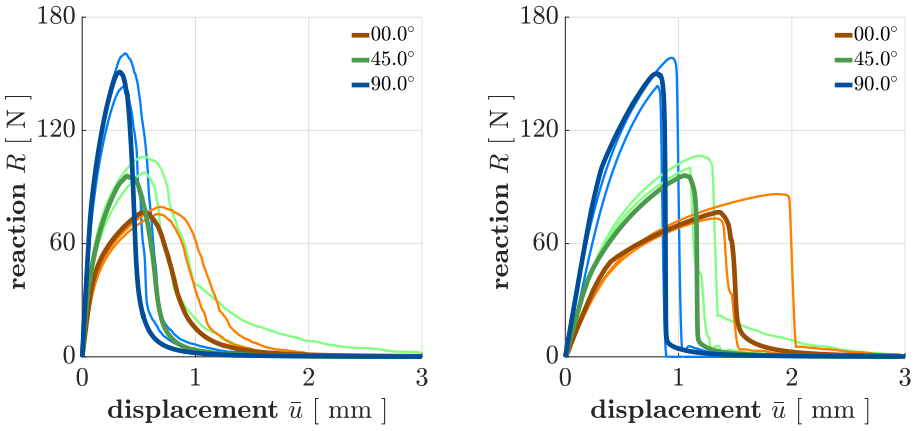


**(a)** Short-span holed strip **(b)** Long-span strip

**Figure 4.13:** Tensile holed strip. Reaction vs displacement. Experimental tests envelopes (thin line) and numerical results (thick line).

holed specimens, the comparison of numerical simulations and experimental evidences is performed in terms of crack pattern for the short-span (Figure 4.14) and the long-span (Figure 4.15). Here, the same comments of the plane strip hold. With respect to the previous cases, the holed strips present the additional

uncertainty related to the exact positioning of the hole and the presence of possible defects along the central circumferential cut. Despite these uncertainties, both the numerical fracture patterns and the reaction-displacement curves satisfactorily reproduce the physical observations for the long-span strip. In the short span case, a slight discrepancy is obtained for the 0° and the 45° orientations. Nevertheless, the attained predictivity of the current model can be deemed as satisfactory.

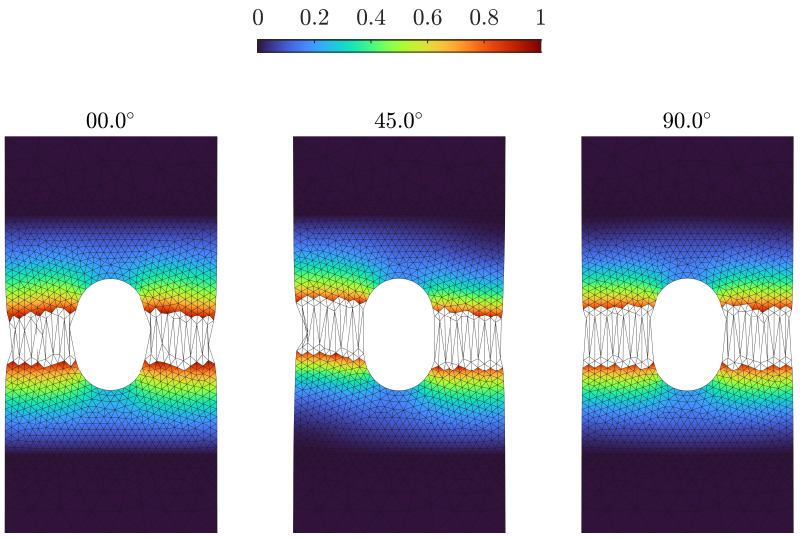


**(a)** Simulation

**(b)** Experimental

**Figure 4.14:** Tensile holed short strip. Phase-field profile and experimental specimens at failure.

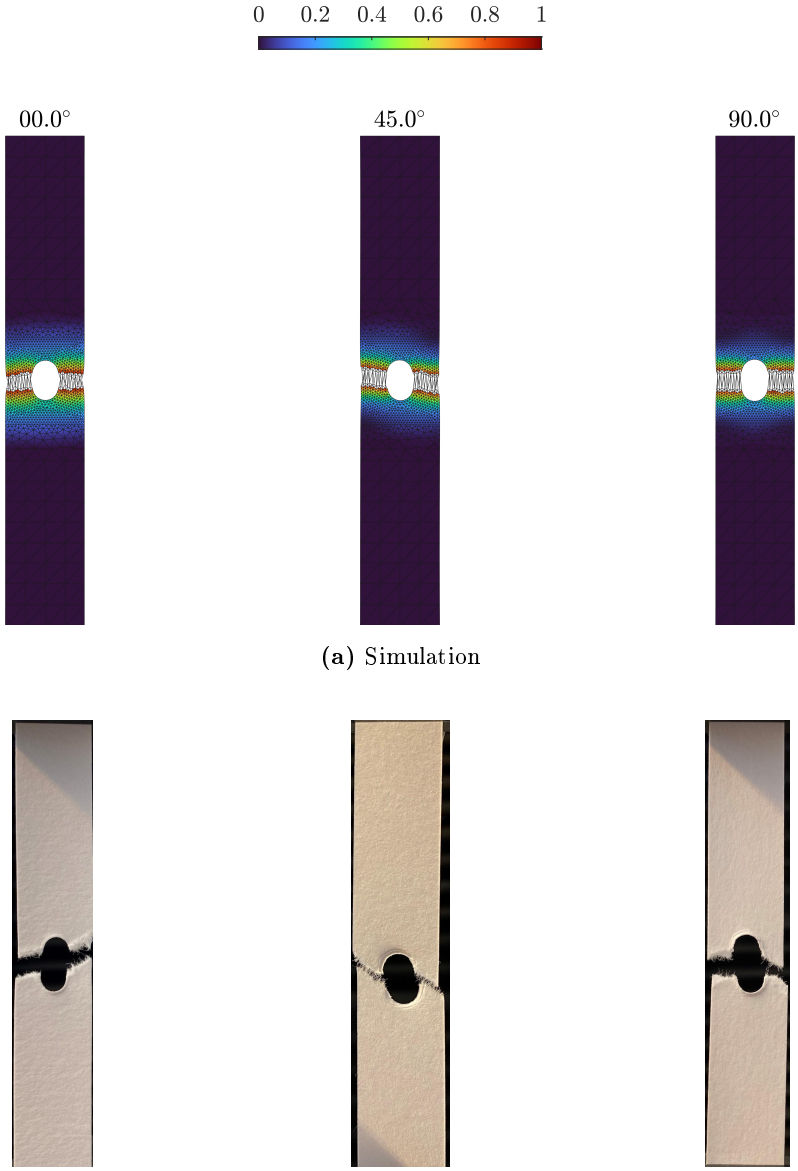


**(a)** Simulation

**(b)** Experimental

**Figure 4.15:** Tensile holed long strip. Phase-field profile and experimental specimens at failure.

# 5 Ductile Fracture in Large Deformations

## 5.1 Introduction

The out-of-plane behaviour of paperboard during the creasing and folding converting procedures involves large plastic deformations and damage. As a preliminary step for the inclusion of the out-of-plane behaviour in the paper model of Chapter 4, the effective stress approach to ductile fracture introduced in Chapter 3 for isotropic materials is extended to the large deformations framework. In the current chapter, the results are presented for local plasticity. As anticipated, mesh-dependence is obtained in the numerical simulations when large plastic strains tend to localize in a one-element-thick band. To correct this pathological behaviour, a gradient plasticity ductile fracture model has been developed in small deformations first (see Chapter 3). The implementation of the same gradient plasticity in large strains is left as a future development.

## 5.2 Phase-field variational formulation

### 5.2.1 Kinematics

#### 5.2.1.1 Effective, nominal, current & reference configurations

Let $\mathbf{F}$ be deformation gradient and $J = \det \mathbf{F}$ the volume ratio. The volume in the reference configuration is $\Omega_0$, and $\Omega$ is the volume in the current configuration. In both configurations an *effective* and *nominal* volume can be defined (see Section 3.2.1) as follows:

$$\overbrace{\underbrace{\mathrm{d}\widetilde{\Omega}}_{\texttt{effective}}}^{\texttt{current}} = \omega \overbrace{\underbrace{\mathrm{d}\Omega}_{\texttt{nominal}}}^{\texttt{current}} = \omega\, J \overbrace{\underbrace{\mathrm{d}\Omega_0}_{\texttt{nominal}}}^{\texttt{reference}} = J \overbrace{\underbrace{\mathrm{d}\widetilde{\Omega}_0}_{\texttt{effective}}}^{\texttt{reference}} \tag{5.1}$$

where the tilde $\widetilde{(\cdot)}$ stands for effective or damaged. The degradation function $\omega(d)$ accounts for the presence of the phase-field damage-like variable and it has the usual properties outlined in Section 2.3.1. Note that, while $\Omega_0$ denotes

the reference nominal volume and $\widetilde{\Omega}_0$ the effective reference volume, in what follows the effective material quantities, i.e., quantities referred to the damaged reference volume, are always denoted with a tilde $\widetilde{(\cdot)}$, while the nominal material quantities, i.e., those referred to the undamaged reference volume, have no tilde $(\cdot)$, since it must hold $(\cdot)\,\mathrm{d}\Omega_0 = \widetilde{(\cdot)}\,\mathrm{d}\widetilde{\Omega}_0$. Thus, $(\cdot) = \omega\,\widetilde{(\cdot)}$.

#### 5.2.1.2 Multiplicative decomposition of deformation gradient

The deformation gradient is assumed to be multiplicatively decomposed into elastic $\mathbf{F}^e$ and plastic $\mathbf{F}^p$ parts according to Lee (1969) as follows

$$\mathbf{F} = \mathbf{F}^e\mathbf{F}^p\,. \tag{5.2}$$

This introduces a stress-free *intermediate* configuration that is obtained by the mapping of the plastic deformation gradient $\mathbf{F}^p$. The volume ratio follows the same multiplicative split $J = J^eJ^p$. The plastic right Cauchy-Green tensor and the elastic Finger tensor are strain measures in the reference and current configurations, respectively,

$$\mathbf{C}^p = \mathbf{F}^{p\mathrm{T}}\mathbf{F}^p\,, \quad \mathbf{b}^e = \mathbf{F}^e\mathbf{F}^{e\mathrm{T}}\,. \tag{5.3}$$

The introduction of the multiplicative split into the definition of $\mathbf{b}^e$ leads to the push-forward operation between reference and current configurations:

$$\mathbf{b}^e = \mathbf{F}\mathbf{C}^{p-1}\mathbf{F}^{\mathrm{T}}\,. \tag{5.4}$$

#### 5.2.1.3 Directional derivatives

A general introduction on the directional derivatives of the kinematic quantities is presented. The generic quantity is denoted with $(\cdot)$. The time increment $d(\cdot) = \dot{\overline{(\cdot)}}\,dt$, being $\dot{\overline{(\cdot)}}$ the rate of $(\cdot)$ and $dt$ the time increment, the virtual variation $\delta(\cdot)$, and the finite-step linearization $\Delta(\cdot)$ are defined as directional derivatives of $(\cdot)$ with respect to the displacement increment $d\mathbf{u} = \dot{\mathbf{u}}dt$, the virtual displacement $\delta\mathbf{u}$, and the displacement increment in the finite-time step $\Delta\mathbf{u} = \mathbf{u}-\mathbf{u}_n$, respectively. In the latter case, a time discretization is introduced. The previous time step is denoted with $t_n$, while the current time step is $t_{n+1}$. Yet, the current quantities are represented without subscript $n+1$ for the sake of simplicity, i.e., $(\cdot) = (\cdot)_{n+1}$.

The generic directional derivative is denoted with $\mathrm{d}(\cdot)$, where the operator d can be a time increment $d$, a variation $\delta$ or a linearization $\Delta$ (see e.g., Holzapfel (2000)). Let $f_0(\mathbf{u})$ be a generic quantity in material description, and let $f(\mathbf{u}) = \Xi_f(f_0(\mathbf{u}))$ be its spatial counterpart, where $\Xi_f(\cdot)$ formally represents the push-forward operation on $f_0$ into the current configuration. The directional derivative of the material and spatial description of the quantity $f$ is defined as:

$$\mathrm{d}f_0 := \frac{\partial f_0}{\partial\epsilon}\big(\mathbf{u}+\epsilon\,\mathrm{d}\mathbf{u}\big)\Big|_{\epsilon=0}\,, \qquad \mathrm{d}f := \Xi_f\big(\mathrm{d}f_0\big)\,. \tag{5.5}$$

The spatial directional derivative along the displacement increment $\dot{\mathbf{u}}dt$ is called Lie derivative $\mathcal{L}_v f = \Xi_f(\dot{f}_0)$. The directional derivative of the displacement gradient in material $\mathrm{d}\boldsymbol{\nabla}_0\mathbf{u}$ and in spatial description $\mathrm{d}\boldsymbol{\nabla}\mathbf{u}$ simply reads:

$$\mathrm{d}\mathbf{F} = \boldsymbol{\nabla}_0 \mathrm{d}\mathbf{u}\,, \qquad \mathrm{d}\mathbf{l} = \boldsymbol{\nabla}\mathrm{d}\mathbf{u} = \mathrm{d}\mathbf{F}\mathbf{F}^{-1}\,. \tag{5.6}$$

In the first relation, the identity $\mathbf{F} = \mathbf{I} + \boldsymbol{\nabla}_0\mathbf{u}$ has been used. Therefore, the directional derivatives of the deformation gradient and the material displacement gradient along $\mathrm{d}\mathbf{u}$ coincide. Thus, the increment $d\mathbf{F} = \dot{\mathbf{F}}dt$ (being $\dot{\mathbf{F}}$ the deformation gradient rate), the virtual variation $\delta\mathbf{F}$, the time linearization $\Delta\mathbf{F}$ of the deformation gradient are directional derivatives of the material gradient $\boldsymbol{\nabla}_0(\cdot)$ along the displacement increment $\dot{\mathbf{u}}dt$, the variation $\delta\mathbf{u}$, and the finite-increment $\Delta\mathbf{u}$, respectively. The second relation $(5.6)_2$ states that the directional derivative of the spatial displacement gradient, defined as $\mathrm{d}\mathbf{l}$, coincide with the push-forward of the directional derivative of the deformation gradient along $\mathrm{d}\mathbf{u}$. Thus, the rate $\mathbf{l}$ is the spatial velocity gradient, its virtual variation is $\delta\mathbf{l}$, and the linearization $\mathbf{L}$ are the directional derivatives of the spatial gradient $\boldsymbol{\nabla}(\cdot)$ along the displacement increment $\dot{\mathbf{u}}dt$, the variation $\delta\mathbf{u}$, and the linearization $\Delta\mathbf{u}$, respectively. The symmetric $\mathrm{sym}\,(\cdot) = 1/2[(\cdot) + (\cdot)^{\mathrm{T}}]$ and skew symmetric $\mathrm{skw}\,(\cdot) = 1/2[(\cdot) - (\cdot)^{\mathrm{T}}]$ operators allow to introduce:

$$\mathrm{d}\mathbf{d} = \mathrm{sym}\,(\mathrm{d}\mathbf{l})\,, \qquad \mathrm{d}\mathbf{w} = \mathrm{skw}\,(\mathrm{d}\mathbf{l})\,. \tag{5.7}$$

For $\mathrm{d}\mathbf{u} = \dot{\mathbf{u}}dt$, they represent the rate of deformation $\mathbf{d} = \mathrm{sym}\,\mathbf{l}$ and the spin tensor $\mathbf{w} = \mathrm{skw}\,\mathbf{l}$. For $\mathrm{d}\mathbf{u} = \delta\mathbf{u}$, they represent the virtual rate of deformation $\delta\mathbf{d} = \mathrm{sym}\,\delta\mathbf{l}$ and the virtual spin tensor $\delta\mathbf{w} = \mathrm{skw}\,\delta\mathbf{l}$. Finally, when $\mathrm{d}\mathbf{u} = \Delta\mathbf{u}$, they are the linearized rate of deformation $\mathbf{D} = \mathrm{sym}\,\mathbf{L}$ and spin tensor $\mathbf{W} = \mathrm{skw}\,\mathbf{L}$.

The differentiation of the multiplicative decomposition (5.2) reads:

$$\mathrm{d}\mathbf{F} = \mathrm{d}\mathbf{F}^e\mathbf{F}^p + \mathbf{F}^e\mathrm{d}\mathbf{F}^p\,. \tag{5.8}$$

The combination of (5.8), (5.6), and (5.2) leads to the directional derivatives:

$$\mathrm{d}\mathbf{l} = (\mathrm{d}\mathbf{F}^e\mathbf{F}^{e-1}) + (\mathbf{F}^e\,\mathrm{d}\mathbf{l}^p_i\,\mathbf{F}^{e-1}) = \mathrm{d}\mathbf{l}^e + \mathrm{d}\mathbf{l}^p\,, \tag{5.9}$$

where $\mathrm{d}\mathbf{l}^e$ is the spatial directional derivative of elastic deformation gradient, $\mathrm{d}\mathbf{l}^p_i = \mathrm{d}\mathbf{F}^p\mathbf{F}^{p-1}$ is the derivative of plastic deformation gradient in the *intermediate* configuration, while $\mathrm{d}\mathbf{l}^p$ is the spatial derivative of the plastic deformation gradient. The operation $\mathrm{d}\mathbf{l}^p = \mathbf{F}^e\,\mathrm{d}\mathbf{l}^p_i\,\mathbf{F}^{e-1}$ pushes forward the tensor $\mathrm{d}\mathbf{l}^p_i$ from the intermediate to the current configuration. It follows:

$$\mathrm{d}\mathbf{d} = \mathrm{sym}\,\mathrm{d}\mathbf{l} = \mathrm{sym}\,\mathrm{d}\mathbf{l}^e + \mathrm{sym}\,\mathrm{d}\mathbf{l}^p = \mathrm{d}\mathbf{d}^e + \mathrm{d}\mathbf{d}^p\,. \tag{5.10}$$

Finally, the differentiation of the elastic Finger tensor follows from the push-forward operation (5.4) and it reads:

$$\mathrm{d}\mathbf{b}^e = \mathrm{d}\big(\mathbf{b}^e\big)|_{\mathbf{F}^p} + \mathrm{d}\big(\mathbf{b}^e\big)|_{\mathbf{F}} = \underbrace{\mathrm{d}\mathbf{l}\,\mathbf{b}^e + \mathbf{b}^e\,\mathrm{d}\mathbf{l}^{\mathrm{T}}}_{\texttt{total}} + \underbrace{\mathbf{F}\,\mathrm{d}\mathbf{C}^{p-1}\mathbf{F}^{\mathrm{T}}}_{\texttt{plastic}}\,, \tag{5.11}$$

where the symbol $\mathrm{d}[\cdot]|_{(\cdot)}$ denotes that the directional derivative of $[\cdot]$ is performed for fixed $(\cdot)$. The last parcel of the sum can be further developed as

$$\begin{aligned}
&\mathbf{F}\,\mathrm{d}\mathbf{C}^{p-1}\mathbf{F}^{\mathrm{T}} = \mathbf{F}\,\mathrm{d}(\mathbf{F}^{p-1}\mathbf{F}^{p-\mathrm{T}})\mathbf{F}^{\mathrm{T}} = -\mathbf{F}\,\mathbf{F}^{p-1}\mathrm{d}\mathbf{F}^{p}\mathbf{F}^{p-1}\mathbf{F}^{p-\mathrm{T}}\mathbf{F}^{\mathrm{T}} - \\
&- \mathbf{F}\,\mathbf{F}^{p-1}\mathbf{F}^{p-\mathrm{T}}\mathrm{d}\mathbf{F}^{p\mathrm{T}}\mathbf{F}^{p-\mathrm{T}}\mathbf{F}^{\mathrm{T}} = -\mathbf{F}^{e}(\mathrm{d}\mathbf{l}_i^{p} + \mathrm{d}\mathbf{l}_i^{p\mathrm{T}})\mathbf{F}^{e\mathrm{T}} = \\
&= -(\mathbf{F}^{e}\mathrm{d}\mathbf{l}_i^{p}\mathbf{F}^{e-1})\mathbf{F}^{e}\mathbf{F}^{e\mathrm{T}} - \mathbf{F}^{e}\mathbf{F}^{e\mathrm{T}}(\mathbf{F}^{e-\mathrm{T}}\mathrm{d}\mathbf{l}_i^{p\mathrm{T}}\mathbf{F}^{e\mathrm{T}}) = -(\mathrm{d}\mathbf{l}^{p}\mathbf{b}^{e} + \mathbf{b}^{e}\mathrm{d}\mathbf{l}^{p\mathrm{T}})\,.
\end{aligned}$$

Thus, the elastic Finger tensor differentiation at fixed deformation gradient reads:

$$\mathrm{d}\big(\mathbf{b}^{e}\big)|_{\mathbf{F}} := \mathbf{F}\,\mathrm{d}\mathbf{C}^{p-1}\mathbf{F}^{\mathrm{T}} = -2\,\mathrm{sym}\,\big(\mathrm{d}\mathbf{l}^{p}\,\mathbf{b}^{e}\big)\,. \tag{5.12}$$

When $\mathrm{d}\mathbf{u} = \dot{\mathbf{u}}dt$, the last quantity represents the Lie derivative of the elastic Finger tensor $\mathcal{L}_v\,\mathbf{b}^{e} = -2\,\mathrm{sym}\,\mathbf{l}^{p}\mathbf{b}^{e}$. Thus, the general format of the directional derivative of the elastic Finger tensor reads:

$$\mathrm{d}\mathbf{b}^{e} = \mathrm{d}\big(\mathbf{b}^{e}\big)|_{\mathbf{F}^{p}} + \mathrm{d}\big(\mathbf{b}^{e}\big)|_{\mathbf{F}} = \underbrace{2\,\mathrm{sym}\,(\mathrm{d}\mathbf{l}\mathbf{b}^{e})}_{\texttt{total}} - \underbrace{2\,\mathrm{sym}\,(\mathrm{d}\mathbf{l}^{p}\mathbf{b}^{e})}_{\texttt{plastic}} = 2\,\mathrm{sym}\,(\mathrm{d}\mathbf{l}^{e}\mathbf{b}^{e})\,. \tag{5.13}$$

### 5.2.2 State variables & evolution laws

The formulation is restricted to the framework of isotropic materials. The thermodynamic state is assumed to be completely defined by the elastic deformation gradient $\mathbf{F}^{e}$, the plastic deformation gradient $\mathbf{F}^{p}$, the hardening internal variable $\alpha$, and the damage-like phase field $d$. They can be cast in

$$\mathcal{S}_v = \big(\,\mathbf{F}^{e}, \mathbf{F}^{p}, \alpha, d\,\big)\,, \tag{5.14}$$

where the elastic and plastic deformation gradients are related as in (5.2). In the current section, all energy and energy rate densities are referred to the reference configuration. The free energy $\psi(\mathbf{F}^{e}, \alpha, d)$ per unit nominal reference volume $\mathrm{d}\Omega_0$ is assumed to be additively decomposed into its elastic (reversible) part $\omega(d)\,\widetilde{\psi}^{e}(\mathbf{F}^{e})$, and hardening (unrecoverable) part $\omega(d)\,\widetilde{\psi}^{p}(\alpha)$, the latter being the internal elastic energy stored in the material because of irreversible deformations of the micro-structure. The energies $\widetilde{\psi}^{e}(\mathbf{F}^{e})$ and $\widetilde{\psi}^{p}(\alpha)$ are the undamaged or *effective* elastic and hardening free energies. The *nominal* $\psi$ and *effective* $\widetilde{\psi}$ reference free energy densities (i.e., per unit initial volume) are:

$$\psi = \omega\,\widetilde{\psi}\,, \quad \widetilde{\psi} := \widetilde{\psi}^{e} + \widetilde{\psi}^{p}\,. \tag{5.15}$$

The Clausius-Duhem inequality states that the dissipation rate density $\dot{\phi}$ in the reference configuration must increase in every transformation, i.e.,

$$\dot{\phi} = \dot{w} - \dot{\psi} \geq 0\,, \tag{5.16}$$

where $\dot{w}$ is the internal mechanical work or stress power, and $\dot{\psi}$ is the free energy rate. The additional constraint to the thermodynamic evolution is the fulfillment of the yield criterion for the static work-conjugated variables:

$$f_y \leq 0 \tag{5.17}$$

being $f_y$ the yield function. In the large deformation framework, the functions $\widetilde{\psi}^e$, $\dot{w}$, and $f_y$ have a different representation whether in material or spatial representation. In the following, the definitions of the static internal variable $\widetilde{\chi}$, work conjugated with the kinematic internal variable rate $\dot{\alpha}$, and the energy release rate $Y$, work-conjugated with the damage variable rate $\dot{d}$,

$$\widetilde{\chi} := \frac{\partial \widetilde{\psi}^p}{\partial \alpha}\,, \quad Y = -\omega' \, \widetilde{\psi} \tag{5.18}$$

will be systematically used.

#### 5.2.2.1 Material description of elastoplastic evolution

The material description of the stress power and elastic free energy density are

$$\dot{w} = \mathbf{P} : \dot{\mathbf{F}}\,, \quad \widetilde{\psi}^e(\mathbf{F}^e)\,, \tag{5.19}$$

where $\mathbf{P}$ is the first Piola-Kirchhoff stress tensor. The introduction of the directional derivative (5.8) in rate form $\dot{\mathbf{F}} = \dot{\mathbf{F}}^e\mathbf{F}^p + \mathbf{F}^e\dot{\mathbf{F}}^p$, and the rate of the free energy

$$\dot{\psi} = \omega \, \partial_{\mathbf{F}^e} \widetilde{\psi}^e : \dot{\mathbf{F}}^e + \omega \, \widetilde{\chi} \, \dot{\alpha} - Y \, \dot{d} \quad , \tag{5.20}$$

into the dissipation inequality reads:

$$\dot{\phi} = \underbrace{\left( \mathbf{P}\mathbf{F}^{p\mathrm{T}} - \omega \, \frac{\partial \widetilde{\psi}^e}{\partial \mathbf{F}^e} \right) : \dot{\mathbf{F}}^e}_{elastic} + \underbrace{\mathbf{F}^{e\mathrm{T}}\mathbf{P} : \dot{\mathbf{F}}^p - \omega \, \widetilde{\chi} \, \dot{\alpha}}_{plastic} + \underbrace{Y \, \dot{d}}_{fracture} \geq 0\,. \tag{5.21}$$

During an elastic or reversible transformation, no evolution of the plastic deformations $\dot{\mathbf{F}}^p = \mathbf{0}$, of the hardening variable $\dot{\alpha} = 0$ or of damage $\dot{d} = 0$ occurs and, hence, no dissipation increase is produced (i.e., $\dot{\phi} = 0$). Therefore, the only term left is $(\mathbf{P}\mathbf{F}^{p\mathrm{T}} - \omega \, \partial_{\mathbf{F}^e} \widetilde{\psi}^e) : \dot{\mathbf{F}}^e = 0$. Since it must hold for all reversible transformations $\dot{\mathbf{F}}^e$, the nominal and effective elastic state equations read:

$$\mathbf{P} = \omega \, \widetilde{\mathbf{P}}\,, \qquad \widetilde{\mathbf{P}} := \frac{\partial \widetilde{\psi}^e}{\partial \mathbf{F}^e} \mathbf{F}^{p-\mathrm{T}}\,. \tag{5.22}$$

The consideration of the dissipation inequality in the conditions of no damage, $\dot{d} = 0$, allows to define the nominal and effective plastic dissipation rate density

$$\dot{\phi}^p = \omega \, \dot{\widetilde{\phi}}^p\,, \qquad \dot{\widetilde{\phi}}^p := \widetilde{\mathbf{P}}^p : \dot{\mathbf{F}}^p - \widetilde{\chi} \, \dot{\alpha} \geq 0\,. \tag{5.23}$$

with the plastic first Piola-Kirchhoff stress tensor, i.e., the stress measure responsible for plastic dissipation being

$$\widetilde{\mathbf{P}}^p := \mathbf{F}^{e\mathrm{T}}\widetilde{\mathbf{P}}\,. \tag{5.24}$$

The effective dissipation inequality $(5.23)_2$ follows $\dot{\widetilde{\phi}}^p \mathrm{d}\widetilde{\Omega}_0 = \dot{\phi}^p \mathrm{d}\Omega_0 \geq 0$. The effective yield stress associated to the internal variable $\alpha$ is $\widetilde{\sigma}_y(\alpha) = \bar{\sigma}_{y0} + \widetilde{\chi}(\alpha)$, where $\bar{\sigma}_{y0}$ is the initial yield stress. The elastoplastic evolution has to satisfy the additional constraint that the admissible set of effective stress and hardening parameter $(\widetilde{\mathbf{P}}^{p*}, \widetilde{\chi}^*)$ have to fulfill the yield criterion $f_y(\widetilde{\mathbf{P}}^{p*}, \widetilde{\chi}^*) \leq 0$, where $f_y$ is the local yield function in material description, convex in the space of stress and static internal variable. The yield criterion is postulated in terms of effective quantities, since only the continuous, non-damaged part of the volume is undergoing plastic deformations. The stationarity conditions associated to the (effective) principle of maximum dissipation provide the *effective elastoplastic evolution laws*:

$$\dot{\mathbf{F}}^p = \dot{\lambda}\,\frac{\partial f_y}{\partial \widetilde{\mathbf{P}}^p}\,, \quad \dot{\alpha} = -\dot{\lambda}\,\frac{\partial f_y}{\partial \widetilde{\chi}}\,, \quad \dot{\lambda} \geq 0\,, \quad f_y \leq 0\,, \quad \dot{\lambda}\, f_y = 0\,, \tag{5.25}$$

where $\dot{\lambda}$ is the non-negative rate of a scalar plastic multiplier. A fundamental remark lies in the flow rule $(5.25)_1$. The latter holds under the assumption of isotropic material only. For anisotropic material, the concept of isoclinic intermediate configuration shall be introduced, see e.g., Dean et al. (2016).

#### 5.2.2.2 Spatial description of elastoplastic evolution

The spatial description of the stress power per unit reference volume, and the isotropic elastic free energy density are

$$\dot{w} = \boldsymbol{\tau} : \mathbf{d}\,, \quad \widetilde{\psi}^e(\mathbf{b}^e)\,. \tag{5.26}$$

where $\boldsymbol{\tau}$ is the Kirchhoff stress tensor, $\mathbf{d} = \operatorname{sym}\mathbf{l}$ is the rate of deformation (being $\mathbf{l} = \dot{\mathbf{F}}\mathbf{F}^{-1}$ the spatial velocity gradient according to the directional derivative (5.6)), and $\mathbf{b}^e = \mathbf{F}^e\mathbf{F}^{e\mathrm{T}}$ the elastic Finger tensor according to $(5.3)_2$. The introduction of the directional derivative (5.10) in rate form $\mathbf{d} = \mathbf{d}^e + \mathbf{d}^p$, and the linearization of the free energy

$$\dot{\psi} = \partial_{\mathbf{b}^e}\widetilde{\psi}^e : \dot{\mathbf{b}}^e + \widetilde{\chi}\,\dot{\alpha} - Y\,\dot{d}\,, \tag{5.27}$$

where the first elastic term can be further developed using (5.13) in rate form

$$\partial_{\mathbf{b}^e}\widetilde{\psi}^e : \dot{\mathbf{b}}^e = \partial_{\mathbf{b}^e}\widetilde{\psi}^e : (2\operatorname{sym}\mathbf{l}^e\mathbf{b}^e) = (2\,\partial_{\mathbf{b}^e}\widetilde{\psi}^e\,\mathbf{b}^e) : \mathbf{d}^e\,, \tag{5.28}$$

lead to the following dissipation inequality in spatial description

$$\dot{\phi} = \underbrace{\left(\boldsymbol{\tau} - \omega\, 2\,\partial_{\mathbf{b}^e}\widetilde{\psi}^e\,\mathbf{b}^e\right) : \mathbf{d}^e}_{elastic} + \underbrace{\boldsymbol{\tau} : \mathbf{d}^p - \omega\,\widetilde{\chi}\,\dot{\alpha}}_{plastic} + \underbrace{Y\,\dot{d}}_{fracture} \geq 0\,. \tag{5.29}$$

During an elastic or reversible transformation, no evolution of the plastic deformations $\mathbf{d}^p = \mathbf{0}$, of the hardening variable $\dot{\alpha} = 0$ or of damage $\dot{d} = 0$ occurs and, hence, no dissipation increase is produced (i.e., $\dot{\phi} = 0$). Therefore, the only term left is $(\boldsymbol{\tau} - \omega\, 2\, \partial_{\mathbf{b}^e} \widetilde{\psi}^e\, \mathbf{b}^e) : \mathbf{d}^e = 0$. Since it must hold for all reversible transformations $\mathbf{d}^e$, the nominal and effective elastic state equations read:

$$\boldsymbol{\tau} = \omega\, \widetilde{\boldsymbol{\tau}}\,, \qquad \widetilde{\boldsymbol{\tau}} := 2\, \frac{\partial \widetilde{\psi}^e}{\partial \mathbf{b}^e}\, \mathbf{b}^e\,. \tag{5.30}$$

The consideration of the dissipation inequality in the conditions of no damage, $\dot{d} = 0$, allows to define the nominal and effective plastic dissipation rate density in spatial description:

$$\dot{\phi}^p = \omega\, \dot{\widetilde{\phi}}^p\,, \qquad \dot{\widetilde{\phi}}^p := \widetilde{\boldsymbol{\tau}}^p : \mathbf{d}^p - \widetilde{\chi}\, \dot{\alpha} \geq 0\,. \tag{5.31}$$

with the plastic Kirchhoff stress tensor, i.e., the stress measure responsible for plastic dissipation being trivially

$$\widetilde{\boldsymbol{\tau}}^p = \widetilde{\boldsymbol{\tau}}\,. \tag{5.32}$$

The spatial plastic power density per unit reference volume can be further manipulated using the relation $\mathcal{L}_v\, \mathbf{b}^e = -2\, \mathrm{sym}\, \mathbf{l}^p \mathbf{b}^e$ from (5.12) and the spatial elastic state equation (5.30), see e.g., Simo and Miehe (1992):

$$\widetilde{\boldsymbol{\tau}} : \mathbf{d}^p = 2\, \partial_{\mathbf{b}^e} \widetilde{\psi}^e\, \mathbf{b}^e : \mathbf{l}^p = 2\, \partial_{\mathbf{b}^e} \widetilde{\psi}^e : (-1/2 \mathcal{L}_v\, \mathbf{b}^e) = \widetilde{\boldsymbol{\tau}} : (-1/2 \mathcal{L}_v\, \mathbf{b}^e\, \mathbf{b}^{e-1}) \tag{5.33}$$

Likewise its material description, the effective elastoplastic dissipation inequality $(5.31)_2$ follows $\dot{\widetilde{\phi}}^p \mathrm{d}\widetilde{\Omega}_0 = \dot{\phi}^p \mathrm{d}\Omega_0 \geq 0$. The effective yield stress associated to the internal variable $\alpha$ is $\widetilde{\sigma}_y(\alpha) = \bar{\sigma}_{y0} + \widetilde{\chi}(\alpha)$, where $\bar{\sigma}_{y0}$ is the initial yield stress. The admissible set of effective stress and hardening parameter $(\widetilde{\boldsymbol{\tau}}^{p*}, \widetilde{\chi}^*)$ have to fulfill the yield criterion $f_y(\widetilde{\boldsymbol{\tau}}^{p*}, \widetilde{\chi}^*) \leq 0$, being $f_y$ is the local yield function in spatial description, convex in the space of stress and static internal variable. The yield criterion is postulated in terms of effective quantities, since only the continuous, non-damaged part of the volume is undergoing plastic deformations. The stationarity conditions associated to the (effective) principle of maximum dissipation provide the *effective elastoplastic evolution laws*:

$$\mathbf{d}^p = \dot{\lambda}\, \frac{\partial f_y}{\partial \widetilde{\boldsymbol{\tau}}^p}\,, \quad \dot{\alpha} = -\dot{\lambda}\, \frac{\partial f_y}{\partial \widetilde{\chi}}\,, \quad \dot{\lambda} \geq 0\,, \quad f_y \leq 0\,, \quad \dot{\lambda}\, f_y = 0\,, \tag{5.34}$$

where $\dot{\lambda}$ is the non-negative rate of a scalar plastic multiplier. The use of (5.33) leads to the alternative flow rule (see e.g., Simo and Miehe (1992)):

$$\mathcal{L}_v\, \mathbf{b}^e = -2\, \dot{\lambda}\, \frac{\partial f_y}{\partial \widetilde{\boldsymbol{\tau}}^p}\, \mathbf{b}^e\,. \tag{5.35}$$

A constitutive hypothesis is introduced on the plastic flow evolution in spatial description. The plastic evolution $(5.34)_1$ provides information on the symmetric part of the plastic velocity gradient $\mathbf{d}^p = \mathrm{sym}\, \mathbf{l}^p$, i.e., the plastic rate of

deformation, while no information arises for the plastic spin $\mathbf{w}^p = \operatorname{skw} \mathbf{l}^p$. The assumption for *isotropic materials* is

$$\mathbf{w}^p = \mathbf{0}\,. \tag{5.36}$$

This assumption of zero plastic spin is compatible with plastic isotropy (see e.g., de Souza Neto et al. (2008)), the condition to which the present formulation is restricted. Plastic anisotropy requires the definition of an appropriate constitutive equation for the plastic spin (see e.g., Dafalias (1984, 1985)).

The plastic rate of deformation can be then defined according to $(5.9)_2$ and cast into the convenient form:

$$\mathbf{d}^p = \mathbf{F}^e \dot{\mathbf{F}}^p \mathbf{F}^{-1}\,. \tag{5.37}$$

#### 5.2.2.3 FRACTURE EVOLUTION

Finally, the ductile-fracture specific dissipation rate reads:

$$\dot{\phi}^{pf} := \omega\, \dot{\widetilde{\phi}}^p + \dot{\phi}^f\,, \quad \dot{\phi}^f := Y\, \dot{d}\,, \tag{5.38}$$

where $\dot{\phi}^f$ is the brittle fracture specific dissipation rate and $Y$ is the fracture driving force. $\dot{\phi}^{pf}$ is the dissipation rate per unit nominal reference volume and, therefore, the elementary dissipation rate is $\dot{\phi}^{pf}\, \mathrm{d}\Omega_0$.

#### 5.2.2.4 CHANGE OF DESCRIPTION

In the previous Sections 5.2.2.1, 5.2.2.2, 5.2.2.3, an abuse of notation has been introduced for the stress power $\dot{w}$, the effective elastic free energy $\widetilde{\psi}^e$, and the yield function $f_y$, i.e., the same symbols have been used for the material and spatial descriptions. The subscript or superscript $(m)$ and $(s)$ will be used to denote the material and spatial description of the scalar-valued functions. The stress power density, referred to the undeformed volume, simply transforms following the relation $(5.6)_2$ as

$$\dot{w}_{(m)} := \mathbf{P} : \dot{\mathbf{F}} = \mathbf{P} : (\mathbf{l}\mathbf{F}) = (\mathbf{P}\mathbf{F}^{\mathrm{T}}) : \mathbf{l} = \boldsymbol{\tau} : \mathbf{d} =: \dot{w}_{(s)}\,.$$

Therefore, the stress transformation is

$$\boldsymbol{\tau} = \mathbf{P}\mathbf{F}^{\mathrm{T}}\,. \tag{5.39}$$

The description change of the effective elastic energy density simply reads

$$\widetilde{\psi}^e_{(m)}(\mathbf{F}^e) = \widetilde{\psi}^e_{(s)}(\mathbf{b}^e)\,.$$

The transformation from the elastic deformation gradient to the Finger tensor is $(5.3)_2$. The following derivative in index notation

$$\frac{\partial b^e_{ij}}{\partial F^e_{mn}} = \frac{\partial (F^e_{ik} F^e_{jk})}{\partial F^e_{mn}} = \delta_{im}\delta_{kn} F^e_{jk} + F^e_{ik}\delta_{jm}\delta_{kn} = \delta_{im} F^e_{jn} + F^e_{in}\delta_{jm}$$

is used in the computation of the description change from material to spatial

$$\frac{\partial \widetilde{\psi}^e_{(m)}}{\partial F^e_{mn}} = \frac{\partial \widetilde{\psi}^e_{(s)}}{\partial b^e_{ij}} \frac{\partial b^e_{ij}}{\partial F^e_{mn}} = \frac{\partial \widetilde{\psi}^e_{(s)}}{\partial b^e_{mj}} F^e_{jn} + \frac{\partial \widetilde{\psi}^e_{(s)}}{\partial b^e_{mi}} F^e_{in} = 2 \frac{\partial \widetilde{\psi}^e_{(s)}}{\partial b^e_{mj}} F^e_{jn} ,$$

where the symmetry of $\mathbf{b}^e$ is used. The final result is summarized in the relation:

$$\frac{\partial \widetilde{\psi}^e_{(m)}}{\partial \mathbf{F}^e} = 2 \frac{\partial \widetilde{\psi}^e_{(s)}}{\partial \mathbf{b}^e} \mathbf{F}^e . \tag{5.40}$$

Therefore, the material elastic state equation $(5.22)_2$ can be directly turned into its spatial counterpart $(5.30)_2$:

$$\widetilde{\mathbf{P}} = \frac{\partial \widetilde{\psi}^e_{(m)}}{\partial \mathbf{F}^e} \mathbf{F}^{p-\mathrm{T}} = 2 \frac{\partial \widetilde{\psi}^e_{(s)}}{\partial \mathbf{b}^e} \mathbf{F}^e \mathbf{F}^{p-\mathrm{T}} = 2 \frac{\partial \widetilde{\psi}^e_{(s)}}{\partial \mathbf{b}^e} \mathbf{b}^e \mathbf{F}^{-\mathrm{T}} = \widetilde{\boldsymbol{\tau}} \mathbf{F}^{-\mathrm{T}} .$$

Likewise, the yield function transforms as a scalar-valued function:

$$f^{(m)}_y(\widetilde{\mathbf{P}}^p) = f^{(s)}_y(\widetilde{\boldsymbol{\tau}}^p) .$$

The conversion from the material plastic stress $\widetilde{\mathbf{P}}^p$ to the spatial plastic stress $\widetilde{\boldsymbol{\tau}}^p$ follows the definitions (5.24), (5.32) and it reads

$$\widetilde{\mathbf{P}}^p = \mathbf{F}^{e\mathrm{T}} \widetilde{\mathbf{P}} = \mathbf{F}^{e\mathrm{T}} \widetilde{\boldsymbol{\tau}} \mathbf{F}^{-\mathrm{T}} = \mathbf{F}^{e\mathrm{T}} \widetilde{\boldsymbol{\tau}}^p \mathbf{F}^{-\mathrm{T}} . \tag{5.41}$$

The derivative of the material plastic stress with respect to the spatial one is

$$\frac{\partial \widetilde{P}^p_{ij}}{\partial \widetilde{\tau}^p_{hk}} = \frac{\partial (F^e_{ri} \widetilde{\tau}^p_{rs} F^{-1}_{js})}{\partial \widetilde{\tau}^p_{hk}} = F^e_{ri} \delta_{rh} \delta_{sk} F^{-1}_{js} = F^e_{hi} F^{-1}_{jk} .$$

The description change of the normal is developed in index notation

$$\frac{\partial f^{(s)}_y}{\partial \widetilde{\tau}^p_{hk}} = \frac{\partial f^{(m)}_y}{\partial \widetilde{P}^p_{ij}} \frac{\partial \widetilde{P}^p_{ij}}{\partial \widetilde{\tau}^p_{hk}} = F^e_{hi} \frac{\partial f^{(m)}_y}{\partial \widetilde{P}^p_{ij}} F^{-1}_{jk} .$$

Finally, the conversion of the yield surface normal reads

$$\frac{\partial f^{(s)}_y}{\partial \widetilde{\boldsymbol{\tau}}^p} = \mathbf{F}^e \frac{\partial f^{(m)}_y}{\partial \widetilde{\mathbf{P}}^p} \mathbf{F}^{-1} . \tag{5.42}$$

Therefore, the transformation from the material flow rule $(5.25)_1$ to the spatial flow rule $(5.34)_1$ with the application of (5.42) is a straightforward application of (5.37) and is restricted to plastic isotropy:

$$\mathbf{d}^p = \mathbf{F}^e \dot{\mathbf{F}}^p \mathbf{F}^{-1} = \dot{\lambda} \mathbf{F}^e \frac{\partial f^{(m)}_y}{\partial \widetilde{\mathbf{P}}^p} \mathbf{F}^{-1} = \dot{\lambda} \frac{\partial f^{(s)}_y}{\partial \widetilde{\boldsymbol{\tau}}^p} .$$

### 5.2.3 VARIATIONAL FORMULATION OF THE FINITE-STEP PROBLEM

#### 5.2.3.1 KINEMATICS & PLASTIC DISSIPATION OF THE FINITE-STEP

The time discretization of the mechanical problem in the large deformations framework is performed through a *linearization* of the kinematic quantities in the finite step. The pseudo-time is discretized into time steps with increment $\Delta t = t_{n+1} - t_n$, being $t_n$ and $t_{n+1}$ the previous and current time, respectively. The generic increment is $\Delta(\cdot) = (\cdot)_{n+1} - (\cdot)_n$. The displacement increment is $\Delta\mathbf{u} := \mathbf{u} - \mathbf{u}_n$. The following linearizations correspond to directional derivatives of the different kinematic quantities along $\Delta\mathbf{u}$ according to Section 5.2.1.3. Thus, the current section has the sole purpose to establish a common notation. The linearization of the material and spatial velocity gradients are

$$\Delta\mathbf{F} := \boldsymbol{\nabla}_0(\Delta\mathbf{u})\,, \quad \mathbf{L} = \Delta\mathbf{F}\,(\mathbf{F}^{n+1})^{-1}\,, \tag{5.43}$$

being the material increment gradient $\Delta\mathbf{F}$ the linearization of the deformation gradient. Note that $\mathbf{L}$ is the result of the integration of the spatial velocity gradient $\mathbf{l}$ over the time increment. Therefore, it is a non-dimensional quantity representing the deformation gradient increment expressed in the current configuration. For notation convenience the $n+1$ will be omitted from now onward. The linearization of the multiplicative split reads

$$\Delta\mathbf{F} = \Delta\mathbf{F}^e\mathbf{F}^p + \mathbf{F}^e\Delta\mathbf{F}^p\,. \tag{5.44}$$

Thus, the time discrete counterpart of the kinematic linearization (5.9) reads:

$$\mathbf{L} = (\Delta\mathbf{F}^e\mathbf{F}^{e-1}) + (\mathbf{F}^e\Delta\mathbf{F}^p\mathbf{F}^{-1}) = \mathbf{L}^e + \mathbf{L}^p\,. \tag{5.45}$$

The symmetric and skew-symmetric parts of $\mathbf{L}^p$ are again the increment of plastic deformation $\mathbf{D}^p$ and of the plastic spin tensor $\mathbf{W}^p$. The introduction of the plastic isotropy assumption as in Section 5.2.2.2 leads to

$$\mathbf{W}^p = \mathbf{0} \quad \rightarrow \quad \mathbf{D}^p = \mathbf{F}^e\Delta\mathbf{F}^p\mathbf{F}^{-1}\,. \tag{5.46}$$

The last linearization concerns the elastic Finger tensor defined in (5.4) for fixed deformation gradient $\mathbf{F}$ already introduced in (5.12):

$$\Delta\big(\mathbf{b}^e\big)|_{\mathbf{F}} = \mathbf{F}\,\Delta\mathbf{C}^{p-1}\mathbf{F}^{\mathrm{T}} = -2\,\mathrm{sym}\,(\mathbf{D}^p\mathbf{b}^e)\,, \tag{5.47}$$

where the constitutive assumption (5.46) has been exploited. From a mechanical stand point, (5.47) corresponds to the time discretization of the elastic Finger tensor Lie derivative (see e.g., Simo and Hughes (1998)).

Finally, the effective plastic dissipation increment can be computed exactly in the material description when a backward-Euler integration scheme is adopted as in the small deformation case (see e.g., Ortiz and Martin (1989)). Thus, the dissipation increment reads:

$$\Delta\widetilde{\phi}^p := \int_{t_n}^{t_{n+1}} \dot{\widetilde{\phi}}^p \,\mathrm{d}t = \widetilde{\mathbf{P}}^p_{n+1} : \Delta\mathbf{F}^p - \widetilde{\chi}_{n+1}\Delta\alpha\,. \tag{5.48}$$

#### 5.2.3.2 HU-WASHIZU MIXED FUNCTIONAL

The solution of the variational formulation is the set

$$\mathcal{S} := (\mathbf{u}, \mathbf{F}^e, \mathbf{F}^p, \widetilde{\mathbf{P}}, \widetilde{\mathbf{P}}^p, \widetilde{\chi}, \Delta\alpha, \Delta\lambda, \Delta d)\,. \tag{5.49}$$

The ductile fracture Hu-Washizu type mixed functional is the Lagrangian:

$$\begin{aligned}
\mathcal{L}^n(\mathcal{S}) := & \underbrace{\int_{\Omega_0} \omega(d)\,\left[\widetilde{\psi}^e(\mathbf{F}^e) + \widetilde{\psi}^p(\alpha^n + \Delta\alpha)\right] \mathrm{d}\Omega_0}_{\textit{stored internal energy } \mathcal{E}} - \\
& - \underbrace{\int_{\Omega_0} \mathbf{b}_0 \cdot \mathbf{u}\,\mathrm{d}\Omega_0 - \int_{\partial\Omega_N} \mathbf{t}_0 \cdot \mathbf{u}\,\mathrm{d}\Gamma}_{\textit{external work } \mathcal{W}} + \\
& + \underbrace{\int_{\Omega_0} \omega(d)\,\left(\widetilde{\mathbf{P}}^p : \Delta\mathbf{F}^p - \widetilde{\chi}\,\Delta\alpha\right) \mathrm{d}\Omega_0}_{\textit{plastic dissipation increment } \Delta\mathcal{D}^p} + \\
& + \underbrace{\int_{\Omega_0} \phi^f(d, \boldsymbol{\nabla}_0 d)\,\mathrm{d}\Omega_0}_{\textit{fracture energy } \mathcal{D}_f} + \underbrace{\int_{\Omega_0} \frac{\eta_f}{2\,\Delta t}\left(\Delta d\right)^2 \mathrm{d}\Omega_0}_{\textit{viscous energy } \mathcal{D}_v} + \\
& + \underbrace{\int_{\Omega_0} \omega(d)\,\widetilde{\mathbf{P}} : (\mathbf{I} + \boldsymbol{\nabla}_0\mathbf{u} - \mathbf{F}^e\mathbf{F}^p)\,\mathrm{d}\Omega_0}_{\textit{compatibility constraint}} - \\
& - \underbrace{\int_{\Omega_0} \omega(d)\,\Delta\lambda\, f_y(\widetilde{\mathbf{P}}^p, \widetilde{\chi})\,\mathrm{d}\Omega_0}_{\textit{plastic admissibility}}\,,
\end{aligned} \tag{5.50}$$

subject to

$$\Delta\lambda \geq 0\,, \quad \Delta d \geq 0\,, \quad \mathbf{u} = \mathbf{u}_D \text{ on } \partial\Omega_D\,, \tag{5.51}$$

where $\widetilde{\mathbf{P}}$ is the effective first Piola-Kirchhoff stress tensor, $\widetilde{\mathbf{P}}^p$ is the plastic first Piola-Kirchhoff stress. In the effective elastic free energy $\widetilde{\psi}^e$, and the yield function $f_y$ the material description is tacitly assumed with the usual abuse of notation. The notion of effective formulation enters in the definition of the integrals evaluated with respect the effective reference volume $\mathrm{d}\widetilde{\Omega}_0 = \omega\mathrm{d}\Omega_0$. With the exception of the fracture energy $\mathcal{D}_f$ and of the external work $\mathcal{W}$, the energies and the constraints are defined on the continuous portion of the material volume $\widetilde{\Omega}_0$ only, hence $\int_{\widetilde{\Omega}_0} \widetilde{(\cdot)}\,\mathrm{d}\widetilde{\Omega}_0 = \int_{\Omega_0} \omega\,\widetilde{(\cdot)}\,\mathrm{d}\Omega_0$, $\Omega_0$ being the reference nominal volume. The vectors $\mathbf{b}_0$ and $\mathbf{t}_0$ are the body forces and the tractions, respectively, applied on the Neumann portion $\partial\Omega_N$ of the nominal reference boundary. In the standard phase-field formulation,

$$\phi^f(d, \boldsymbol{\nabla}_0 d) = w(d) + {}^1\!/_2\, c_d\, \boldsymbol{\nabla}_0 d \cdot \boldsymbol{\nabla}_0 d\,, \tag{5.52}$$

where $w(d)$ is the local phase-field specific dissipation, and $\boldsymbol{\nabla}_0(\cdot)$ is the gradient with respect the reference configuration (see Section 2.3.2). The constant

parameter $c_d$ measures the damage diffusion bandwidth and it is related to the fracture internal length $l_{0d}$. An important remark concerns the definition of such parameter in the reference configuration. This involves the distortion of the internal length together with the solid. The viscous coefficient $\eta_f$ introduces a pseudo-time measure of the crack propagation rate, while $\Delta t = t_{n+1} - t_n$ is the current time-step size. This dissipative term is introduced for algorithmic reasons as in the small deformation framework (see Section 3.2). The solution of the considered ductile fracture boundary value problem makes the functional $\mathcal{L}^n(\mathcal{S})$ stationary with respect to variations of the fields in $\mathcal{S}$. The inequality constraints on $\Delta\lambda$ and $\Delta d$ turns stationarity into a variational inequality.

#### 5.2.3.3 Stationarity conditions

The stationarity conditions for $\mathcal{L}^n(\mathcal{S})$ read:

$$\partial_{\mathbf{u}}\mathcal{L}^n(\mathcal{S})[\delta\mathbf{u}] = 0 \quad \rightarrow \quad \begin{aligned} &\int_{\Omega_0} \omega\, \widetilde{\mathbf{P}} : \boldsymbol{\nabla}_0 \delta\mathbf{u}\, \mathrm{d}\Omega_0 - \\ &- \int_{\Omega_0} \mathbf{b}_0 \cdot \delta\mathbf{u}\, \mathrm{d}\Omega_0 - \int_{\partial\Omega_N} \mathbf{t}_0 \cdot \delta\mathbf{u}\, \mathrm{d}\Gamma = 0\,, \end{aligned} \tag{5.53a}$$

$$\partial_{\mathbf{F}^e}\mathcal{L}^n(\mathcal{S})[\delta\mathbf{F}^e] = 0 \quad \rightarrow \quad \int_{\Omega_0} \omega \left( \partial_{\mathbf{F}^e}\widetilde{\psi}^e - \widetilde{\mathbf{P}}\mathbf{F}^{p\mathrm{T}} \right) : \delta\mathbf{F}^e\, \mathrm{d}\Omega_0 = 0\,, \tag{5.53b}$$

$$\partial_{\mathbf{F}^p}\mathcal{L}^n(\mathcal{S})[\delta\mathbf{F}^p] = 0 \quad \rightarrow \quad \int_{\Omega_0} \omega \left( \widetilde{\mathbf{P}}^p - \mathbf{F}^{e\mathrm{T}}\widetilde{\mathbf{P}} \right) : \delta\mathbf{F}^p\, \mathrm{d}\Omega_0 = 0\,, \tag{5.53c}$$

$$\partial_{\widetilde{\mathbf{P}}}\mathcal{L}^n(\mathcal{S})[\delta\widetilde{\mathbf{P}}] = 0 \quad \rightarrow \quad \int_{\Omega_0} \omega \left( \mathbf{I} + \boldsymbol{\nabla}_0\mathbf{u} - \mathbf{F}^e\mathbf{F}^p \right) : \delta\widetilde{\mathbf{P}}\, \mathrm{d}\Omega_0 = 0\,, \tag{5.53d}$$

$$\partial_{\alpha}\mathcal{L}^n(\mathcal{S})[\delta\alpha] = 0 \quad \rightarrow \quad \int_{\Omega_0} \omega \left( \partial_{\alpha}\widetilde{\psi}^p - \widetilde{\chi} \right) \delta\alpha\, \mathrm{d}\Omega_0 = 0\,, \tag{5.53e}$$

$$\partial_{\widetilde{\mathbf{P}}^p}\mathcal{L}^n(\mathcal{S})[\delta\widetilde{\mathbf{P}}^p] = 0 \quad \rightarrow \quad \int_{\Omega_0} \omega \left( \Delta\mathbf{F}^p - \Delta\lambda\, \partial_{\widetilde{\mathbf{P}}^p} f_y \right) : \delta\widetilde{\mathbf{P}}^p\, \mathrm{d}\Omega_0 = 0\,, \tag{5.53f}$$

$$\partial_{\widetilde{\chi}}\mathcal{L}^n(\mathcal{S})[\delta\widetilde{\chi}] = 0 \quad \rightarrow \quad \int_{\Omega_0} -\omega \left( \Delta\alpha + \Delta\lambda\, \partial_{\widetilde{\chi}} f_y \right) \delta\widetilde{\chi}\, \mathrm{d}\Omega_0 = 0\,, \tag{5.53g}$$

$$\partial_{\lambda}\mathcal{L}^n(\mathcal{S})[\delta\lambda] \geq 0 \quad \rightarrow \quad \int_{\Omega_0} \omega \left( -\delta\lambda\, f_y \right) \mathrm{d}\Omega_0 \geq 0\,, \tag{5.53h}$$

$$\partial_{d}\mathcal{L}^n(\mathcal{S})[\delta d] \geq 0 \quad \rightarrow \quad \begin{aligned} &\int_{\Omega_0} \left\{ \left[ \omega'\, \widetilde{\psi}_{ep} + w' + \frac{\eta_f}{\Delta t}\, \Delta d \right] \delta d + \right. \\ &\left. + c_d\, \boldsymbol{\nabla}_0 d \cdot \boldsymbol{\nabla}_0 \delta d \right\} \mathrm{d}\Omega_0 \geq 0\,, \end{aligned} \tag{5.53i}$$

where $\delta\lambda = \Delta\lambda' - \Delta\lambda$, $\delta d = \Delta d' - \Delta d$ are not sign-constrained, while $\Delta\lambda' \geq 0$, $\Delta d' \geq 0$ are arbitrary, non-negative scalar functions belonging to the same spaces of $\Delta\lambda$ and $\Delta d$, respectively, and

$$\Delta\lambda \geq 0, \quad \Delta d \geq 0, \quad \mathbf{u} = \mathbf{u}_D \text{ on } \partial\Omega_D\,.$$

The driving energy $\widetilde{\psi}_{ep}$ in (5.53i) is defined as

$$\widetilde{\psi}_{ep} := \widetilde{\psi} + \Delta\widetilde{\phi}^p = \widetilde{\psi}^e + \widetilde{\psi}^p + \Delta\widetilde{\phi}^p \,. \tag{5.54}$$

The conditions above correspond to: (5.53a) equilibrium equations, (5.53b) elastic state equations, (5.53d) compatibility conditions, (5.53e) static hardening variable state equation, (5.53c) the definition of the plastic first Piola-Kirchhoff stress tensor, (5.53f) plastic strains evolution, (5.53g) hardening variable evolution, (5.53h) plastic consistency, (5.53i) non-local fracture evolution criterion. To simplify the notation in what follows, the symbols $\alpha, \lambda, d$ are used to express the functional dependencies, rather than the corresponding increments $\Delta\alpha, \Delta\lambda, \Delta d$.

#### 5.2.3.4 GOVERNING EQUATIONS OF THE NON-LOCAL PROBLEM

In the implemented formulation, the compatibility condition (5.53d) is enforced in strong form as in standard compatible finite elements, i.e.,

$$\mathbf{F} := \mathbf{F}^e\mathbf{F}^p = \mathbf{I} + \boldsymbol{\nabla}_0\mathbf{u} \,. \tag{5.55}$$

The equilibrium equation in material description can be written as:

$$\int_{\Omega_0} \omega\, \widetilde{\mathbf{P}} : \boldsymbol{\nabla}_0\delta\mathbf{u}\, \mathrm{d}\Omega_0 = \int_{\Omega_0} \mathbf{b}_0 \cdot \delta\mathbf{u}\, \mathrm{d}\Omega_0 + \int_{\partial\Omega_N} \mathbf{t}_0 \cdot \delta\mathbf{u}\, \mathrm{d}\Gamma \,, \tag{5.56}$$

The material elastic (5.53b), and the hardening state equations (5.53e), the material flow rule (5.53f), and the internal variable evolution law (5.53g) read

$$\widetilde{\mathbf{P}} = \frac{\partial\widetilde{\psi}^e}{\partial\mathbf{F}^e}\mathbf{F}^{p-\mathrm{T}} \,, \quad \widetilde{\chi} := \frac{\partial\widetilde{\psi}^p}{\partial\alpha} \,, \quad \Delta\mathbf{F}^p = \Delta\lambda\, \frac{\partial f_y}{\partial\widetilde{\mathbf{P}}^p} \,, \quad \Delta\alpha = -\Delta\lambda\, \frac{\partial f_y}{\partial\widetilde{\chi}} \,. \tag{5.57}$$

Using standard arguments for variational inequalities, condition (5.53h) can be cast in the equivalent set of material elastoplastic loading-unloading conditions:

$$\Delta\lambda \geq 0 \,, \quad f_y(\widetilde{\mathbf{P}}^p, \widetilde{\chi}) \leq 0 \,, \quad f_y(\widetilde{\mathbf{P}}^p, \widetilde{\chi})\Delta\lambda = 0 \tag{5.58}$$

where the plastic first Piola-Kirchhoff stress is $\widetilde{\mathbf{P}}^p = \mathbf{F}^{e\mathrm{T}}\widetilde{\mathbf{P}}$ according to (5.53c).

The use of (5.6), and the transformation rule (5.39) allow to write the equilibrium equation into its spatial counterpart:

$$\int_{\Omega_0} \omega\, \widetilde{\boldsymbol{\tau}} : \boldsymbol{\nabla}^s\delta\mathbf{u}\, \mathrm{d}\Omega_0 = \int_{\Omega_0} \mathbf{b}_0 \cdot \delta\mathbf{u}\, \mathrm{d}\Omega_0 + \int_{\partial\Omega_N} \mathbf{t}_0 \cdot \delta\mathbf{u}\, \mathrm{d}\Gamma \,, \tag{5.59}$$

The use of the transformation rules (5.40), (5.41), (5.42), together with the assumption (5.46) lead to the spatial elastoplastic evolution laws:

$$\widetilde{\boldsymbol{\tau}} = 2\,\frac{\partial\widetilde{\psi}^e}{\partial\mathbf{b}^e}\,\mathbf{b}^e \,, \quad \widetilde{\chi} := \frac{\partial\widetilde{\psi}^p}{\partial\alpha} \,, \quad \mathbf{D}^p = \Delta\lambda\, \frac{\partial f_y}{\partial\widetilde{\boldsymbol{\tau}}} \,, \quad \Delta\alpha = -\Delta\lambda\, \frac{\partial f_y}{\partial\widetilde{\chi}} \,, \tag{5.60}$$

where the relation $\widetilde{\boldsymbol{\tau}}^p = \widetilde{\boldsymbol{\tau}}$ from (5.32) is exploited into the flow rule. The manipulation of the plastic stress power density as in (5.33) leads to:

$$\widetilde{\boldsymbol{\tau}} : \mathbf{D}^p = \widetilde{\boldsymbol{\tau}} : \Big( - {}^1\!/_2 \Delta(\mathbf{b}^e)|_{\mathbf{F}} \mathbf{b}^{e-1} \Big) , \tag{5.61}$$

where $\Delta(\mathbf{b}^e)|_{\mathbf{F}}$ is the finite-step counterpart of the Lie derivative $\mathcal{L}_v \, \mathbf{b}^e$ according to (5.12). Thus, the use of (5.61) and $(5.60)_3$ leads to the alternative spatial flow rule:

$$\Delta(\mathbf{b}^e)|_{\mathbf{F}} = -2 \, \Delta\lambda \, \frac{\partial f_y}{\partial \widetilde{\boldsymbol{\tau}}} \, \mathbf{b}^e \, . \tag{5.62}$$

The spatial counterpart of the elastoplastic loading-unloading conditions (5.58) reads:

$$\Delta\lambda \geq 0 \, , \quad f_y(\widetilde{\boldsymbol{\tau}}, \widetilde{\chi}) \leq 0 \, , \quad f_y(\widetilde{\boldsymbol{\tau}}, \widetilde{\chi}) \Delta\lambda = 0 \, . \tag{5.63}$$

The energy release rate $\mathcal{Y}$ and critical energy release rate $\mathcal{Y}_c$ functionals are:

$$\mathcal{Y}(\mathbf{F}^e, \mathbf{F}^p, \alpha, d)[\delta d] := - \int_{\Omega_0} \omega'(d) \, \widetilde{\psi}_{ep}(\mathbf{F}^e, \mathbf{F}^p, \alpha) \, \delta d \, \mathrm{d}\Omega_0 \, , \tag{5.64a}$$

$$\mathcal{Y}_c(d)[\delta d] := \int_{\Omega_0} \Big\{ \Big[ w'(d) + \frac{\eta_f}{\Delta t} \, \Delta d \Big] \, \delta d + c_d \, \boldsymbol{\nabla}_0 d \cdot \boldsymbol{\nabla}_0 \delta d \Big\} \, \mathrm{d}\Omega_0 \, , \tag{5.64b}$$

where the state equations and the evolution laws have been used to reduce the number of independent fields in the driving energy $\widetilde{\psi}_{ep}$. The non-local fracture activation functional $\mathcal{F}_d$ is then defined as:

$$\mathcal{F}_d(\mathbf{F}^e, \mathbf{F}^p, \alpha, d)[\delta d] := \Big( \mathcal{Y}(\mathbf{F}^e, \mathbf{F}^p, \alpha, d) - \mathcal{Y}_c(d) \Big)[\delta d] \tag{5.65}$$

and condition (5.53i) is rewritten in the equivalent form

$$\Delta d \geq 0 \quad , \quad \mathcal{F}_d(\mathbf{F}^e, \mathbf{F}^p, \alpha, d) \leq 0 \quad , \quad \mathcal{F}_d(\mathbf{F}^e, \mathbf{F}^p, \alpha, d)[\Delta d] = 0 \tag{5.66}$$

providing the non-local fracture activation criterion for elastoplastic brittle fracture. It should be noted that in this elastoplastic-brittle-fracture model the only coupling between plastic and fracture dissipation mechanisms is present in the fracture driving force $\mathcal{Y}$, while the fracture dissipation $\mathcal{Y}_c$ is the same as the one of the purely brittle case.

Finally, the current formulation for large deformations ductile fracture relies on the coupling between the plastic and brittle dissipation mechanisms proposed in Section 3.3 for small strains.

### 5.2.4 CONSTITUTIVE ASSUMPTIONS

#### 5.2.4.1 METAL PLASTICITY

For the implementation considered in this work, the general framework described so far is restricted to metal plasticity. The assumption of incompressible

plastic deformations $J^p = \det \mathbf{F}^p = 1$ is introduced. Therefore, the volumetric deformation is totally elastic $J^e = J$. The isotropic elastic energy follows a Neo-Hookean material behaviour (see e.g., Holzapfel (2000)):

$$\widetilde{\psi}^e(\mathbf{b}^e) = \widetilde{\psi}^e_{vol}(J) + \widetilde{\psi}^e_{iso}(\overline{\mathbf{b}}^e) := \frac{K_0}{2}\left(\frac{J^2-1}{2} - \log J\right) + \frac{G_0}{2}\Big(\operatorname{tr}\overline{\mathbf{b}}^e - 3\Big)\,. \quad (5.67)$$

where $\widetilde{\psi}_{vol}$, $\widetilde{\psi}_{iso}$ are the volumetric and isochoric parts of the energy, respectively. While, $\overline{\mathbf{b}}^e = J^{-2/3}\mathbf{b}^e$ is the isochoric elastic Finger tensor, and $K_0$, $G_0$ are the bulk and shear modulus, respectively. The effective elastic evolution can be additively decomposed into volumetric and isochoric part:

$$\widetilde{\boldsymbol{\tau}} = \widetilde{\boldsymbol{\tau}}_{vol} + \widetilde{\boldsymbol{\tau}}_{iso} = K_0\, {}^1\!/_2(J^2-1)\,\mathbf{I} + G_0 \operatorname{dev}\overline{\mathbf{b}}^e \quad (5.68)$$

being $\widetilde{\boldsymbol{\tau}}_{vol} = 2\,\partial_{\mathbf{b}^e}\widetilde{\psi}^e_{vol}\mathbf{b}^e$, $\widetilde{\boldsymbol{\tau}}_{iso} = 2\,\partial_{\mathbf{b}^e}\widetilde{\psi}^e_{iso}\mathbf{b}^e = \operatorname{dev}\left(\partial_{\overline{\mathbf{b}}^e}\widetilde{\psi}^e_{iso}\overline{\mathbf{b}}^e\right)$ the effective volumetric and isochoric Kirchhoff stress tensor, respectively. Moreover, $\operatorname{dev}(\cdot) = (\cdot) - 1/3\operatorname{tr}(\cdot)\mathbf{I}$ is the deviatoric tensor operator. The von-Mises yield function reads

$$f_y(\widetilde{\boldsymbol{\tau}}_{iso}, \widetilde{\chi}) := \sqrt{\widetilde{\boldsymbol{\tau}}_{iso} : \widetilde{\boldsymbol{\tau}}_{iso}} - \sqrt{{}^2\!/_3}\,(\bar{\sigma}_{y0} + \widetilde{\chi})\,, \quad (5.69)$$

being $\bar{\sigma}_{y0}$ the initial yield stress. The exponential hardening law is used:

$$\widetilde{\chi}(\alpha) = (\sigma_\infty - \bar{\sigma}_{y0})(1 - \exp(-\delta_p\alpha)) + H_0\alpha\,, \quad (5.70)$$

where $\sigma_\infty$ and $\delta_p$ are the saturation stress and coefficient, respectively. While $H_0$ is the linear hardening modulus.

Finally, the spatial flow rule (5.62) is used:

$$\Delta\big(\mathbf{b}^e\big)|_{\mathbf{F}} = \mathbf{F}\,\Delta\mathbf{C}^{p-1}\mathbf{F}^{\mathrm{T}} = -2\,\Delta\lambda\,\partial_{\widetilde{\boldsymbol{\tau}}} f_y\,\mathbf{b}^e = -2\,\Delta\lambda\,\mathbf{n}\,\mathbf{b}^e\,,$$

where the yield surface unit normal tensor is defined as

$$\mathbf{n} := \frac{\partial f_y}{\partial \widetilde{\boldsymbol{\tau}}} = \frac{\widetilde{\boldsymbol{\tau}}_{iso}}{|\widetilde{\boldsymbol{\tau}}_{iso}|}\,. \quad (5.71)$$

The last step consists in the development of the term

$$\mathbf{n}\,\mathbf{b}^e = J^{2/3}\,\mathbf{n}\,\overline{\mathbf{b}}^e = J^{2/3}\,\mathbf{n}\left(\frac{1}{3}\operatorname{tr}\overline{\mathbf{b}}^e\,\mathbf{I} + \operatorname{dev}\overline{\mathbf{b}}^e\right) = J^{2/3}\left(\frac{1}{3}\operatorname{tr}\overline{\mathbf{b}}^e\,\mathbf{n} + \frac{|\widetilde{\boldsymbol{\tau}}_{iso}|}{G_0}\mathbf{n}\,\mathbf{n}\right),$$

where the isochoric elastic law was used. If the common assumption for metals ${}^{|\widetilde{\boldsymbol{\tau}}_{iso}|}\!/_{G_0} \approx 0$ is introduced (see Simo (1988)), the spatial flow rule reads

$$\overline{\mathbf{F}}\,\Delta\mathbf{C}^{p-1}\overline{\mathbf{F}}^{\mathrm{T}} = -{}^2\!/_3\,\Delta\lambda\operatorname{tr}\overline{\mathbf{b}}^e\,\mathbf{n}\,,$$

where $\overline{\mathbf{F}} = J^{-1/3}\mathbf{F}$ is the isochoric deformation gradient. The use of the time linearization $\Delta\mathbf{C}^{p-1} = \mathbf{C}^{p-1} - \mathbf{C}^{p-1}_n$, together with the definition (5.4) leads to

$$\overline{\mathbf{F}}\,\mathbf{C}^{p-1}\overline{\mathbf{F}}^{\mathrm{T}} = \overline{\mathbf{F}}\,\mathbf{C}^{p-1}_n\overline{\mathbf{F}}^{\mathrm{T}} - {}^2\!/_3\,\Delta\lambda\operatorname{tr}\overline{\mathbf{b}}^e\,\mathbf{n}\,.$$

The definition of the trial elastic isochoric Finger tensor $\overline{\mathbf{b}}^{e,tr} := \overline{\mathbf{F}}\,\mathbf{C}_n^{p-1}\overline{\mathbf{F}}^{\mathrm{T}}$ allows the introduction of the update of the isochoric elastic Finger tensor:

$$\overline{\mathbf{b}}^{e} = \overline{\mathbf{b}}^{e,tr} - 2/3\,\Delta\lambda\,\mathrm{tr}\,\overline{\mathbf{b}}^{e}\,\mathbf{n}\,. \tag{5.72}$$

Then, the return mapping algorithm outlined in Simo and Hughes (1998) can be directly employed.

#### 5.2.4.2 BRITTLE FRACTURE

The phase-field functions $\omega(d)$ and $w(d)$ are defined as

$$\omega(d) = (1-d)^2, \quad w(d) = \frac{3G_c}{8l_{0d}}\,d\,. \tag{5.73}$$

where $G_c$ is the material toughness and $l_{0d}$ the phase-field internal length. This definition of $w(d)$ corresponds to an AT1 approach (see Section 2.2), implying that damage cannot develop until a critical value of the damage driving force has been achieved. Finally, the viscous coefficient $\eta_f$ is defined as $\eta_f = \bar{\eta}\left(G_c/l_{0d}\right)$.

To avoid the promotion of crack propagation by predominantly compressive states, the deviatoric-volumetric elastic energy split is adopted (see, e.g.Amor et al. (2009); Comi and Perego (1996a)). According to this technique, the elastic energy is split into an *Inactive* part $\widetilde{\psi}^{eI}$, due to negative volumetric strains, and an *Active* remainder $\widetilde{\psi}^{eA}$, which are defined as:

$$\widetilde{\psi}^{eA}(\mathbf{b}^e) = \widetilde{\psi}^{e}_{vol}(J^+) + \widetilde{\psi}^{e}_{iso}(\overline{\mathbf{b}}^{e})\,, \quad \widetilde{\psi}^{eI}(\mathbf{b}^e) = \widetilde{\psi}^{e}_{vol}(J^-)\,. \tag{5.74}$$

being $J^{\pm}(J) = \langle J-1\rangle_{\pm} + 1$, where $\langle\cdot\rangle_{\pm}$ are the Macaulay functions. Thus, $J^+ = J$ if $J > 1$, and $J^+ = 1$ if $J < 1$, while $J^- = J$ if $J < 1$, and $J^- = 1$ if $J > 1$. In view of the purely deviatoric nature of plastic strains in von-Mises plasticity, no distinction is made between the tensile/compressive parts of the plastic component $\widetilde{\psi}^{p}$ of the free energy density. The assumed energy split has implications on the definition of the nominal Kirchhoff stress and of the plastic dissipation rate. Taking into account the elastic energy split, the nominal reference free energy is defined as

$$\psi = \omega\left(\widetilde{\psi}^{eA} + \widetilde{\psi}^{p}\right) + \widetilde{\psi}^{eI}\,. \tag{5.75}$$

Then, the active and inactive effective Kirchhoff stresses are defined

$$\widetilde{\boldsymbol{\tau}}^{A} = 2\,\frac{\partial\widetilde{\psi}^{eA}}{\partial\mathbf{b}^e}\mathbf{b}^e\,, \quad \widetilde{\boldsymbol{\tau}}^{I} = 2\,\frac{\partial\widetilde{\psi}^{eI}}{\partial\mathbf{b}^e}\mathbf{b}^e\,; \quad \widetilde{\boldsymbol{\tau}} = \widetilde{\boldsymbol{\tau}}^{A} + \widetilde{\boldsymbol{\tau}}^{I}\,. \tag{5.76}$$

## 5.3 Space discretization

The space discretization resembles the one outlined in the small deformation framework in section 3.4, where all relevant definitions have been introduced already. The element local solution differs from the small strain framework for the gradients, i.e., the spatial symmetric displacement gradient $\boldsymbol{\nabla}^s\mathbf{u}$ $(n_\varepsilon, 1)$, and material the phase-field gradient $\boldsymbol{\nabla}_0 d$ $(n_{dim}, 1)$ are modeled as:

$$\boldsymbol{\nabla}^s\mathbf{u} = \mathbf{B}_\mathrm{u}\,\widehat{\mathbf{u}}_e\,, \qquad \boldsymbol{\nabla}_0 d = \mathbf{B}_\mathrm{d}\,\widehat{\mathbf{d}}_e\,. \tag{5.77}$$

### 5.3.1 Governing equations

The weak form of the spatial equilibrium equation (5.59), and the fracture complementarity equations $(5.66)_3$ are spatially discretized:

$$\delta\widehat{\mathbf{u}}^\mathrm{T}\left[\sum_{e=1}^{n_{el}}\mathbf{C}_{e,\mathrm{u}}^\mathrm{T}\left(\mathbf{F}_{\mathrm{I},e}-\mathbf{F}_{\mathrm{E},e}\right)\right]=0\,,\quad \Delta\widehat{\mathbf{d}}^\mathrm{T}\left[\sum_{e=1}^{n_{el}}\mathbf{C}_{e,\mathrm{d}}^\mathrm{T}\,\mathbf{f}_{\mathrm{D},e}\right]=0\,. \tag{5.78}$$

where $e$ denotes the element number and $n_{el}$ is the total number of elements in the mesh. The element internal force $\mathbf{F}_{\mathrm{I},e}$ $(n_{ldof}, 1)$, the external force $\mathbf{F}_{\mathrm{E},e}$ $(n_{ldof}, 1)$, and the fracture activation $\mathbf{f}_{\mathrm{D},e}$ $(n_{en}, 1)$ vectors are defined as:

$$\mathbf{F}_{\mathrm{I},e} := \int_{\Omega_{0e}}\mathbf{B}_\mathrm{u}^\mathrm{T}\left(\omega\,\widetilde{\boldsymbol{\tau}}^A+\widetilde{\boldsymbol{\tau}}^I\right)\mathrm{d}\Omega_{0e}\,, \tag{5.79a}$$

$$\mathbf{F}_{\mathrm{E},e} := \int_{\Omega_{0e}}\mathbf{N}_\mathrm{u}^\mathrm{T}\,\mathbf{b}_0\,\mathrm{d}\Omega_{0e}+\int_{\partial\Omega_{0e}}\mathbf{N}_\mathrm{u}^\mathrm{T}\,\mathbf{t}_0\,\mathrm{d}\Gamma_{0e}\,, \tag{5.79b}$$

$$\mathbf{f}_{\mathrm{D},e} := -\int_{\Omega_{0e}}\left\{\mathbf{N}_\mathrm{d}^\mathrm{T}\left[\omega'\,\widetilde{\psi}_{ep}+(f+1)\,w'+w'_\epsilon+\frac{\eta_f}{\Delta t}\,\Delta d\right]+c_d\,\mathbf{B}_\mathrm{d}^\mathrm{T}\,\boldsymbol{\nabla}_0 d\right\}\mathrm{d}\Omega_{0e}\,, \tag{5.79c}$$

where $\widetilde{\boldsymbol{\tau}}^A$, $\widetilde{\boldsymbol{\tau}}^I$ are the active and inactive effective Kirchhoff stresses defined in (5.76) in Voigt notation with dimension $(n_\sigma, 1)$, being $n_\sigma = n_\varepsilon$ the number of independent stress components. The element integrals are evaluated over the element nominal reference volume $\Omega_{0e}$. The definition of the phase-field activation vector $\mathbf{f}_{\mathrm{D},e}$ introduces the modulation function approach already outlined in Section 3.3. The additional constant term $w'_\epsilon$ is introduced to avoid spurious damage activations when $\alpha < \alpha_{cr}$ and is defined as in (3.51). The spatial discretization of the governing equations reads:

$$\mathbf{F}_\mathrm{I}-\mathbf{F}_\mathrm{E}=\mathbf{0}\,, \tag{5.80a}$$

$$\Delta\widehat{\mathbf{d}}\geq\mathbf{0}\,,\quad \mathbf{f}_\mathrm{D}\leq\mathbf{0}\,,\quad \Delta\widehat{\mathbf{d}}^\mathrm{T}\,\mathbf{f}_\mathrm{D}=0\,. \tag{5.80b}$$

## 5.4 Algorithmic implementation

The solution of the finite element discretized governing equations (5.80) is performed with a staggered scheme that perfectly resembles the one described in the previous chapters (see e.g., Section 3.5.1).

The effective stress approach proposed in the ductile fracture formulation has an important consequence: plastic deformations develop in the continuous part of the material until complete failure. From a practical point of view, this involves very large plastic strains that induce a severe locking of the response. A possible solution to the problem is the use of F-bar approaches as in Simo et al. (1985) and de Souza Neto et al. (1996). Nevertheless, the use of a staggered solution procedure (see Chapter 3) for a general three-dimensional problem with a selective-reduced integration scheme would significantly increase the computational burden. Therefore, the solution of reduced single-point integration has been chosen instead. Two-dimensional four-nodes and three-dimensional eight-node elements have been used.

### 5.4.1 REDUCED INTEGRATION WITH HOURGLASS CONTROL

#### 5.4.1.1 NONLINEAR KINEMATICS

The nonlinear kinematics concerns the displacement field of the large deformation framework. The formulation comes from Bonet and Bhargava (1995). Let the $i$-th coordinate in the reference $x_{0i}$ and current $x_i$ configurations be spatially discretized according to (F.5):

$$x_i = \underbrace{\left(\widehat{\mathbf{x}}_i^{\mathrm{T}}\mathbf{1}\right) + \left(\widehat{\mathbf{x}}_i^{\mathrm{T}}\widehat{\boldsymbol{\xi}}_1\right)\xi_1 + \left(\widehat{\mathbf{x}}_i^{\mathrm{T}}\widehat{\boldsymbol{\xi}}_2\right)\xi_2}_{\texttt{linear } x_i^{lin}} + \underbrace{\left(\widehat{\mathbf{x}}_i^{\mathrm{T}}\widehat{\mathbf{h}}\right)\xi_1\xi_2}_{\texttt{hourglass } x_i^{hg}} , \tag{5.81}$$

where, for the sake of compactness, only the current quantities are represented, yet for the reference ones it is enough to add a zero subscript. The definitions of $\mathbf{1}$, $\widehat{\boldsymbol{\xi}}_1$, $\widehat{\boldsymbol{\xi}}_2$, and $\widehat{\mathbf{h}}$ are in Appendix F. The nodal coordinates vector in the current configuration reads:

$$\widehat{\mathbf{x}}_i := \begin{pmatrix} \widehat{x}_i^{(1)} & \widehat{x}_i^{(2)} & \widehat{x}_i^{(3)} & \widehat{x}_i^{(4)} \end{pmatrix}^{\mathrm{T}} , \tag{5.82}$$

being $\widehat{x}_{0i}^{(a)}, \widehat{x}_i^{(a)}$ the $x_i$-coordinate of the $a$-th node in the reference and current configuration respectively. The one-point integration implies the evaluation of the deformation gradient at the element centroid $\mathbf{F}_c$:

$$(F_c)_{ij} = \frac{\partial x_{c,i}}{\partial x_{0j}} = \frac{\partial N_c^{(a)}}{\partial x_{0j}}\widehat{x}_i^{(a)} = \widehat{\mathbf{x}}_i^{\mathrm{T}}\mathbf{b}_{0j} , \tag{5.83}$$

where $x_{c,i}$, $N_c^{(a)}$, $\mathbf{b}_{0i}$ are the $i$-th spatial coordinate, the $a$-th node shape function, and the $i$-th gradient component vector at the element centroid already introduced in Appendix F. The latter must be computed with respect the material coordinates. The centroid deformation gradient $\mathbf{F}_c$ is unique for the single finite element. Thus, a *uniform* deformation gradient is used to model a non-uniform response. A uniform response $\mathring{x}_i$, i.e., when $\mathring{F}_{ij}$ is constant over the

element, involves no displacement hourglass modes, and the coordinates map is

$$\mathring{x}_i = \mathring{F}_{ij} x_{0j} \quad \rightarrow \quad \mathring{x}_i^{lin} = \mathring{F}_{ij} x_{0j}^{lin} \,, \qquad \mathring{x}_i^{hg} = \mathring{F}_{ij} x_{0j}^{hg} \,, \tag{5.84}$$

where the last two relations are a trivial consequence of (5.81). The use of (5.81) allows to write the conditions (5.84) in their nodal counterpart, since it must hold in each point of the element, i.e., for every $\xi_1, \xi_2$, then

$$\big(\mathring{\widehat{\mathbf{x}}}_i^{\mathrm{T}} \widehat{\boldsymbol{\xi}}_k\big) = \mathring{F}_{ij} \big(\widehat{\mathbf{x}}_{0j}^{\mathrm{T}} \widehat{\boldsymbol{\xi}}_k\big) \quad k = 1, 2; \qquad \big(\mathring{\widehat{\mathbf{x}}}_i^{\mathrm{T}} \widehat{\mathbf{h}}\big) = \mathring{F}_{ij} \big(\widehat{\mathbf{x}}_{0j}^{\mathrm{T}} \widehat{\mathbf{h}}\big) \,. \tag{5.85}$$

Nevertheless, the definition of the centroid (constant) deformation gradient in the case of one-point integration leads to equation

$$(F_c)_{ij} := \frac{\partial x_i}{\partial \xi_k} \left[\frac{\partial x_{0j}}{\partial \xi_k}\right]^{-1} \Big|_{\boldsymbol{\xi}=\mathbf{0}} \quad \rightarrow \quad \frac{\partial}{\partial \xi_k} \Big[x_i - (F_c)_{ij} x_{0j}\Big] \Big|_{\boldsymbol{\xi}=\mathbf{0}} = 0 \,. \tag{5.86}$$

The insertion of (5.81) into the last equality (5.86) leads to the conditions:

$$\big(\widehat{\mathbf{x}}_i^{\mathrm{T}} \widehat{\boldsymbol{\xi}}_k\big) = (F_c)_{ij} \big(\widehat{\mathbf{x}}_{0j}^{\mathrm{T}} \widehat{\boldsymbol{\xi}}_k\big) \quad , \quad k = 1, 2 \,, \tag{5.87}$$

where the relation $\partial_{\xi_k}(\xi_1 \xi_2)|_{\boldsymbol{\xi}=\mathbf{0}} = 0$ has been used. The comparison of (5.87) with $(5.85)_1$ allows to state that the linear part of the reference and current coordinates transforms as the uniform case when a single integration point is used, but in general the hourglass portion $(5.85)_2$ will not. Therefore, a resonable measure of the hourglass $i$-th component comes from $(5.85)_2$

$$u_i^{hg}(\widehat{\mathbf{x}}_i) = \big(\widehat{\mathbf{x}}_i^{\mathrm{T}} \widehat{\mathbf{h}}\big) - \big(\widehat{\mathbf{x}}_i^{\mathrm{T}} \mathbf{b}_{0j}\big)\big(\widehat{\mathbf{x}}_{0j}^{\mathrm{T}} \widehat{\mathbf{h}}\big) = \widehat{\mathbf{x}}_i^{\mathrm{T}} \big[\widehat{\mathbf{h}} - \big(\widehat{\mathbf{x}}_{0j}^{\mathrm{T}} \widehat{\mathbf{h}}\big) \mathbf{b}_{0j}\big] = \widehat{\mathbf{x}}_i^{\mathrm{T}} \widehat{\boldsymbol{\gamma}}_0 \,, \tag{5.88}$$

since it measures how much is the discrepancy from the uniform case. Here $\widehat{\boldsymbol{\gamma}}_0$ is the large strain counterpart of the $\gamma$-projection vector (3.62) and is defined

$$\widehat{\boldsymbol{\gamma}}_0 = \widehat{\mathbf{h}} - \Big(\widehat{\mathbf{x}}_{01}^{\mathrm{T}} \widehat{\mathbf{h}}\Big) \mathbf{b}_{01} - \Big(\widehat{\mathbf{x}}_{02}^{\mathrm{T}} \widehat{\mathbf{h}}\Big) \mathbf{b}_{02} \,, \tag{5.89}$$

where the nodal position vectors $\widehat{\mathbf{x}}_{0i}$ and the centroid gradient vectors $\mathbf{b}_{0i}$ correspond to the reference configuration. In the variational formulations outlined in the previous sections, the total energy or the Lagrangian functionals to be minimized are enriched with the additional term at the element level:

$$\Pi_e^{hg}(\hat{\mathbf{u}}_i) = {}^1\!/_2 \, k_{u_i 0}^{hg} \, u_i^{hg} \, u_i^{hg} \,, \tag{5.90}$$

where $k_{u_i 0}^{hg}$ is the hourglass *stiffness* related to the $i$-th displacement direction. The corresponding stationarity with respect to the variable $u_i$ reads:

$$\partial_{\hat{\mathbf{u}}_i} \Pi_e^{hg}(\hat{\mathbf{u}}_i)[\delta \hat{\mathbf{u}}_i] = \delta u_i^{hg} (k_{u_i 0}^{hg} \, u_i^{hg}) = \delta \hat{\mathbf{u}}_i^{\mathrm{T}} \mathbf{f}_{i,e}^{hg} \,,$$

being $\delta \widehat{\mathbf{x}}_i = \delta \hat{\mathbf{u}}_i$. The nodal hourglass forces in the $i$-th physical direction are

$$\mathbf{f}_{i,e}^{hg}(\widehat{\mathbf{x}}_i) = (k_{u_i 0}^{hg} \, \widehat{\boldsymbol{\gamma}}_0 \widehat{\boldsymbol{\gamma}}_0^{\mathrm{T}}) \widehat{\mathbf{x}}_i = \mathbf{K}_{i,e}^{hg} \, \widehat{\mathbf{x}}_i \,, \tag{5.91}$$

where $\mathbf{K}_{i,e}^{hg} = k_{u_i 0}^{hg} \, \widehat{\boldsymbol{\gamma}}_0 \widehat{\boldsymbol{\gamma}}_0^{\mathrm{T}}$ is the element hourglass tangent stiffness of the $i$-th physical direction, since the linearization of the first variation $\partial_{\hat{\mathbf{u}}_i} \Pi_e^{hg}$ reads:

$$\Delta \partial_{\hat{\mathbf{u}}_i} \Pi_e^{hg}(\hat{\mathbf{u}}_i)[\delta \hat{\mathbf{u}}_i, \Delta \hat{\mathbf{u}}_i] = \delta \hat{\mathbf{u}}_i^{\mathrm{T}} \mathbf{K}_{i,e}^{hg} \Delta \hat{\mathbf{u}}_i \,.$$

#### 5.4.1.2 Displacement hourglass stiffness

In both the linear and nonlinear kinematics cases, the hourglass nodal forces correspond to a linear spring with constant stiffness. The definition of hourglass coefficient $k^{hg}_{u_i 0}$ (see e.g., Belytschko et al. (2014, 1984); Bonet and Bhargava (1995)) reads:

$$k^{hg}_{u_i 0} = \bar{k}_{u_i 0} \left[ 2\, G_0 \big( \mathbf{b}^{\mathrm{T}}_{0i} \mathbf{b}_{0i} \big)\, \Omega_{0e} \right], \tag{5.92}$$

where the quantities inside the bracket are problem dependent, i.e., the shear modulus $G_0$, the element reference volume $\Omega_{0e}$, and the one-integration point material gradients of the shape functions $\mathbf{b}_{0i}$. Conversely, the user-defined non-dimensional coefficient $\bar{k}_{u_i 0}$ has typical values of the order 0.01.

The nonlinear behaviour of the material is accounted through a reduction of the constant hourglass coefficient $\bar{k}_{u_i 0}$ with the same procedure outlined in Section 3.5.3.2 for linear kinematics.

## 5.5 Numerical simulations

The current section aims to validate the large strain ductile fracture model with the experimental results in Boyce et al. (2013). The material under investigation is stainless steel. A plate of thickness 3.124 mm is used to extract two families of specimens. The I-shaped samples are used for the calibration of the elastoplastic and ductile fracture parameters. Here, only the experimental curves of reaction force versus displacement are provided. The second family consists of holed compact tension specimens. The material properties of the current model have been calibrated with the I-shaped specimens, and the same data are used to predict the response of the holed compact tension. The values are reported in Table 5.1.

| $E_0$ | $\nu$ | $\bar{\sigma}_{y0}$ | $\sigma_\infty$ | $H_0$ | $\delta_p$ | $G_c$ | $l_{0d}$ | $\alpha_{cr}$ | $\Delta\alpha_{cr}$ |
|---|---|---|---|---|---|---|---|---|---|
| 195 | 0.30 | 1100 | 1200 | 500 | 10 | 100 | 1.5 | 0.4 | 1.0 |
| GPa | - | MPa | MPa | MPa | - | N/mm | mm | - | - |

**Table 5.1:** Material properties

The numerical simulations has been performed with eight-nodes brick elements with single integration point and hourglass control according to the procedure outlined in Section 5.4.1. The residual for the Newton-Raphson scheme $\mathtt{Res}_{\mathrm{NR}}$ used to solve the balance of linear momentum (5.80a), and the residual for the solution of the staggered scheme $\mathtt{Res}_{\mathrm{STAG}}$ of the coupled problem (5.80) are the magnitude of the out-of-balance forces:

$$\mathtt{Res}_{\mathrm{NR}} = \mathtt{Res}_{\mathrm{STAG}} = (\mathbf{F}_{\mathrm{I}} - \mathbf{F}_{\mathrm{E}})^{\mathrm{T}} (\mathbf{F}_{\mathrm{I}} - \mathbf{F}_{\mathrm{E}})\,. \tag{5.93}$$

The used tolerances for the Newton-Raphson and the staggered scheme are:

$$\mathtt{TOL}_{\mathrm{NR}} = 10^{-6}\mathrm{N}^2\,, \quad \mathtt{TOL}_{\mathrm{STAG}} = 10^{-3}\mathrm{N}^2\,. \tag{5.94}$$

The tolerances are provided in absolute value and they must be compared with the maximum value of the reaction forces involved in the following tests, being the order of magnitude $10^4$ N.

### 5.5.1 I-shaped specimen

The I-shaped specimen is subject to uniaxial tensile boundary conditions. This allows to exploit the problem's symmetry and thus only one eight-th of the specimen is studied. In Figure 5.1a the implemented geometry and boundary conditions are shown. The thickness is divided in two, so $t = 1.562$ mm. The symmetry boundary conditions are introduced with rollers acting on the faces of coordinates $x = 0$, $y = 0$, and $z = 0$, respectively. Therefore, only the normal direction to the three surfaces is set to zero, while the tangential directions are free. The external load is enforced by the clamps acting on the top face where a displacement $\bar{u}$ is prescribed in $y$ direction and the reaction force is measured, see Figure 5.1. The reference displacement is $\bar{u}_r$ and it corresponds to half of the gage length as in Figure 5.1a. The structured mesh used for the simulation is depicted in Figure 5.1b. Four elements have been used along the thickness $t$. The number of elements is $n_{el} = 896$, with local refinement close to the symmetry plane $y = 0$. The minimum element size is $h_e = 0.4$ mm, with a ratio $h_e/l_{0d} = 3.75$. The time history for the enforcement of the non-homogeneous Dirichelet boundary condition $\bar{u}(t)$ is discretized into time steps $t_1, ..., t_n, t_{n+1}, ..., t_{n_{st}}$, being $n_{st}$ the total number of steps, $\bar{u}_n := \bar{u}(t_n)$, and $\Delta\bar{u}_n := \bar{u}_{n+1} - \bar{u}_n$. In the interval $n \in [1, 140]$, the displacement increment is $\Delta\bar{u}_n = 0.01$ mm, while in the interval $n \in [141, 2140]$ the increment is $\Delta\bar{u}_n = 0.001$ mm. Thus, the total number of steps is $n_{st} = 2140$.

In Figure 5.2 the reaction force-displacement curve is represented. The two quantities are adimensionalized with respect to the specimen geometry. The engineering stress is defined as $\sigma = R/A$, being $R$ the vertical reaction force of the top clamp corresponding to $\bar{u}$, and $A = 3.124 \cdot 6.35\,\text{mm}^2$ the cross-section corresponding to the cutting plane $y = 0$. The engineering strain is the average deformation $\varepsilon = \bar{u}_r/l_{0r}$, being the reference length $l_{0r} = 12.7$ mm the initial distance between the cutting plane $y = 0$ and the strain gage. The experimental results reported in Boyce et al. (2013) are denoted with a dashed line, while those of the current model are in solid line. The good agreement of the formulation with the experimental data hides the fundamental problem of the proposed model: the effective stress approach, together with the plasticity-driven nature of the crack evolution, induces a mesh dependent behaviour of the ductile fracture response both in term of plastic deformation and phase-field (see e.g., Miehe et al. (2017)). The observation is that the following mechanism is triggered: the plastic deformation drives the evolution of the phase-field, and the effective stress approach involves that plasticity continues to develop until complete failure. The beginning of a softening response promoted by damage introduces a localization of the plastic deformation, and, hence, a localization

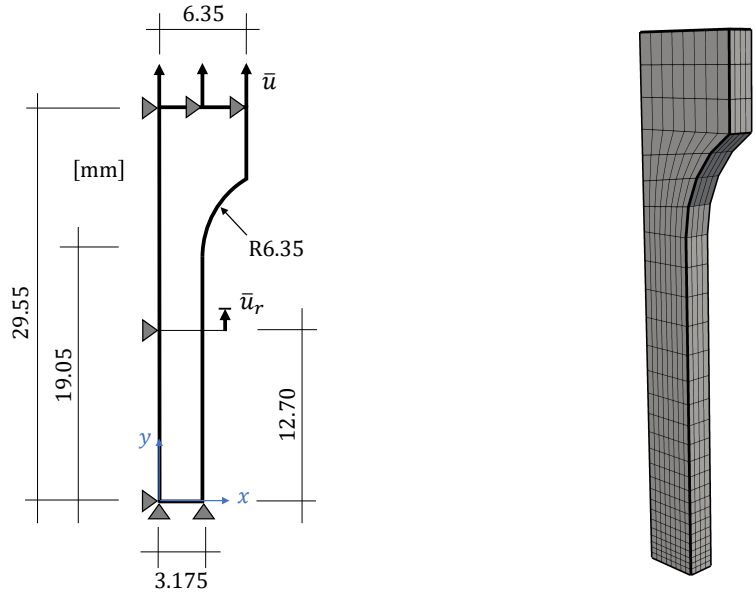


**(a)** Geometry & boundary conditions **(b)** Mesh

**Figure 5.1:** I-shaped specimen. Geometry in [mm], boundary conditions and mesh.

of the phase-field driving force. As a consequence, damage and plastic deformations localize on a single row of elements and the phase-field is not able to reach the value $d = 1$ at the Gauss points. Thus, the finite element is not able to reproduce the correct stiffness of the fractured response. The result is the long non-physical tale of the reaction force in the final part of the softening branch.

In Figure 5.3 the deformed shape, the equivalent plastic strain and the phase-field contour plots are shown for different stages of the ductile response and they are superimposed to the undeformed configuration. In Step 1400 the localization of the response is evident. The only nodes reaching $d = 1$ lie on the plane symmetry $y = 0$, while the upper set of nodes have $d \approx 0.7$. Thus, the first layer of elements is not able to represent a full crack, since the integration points never reach $d = 1$.

### 5.5.2 HOLED COMPACT TENSION SPECIMEN

The material parameters of the ductile fracture model with modulation function have been calibrated with the I-shaped specimen of the previous Section 5.5.1. The same parameters have been used to predict the response of the holed compact tension specimen. The geometry and boundary conditions are shown in Figure 5.4a. The load is enforced with a set of two pins passing through the plate's holes. The correct modeling of this boundary condition would require the simulation of contact between the pin and the hole. Yet,

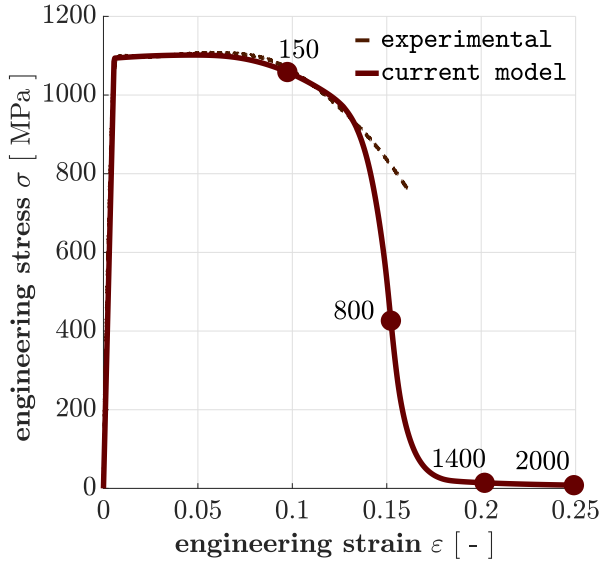


**Figure 5.2:** I-shaped specimen. Engineering stress vs strain.

the current implementation models half pin, that is clamped to the hole, as a Neo-Hookean material (i.e., no irreversible deformations and no damage) with a higher stiffness with respect to the plate. Finally, a displacement $\bar{u}$ is enforced at the half pin center. The reaction force is measured along $\bar{u}$, while the reference displacement is the Crack Opening Displacement (COD) (see Figure 5.4a). Likewise the I-shaped specimen, the symmetry condition along the plate thickness is exploited. Therefore, only half-thickness of the specimen is used $t = 1.562$ mm. The unstructured mesh is shown in Figure 5.4b. A local refinement is performed in the surrounding of the circular notch A, the holes B,C,D, and along the expected crack path towards point E. The number of elements is $n_{el} = 16835$. The minimum element size is $h_e = 0.2$ mm, with a ratio $h_e/l_{0d} = 7.50$. The thickness is resolved with 5 elements. The time history for the enforcement of the non-homogeneous Dirichelet boundary condition $\bar{u}(t)$ is discretized into time steps $t_1, ..., t_n, t_{n+1}, ..., t_{n_{st}}$, being $n_{st}$ the total number of steps, $\bar{u}_n := \bar{u}(t_n)$, and $\Delta\bar{u}_n := \bar{u}_{n+1} - \bar{u}_n$. In the interval $n \in [1, 94]$, the displacement increment is $\Delta\bar{u}_n = 0.01$ mm, while in the interval $n \in [95, 3000]$ the increment is $\Delta\bar{u}_n = 0.001$ mm. Thus, the total number of steps is $n_{st} = 3095$.

In Figure 5.5 the reaction force versus COD is shown. The experimental curves from Boyce et al. (2013) are represented in dashed line. The minimum and maximum envelopes of the data are reported only. The problem of localization for the internal variables is here evident because of the fracture propagation process. The crack pattern of the current model resembles the path A-C-E. The first drop in the reaction force corresponds to the crack propagation from the round notch A to the hole C. This is somehow reproduced by the ductile formulation and it corresponds to the reaction decrease from step

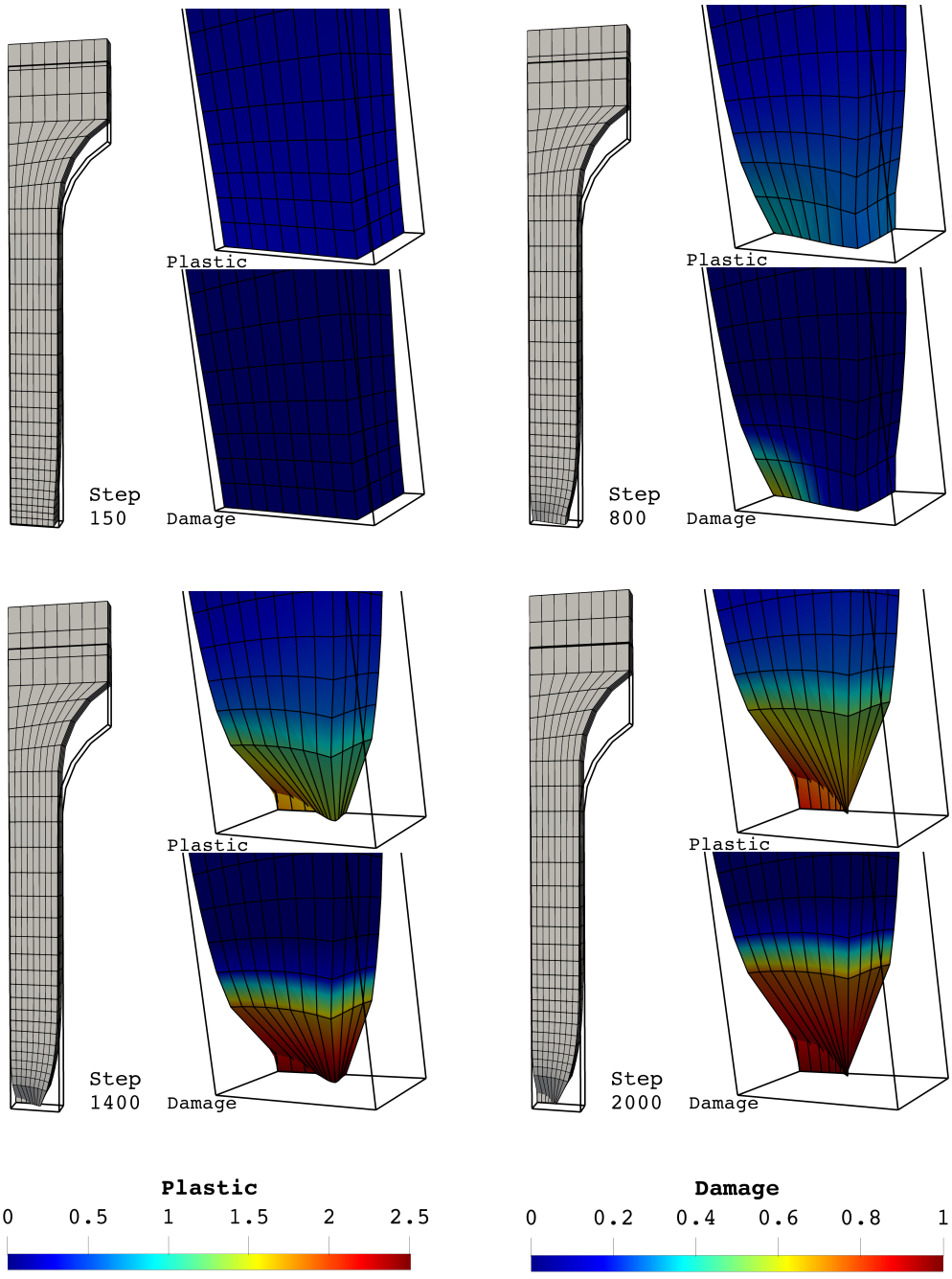


**Figure 5.3:** I-shaped specimen. Equivalent plastic strain and phase-field.

700 to step 1400. Yet, the slope of the softening branch is much less steep, compared to the experimental evidence. The reason lies exactly in the localization phenomenon outlined in Section 5.5.1 for the I-shaped specimen. The damage mesh-dependence does not allow the finite elements to develop a full crack, i.e.,

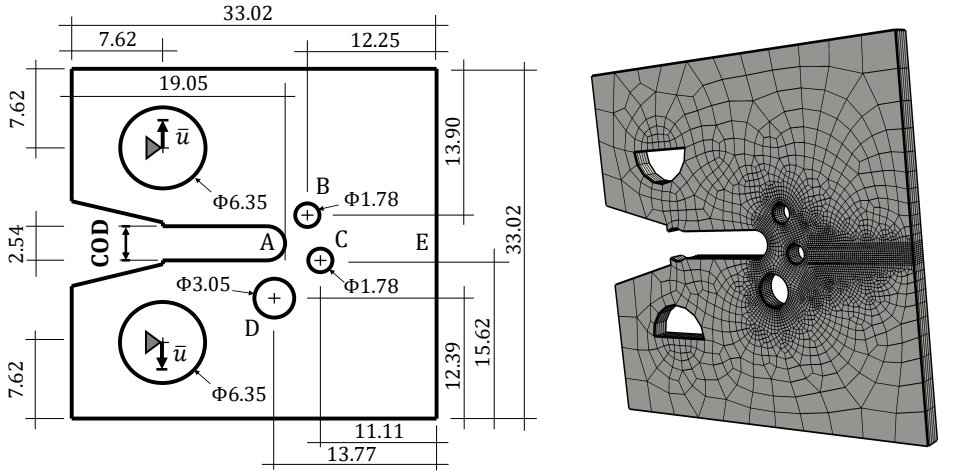


**(a)** Geometry & boundary conditions **(b)** Mesh

**Figure 5.4:** Holed compact tension specimen. Geometry in [mm], boundary conditions and mesh.

to reach $d = 1$ at the integration points. The consequence on the propagation is that the stiffness corresponding to the presence of a fracture along the path A-C is not correctly reproduced. Thus, the subsequent evolution of the crack from hole C to point E does not match the experimental result, and the propagation occurs at a much smaller time rate.

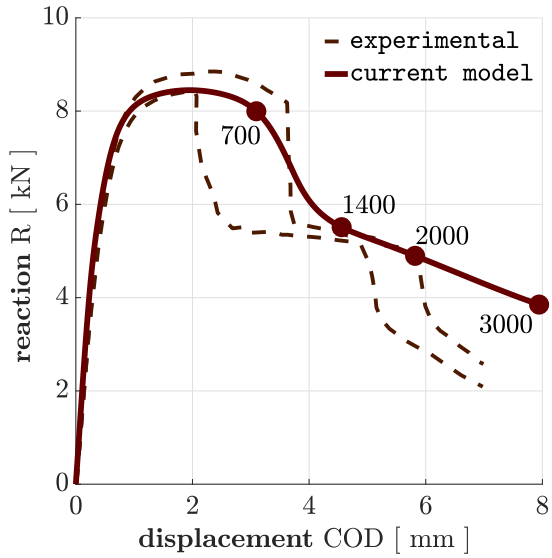


**Figure 5.5:** Holed compact tension specimen. Reaction force versus displacement.

In Figure 5.6 the deformed shape and contour plots of the phase-field are depicted. The elements reaching $d \geq 0.96$ at each node are erased from the

visualization to better render the crack pattern and propagation.

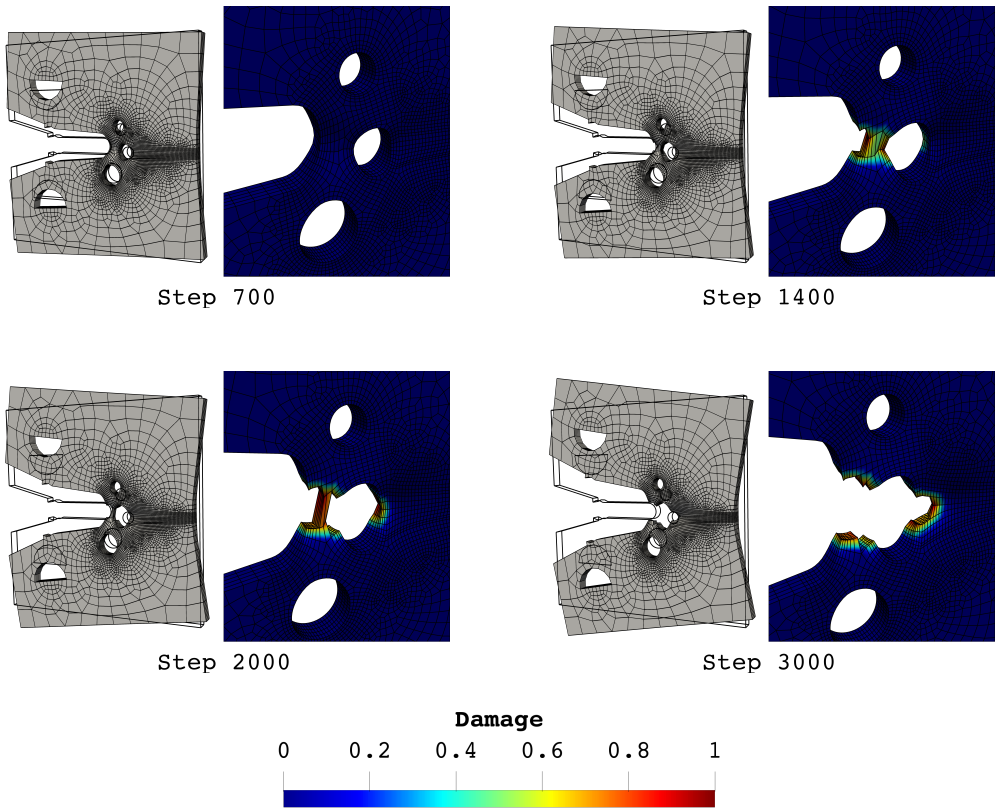


**Figure 5.6:** Holed compact tension specimen. Phase-field.

# 6 Conclusions and future developments

The aim of the current thesis has been the introduction of damage and fracture in the mechanical model of paperboard.

The first step towards this result has involved the study of a robust and reliable formulation for brittle fracture, i.e., the simplest model that couples the elastic and fracturing behavior of the material. The phase-field formulation, among many other approaches, such as XFEM, cohesive models, etc., has the advantage of being the regularization of a discontinuous problem. Thus, a continuous model renders the approach more appealing for the finite element implementation, where *continuity* is the main feature. Moreover, the variational formulation underlying such regularization provides mathematical robustness to the approach (e.g., the property of $\Gamma$-convergence). In the present work, the application to brittle materials has been limited to a standard formulation, while the attention has been shifted to a rigorous and efficient solution of the non-local problem of fracture activation arising from the phase-field approach.

The subsequent step has been the study of crack propagation in elastoplastic media. Contrary to the brittle problem, for ductile fracture there is no variational formulation in the sharp framework to be regularized. Therefore, a widely employed approach in the literature consists of the extension of the phase-field brittle model with the inclusion of the plastic dissipation in the energy formulation, based on some internal variables accounting for the evolution of plastic deformation. Conversely, the current thesis proposes a different point of view: instead of extending the brittle model with plastic internal variables, a well-established finite-step elastoplastic formulation for standard materials is enhanced with a damage-like internal variable, i.e., the phase-field. The first ingredient introduced in the formulation is a clear distinction between nominal and effective quantities, i.e., referred to nominal (undamaged) or effective (damaged) volume of the material, respectively. The importance of this differentiation lies in the suitable definition of the yield criterion for the evolution of irreversible deformations. Here, it is assumed to depend on the *effective quantities*, since plastic strains are developing in the continuous part of the medium

only. Moreover, the effective approach to ductile fracture introduces a mesh-dependence in the finite element solution: while the phase-field formulation can be regarded as a gradient-extended damage model, the local nature of plastic strain evolution, even of hardening type, may be influenced by the overall softening response. The final outcome, for plasticity-driven fracture evolution, may be a mesh-dependence of both plastic and damage internal variables. To overcome this pathological aspect of the formulation, a *gradient-extended plasticity* model is employed. Thus, two internal lengths dominate the localization of the plastic strain and of the damage field. In the current thesis, a novel algorithm for the solution of the equilibrium equations of an elastoplastic solid with non-local plasticity has been proposed and has proven to be robust and computationally efficient. Moreover, a novel formulation to model the competition between the plastic and fracture dissipation mechanisms has been presented. The idea lies in the non-variational modification of the fracture activation criterion with the introduction of a *modulation function* accounting for the coupling. This function has been calibrated in a one-dimensional uniform case to gain some better insight into its physical interpretation. A final aspect concerns the implementation of the proposed model. The effective approach involves the development of plastic deformations after the onset of damage. Therefore, large irreversible strains arise and they might induce a severe locking of the finite element solution. The strategy to solve this issue has been the use of a *reduced one-point integration* technique for 4-nodes and 8-nodes elements with *hourglass control*. While the formulation of the hourglass stabilization is rather standard, a novel approach has been proposed to account for the material non-linearity into the hourglass internal forces.

Finally, the last ingredient to be considered to address paperboard modeling is its orthotropic behavior. The current thesis proposes an entirely novel approach. The simple idea consists of the extension of the modulation function formulation introduced for isotropic ductile materials. The modulation function is a scalar quantity and its argument is a scalar quantity too. First, a damage activation criterion is stated in the plastic strain space of the material reference frame. Then, a suitable scalar variable is introduced to measure the distance of the current plastic strain state from the activation condition. The last quantity, called the *plastic strain measure*, encapsulates the orthotropic nature of the plasticity-driven crack evolution and it is used as the sole argument of the modulation function controlling the fracture activation criterion. The proposed approach can be applied to a general class of orthotropic ductile materials, and it has been successfully validated with experimental data on paperboard.

The current work leaves many open issues. The large strain ductile fracture model presented in the last chapter has been formulated within the framework of local plasticity only. A needed future development would be the gradient-extension of plasticity in the ductile fracture model at large strains. Conversely, the thesis addresses the mechanical modeling of fracture in paperboard with a focus on the in-plane, small strain behavior of the material only. Still, the sub-

sequent challenge would be the modeling of the out-of-plane response, which necessarily requires a large strain formulation. Here, the fracture mechanism occurs in the form of delamination between the different plies. To treat this case, characterized by material properties and failure mechanism substantially different from those considered for the in-plane model, a natural choice might be the introduction of an additional damage variable controlling the new dissipation mechanism.

# Appendices

# A PSOR for Sparse Matrices

The implementation of the PSOR algorithm in Section 2.6.3 for a symmetric sparse square matrix of dimension $n_{np}$ and number of non-zero entries $n_{nz}$, according to the *Compressed Column Storage* representation CCS, is shown in Algorithm 4. The input data are the three arrays $PA$ (matrix entry values), $IR$ (matrix entry row indices), and $JC$ (pointer to entries of the $IR$ array) for the description of the matrix, and the driving vector $\mathbf{q}$ that here is treated as an array $q$. The While loop iterates until a suitable convergence criterion is met. Here, only the infinite norm of the solution variation between two subsequent iterations is shown, but for a comprehensive discussion see Section 2.6.3.
The first For loop runs over the sparse matrix columns $j_{col}$ (i.e., over the solution array's components $\Delta d^k(j_{col})$). Here, the explicitness of the algorithm is clear, since the solution at every $k$-th iteration is built component-wise and the $j_{col}$-th component depends on all its previous components (from 1 to $j_{col}-1$). The scheme exploits the strict lower triangular nature of $\mathbf{L}$. In light of the CCS representation, the For loop runs over the columns of the sparse matrix.
The second For loop runs over the sparse matrix rows $h$ of the $j_{col}$-th column. The matrix-to-vector products are performed according to the standard description of sparse matrices. For fixed $r$-index, the product $Q_{rc}\,\Delta d_c^{k-1}$ of (2.46) returns a scalar, which is stored into the quantity $Q\Delta d$.
The first If statement ($i_{row} == j_{col}$) extracts the diagonal term, computes its inverse, and stores it into the scalar variable $D^{-1}$. The second If statement ($i_{row} < j_{col}$) computes the product $Q_{r>c}\,(\Delta d_c^k - \Delta d_c^{k-1})$ of (2.46). This is the scalar product between the $\mathbf{L}$ matrix's $r$-th row and a vector. Yet, the column-wise storing of the sparse matrix requires to perform that product between the $r$-th column of the $\mathbf{L}^T$ matrix and the vector. Since $\mathbf{L}^T$ is the strict upper triangular part of the sparse matrix, the If statement reads $i_{row} < j_{col}$. The result of the scalar product $Q_{r<c}\,(\Delta d_c^k - \Delta d_c^{k-1})$ is stored into the quantity $L\Delta\Delta d$, where $\Delta\Delta d$ refers to the variation of the solution between two subsequent iterations $k-1$ and $k$.

**Algorithm 4:** Projected Successive Over-Relaxation

**input :** $PA(n_{nz},1)$, $IR(n_{nz},1)$, $JC(n_{np}+1,1)$, $q(n_{np},1)$
$\Delta d^k(n_{np},1) = 0$
**while** $Res_d^{(k)} > \texttt{TOL}_d$ **do**
  $\Delta d^{k-1} = \Delta d^k$
  **for** $j_{col} \leftarrow 1$ **to** $n_{np}$ **do**
    $Q\Delta d \ = 0$
    $L\Delta\Delta d = 0$
    **for** $h \leftarrow JC(j_{col})$ **to** $JC(j_{col}+1)-1$ **do**
      $i_{row} \ = IR(h)$
      $Q\Delta d = Q\Delta d + PA(h)\,\Delta d^{k-1}(i_{row})$
      **if** $(i_{row} == j_{col})$ **then**
        $D^{-1} = [PA(k)]^{-1}$
      **end**
      **if** $(i_{row} < j_{col})$ **then**
        $L\Delta\Delta d = L\Delta\Delta d + PA(h)\ \left[\Delta d^k(i_{row}) - \Delta d^{k-1}(i_{row})\right]$
      **end**
    **end**
    $\Delta d^k(j_{col}) = \left\langle \Delta d^{k-1}(j_{col}) - D^{-1}\Big[\, Q\Delta d + q(j_{col}) + L\Delta\Delta d \,\Big] \right\rangle_+$
  **end**
  $Res_d^{(k)} = \left|\Delta d^k - \Delta d^{k-1}\right|_\infty$
**end**
**output:** $\Delta d^k(n_{np},1)$

# B Von-Mises gradient plasticity

The linearizations needed for the solution of the gradient elastoplastic problem in Section 3.5.2 with the monolithic scheme in Algorithm 3 are developed below. All operations are performed for the von-Mises plasticity without damage (see Section 3.2.4 for the constitutive functionals), thus, the tilde symbol for the effective response is omitted for the sake of clarity. Voigt notation is used throughout this appendix. For instance, the stress vector is denoted with $\boldsymbol{\sigma} = (\sigma_1, \sigma_2, \sigma_3, \tau_{12}, \tau_{13}, \tau_{23})^{\mathrm{T}}$. The element shape functions and shape functions gradients are introduced in Section 3.4. The linearization of the element internal forces vector reads:

$$\begin{aligned}
\delta \mathbf{F}_{\mathrm{I},e} &= \int_{\Omega_e} \mathbf{B}_{\mathrm{u}}^{\mathrm{T}}\, \delta\boldsymbol{\sigma}\, \mathrm{d}\Omega_e = \\
&= \underbrace{\left[\int_{\Omega_e} \mathbf{B}_{\mathrm{u}}^{\mathrm{T}} \left(\mathbf{D}^{el} - \Delta\lambda\, \mathbf{D}_{dev}^{el}\, \partial^2_{\boldsymbol{\sigma}\boldsymbol{\sigma}} f_y\, \mathbf{D}_{dev}^{el}\right) \mathbf{B}_{\mathrm{u}}\, \mathrm{d}\Omega_e\right]}_{\mathbf{K}_{\mathrm{uu},e}} \delta\widehat{\mathbf{u}}_e + \\
&+ \underbrace{\left[\int_{\Omega_e} \mathbf{B}_{\mathrm{u}}^{\mathrm{T}} \left(-\mathbf{D}_{dev}^{el}\, \partial_{\boldsymbol{\sigma}} f_y\right) \mathbf{N}_\lambda\, \mathrm{d}\Omega_e\right]}_{\mathbf{K}_{\mathrm{u}\lambda,e}} \delta\widehat{\boldsymbol{\lambda}}_e
\end{aligned} \tag{B.1}$$

where $\mathbf{D}^{el} = \partial^2_{\boldsymbol{\varepsilon}\boldsymbol{\varepsilon}} \psi^e$ is the matrix of elastic moduli and the deviatoric nature of the plastic deformation vector $\boldsymbol{\varepsilon}^p$ has been exploited. $\mathbf{D}_{dev}^{el}$ is the deviatoric elastic stiffness matrix. The linearization of the element yield vector reads:

$$\begin{aligned}
\delta \mathbf{f}_{\mathrm{Y},e} &= \int_{\Omega_e} \left[\mathbf{N}_\lambda^{\mathrm{T}}\, \delta f_y - c_p\, \mathbf{B}_\lambda^{\mathrm{T}}\, \boldsymbol{\nabla}\delta\lambda\right] \mathrm{d}\Omega_e = \\
&= \underbrace{\left[\int_{\Omega_e} \mathbf{N}_\lambda^{\mathrm{T}} \left(\mathbf{D}_{dev}^{el}\, \partial_{\boldsymbol{\sigma}} f_y\right)^{\mathrm{T}} \mathbf{B}_{\mathrm{u}}\, \mathrm{d}\Omega_e\right]}_{\mathbf{K}_{\lambda\mathrm{u},e}} \delta\widehat{\mathbf{u}}_e + \\
&\underbrace{- \left[\int_{\Omega_e} \left\{\mathbf{N}_\lambda^{\mathrm{T}} \left(\partial_{\boldsymbol{\sigma}} f_y^{\mathrm{T}}\, \mathbf{D}_{dev}^{el}\, \partial_{\boldsymbol{\sigma}} f_y + \partial_\lambda \chi\right) \mathbf{N}_\lambda + c_p\, \mathbf{B}_\lambda^{\mathrm{T}}\, \mathbf{B}_\lambda\right\}\, \mathrm{d}\Omega_e\right]}_{\mathbf{K}_{\lambda\lambda,e}} \delta\widehat{\boldsymbol{\lambda}}_e
\end{aligned} \tag{B.2}$$

The deviatoric elastic stiffness matrix for the isotropic case is $\mathbf{D}^{el}_{dev} = 2G_0\,\mathbf{I}_{dev}$, where $\mathbf{I}_{dev}$ is the deviatoric projection matrix. The use of von-Mises yield function with isotropic linear hardening leads to:

$$\Delta\lambda\,\mathbf{D}^{el}_{dev}\,\partial^2_{\boldsymbol{\sigma}\boldsymbol{\sigma}} f_y\,\mathbf{D}^{el}_{dev} = 2G_0\,\beta\left(\mathbf{I}_{dev} - \mathbf{n}^{tr}\,\mathbf{n}^{tr\mathrm{T}}\right)$$

$$\mathbf{D}^{el}_{dev}\,\partial_{\boldsymbol{\sigma}} f_y = 3G_0\,\frac{\mathbf{s}^{tr}}{\sigma^{tr}_{eq}} \quad , \quad \partial_{\boldsymbol{\sigma}} f_y^{\mathrm{T}}\,\mathbf{D}^{el}_{dev}\,\partial_{\boldsymbol{\sigma}} f_y = 3G_0$$

where $\mathbf{s}^{tr}$ is the trial elastic deviatoric stress vector, $\mathbf{n}^{tr} = \mathbf{s}^{tr}/|\mathbf{s}^{tr}|$ is the trial yield surface unit normal vector, $\sigma^{tr}_{eq} = \sqrt{3/2\,\mathsf{s}^{tr} : \mathsf{s}^{tr}}$ is the trial equivalent stress (being $\mathsf{s}$ the deviatoric stress tensor with Voigt notation $\mathbf{s}$), and $\beta := {}^{3G_0\,\Delta\lambda}/_{\sigma^{tr}_{eq}}$. The element tangent stiffness matrices and the internal forces vector are:

$$\mathbf{K}_{\mathrm{uu},e} = \int_{\Omega_e} \mathbf{B}_{\mathrm{u}}^{\mathrm{T}}\left[\mathbf{D}^{el} - 2G\,\beta\left(\mathbf{I}_{dev} - \mathbf{n}^{tr}\,\mathbf{n}^{tr\mathrm{T}}\right)\right]\mathbf{B}_{\mathrm{u}}\,\mathrm{d}\Omega_e \tag{B.3a}$$

$$\mathbf{K}_{\mathrm{u}\lambda,e} = \int_{\Omega_e} \mathbf{B}_{\mathrm{u}}^{\mathrm{T}}\left(-3G_0\,\frac{\mathbf{s}^{tr}}{\sigma^{tr}_{eq}}\right)\mathbf{N}_\lambda\,\mathrm{d}\Omega_e = \mathbf{K}^{\mathrm{T}}_{\lambda\mathrm{u},e} \tag{B.3b}$$

$$\mathbf{K}_{\lambda\lambda,e} = -\int_{\Omega_e}\left[\left(3G_0 + H_0\right)\mathbf{N}_\lambda^{\mathrm{T}}\,\mathbf{N}_\lambda + c_p\,\mathbf{B}_\lambda^{\mathrm{T}}\,\mathbf{B}_\lambda\right]\mathrm{d}\Omega_e \tag{B.3c}$$

$$\mathbf{F}_{\mathrm{I},e} = \int_{\Omega_e} \mathbf{B}_{\mathrm{u}}^{\mathrm{T}}\left[p\,\mathbf{m} + (1-\beta)\,\mathbf{s}^{tr}\right]\mathrm{d}\Omega_e \tag{B.3d}$$

where $\mathbf{m} = (1,1,1,0,0,0)^{\mathrm{T}}$ is the spherical projection vector in Voigt notation, and $p = {}^1/_3\,\mathbf{m}^{\mathrm{T}}\,\boldsymbol{\sigma}$ is the hydrostatic pressure.

# C Line search

The implemented line search procedure is based on what proposed in Nocedal and Wright (2006). The global return mapping outlined in Section 3.5.2 for the elastoplastic gradient problem with fixed damage shows how the loading-unloading condition (3.52b) is a purely displacement driven problem. Therefore, without loss of generality, it can be stated that the Lagrangian (3.19) (hereafter denoted as $\mathcal{L}$ for the sake of compactness) depends on the displacement only $\mathcal{L}(\Delta\widehat{\mathbf{u}})$, being $\Delta\widehat{\mathbf{u}}$ the global nodal displacement vector of the spatial discretization in Section 3.4. The solution update $\delta\Delta\widehat{\mathbf{u}}_k$ between two subsequent Newton iterations $k-1$ and $k$ is the result of the monolithic system (3.57) and the current solution can be written as follows:

$$\Delta\widehat{\mathbf{u}}_k = \Delta\widehat{\mathbf{u}}_{k-1} + \delta\Delta\widehat{\mathbf{u}}_k \,. \tag{C.1}$$

The new solution estimate should satisfy the condition

$$\mathcal{L}(\Delta\widehat{\mathbf{u}}_k) < \mathcal{L}(\Delta\widehat{\mathbf{u}}_{k-1}) \,.$$

Yet, this condition may not be always fulfilled by the Newton algorithm. Therefore, a line search procedure has been implemented. The step length parameter $\gamma_k$ is defined such that:

$$\Delta\widehat{\mathbf{u}}_k = \Delta\widehat{\mathbf{u}}_{k-1} + \gamma_k \, \delta\Delta\widehat{\mathbf{u}}_k \,. \tag{C.2}$$

The optimal step length minimizes the total energy between the two iterations $k-1$ and $k$:

$$\gamma_k = \arg\min_{\gamma_k^*} \left[ \mathcal{L}\Big( \Delta\widehat{\mathbf{u}}_{k-1} + \gamma_k^* \, \delta\Delta\widehat{\mathbf{u}}_k \Big) \right] \,. \tag{C.3}$$

For non-quadratic objective functions $\mathcal{L}(\Delta\widehat{\mathbf{u}})$ there is no closed form solution of the problem (C.3). Therefore, a standard procedure involves the satisfaction of the so-called Wolfe condition:

$$\mathcal{L}\big( \Delta\widehat{\mathbf{u}}_{k-1} + \gamma_k \, \delta\Delta\widehat{\mathbf{u}}_k \big) < \mathcal{L}\big( \Delta\widehat{\mathbf{u}}_{k-1} \big) + c_1 \, \gamma_k \, \delta\Delta\widehat{\mathbf{u}}_k^{\mathrm{T}} \, \mathbf{R}_{\mathrm{u}}^{(k-1)} \,, \tag{C.4}$$

where $\mathbf{R}_{\mathrm{u}}$ is the global displacement residual vector defined in (3.53) and $\mathbf{R}_{\mathrm{u}}^{(k-1)} := \mathbf{R}_{\mathrm{u}}(\Delta\widehat{\mathbf{u}}_{k-1})$ is the residual at the previous iteration used for the

**Algorithm 5:** Backtracking or steepest descent line search

```
set      γ_k = 1
while ( .not. Wolfe ) do
    update    γ_k = γ_k ρ
    Wolfe     L(Δû_{k-1} + γ_k δΔû_k) < L(Δû_{k-1}) + c_1 γ_k δΔû_k^T R_u^{(k-1)}
end
```

computation of $\delta\Delta\widehat{\mathbf{u}}_k$. The constant parameter $c_1$ for Newton type solver has the typical value $10^{-4}$ (see Nocedal and Wright (2006)).

The backtracking or steepest descent line search algorithm is shown in Algorithm 5. The idea is that the step length $\gamma_k$ is reduced by a constant parameter $\rho \in [1/10, 1/2]$. Furthermore, a minimum value $\gamma_{k,min}$ should not be reached as suggested in Nocedal and Wright (2006). An important remark must be done on the Dirichelet boundary condition of the displacement field. The minimization outlined in (C.4) must hold for all the active degrees of freedom, i.e., the degrees of freedom that contribute to the minimization of the total energy in the time step. Therefore, the constrained degrees of freedom must be excluded from the algorithm. Yet, in order to avoid a too large difference in the increment update of the active degrees of freedom and the constrained degrees of freedom a not too small threshold must be used for the step length. The chosen value is $\gamma_{k,min} = 1/2$.

# D Linear activation criteria for gradient plasticity and damage

The use of von-Mises plasticity with linear isotropic hardening (see Section 3.2.4 for the constitutive functionals) leads the element yield vector $\mathbf{f}_{\mathrm{Y},e}$ (3.50c) to be a linear function of the element plastic multiplier increment vector $\Delta\widehat{\boldsymbol{\lambda}}_e$ as follows:

$$\begin{aligned}\mathbf{f}_{\mathrm{Y},e} = &\underbrace{\int_{\Omega_e} \omega \left[\mathbf{N}_\lambda^{\mathrm{T}} \left(\sigma_{eq}^{tr} - \bar{\sigma}_{y0} - H_0\,\lambda_n\right) - c_p\,\mathbf{B}_\lambda^{\mathrm{T}}\,\boldsymbol{\nabla}\lambda_n\right] \mathrm{d}\Omega_e}_{\mathbf{f}_{\mathrm{Y},e}^{tr}} + \\ &\underbrace{-\left\{\int_{\Omega_e} \omega \left[\left(3G_0 + H_0\right)\mathbf{N}_\lambda^{\mathrm{T}}\,\mathbf{N}_\lambda + c_p\,\mathbf{B}_\lambda^{\mathrm{T}}\,\mathbf{B}_\lambda\right] \mathrm{d}\Omega_e\right\}}_{\mathbf{K}_{\lambda\lambda,e}} \Delta\widehat{\boldsymbol{\lambda}}_e\,,\end{aligned} \tag{D.1}$$

where the constant matrix $\mathbf{K}_{\lambda\lambda,e}$ and the trial equivalent stress $\sigma_{eq}^{tr}$ have already been defined in Appendix B, while the element trial yield vector is defined as:

$$\mathbf{f}_{\mathrm{Y},e}^{tr} := \int_{\Omega_e} \omega \left[\mathbf{N}_\lambda^{\mathrm{T}} \left(\sigma_{eq}^{tr} - \bar{\sigma}_{y0} - H_0\,\lambda_n\right) - c_p\,\mathbf{B}_\lambda^{\mathrm{T}}\,\boldsymbol{\nabla}\lambda_n\right] \mathrm{d}\Omega_e\,. \tag{D.2}$$

On the other hand, the choices of a quadratic degradation function and the use of an AT1 dissipation functional for the phase field lead to the following definition of the phase-field element activation vector $\mathbf{f}_{\mathrm{D},e}$ (3.50d):

$$\begin{aligned}\mathbf{f}_{\mathrm{D},e} = &\underbrace{\int_{\Omega_e} \left[\mathbf{N}_{\mathrm{d}}^{\mathrm{T}} \left(2(1-d_n)\,\widetilde{\psi}_{ep} - (f+1)\,\frac{3G_c}{8l_{0d}} + w'_\epsilon\right) - \frac{3G_c l_{0d}}{4}\,\mathbf{B}_{\mathrm{d}}^{\mathrm{T}}\,\boldsymbol{\nabla}d_n\right] \mathrm{d}\Omega_e}_{\mathbf{f}_{\mathrm{D},e}^{tr}} - \\ &\underbrace{-\left\{\int_{\Omega_e} \left[\mathbf{N}_{\mathrm{d}}^{\mathrm{T}}\,\mathbf{N}_{\mathrm{d}} \left(2\,\widetilde{\psi}_{ep} + \frac{\eta_f}{\Delta t}\right) + \frac{3G_c l_{0d}}{4}\,\mathbf{B}_{\mathrm{d}}^{\mathrm{T}}\,\mathbf{B}_{\mathrm{d}}\right] \mathrm{d}\Omega_e\right\}}_{\mathbf{K}_{dd,e}} \Delta\widehat{\mathbf{d}}_e\,,\end{aligned}$$

where the trial fracture activation vector $\mathbf{f}_{\mathrm{D},e}^{tr}$ and the the matrix $\mathbf{K}_{dd,e}$ have been defined:

$$\mathbf{f}_{\mathrm{D},e}^{tr} := \int_{\Omega_e} \left[ \mathbf{N}_{\mathrm{d}}^{\mathrm{T}} \left( 2(1-d_n)\, \widetilde{\psi}_{ep} - (f+1)\, \frac{3G_c}{8l_{0d}} + w'_{\epsilon} \right) - \right. \\ \left. - \frac{3G_c l_{0d}}{4}\, \mathbf{B}_{\mathrm{d}}^{\mathrm{T}}\, \boldsymbol{\nabla} d_n \right] \mathrm{d}\Omega_e \,, \tag{D.3a}$$

$$\mathbf{K}_{dd,e} := -\int_{\Omega_e} \left[ \mathbf{N}_{\mathrm{d}}^{\mathrm{T}}\, \mathbf{N}_{\mathrm{d}} \left( 2\, \widetilde{\psi}_{ep} + \frac{\eta_f}{\Delta t} \right) + \frac{3G_c l_{0d}}{4}\, \mathbf{B}_{\mathrm{d}}^{\mathrm{T}}\, \mathbf{B}_{\mathrm{d}} \right] \mathrm{d}\Omega_e \,. \tag{D.3b}$$

Finally, the yielding and fracture activation criteria (3.52b) and (3.52c) can be written as follows:

$$\Delta\widehat{\boldsymbol{\lambda}} \geq \mathbf{0}\,, \quad \left(\mathbf{f}_{\mathrm{Y}}^{tr} + \mathbf{K}_{\lambda\lambda}\, \Delta\widehat{\boldsymbol{\lambda}}\right) \leq \mathbf{0}\,, \quad \Delta\widehat{\boldsymbol{\lambda}}^{\mathrm{T}} \left(\mathbf{f}_{\mathrm{Y}}^{tr} + \mathbf{K}_{\lambda\lambda}\, \Delta\widehat{\boldsymbol{\lambda}}\right) = 0\,, \tag{D.4a}$$

$$\Delta\widehat{\mathbf{d}} \geq \mathbf{0}\,, \quad \left(\mathbf{f}_{\mathrm{D}}^{tr} + \mathbf{K}_{dd}\, \Delta\widehat{\mathbf{d}}\right) \leq \mathbf{0}\,, \quad \Delta\widehat{\mathbf{d}}^{\mathrm{T}} \left(\mathbf{f}_{\mathrm{D}}^{tr} + \mathbf{K}_{dd}\, \Delta\widehat{\mathbf{d}}\right) = 0\,. \tag{D.4b}$$

They correspond to the Karush-Kuhn-Tucker conditions associated to the constrained minimization of the total energy with respect to the plastic multiplier and the phase field. The specific choices adopted for the constitutive functionals make them two symmetric linear complementarity problems (SLCP) of the standard form:

$$\mathbf{x} \geq \mathbf{0}\,, \quad \left(\mathbf{q} + \mathbf{Q}\,\mathbf{x}\right) \leq \mathbf{0}\,, \quad \mathbf{x}^{\mathrm{T}} \left(\mathbf{q} + \mathbf{Q}\,\mathbf{x}\right) = 0\,.$$

The solution of these variational inequalities is sought by means of a Projected Successive Over-Relaxation algorithm (PSOR) as introduced in Mangasarian (1977) and already outlined in Section 2.6.3 and Appendix A.

# E In-plane elastoplastic model for paperboard

The tilde symbol for the effective quantities is omitted for the sake of clarity. All the quantities are written in the material reference frame where the indices 1,2 refer to the MD and CD directions, respectively. In Voigt notation, the in-plane stress and strain vector are $\boldsymbol{\sigma} = (\sigma_1, \sigma_2, \tau_{12})^{\mathrm{T}}$ and $\boldsymbol{\varepsilon} = (\varepsilon_1, \varepsilon_2, \gamma_{12})^{\mathrm{T}}$ (the same symbol is used for the tensorial and Voigt quantities with abuse of notation). The elastic evolution is stated as $\boldsymbol{\sigma} = \mathbf{D}(\boldsymbol{\varepsilon} - \boldsymbol{\varepsilon}^p)$ (see e.g., Mäkelä and Östlund (2003)), where the elastic stiffness matrix, expressed in the material reference frame, reads

$$\mathbf{D} = \frac{1}{1 - \nu_{12}\nu_{21}} \begin{bmatrix} E_1 & \nu_{21}E_1 & 0 \\ \nu_{12}E_2 & E_2 & 0 \\ 0 & 0 & G_{12}\left(1 - \nu_{12}\nu_{21}\right) \end{bmatrix}. \tag{E.1}$$

Here, $E_1$, $E_2$ are the elastic moduli in the orthotropy directions, while $\nu_{12}$ and $\nu_{21}$ are the Poisson ratios. Finally, $G_{12}$ is the in-plane shear modulus. The Xia's yield function is

$$f_y(\boldsymbol{\sigma}, \boldsymbol{\chi}) = \sum_{s=1}^{6} \left[ \left( \frac{\langle \sigma_n^{(s)}(\boldsymbol{\sigma}) \rangle_+}{\sigma_y^{(s)}(\boldsymbol{\chi})} \right)^{2k} \right] - 1\,, \tag{E.2}$$

where the normal stress $\sigma_n^{(s)}(\boldsymbol{\sigma}) = \mathbf{n}^{(s)\mathrm{T}}\boldsymbol{\sigma}$ is the projection of the stress vector along the $s$-th mechanism unit normal in the stress space. The latter in Voigt notation reads

$$\mathbf{n}^{(s)} = \left( n_1^{(s)}, n_2^{(s)}, 2n_{12}^{(s)} \right)^{\mathrm{T}}. \tag{E.3}$$

The components of each normal are material parameters to be determined experimentally Borgqvist et al. (2015), or using analytical relations Borgqvist et al. (2014). The components always refer to the material reference frame and are shown in Table E.1.

| s | $n_1$ | $n_2$ | $n_{12}$ |
|---|---|---|---|
| 1 | $n_1^{(1)}$ | $-\left(1-\left(n_1^{(1)}\right)^2\right)^{1/2}$ | 0 |
| 2 | $-\left(1-\left(n_2^{(2)}\right)^2\right)^{1/2}$ | $n_2^{(2)}$ | 0 |
| 3 | 0 | 0 | $1/\sqrt{2}$ |
| 4 | $-1$ | 0 | 0 |
| 5 | 0 | $-1$ | 0 |
| 6 | 0 | 0 | $-1/\sqrt{2}$ |

**Table E.1:** Yield unit normals components

The independent components are

$$n_1^{(1)} = \frac{1}{\sqrt{1+\nu_{12}^2}}\,, \quad n_2^{(2)} = \frac{1}{\sqrt{1+\nu_{21}^2}}\,. \tag{E.4}$$

The yield mechanisms are postulated to be uncoupled leading to the yield stresses $\sigma_y^{(s)}(\boldsymbol{\chi}) = \bar{\sigma}_{y0}^{(s)} + \chi^{(s)}$ (see e.g., Borgqvist et al. (2015)), where $\bar{\sigma}_{y0}^{(s)}$ is the initial effective yield stress of the $s$-th mechanism. The first derivatives of the Xia's yield function used in the plastic evolution laws read:

$$\frac{\partial f_y}{\partial \boldsymbol{\sigma}} = \sum_{s=1}^{6} \left[ \frac{2k}{\sigma_y^{(s)}} \left( \frac{\langle \sigma_n^{(s)} \rangle_+}{\sigma_y^{(s)}} \right)^{2k-1} \mathbf{n}^{(s)} \right], \tag{E.5a}$$

$$\frac{\partial f_y}{\partial \chi^{(s)}} = -\frac{2k}{\sigma_y^{(s)}} \left( \frac{\langle \sigma_n^{(s)} \rangle_+}{\sigma_y^{(s)}} \right)^{2k}. \tag{E.5b}$$

The elastoplastic evolution requires the solution of a local nonlinear and coupled set of equations. The integration algorithm and the computation of the consistent algorithmic tangent stiffness can be found in e.g., Ottosen and Ristinmaa (2005).

# F One-point reduced integration

In the current appendix , the nomenclature is stated for the element quantities, i.e., the shape functions and their gradients. The attention is restricted to the 4-nodes element for the sake of compactness, but the same concepts can be easily extended to the 8-nodes element. Let $\varphi$ be a generic scalar field defined over the element. The nodal quantities are denoted with $\widehat{(\cdot)}$. The nodal value of the scalar field $\varphi$ is $\widehat{\varphi}^{(a)}$, being $a$ the node label. The nodal values of the scalar field are collected into a nodal vector $\widehat{\boldsymbol{\varphi}}_e = (\widehat{\varphi}^{(1)}, \dots, \widehat{\varphi}^{(a)}, \dots, \widehat{\varphi}^{(n_{en})})^{\mathrm{T}}$.

## F.1 Modal representation

The master element is depicted in Figure F.1. The element's node label is denoted with the integer $a$ and it spans from 1 to $n_{en} = 4$.

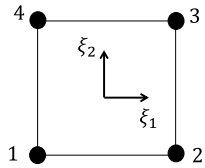


**Figure F.1:** Master four-nodes element

The shape function of the $a$-th node is $N^{(a)}(\xi_1, \xi_2) = 1/4\,(1 + \widehat{\xi}_1^{(a)}\,\xi_1)\,(1 + \widehat{\xi}_2^{(a)}\,\xi_2)$, and it can be recast into the linear $(\xi_1, \xi_2)$ and bilinear (i.e., hourglass $h := \xi_1\,\xi_2$) contributions:

$$N^{(a)}(\xi_1, \xi_2) = 1/4\Big[\underbrace{(1) + \big(\widehat{\xi}_1^{(a)}\big)\,\xi_1 + \big(\widehat{\xi}_2^{(a)}\big)\,\xi_2}_{\texttt{linear}} + \underbrace{\big(\widehat{h}^{(a)}\big)\,h}_{\texttt{hourglass}}\Big] \tag{F.1}$$

The values of the linear $\widehat{\xi}_1^{(a)}, \widehat{\xi}_2^{(a)}$ and hourglass $\widehat{h}^{(a)}$ nodal coordinates are in Table F.1.

Let $\varphi$ be a generic scalar field to be spatially discretized with finite elements, and $\varphi^h$ its element discretization. The *nodal representation* reads

$$\varphi^h(\xi_1, \xi_2) = \textstyle\sum_{a=1}^{4} N^{(a)}(\xi_1, \xi_2)\,\widehat{\varphi}^{(a)} \tag{F.2}$$

| node $a$ | 1 | 2 | 3 | 4 |
|---|---|---|---|---|
| $\widehat{\xi}_1$ | $-1$ | $+1$ | $+1$ | $-1$ |
| $\widehat{\xi}_2$ | $-1$ | $-1$ | $+1$ | $+1$ |
| $\widehat{h}$ | $+1$ | $-1$ | $+1$ | $-1$ |

**Table F.1:** Nodal $\xi_1, \xi_2$ and hourglass $h = \xi_1 \xi_2$ coordinates of four-nodes master element

being $\widehat{\varphi}^{(a)}$ the value of $\varphi$ in the $a$-th node. The manipulation of the last relation and the definition of the new coefficients:

$$c_1 := \sum_{a=1}^{4} 1/4\, \widehat{\varphi}^{(a)} \quad = \widehat{\boldsymbol{\varphi}}_e^{\mathrm{T}} \mathbf{1} \quad , \quad c_2 := \sum_{a=1}^{4} 1/4\, \xi_1^{(a)}\, \widehat{\varphi}^{(a)} = \widehat{\boldsymbol{\varphi}}_e^{\mathrm{T}} \widehat{\boldsymbol{\xi}}_1 \, ,$$
$$c_3 := \sum_{a=1}^{4} 1/4\, \xi_2^{(a)}\, \widehat{\varphi}^{(a)} = \widehat{\boldsymbol{\varphi}}_e^{\mathrm{T}} \widehat{\boldsymbol{\xi}}_2 \, , \quad c_4 := \sum_{a=1}^{4} 1/4\, h^{(a)}\, \widehat{\varphi}^{(a)} = \widehat{\boldsymbol{\varphi}}_e^{\mathrm{T}} \widehat{\mathbf{h}}$$

where th enodal vectors of the constant $\mathbf{1}$, linear $\widehat{\boldsymbol{\xi}}_1, \widehat{\boldsymbol{\xi}}_2$, and hourglass $\widehat{\mathbf{h}}$ coordinates are:

$$[\mathbf{1}]_a = 1/4 \quad , \quad [\widehat{\boldsymbol{\xi}}_k]_a = 1/4\, \xi_k^{(a)} \quad , \quad [\widehat{\mathbf{h}}]_a = 1/4\, h^{(a)} \tag{F.3}$$

The nodal coordinates vectors have unit norm and they are endowed with the fundamental orthogonality properties:

$$\mathbf{1}^{\mathrm{T}} \widehat{\boldsymbol{\xi}}_k = 0 \quad , \quad \mathbf{1}^{\mathrm{T}} \widehat{\mathbf{h}} = 0 \quad , \quad \widehat{\boldsymbol{\xi}}_k^{\mathrm{T}} \widehat{\mathbf{h}} = 0 \tag{F.4}$$

The *modal representation* of the element solution then reads:

$$\varphi^h(\xi_1, \xi_2) = \left(\widehat{\boldsymbol{\varphi}}_e^{\mathrm{T}} \mathbf{1}\right) + \left(\widehat{\boldsymbol{\varphi}}_e^{\mathrm{T}} \widehat{\boldsymbol{\xi}}_1\right) \xi_1 + \left(\widehat{\boldsymbol{\varphi}}_e^{\mathrm{T}} \widehat{\boldsymbol{\xi}}_2\right) \xi_2 + \left(\widehat{\boldsymbol{\varphi}}_e^{\mathrm{T}} \widehat{\mathbf{h}}\right) h \tag{F.5}$$

The relation between the nodal representation and the modal representation is obtained evaluating the expression (F.5) at each node.

$$\widehat{\boldsymbol{\varphi}}_e = \underbrace{c_1\, \mathbf{1} + c_2\, \widehat{\boldsymbol{\xi}}_1 + c_3\, \widehat{\boldsymbol{\xi}}_2}_{\texttt{linear } \widehat{\boldsymbol{\varphi}}_e^{lin}} + \underbrace{c_4\, \widehat{\mathbf{h}}}_{\texttt{hourglass } \widehat{\boldsymbol{\varphi}}_e^{hg}} = \widehat{\boldsymbol{\varphi}}_e^{lin} + \widehat{\boldsymbol{\varphi}}_e^{hg} \tag{F.6}$$

where all the modal vectors have dimension $n_{en} = 4$. The `rigid body mode` vector is $\mathbf{1}$. The `tensile mode` vector $\widehat{\boldsymbol{\xi}}_1$ and the `shear mode` vector $\widehat{\boldsymbol{\xi}}_2$ have components provided by the nodal coordinates $(\xi_1, \xi_2)$ in Table F.1. The `hourglass mode` $\widehat{\mathbf{h}}$ has components provided by the nodal hourglass coordinate $h = \xi_1 \xi_2$ in Table F.1. The fundamental modes of the $i$-th component of the displacement are shown in Figure F.2.

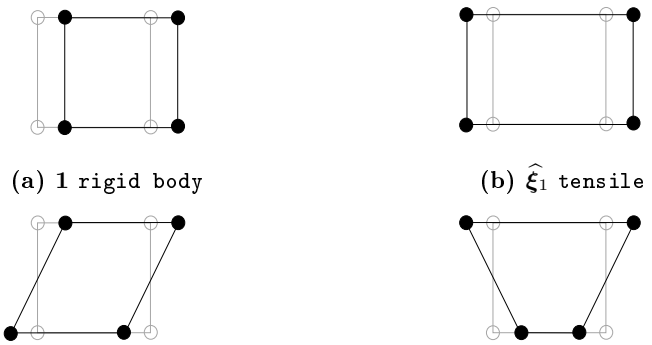

(a) 1 rigid body (b) $\widehat{\boldsymbol{\xi}}_1$ tensile

(c) $\widehat{\boldsymbol{\xi}}_2$ shear (d) $\widehat{\mathbf{h}}$ hourglass

**Figure F.2:** Fundamental modes in the $i$-th physical component of the displacement.

## F.2 PHYSICAL GRADIENTS

The vectors of the nodal coordinates in each $i$-th physical direction and the shape functions are defined as

$$\hat{\mathbf{x}}_i := \begin{pmatrix} \widehat{x}_i^{(1)} & \widehat{x}_i^{(2)} & \widehat{x}_i^{(3)} & \widehat{x}_i^{(4)} \end{pmatrix}^{\mathrm{T}} \tag{F.7}$$

$$\mathbf{N} := \begin{pmatrix} N^{(1)} & N^{(2)} & N^{(3)} & N^{(4)} \end{pmatrix}^{\mathrm{T}} \tag{F.8}$$

The physical gradients of the shape functions in each physical direction in the centroid of the element are

$$\mathbf{b}_1 := \frac{\partial \mathbf{N}}{\partial x_1}(\boldsymbol{\xi} = \mathbf{0}) = \frac{1}{2\,\Omega_e} \begin{bmatrix} \widehat{x}_2^{(24)} & \widehat{x}_2^{(31)} & \widehat{x}_2^{(42)} & \widehat{x}_2^{(13)} \end{bmatrix}^{\mathrm{T}} \tag{F.9}$$

$$\mathbf{b}_2 := \frac{\partial \mathbf{N}}{\partial x_2}(\boldsymbol{\xi} = \mathbf{0}) = \frac{1}{2\,\Omega_e} \begin{bmatrix} \widehat{x}_1^{(42)} & \widehat{x}_1^{(13)} & \widehat{x}_1^{(24)} & \widehat{x}_1^{(31)} \end{bmatrix}^{\mathrm{T}} \tag{F.10}$$

where the relative $i$-th coordinates of each $kh$-th couple of nodes are defined:

$$\widehat{x}_i^{(kh)} := \widehat{x}_i^{(k)} - \widehat{x}_i^{(h)} \qquad \text{with} \qquad \widehat{x}_i^{(kh)} = -\widehat{x}_i^{(kh)} \tag{F.11}$$

The fundamental orthogonality property that induces spurious modes in the reduced integration is

$$\widehat{\mathbf{h}}^{\mathrm{T}} \mathbf{b}_i = 0 \tag{F.12}$$

# Bibliography


Aifantis, E. C. (1992). On the role of gradients in the localization of deformation and fracture. *International Journal of Engineering Science*, 30(10):1279–1299.

Alessi, R., Ambati, M., Gerasimov, T., Vidoli, S., and De Lorenzis, L. (2018a). Comparison of phase-field models of fracture coupled with plasticity. In *Computational Methods in Applied Sciences*, volume 46, pages 1–21. Springer Netherland.

Alessi, R., Marigo, J.-J., Maurini, C., and Vidoli, S. (2018b). Coupling damage and plasticity for a phase-field regularisation of brittle, cohesive and ductile fracture: one-dimensional examples. *International Journal of Mechanical Sciences*, 149:559–576.

Alessi, R., Marigo, J. J., and Vidoli, S. (2014). Gradient damage models coupled with plasticity and nucleation of cohesive cracks. *Archive for Rational Mechanics and Analysis*, 214:575–615.

Ambati, M., Gerasimov, T., and De Lorenzis, L. (2015a). A review on phase-field models of brittle fracture and a new fast hybrid formulation. *Computational Mechanics*, 55:383–405.

Ambati, M., Gerasimov, T., and De Lorenzis, L. (2015b). Phase-field modeling of ductile fracture. *Computational Mechanics*, 46:1017–1040.

Ambati, M., Kruse, R., and De Lorenzis, L. (2016). A phase-field model for ductile fracture at finite strains and its experimental verification. *Computational Mechanics*, 57.

Ambrosio, L. and Tortorelli, V. M. (1990). Approximation of functional depending on jumps by elliptic functional via gamma-convergence. *Communications on Pure and Applied Mathematics*, 43(8):999–1063.

Amor, H., Marigo, J. J., and Maurini, C. (2009). Regularized formulation of the variational brittle fracture with unilateral contact: Numerical experiments. *Journal of the Mechanics and Physics of Solids*, 57:1209–1229.

Belytschko, T. and Bachrach, W. E. (1986). Efficient implementation of quadrilaterals with high coarse-mesh accuracy. *Computer Methods in Applied Mechanics and Engineering*, 54(3):279–301.

Belytschko, T. and Bindeman, L. P. (1991). Assumed strain stabilization of the 4-node quadrilateral with 1-point quadrature for nonlinear problems. *Applied Mechanics and Engineering*, 88:311–340.

Belytschko, T., Liu, W. K., Moran, B., and Elkhodary, K. (2014). *Nonlinear finite elements for continua and structures*. John wiley & sons.

Belytschko, T., Ong, J. S.-J., Wing Kam Liu, and Kennedy, J. M. (1984). Hourglass control in linear and nonlinear problems. *Computer Methods in Applied Mechanics and Engineering*, 43(3):251–276.

Bleyer, J. and Alessi, R. (2018). Phase-field modeling of anisotropic brittle fracture including several damage mechanisms. *Computer Methods in Applied Mechanics and Engineering*, 336:213–236.

Bonet, J. and Bhargava, P. (1995). A uniform deformation gradient hexahedron element with artificial hourglass control. *International Journal for Numerical Methods in Engineering*, 38(16):2809–2828.

Borden, M. J., Hughes, T. J., Landis, C. M., Anvari, A., and Lee, I. J. (2016). A phase-field formulation for fracture in ductile materials: Finite deformation balance law derivation, plastic degradation, and stress triaxiality effects. *Computer Methods in Applied Mechanics and Engineering*, 312:130–166.

Borgqvist, E., Lindström, T., Tryding, J., Wallin, M., and Ristinmaa, M. (2014). Distortional hardening plasticity model for paperboard. *International Journal of Solids and Structures*, 51(13):2411–2423.

Borgqvist, E., Wallin, M., Ristinmaa, M., and Tryding, J. (2015). An anisotropic in-plane and out-of-plane elasto-plastic continuum model for paperboard. *Composite Structures*, 126:184–195.

Borgqvist, E., Wallin, M., Tryding, J., Ristinmaa, M., and Tudisco, E. (2016). Localized deformation in compression and folding of paperboard. *Packaging Technology and Science*, 29(7):397–414.

Bourdin, B. (2007). Numerical implementation of the variational formulation for quasi-static brittle fracture. *Interfaces and Free Boundaries*, 9(3):411–430.

Bourdin, B., Francfort, G. A., and Marigo, J. J. (2000). Numerical experiments in revisited brittle fracture. *Journal of the Mechanics and Physics of Solids*, 48:797–826.

Boyce, B., Kramer, S., Fang, H., Cordova, T., Neilsen, M., Dion, K., Kaczmarowski, A., Karasz, E., Xue, L., Gross, A., Ghahremaninezhad, A., Ravi-Chandar, K., Lin, S.-P., Chi, S.-W., Chen, J.-S., Yreux, E., Rüter, M., Qian, D., Zhou, Z., and Wierzbicki, T. (2013). The sandia fracture challenge: blind round robin predictions of ductile tearing. *International Journal of Fracture*, 10:1007.

Chambolle, A., Conti, S., and Francfort, G. (2018). Approximation of a brittle fracture energy with a constraint of non-interpenetration. *Archive for Rational Mechanics and Analysis*, 228(3):867–889.

Chen, N. and Silberstein, M. N. (2019). A micromechanics-based damage model for non-woven fiber networks. *International Journal of Solids and Structures*, 160:18–31.

Choo, J. and Sun, W. C. (2018). Coupled phase-field and plasticity modeling of geological materials: From brittle fracture to ductile flow. *Computer Methods in Applied Mechanics and Engineering*, 330:1–32.

Comi, C., Corigliano, A., and Maier, G. (1991). Extremum properties of finite-step solutions in elastoplasticity with nonlinear mixed hardening. *International Journal of Solids and Structures*, 27(8):965–981.

Comi, C., Maier, G., and Perego, U. (1992). Generalized variable finite element modeling and extremum theorems in stepwise holonomic elastoplasticity with internal variables. *Computer Methods in Applied Mechanics and Engineering*, 96(2).

Comi, C. and Perego, U. (1995). A unified approach for variationally consistent finite elements in elastoplasticity. *Computer Methods in Applied Mechanics and Engineering*, 121(1):323–344.

Comi, C. and Perego, U. (1996a). A generalized variable formulation for gradient dependent softening plasticity. *International Journal for Numerical Methods in Engineering*, 39:3731–3755.

Comi, C. and Perego, U. (1996b). A generalized variable formulation for gradient dependent softening plasticity. *International Journal for Numerical Methods in Engineering*, 39:3731–3755.

Comi, C. and Perego, U. (2001). Fracture energy based bi-dissipative damage model for concrete. *International Journal of Solids and Structures*, 38:6427–6454.

Corigliano, A. (1994). Numerical analysis of discretized elastoplastic systems using the generalized mid-point time integration. *Engineering Computations*, 11(5):389–411.

Dafalias, Y. F. (1984). The plastic spin concept and a simple illustration of its role in finite plastic transformations. *Mechanics of Materials*, 3(3):223–233.

Dafalias, Y. F. (1985). The Plastic Spin. *Journal of Applied Mechanics*, 52(4):865–871.

Dal Maso, G. (1993). *An Introduction to gamma-convergence.*

De Borst, R. and Mühlhaus, H. B. (1992). Gradient-dependent plasticity: Formulation and algorithmic aspects. *International Journal for Numerical Methods in Engineering*, 35(3):521–539.

de Souza Neto, E., Perić, D., Dutko, M., and Owen, D. (1996). Design of simple low order finite elements for large strain analysis of nearly incompressible solids. *International Journal of Solids and Structures*, 33(20):3277–3296.

de Souza Neto, E., Peric, D., and Owen, D. (2008). *Computational methods for plasticity: theory and applications.* John Wiley and Sons.

Dean, A., Reinoso, J., Jha, N., Mahdi, E., and Rolfes, R. (2020). A phase field approach for ductile fracture of short fibre reinforced composites. *Theoretical and Applied Fracture Mechanics*, 106:102495.

Dean, A., Sahraee, S., Reinoso, J., and Rolfes, R. (2016). Finite deformation model for short fiber reinforced composites: Application to hybrid metal-composite clinching joints. *Composite Structures*, 151:162–171.

Dittmann, M., Aldakheel, F., Schulte, J., Wriggers, P., and Hesch, C. (2018). Variational phase-field formulation of non-linear ductile fracture. *Computer Methods in Applied Mechanics and Engineering*, 342:71–94.

Duda, F. P., Ciarbonetti, A., Sánchez, P. J., and Huespe, A. E. (2015). A phase-field/gradient damage model for brittle fracture in elastic–plastic solids. *International Journal of Plasticity*, 65:269–296.

Fang, J., Wu, C., Li, J., Liu, Q., Wu, C., Sun, G., and Li, Q. (2019). Phase field fracture in elasto-plastic solids: Variational formulation for multi-surface plasticity and effects of plastic yield surfaces and hardening. *International Journal of Mechanical Sciences*, 156:382–396.

Flanagan, D. P. and Belytschko, T. (1981). A uniform strain hexahedron and quadrilateral with orthogonal hourglass control. *International Journal for Numerical Methods in Engineering*, 17(5):679–706.

Forest, S. (2009). Micromorphic Approach for Gradient Elasticity, Viscoplasticity, and Damage. *Journal of Engineering Mechanics*, 135(3):117–131.

Francfort, G. A., Bourdin, B., and Marigo, J. J. (2008). The variational approach to fracture. *Journal of Elasticity*, 91:5–148.

Francfort, G. A. and Marigo, J. J. (1998). Revisiting brittle fracture as an energy minimization problem. *Journal of the Mechanics and Physics of Solids*, 46(8):1319–1342.

Garrison, W. M. and Moody, N. R. (1987). Ductile fracture. *Journal of Physics and Chemistry of Solids*, 48(11):1035–1074.

Gerasimov, T. and De Lorenzis, L. (2016). A line search assisted monolithic approach for phase-field computing of brittle fracture. *Computer Methods in Applied Mechanics and Engineering*, 312:276–303.

Gerasimov, T. and De Lorenzis, L. (2019). On penalization in variational phase-field models of brittle fracture. *Computer Methods in Applied Mechanics and Engineering*, 354:990–1026.

Giacomini, A. (2005). Ambrosio-Tortorelli approximation of quasi-static evolution of brittle fractures. *Calculus of Variations and Partial Differential Equations*, 22(2):129–172.

Griffith, A. (1920). The phenomena of rupture and flow in solids. *Philosophical Transactions of the Royal Society of London*, 221-A:163–198.

Halphen, B. and Son, N. Q. (1975). On generalized standard materials. [sur les materiaux standards generalises.]. *J Mec*, 14(1):39–63.

Han, J., Matsubara, S., Moriguchi, S., Kaliske, M., and Terada, K. (2022). Crack phase-field model equipped with plastic driving force and degrading fracture toughness for ductile fracture simulation. *Computational Mechanics*, 69:151–175.

Holzapfel, G. (2000). *Nonlinear solid mechanics: a continuum approach for engineering*. John Wiley and Sons.

Hu, T., Talamini, B., Stershic, A. J., Tupek, M. R., and Dolbow, J. E. (2021). A variational phase-field model for ductile fracture with coalescence dissipation. *Computational Mechanics*, 68:311–335.

Huang, C. and Gao, X. (2019). Development of a phase field method for modeling brittle and ductile fracture. *Computational Materials Science*, 169:109089.

Isaksson, P., Gradin, P., and Kulachenko, A. (2006). The onset and progression of damage in isotropic paper sheets. *International Journal of Solids and Structures*, 43(3):713–726.

Isaksson, P. and Hägglund, R. (2009). Structural effects on deformation and fracture of random fiber networks and consequences on continuum models. *International Journal of Solids and Structures*, 46(11):2320–2329.

Isaksson, P., Hägglund, R., and Gradin, P. (2004). Continuum damage mechanics applied to paper. *International Journal of Solids and Structures*, 41(16):4731–4755.

Kumar, A., Bourdin, B., Francfort, G. A., and Lopez-Pamies, O. (2020). Revisiting nucleation in the phase-Field approach to brittle fracture. *Journal of the Mechanics and Physics of Solids*, 142:104027.

Lee, E. H. (1969). Elastic-Plastic Deformation at Finite Strains. *Journal of Applied Mechanics*, 36(1):1–6.

Li, B. and Maurini, C. (2019). Crack kinking in a variational phase-field model of brittle fracture with strongly anisotropic surface energy. *Journal of the Mechanics and Physics of Solids*, 125:502–522.

Li, H., Fu, M., Lu, J., and Yang, H. (2011). Ductile fracture: Experiments and computations. *International Journal of Plasticity*, 27(2):147–180.

Mangasarian, O. (1977). Solution of Symmetric Linear Complementarity Problems by Iterative methods. *Journal of Optimization Theory and Applications*, 22:465–485.

Marengo, A., Patton, A., Negri, M., Perego, U., and Reali, A. (2021). A rigorous and efficient explicit algorithm for irreversibility enforcement in phase-field finite element modeling of brittle crack propagation. *Computer Methods in Applied Mechanics and Engineering*, 387:114137.

Miehe, C., Aldakheel, F., and Mauthe, S. (2013). Mixed variational principles and robust finite element implementations of gradient plasticity at small strains. *International Journal for Numerical Methods in Engineering*, 94:1037–1074.

Miehe, C., Aldakheel, F., and Raina, A. (2016). Phase field modeling of ductile fracture at finite strains: A variational gradient-extended plasticity-damage theory. *International Journal of Plasticity*, 84:1–32.

Miehe, C., Aldakheel, F., and Teichtmeister, S. (2017). Phase-field modeling of ductile fracture at finite strains: A robust variational-based numerical implementation of a gradient-extended theory by micromorphic regularization. *International Journal for Numerical Methods in Engineering*, 111:816–863.

Miehe, C., Hofacker, M., and Welschinger, F. (2010a). A phase field model for rate-independent crack propagation: Robust algorithmic implementation based on operator splits. *Computer Methods in Applied Mechanics and Engineering*, 199:2765–2778.

Miehe, C., Welschinger, F., and Hofacker, M. (2010b). Thermodynamically consistent phase-field models of fracture: Variational principles and multi-field FE implementations. *International Journal for Numerical Methods in Engineering*, 83(10):1273–1311.

Mäkelä, P. and Östlund, S. (2003). Orthotropic elastic–plastic material model for paper materials. *International Journal of Solids and Structures*, 40(21):5599–5620.

Mumford, D. and Shah, J. (1989). Optimal approximations by piecewise smooth functions and associated variational problems. *Communications on Pure and Applied Mathematics*, 42(5):577–685.

Niskanen, K., Kettunen, H., and Yu, Y. (2001). Damage width: a measure of the size of fracture process zone. In *The science of papermaking, transactions of the 12th fundamental research symposium, Oxford.*

Nocedal, J. and Wright, S. J. (2006). *Numerical Optimization.* Springer, New York, NY, USA, 2e edition.

Nygårds, M., Hallbäck, N., Just, M., and Tryding, J. (2005). A finite element model for simulations of creasing and folding of paperboard. In *Abaqus users' conference.*

Nygårds, M., Just, M., and Tryding, J. (2009). Experimental and numerical studies of creasing of paperboard. *International Journal of Solids and Structures*, 46(11):2493–2505.

Ortiz, M. and Martin, J. B. (1989). Symmetry-preserving return mapping algorithms and incrementally extremal paths: A unification of concepts. *International Journal for Numerical Methods in Engineering*, 28(8):1839–1853.

Ottosen, N. S. and Ristinmaa, M. (2005). *The mechanics of constitutive modeling.* Elsevier.

Quintanas-Corominas, A., Reinoso, J., Casoni, E., Turon, A., and Mayugo, J. (2019). A phase field approach to simulate intralaminar and translaminar fracture in long fiber composite materials. *Composite Structures*, 220:899–911.

Raina, A. and Miehe, C. (2016). A phase-field model for fracture in biological tissues. *Biomechanics and modeling in mechanobiology*, 15(3):479–496.

Razanica, S., Larsson, R., and Josefson, B. (2019). A ductile fracture model based on continuum thermodynamics and damage. *Mechanics of Materials*, 139:103197.

Reddy, B. D., Martin, J. B., and Griffin, T. B. (1987). Extremal paths and holonomic constitutive laws in elastoplasticity. *Quarterly of Applied Mathematics*, 45(3):487–502.

Rodriguez, P., Ulloa, J., Samaniego, C., and Samaniego, E. (2018). A variational approach to the phase field modeling of brittle and ductile fracture. *International Journal of Mechanical Sciences*, 144:502–517.

Samaniego, C., Ulloa, J., Rodríguez, P., Houzeaux, G., Vázquez, M., and Samaniego, E. (2021). A phase-field model for ductile fracture with shear bands: A parallel implementation. *International Journal of Mechanical Sciences*, 200:106424.

Shishvan, S. S., Assadpour-asl, S., and Martínez-Pañeda, E. (2021). A mechanism-based gradient damage model for metallic fracture. *Engineering Fracture Mechanics*, 255:107927.

Simo, J. (1988). A framework for finite strain elastoplasticity based on maximum plastic dissipation and the multiplicative decomposition: Part i. continuum formulation. *Computer Methods in Applied Mechanics and Engineering*, 66(2):199–219.

Simo, J. and Hughes, T. (1998). *Computational Inelasticity*. Springer-Verlag, New York.

Simo, J. and Miehe, C. (1992). Associative coupled thermoplasticity at finite strains: Formulation, numerical analysis and implementation. *Computer Methods in Applied Mechanics and Engineering*, 98(1):41–104.

Simo, J., Taylor, R., and Pister, K. (1985). Variational and projection methods for the volume constraint in finite deformation elasto-plasticity. *Computer Methods in Applied Mechanics and Engineering*, 51(1):177–208.

Simo, J. C. and Honein, T. (1990). Variational formulation, discrete conservation laws, and path-domain independent integrals for elasto-viscoplasticity. *Journal of Applied Mechanics*, 57(3):488–497.

Simon, J.-W. (2021). A review of recent trends and challenges in computational modeling of paper and paperboard at different scales. *Archives of Computational Methods in Engineering*, 28(4):2409–2428.

Stenberg, N. and Fellers, C. (2002). Out-of-plane poisson's ratios of paper and paperboard. *Nordic pulp & paper research journal*, 17(4):387–394.

Talamini, B., Tupek, M. R., Stershic, A. J., Hu, T., Foulk, J. W., Ostien, J. T., and Dolbow, J. E. (2021). Attaining regularization length insensitivity in phase-field models of ductile failure. *Computer Methods in Applied Mechanics and Engineering*, 384:113936.

Tanné, E., Li, T., Bourdin, B., Marigo, J.-J., and Maurini, C. (2018). Crack nucleation in variational phase-field models of brittle fracture. *Journal of the Mechanics and Physics of Solids*, 110:80–99.

Teichtmeister, S., Kienle, D., Aldakheel, F., and Keip, M.-A. (2017). Phase field modeling of fracture in anisotropic brittle solids. *International Journal of Non-Linear Mechanics*, 97:1–21.

Ulloa, J., Rodríguez, P., and Samaniego, E. (2016). On the modeling of dissipative mechanisms in a ductile softening bar. *Journal of Mechanics of Materials and Structures*, 11(4):463–490.

Wambacq, J., Ulloa, J., Lombaert, G., and François, S. (2021). Interior-point methods for the phase-field approach to brittle and ductile fracture. *Computer Methods in Applied Mechanics and Engineering*, 375:113612.

Winkler, B. (2001). *Traglastuntersuchungen von unbewehrten und bewehrten Betonstrukturen auf der Grundlage eines objektiven Werkstoffgesetzes fur Beton*. PhD thesis, Innsbruck University Press.

Xia, Q. S., Boyce, M. C., and Parks, D. M. (2002). A constitutive model for the anisotropic elastic–plastic deformation of paper and paperboard. *International Journal of Solids and Structures*, 39(15):4053–4071.

Yin, B. and Kaliske, M. (2020). A ductile phase-field model based on degrading the fracture toughness: Theory and implementation at small strain. *Computer Methods in Applied Mechanics and Engineering*, 366:113068.